SEISMIC CONSTRAINTS ON SHALLOW CRUSTAL PROCESSES
AT THE EAST PACIFIC RISE

by

GAIL LYNN CHRISTESON

B.S., Texas A&M University (1988)

SUBMITTED IN PARTIAL FULFILLMENT
OF THE REQUIREMENTS FOR THE DEGREE OF

DOCTOR OF PHILOSOPHY

at the

MASSACHUSETTS INSTITUTE OF TECHNOLOGY

and the

WOODS HOLE OCEANOGRAPHIC INSTITUTION

February, 1994

© Gail L. Christeson, 1994

The author hereby grants to MIT and WHOI permission to reproduce and distribute copies of this thesis document in whole or in part.

Signature of Author___

Joint Program in Oceanography/
Applied Ocean Science and Engineering
Massachusetts Institute of Technology/
Woods Hole Oceanographic Institution
February, 1994

Certified by___

G.M. Purdy, Thesis Supervisor

Accepted by_____

M.K. McNutt
Chair, Joint Committee for Marine Geology and Geophysics

SEISMIC CONSTRAINTS ON SHALLOW CRUSTAL PROCESSES AT THE EAST PACIFIC RISE

by

Gail Lynn Christeson

submitted to the Department of Earth, Atmospheric, and Planetary Sciences,
Massachusetts Institute of Technology
and
the Department of Geology and Geophysics,
Woods Hole Oceanographic Institution
on December 20, in partial fulfillment of the requirements for the degree of Doctor of
Philosophy

ABSTRACT

This thesis is concerned with understanding how oceanic crust is emplaced at mid-ocean ridges. The emphasis is upon fast-spreading ridges, and the use of seismic techniques to image the uppermost several hundred meters of the crust. We present the results of nine on-bottom seismic refraction experiments carried out over young East Pacific Rise (EPR) crust. The experiments are unusual in that both the source and receiver are located within a few meters of the seafloor, allowing high-resolution determinations of shallow crustal structure. Three experiments were located within the axial summit caldera (ASC), over 'zero-age' crust. The seismic structure at these three locations is fundamentally the same, with a thin (<60 m) surficial low-velocity (<2.5 km/s) layer, a 100-150 m thick transition zone with velocities increasing by approximately 2.5 km/s, and a layer with velocities of ~5 km/s at a depth below the seafloor of 130-190 m. The surficial low-velocity layer and transition zone are defined as seismic layer 2A, and the ~5 km/s layer as layer 2B. Both the surficial low-velocity layer and the transition zone double in thickness within ~1 km of the rise axis, with the depth to the 2A/2B boundary increasing from ~150 m to 300-350 m over this range. The doubling of layer 2A thickness within 1-2 km of the rise axis is confirmed by multi-channel seismic (MCS) and wide-angle profile (WAP) data, which also indicate that there is no further systematic change in thickness with greater range from the rise axis. Inversions for attenuation structure demonstrate that the layer 2A/2B interface is not only a velocity boundary, but also an attenuation boundary, with Q increasing from 10-20 within layer 2A to >70 in layer 2B.

The results of MCS and wide-angle experiments over plausible velocity structures are predicted quantitatively, based on velocity models constructed from on-bottom seismic refraction experiments and expanding spread profiles. We conclude that the accuracy of correlating the prominent shallow reflector observed in MCS and WAP data with the layer 2A/2B boundary is strongly dependent on the structure within layer 2A. If layer 2A consists of a surficial low-velocity layer overlying a steep velocity gradient (our gradient model), then there is an excellent correspondence between the two-way travel times to the shallow reflector and the base of layer 2A. However, the shallow reflector may follow structure within layer 2A if the upper crust contains more than one high-gradient region (our step model). A shallow structure similar to the step model is consistent with on-bottom refraction experiments and expanding spread profiles located over zero-age EPR crust. With distance from the rise axis, this step-like structure is apparently destroyed, and is converted into a single steep gradient similar in appearance to our gradient model.

Layer 2A is interpreted to be composed of the extrusive section and transition zone, with layer 2B consisting of the sheeted dike complex. This implies that the top of the dikes subsides from 150-200 m to 250-450 m within 1-2 km of the rise axis, and then remains at a relatively constant depth beneath the seafloor. The thickening of the extrusive layer is interpreted to be due to lava that either overflows the ASC walls, is emplaced through eruptions outside of the ASC, or travels laterally from the ASC through subseafloor conduits. Off-axis sill emplacement also contributes to the thickening of layer 2A. According to this model, the shallow crustal architecture is in place within 1-2 km of the rise axis.

We suggest that the process of dike subsidence is controlled by the axial magma chamber (AMC), which we define as the melt lens and underlying mush zone. Within the neovolcanic zone, buoyancy forces associated with the AMC are supporting the extrusive layer and sheeted dikes. With distance from the rise axis, the AMC solidifies, the crust cools, the buoyancy forces are reduced, and the sheeted dike complex subsides. Concurrently, the extrusive layer thickens resulting in significantly less subsidence of the seafloor. The primary implication of this model is that dikes will subside to a greater depth for a robust magma chamber than for a weak magma chamber. A prominent deval is located at latitude 9°35'N, and this is coincident with our observations of a 50% decrease in dike subsidence as determined from MCS, WAP, conventional airgun refraction, and tomography data. Our subsidence model would predict that a relatively weak magma chamber is located at 9°35'N. A low magma supply at the deval location is compatible with tomography and MCS seismic data. The decrease in layer 2A thickness suggests that the localized region of low magma supply has persisted for 175,000-275,000 years.

Knowledge of shallow crustal structure is the key to understanding emplacement processes at mid-ocean ridges. Seismic studies at the fast-spreading East Pacific Rise indicate that each technique has advantages and disadvantages. On-bottom seismic refraction experiments can provide high-resolution determinations of upper crustal velocities, but only for limited areas. Conventional airgun refraction studies can extend the velocity structure to a larger region, at the expense of resolution. Multi-channel seismic and wide-angle profile data can map horizons in the shallow crust over large areas, but require good velocity information to be properly interpreted. Future work can ground truth seismic observations with observed lithology, and expand our knowledge of emplacement processes to intermediate-spreading and slow-spreading ridges.

Thesis Supervisor: Dr. G.M. Purdy
                             Senior Scientist, WHOI

ACKNOWLEDGEMENTS

As with any thesis, this document could not have been written without the encouragement and support of family, friends, and co-workers. Special thanks go to Mike Purdy, for his excellent guidance during the past five years.

Discussions with Bill Bryan, Dan Fornari, and Kathy Gillis have filled in some of the gaps in my knowledge of geologic processes. The Keck Geodynamics Program, led by Henry Dick, has allowed me to travel to Cyprus, Iceland, the Canary Islands, and Oregon. These field trips have given me a first hand look at what the oceanic crust might be like. Plus some of the better meals of my life! My thesis has also benefitted from discussions with Chris Bradley, Joe Cann, John Collins, Bob Detrick, Gerard Fryer, John Goff, Steve Holbrook, Graham Kent, Marty Kleinrock, Jian Lin, Marcia McNutt, Kristen Rohr, Hans Schouten, Peter Shaw, Debbie Smith, Ralph Stephen, Steve Swift, Maurice Tivey, Doug Toomey, and Will Wilcock, and Cecily Wolfe.

Doug Toomey not only spent a month teaching me tomography, but also put me up in his house and introduced me to the local microbreweries. Will Wilcock provided the codes for attenuation tomography used in Chapter 4, and also kept the internet busy answering all of my questions. John Collins has patiently responded to all my queries about reflectivity. Through the efforts of David DuBois and Jim Dolan, the lab and computer system have run smoothly during the last 5 years. The credit for the excellent quality of the NOBEL data goes to Jim Broda, David DuBois, Rob Handy, Don Koelsch, and Ken Peal.

Carl and Marj Friedrichs spent many nights with John and me, playing bridge and repudiating the laws of statistics by consistently getting better cards than us. Debbie Smith and Joe LaCasce have been instrumental in keeping me sane the past year, by persuading me to trade the office for the soccer field several times a week. This also prepared me for the life of a postal worker, as neither rain, sleet, or snow kept us from our appointed soccer game. Raptors Graham Kent, Steve Holbrook, and Dave DuBois introduced me to sand volleyball, and were always available for a game on a sunny summer day.

Fellow students Chris Bradley, Elise Ralph, Cecily Wolfe, Gary Jaroslow, Dan Lizarralde, Marj Friedrichs, Carl Friedrichs, Rafi Katzman, Garrett Ito, Joe LaCasce, and Emilie Hooft have helped me enjoy my time at WHOI. Dinner parties, afternoons at the Kidd, summer bbqs, and office bull sessions have enlivened the graduate experience. Carolyn Ruppel provided a sympathetic ear for the past five years, and especially during my thesis crunch. Stitch and Bitches with Hege, Bonnie, Elise, Marj, and Cecily were a welcome refuge from the male-dominated work place.

Lastly, I thank my husband for his support, especially in the past year. John, I couldn't have done it without you.

6

TABLE OF CONTENTS

CHAPTER 4
THE SHALLOW ATTENUATION STRUCTURE OF THE FAST-SPREADING
EAST PACIFIC RISE NEAR 9°30'N

CHAPTER 5
SEISMIC TECHNIQUES AND RESOLUTION IN THE SHALLOW CRUST

CHAPTER 6
CONCLUSIONS

CHAPTER 1

SHALLOW STRUCTURE OF OCEANIC CRUST

Introduction

This thesis is concerned with increasing our understanding of how oceanic crust is emplaced at mid-ocean ridges. The emphasis is upon fast-spreading ridges, and the use of seismic techniques to image the uppermost several hundred meters of the crust. Although knowledge of the velocity structure of the upper crust can help constrain models of the emplacement of both the extrusive sequence and sheeted dike complex, it has for decades been the least well-resolved section of the oceanic crust. Recent advances in seismic sources, receivers, and processing techniques are helping to change this situation and to improve our knowledge of shallow structure. This thesis focuses on nine on-bottom refraction experiments carried out over young crust on the East Pacific Rise near 9°30'N, a region that has been extensively studied by submersible [*Fornari et al.*, 1992], near-bottom imaging [*Haymon et al.*, 1991], seismic tomography [*Toomey et al.*, 1990], multi-channel seismic studies [*Detrick et al.*, 1987; *Harding et al.*, 1993; *Kent et al.*, 1993a], expanding spread profiles [*Vera et al.*, 1990], and attenuation tomography [*Wilcock et al.*, 1992]. The variety of experiments in the region allows the shallow velocity structure determined in this thesis to be placed in context with both the seafloor morphology and the geometry of the underlying magma chamber.

Seismic Terminology for the Shallow Crust

Early seismic studies produced a simple layered structure for the oceanic crust, with the oceanic crust divided into layers 1 (sediments), 2 (extrusives and sheeted dikes), and 3 (gabbros) (e.g. [*Raitt*, 1963; *Fox et al.*, 1973]). Layer 2 was further subdivided into layers

2A, 2B, and 2C according to seismic velocities of approximately 3.6 km/s, 5.2 km/s, and 6.1 km/s, respectively [*Houtz and Ewing*, 1976]. As seismic techniques improved, these simple models were abandoned for a more complex structure composed of continuous velocity gradients (e.g. [*Spudich and Orcutt*, 1980]); however, terminology from these early layered models remains (with some confusion) in the literature today. In the work presented here, the upper crust with average velocities <5 km/s is termed layer 2A. A significant feature of layer 2A is a surficial low-velocity layer (SLVL), which typically has a velocity <3 km/s and a low velocity gradient (Figure 1). At young locations a high-gradient region or discontinuity to a layer with velocities >5 km/s underlies the SLVL; the 5 km/s material is referred to here as layer 2B. If an obvious change in velocity gradient to a region with velocities of ~6 km/s exists, then this layer with ~6 km/s velocities is termed 2C; otherwise the depth interval between layer 2A (velocities <5 km/s) and layer 3 (velocities ~6.8 km/s) will be referred to as layer 2B. This terminology is demonstrated in Figure 1.1 for two velocity models.

Shallow Velocity Structure of Oceanic Crust

In a classic paper, *Houtz and Ewing* [1976] determined the shallow velocity structure at locations in the Atlantic and Pacific from several hundred sonobuoy records. At young locations, they observed a thick (0.7 km in the Pacific and 1.5 km in the Atlantic), low-velocity (~3.3 km/s) layer 2A. The primary conclusion of their work was that this layer thinned with age to ~100 m at about 40 m.y., associated with an increase in velocity to ~5.2 km/s. However, a reexamination of the sonobuoy data suggests that many of the layer 2A arrivals identified by *Houtz and Ewing* [1976] are diffractions or converted shear arrivals [*Diebold and Carlson*, 1993]; thus, higher-resolution data is needed to test the conclusions concerning the evolution of layer 2A with age.

Fast-spreading ridges

Recent seismic studies on the East Pacific Rise (EPR) have greatly increased our knowledge of the shallow velocity structure of fast-spreading centers (>4.5 cm/yr half rate). These studies include expanding spread profiles (ESPs), wide angle profiles (WAPs), multi-channel seismic (MCS) data, and refraction tomography. The majority of these seismic experiments were located on the EPR near 9°30'N, with additional experiments near 13°N, and 20°S-13°30'S (Figure 1.2). The following section will describe what these studies reveal about the shallow structure of the EPR near 9°30'N, and then briefly describe the results from other study areas.

The experiments described in Chapters 2 and 3 provide detailed determinations of velocity structure within the upper 500 m (e.g. Figures 2.4, 3.7, and 3.13) at several sites on the EPR near 9°30'N (Figure 1.2). The resolution is lower, but the depth interval greater, in the models produced from nearby ESPs [*Vera and Diebold*, 1993]. The four ESP velocity models (Figure 1.3) include a surficial low-velocity layer, with an average velocity of 2.3 km/s, and an average thickness of 140 m. This layer is underlain by a high-gradient region, with layer 2B velocities obtained at an average depth of 500 m. The thickness of layer 2A varies from 250-780 m. Refraction tomography, multi-channel seismic (MCS) experiments, and wide-angle profiles (WAPs) provide constraints on the lateral variability of seismic layer 2A. A tomography experiment centered at 9°30'N (Figure 1.2) imaged a narrow (2-4 km), axis-parallel zone of high-velocities centered over the rise axis, that was interpreted to be the result of rapid lateral thickening of layer 2A with age [*Toomey et al.*, 1990]. MCS and WAP experiments (Figure 1.2) both image a shallow "reflector," interpreted to be formed by refracted energy that has turned in the steep gradient at the base of layer 2A [*Harding et al.*, 1993; *Vera and Diebold*, 1993]. In agreement with the tomography image, this reflector deepens rapidly within 2-4 km of the rise axis, and then remains approximately at a constant depth beneath the seafloor [*Harding et al.*, 1993; *Vera and Diebold*, 1993]. On five cross-axis MCS lines, layer 2A thickens from ~200 m at

the rise axis to ~400-600 m outside the neovolcanic zone [*Harding et al.*, 1993]. The one cross-axis WAP, which has a receiver aperture of 5 km (as compared to a receiver aperture of 2.4 km for the MCS lines interpreted by *Harding et al.* [1993]), suggests a thinner layer 2A for both zero-age crust (~130 m) and for crust outside the neovolcanic zone (~200-300 m) [*Vera and Diebold*, 1993]. The along-axis WAP indicates only small changes in layer 2A thickness (thickness varies between 100-150 m) over a distance of 60 km [*Vera and Diebold*, 1993]. It is interesting that even when the AMC reflector is offset beneath the rise axis, the minimum thickness of layer 2A is centered at zero-age crust [*Harding et al.*, 1993].

Studies of the EPR at other locations (Figure 1.2) indicate similar seismic structures to that observed near 9°30'N. Layer 2A has a minimum thickness at the rise crest, averaging ~185 m along an 800-km section of the EPR from 20°S-13°30'S [*Detrick et al.*, 1993], and ~200 m along 50 km of the EPR from 13°N-13°30'N [*Kappus*, 1991]. Layer 2A approximately doubles in thickness within 2-4 km of the rise axis, reaching average depths of ~510-570 m at the EPR near 14°15'S [*Kent et al.*, 1993b], and ~300-400 m near 13°N [*Harding et al.*, 1989; *Kappus*, 1991]. (Note that these 2A thicknesses are greater than stated by *Kappus* [1991], based on use of the terminology discussed previously.) *Kappus* [1991] observes a slight increase in seafloor velocity with age near 13°N, from ~2.45 km/s for zero-age crust to ~2.75 km/s for crust located 9.5 km off-axis.

Intermediate-spreading ridges

The Juan de Fuca Ridge has been the location of several seismic experiments that help constrain the shallow velocity structure of intermediate-spreading ridges (2.5-4.5 cm/yr half rate). In contrast to the EPR, energy turning within the upper few hundred meters is often observed with conventional refraction surveys (with close shot spacing at ranges <4 km), due to a surficial low-velocity layer that is thicker than modeled for the fast-spreading ridge. A typical velocity model is shown in Figure 1.4, from a survey carried out over the

Endeavour Segment near 48°N [*Cudrak and Clowes*, 1993]. Layer 2A has an average velocity of ~2.5-2.7 km/s, and a thickness of 200-600 m (average = 400 m). A shallow intermittent reflector observed on MCS data from the region suggests a slightly thicker 2A (600±200-300 m) [*Rohr et al.*, 1988; *Rohr et al.*, 1992]. Both the MCS data and a seismic refraction tomography study indicate that layer 2A is thicker under abyssal hills than beneath inter-ridge valleys [*White and Clowes*, 1990; *Rohr et al.*, 1992]. Unfortunately, there are no constraints on layer 2A thickness for zero-age crust on the Endeavor Segment from either MCS data or seismic refraction experiments. However, a seismic refraction experiment located on the Cleft Segment near 45°N indicates that layer 2A is thinnest (~200-300 m) within the axial valley, and thickens to ~300-500 m outside the axial valley [*McDonald et al.*, 1993]. Plotted in Figure 1.4 are the average shallow velocity models for the Endeavor and Cleft Segments.

Slow-spreading ridges

In contrast to fast-spreading and intermediate-spreading ridges, few seismic experiments have resolved structure in the shallow crust of a slow-spreading center (0.5-2.5 cm/yr half rate). The primary exceptions are the on-bottom seismic refraction experiments of *Purdy* [1987], carried out over young crust created at the Mid-Atlantic Ridge near 23°N. With both the source and receiver located close to the seafloor, *Purdy* [1987] could observe energy directly turning in the upper crust. The data indicate an increase in seafloor velocity with age, from ~2.1 km/s for 0 m.y. crust to ~4.1 km/s for 7 m.y. crust (Figure 1.5). Additionally, the vertical velocity gradient decreases from ~4 s^{-1} for the younger crust to 0-0.5 s^{-1} for the older crust. The on-bottom experiments resolve crustal structure in the upper 250 m, with no constraints on the depth to the base of layer 2A. A conventional air gun profile located close to the 0 m.y. on-bottom experiment is also plotted in Figure 1.5; the 450 m thick surficial low-velocity layer was constrained by modeling a low-velocity phase emerging tangentially from the water wave [*Purdy and Detrick*, 1986]. No obvious

layer 2A/2B boundary is observed in Figure 1.5, but velocities of 5 km/s are reached at a depth of ~1.5 km beneath the seafloor.

Geologic Interpretation

From submersible observations and camera tows, we know that the seafloor, and therefore at least the upper portion of layer 2A, is composed primarily of sheet flows, pillow lavas, and rubble layers (e.g. [*Ballard and van Andel*, 1977; *Ballard et al.*, 1979; *CYAMEX scientific team*, 1981; *Choukroune et al.*, 1984]). Lithologic predictions for the remainder of layer 2 typically rely on drilling results, submersible observations of seafloor scarps, and the use of ophiolites as analogues for oceanic crust. Estimations of lithology from drilling results are difficult because only four holes penetrate a significant portion of layer 2. The deepest drill hole in oceanic crust is DSDP Hole 504B on 6 my old crust south of the Costa Rica Rift [*Anderson et al.*, 1982]. At this location the lithology consists of a 575 m thick extrusive section, a 210 m thick transition zone, and 945 m of sheeted dikes and massive units [*Dick et al.*, 1992]. The crust at Hole 504B was emplaced at the intermediate-spreading Costa Rica Rift, at a half spreading rate of ~3.6-3.8 cm/yr. Drilling at three locations in crust formed at the slow-spreading MAR (Holes 332B, 395A, 418A) has encountered 300-580 m of extrusives [*Aumento et al.*, 1977; *Melson and et al.*, 1979; *Donnelly and et al.*, 1980], but has not reached the sheeted dike sequence. At present, no drill hole has penetrated more than a few tens of meters into oceanic crust formed at a fast-spreading center. Multichannel full waveform acoustic logs from Holes 418A, 395A, and 504B indicate that velocities of the extrusive layer vary from 3-6.5 km/s with an average velocity of ~5 km/s, and velocities of the sheeted dike complex from 5.8-6.5 km/s [*Moos et al.*, 1990]. The upper 100 m of basement at Hole 504B is marked by lower velocities and higher porosities than the remainder of the extrusive section [*Anderson et al.*, 1982]; no comparable low-velocity layer is identified at Holes 418A or 395A [*Moos et al.*, 1990], although there is a sharp decrease in porosity at a depth of ~350 m within the extrusives at

Hole 395A [*Bryan and et al.*, 1988]. Based strictly on a comparison of logging velocities and lithology with layer 2 definitions, the layer 2A/2B boundary corresponds to a velocity/porosity boundary within the extrusive sequence, and layer 2C (or the lower portion of layer 2B if no clear 2B/2C boundary exists) corresponds to the sheeted dike complex.

Other estimates of layer 2 lithology can be obtained from submersible observations of seafloor scarps. At the Vema fracture zone located on the slow-spreading Mid-Atlantic Ridge, *Cannat et al.* [1991] observe a 280-420 m thick extrusive sequence, a 60-300 m thick transition zone, and a 750-1000 m thick sheeted dike complex; however, the authors state that true thicknesses cannot be determined because the observed sequences may be faulted. If the section is unfaulted, the depth to the top of the sheeted dike complex is ~340-720 m. A similar lithology is found for the Blanco transform at the intermediate-spreading Juan de Fuca Ridge, where a 475 m thick extrusive layer, 785 m thick transition zone, and 635-685 m thick sheeted dike complex were mapped by the submersible *Nautile* [*Naidoo et al.*, 1992]. In contrast, a thin extrusive sequence (100-200 m) is observed along the walls of Hess Deep, a section of crust emplaced at the fast-spreading EPR [*Francheteau et al.*, 1992]. The extrusive section is underlain by a 50-500 m thick transition zone and a 1200 m thick sheeted dike complex [*Francheteau et al.*, 1992]. The average depth to the top of the sheeted dike sequence is ~350 m. The extrusive sequence in ophiolites is generally thicker (1000-2000 m [*deWit and Stern*, 1978; *Alabaster et al.*, 1982; *Schmincke et al.*, 1983]) than at the Vema, Blanco, or Hess Deep scarps, and is underlain by a 50-300 m thick transition zone [*Alabaster et al.*, 1982; *Moores*, 1982; *Rosencrantz*, 1983].

A comparison of the observed extrusive sequence and transition zone thicknesses (Table 1.1) with average layer 2A thicknesses (Table 1.2) suggests that the layer 2A/2B boundary may either lie within the extrusive sequence, or correspond with the top of the sheeted dike

complex. The nature of the layer 2A/2B boundary will be examined in greater detail in later thesis chapters.

Thesis Overview

In Chapters 2, 3, and 4, different interpretation techniques are applied to a data set consisting of nine on-bottom seismic refraction experiments, located on young crust formed at the East Pacific Rise near 9°30'N. Chapter 2 presents the results of one- and two-dimensional ray tracing. Chapter 3 discusses forward modeling of the refracted waveforms using the reflectivity technique. This not only provides a detailed velocity structure, but also constrains the Poisson's ratio and attenuation structure of the shallow crust. Chapter 4 applies a spectral method to the on-bottom refraction data to invert for the shallow attenuation structure. Chapter 5 examines seismic techniques (multi-channel seismic data and conventional airgun profiles) that help constrain lateral changes in shallow structure over a larger region than sampled by the on-bottom experiments. Chapter 6 explores geological implications of the seismic results discussed in Chapters 2-5.

Several of these chapters have been published or submitted to journals as multi-author papers. Chapter 2 was published in 1992 in *Geophysical Research Letters*, and Chapter 3 is submitted to the *Journal of Geophysical Research*. Both of these papers are co-written with G.M. Purdy and Gerard Fryer. Chapter 4 is in press in *Geophysical Research Letters*, with co-authors Will Wilcock and G.M. Purdy. I plan on submitting a revised version of Chapters 5 and 6 to *Journal of Geophysical Research*; the co-authors on this work are Graham Kent, Bob Detrick, and G.M. Purdy. For all chapters I did the primary modeling of the data sets, with advice from my co-authors. I wrote the original and final drafts of each manuscript, again with advice from my co-authors. The full citations for the chapters published, in press, and submitted are listed below.

Christeson, G.L., G.M. Purdy and G.J. Fryer, Structure of young upper crust at the East Pacific Rise near 9°30'N, *Geophys. Res. Lett.*, *19*, 1045-1048, 1992.

Christeson, G.L., G.M. Purdy and G.J. Fryer, Seismic constraints on shallow crustal emplacement processes at the fast-spreading East Pacific Rise, *J. Geophys. Res.*, *submitted*, 1993a.

Christeson, G.L., W.S.D. Wilcock and G.M. Purdy, The shallow attenuation structure of the fast-spreading East Pacific Rise near 9°30'N, *Geophys. Res. Lett.*, *in press*, 1993b.

References

Alabaster, T., J.A. Pearce and J. Malpas, The volcanic stratigraphy and petrogenesis of the Oman ophiolite complex, *Contrib. Mineral. Petrol.*, *81*, 168-183, 1982.

Anderson, R.N. et al., DSDP Hole 504B, the first reference section over 1 km through Layer 2 of the oceanic crust, *Nature*, *300*, 589-594, 1982.

Aumento, F., W.G. Melson and et al., *Init. Repts. DSDP, 37*, US Govt. Printing Office, Washington, D.C., 1977.

Ballard, R.D., R.T. Holcomb and T.H. van Andel, The Galapagos rift at 86°W: 3. Sheet flows, collapse pits, and lava lakes of the rift valley, *J. Geophys. Res.*, *84*, 5407-5422, 1979.

Ballard, R.D. and T.H. van Andel, Morphology and tectonics of the inner rift valley at lat. 36°50'N on the Mid-Atlantic Ridge, *Geol. Soc. Am. Bull.*, *88*, 507-530, 1977.

Bryan, W.B. and et al., *Proc. ODP, Init. Repts., 109*, Ocean Drilling Program, College Station, Tx, 1988.

Cannat, M., V. Mamaloukas-Frangoulis, J.-M. Auzende, D. Bideau, E. Bonatti, J. Honnorez, Y. Lagabrielle, J. Malavieille and C. Mevel, A geological cross-section of the Vema fracture zone transverse ridge, Atlantic ocean, *J. Geodynamics*, *13*, 97-118, 1991.

Choukroune, P., J. Francheteau and R. Hekinian, Tectonics of the East Pacific Rise near 12°50'N: a submersible study, *Earth Planet. Sci. Lett.*, *68*, 115-127, 1984.

Cudrak, C.F. and R.M. Clowes, Crustal structure of Endeavour ridge segment, Juan de Fuca ridge, from a detailed seismic refraction survey, *J. Geophys. Res.*, *98*, 6329-6349, 1993.

CYAMEX scientific team, First manned submersible dives on the East Pacific Rise at 21°N (project RITA): general results, *Mar. Geophys. Res.*, *4*, 345-379, 1981.

Detrick, R.S., P. Buhl, E. Vera, J. Mutter, J. Orcutt, J. Madsen and T. Brocher, Multichannel seismic imaging of an axial magma chamber along the East Pacific Rise between 9°N and 13°N, *Nature*, *326*, 35-41, 1987.

Detrick, R.S., A.J. Harding, G.M. Kent, J.A. Orcutt, J.C. Mutter and P. Buhl, Seismic structure of the southern East Pacific Rise, *Science*, *259*, 499-503, 1993.

deWit, M.J. and C. Stern, Pillow talk, *J. Volcanol. Geotherm. Res.*, *4*, 55-80, 1978.

Dick, H.J.B., J. Erzinger, L.B. Stokking and et al., *Proc. ODP, Init. Repts.*, *140*, Texas A&M Univ., College Station, TX, 1992.

Diebold, J. and R. Carlson, Layer 2A revisited (abstract), *EOS Trans. AGU*, *74* (43), Fall Supp., 603, 1993.

Donnelly, T. and et al., *Init. Repts. DSDP*, *51-53*, US Govt. Printing Office, Washington, D.C., 1980.

Fornari, D.J., M.R. Perfit, R. Batiza and M.H. Edwards, Submersible transects across the East Pacific Rise crest and upper-flanks at 9°31'-32'N: 1. Observations of seafloor morphology and evidence for young volcanism off-axis (abstract), *EOS Trans. AGU*, *73* (43), Fall Supp., 525, 1992.

Fox, P.J., E. Schreiber and J.J. Peterson, The geology of the oceanic crust: compressional wave velocities of oceanic rocks, *J. Geophys. Res.*, *78*, 5155-5172, 1973.

Francheteau, J., R. Armijo, J.L. Cheminee, R. Hekinian, P. Lonsdale and N. Blum, Dyke complex of the East Pacific Rise exposed in the walls of Hess Deep and the structure of the upper oceanic crust, *Earth Planet. Sci. Lett., 111,* 109-121, 1992.

Harding, A.J., G.M. Kent and J.A. Orcutt, A multichannel seismic investigation of upper crustal structure at 9°N on the East Pacific Rise: Implications for crustal accretion, *J. Geophys. Res., 98,* 13925-13944, 1993.

Harding, A.J., J.A. Orcutt, M.E. Kappus, E.E. Vera, J.C. Mutter, P. Buhl, R.S. Detrick and T.M. Brocher, Structure of young oceanic crust at 13°N on the East Pacific Rise from expanding spread profiles, *J. Geophys. Res., 94,* 12163-12196, 1989.

Haymon, R.M., D.J. Fornari, M.H. Edwards, S. Carbotte, D. Wright and K. Macdonald, Hydrothermal vent distribution along the East Pacific Rise crest (9°09'-54'N) and its relationship to magmatic and tectonic processes on fast-spreading mid-ocean ridges, *Earth Planet. Sci. Lett., 104,* 513-534, 1991.

Houtz, R. and J.I. Ewing, Upper crustal structure as a function of plate age, *J. Geophys. Res., 81,* 2490-2498, 1976.

Kappus, M.E., A baseline for upper crustal velocity variations along the East Pacific Rise, Ph.D. Thesis, 158 pp., University of California, San Diego, 1991.

Kent, G.M., A.J. Harding and J.A. Orcutt, Distribution of magma beneath the East Pacific Rise between the Clipperton Transform and the 9°17'N deval from forward modeling of common depth point data, *J. Geophys. Res., 98,* 13945-13969, 1993a.

Kent, G.M., A.J. Harding, J.A. Orcutt, R.S. Detrick, J.C. Mutter and P. Buhl, The uniform accretion of oceanic crust south of the Garrett Transform at 14°15'S on the East Pacific Rise, *J. Geophys. Res., in press,* 1993b.

McDonald, M.A., J.A. Hildebrand, S.C. Webb and C.G. Fox, Seismic structure and anisotropy of the Juan de Fuca Ridge at 45°N, *J. Geophys. Res., in press,* 1993.

Melson, W.P. and et al., *Init. Repts. DSDP, 45,* US Govt. Printing Office, Washington, D.C., 1979.

Moores, E.M., Origin and emplacement of ophiolites, *Rev. Geophys. Space Phys.*, *20*, 735-760, 1982.

Moos, D., P. Pezard and M. Lovell, Elastic wave velocities within oceanic layer 2 from sonic full waveform logs in Deep Sea Drilling Project Holes 395A, 418A, and 504B, *J. Geophys. Res.*, *95*, 9189-9207, 1990.

Naidoo, D.D., J.R. Delaney and T. Juteau, A scarp-map profile of upper oceanic crust at the West Blanco Transform (WBT): insights into magmatic accretion (abstract), *EOS Trans. AGU*, *73* (43), Fall Supp., 502, 1992.

Purdy, G.M., New observations of the shallow seismic structure of young oceanic crust, *J. Geophys. Res.*, *92*, 9351-9362, 1987.

Purdy, G.M. and R.S. Detrick, The crustal structure of the mid-Atlantic Ridge at 23°N from seismic refraction studies, *J. Geophys. Res.*, *91*, 3739-3762, 1986.

Raitt, R.W., The crustal rocks, in *The Sea*, edited by M. N. Hill, 85-100, Interscience, New York, 1963.

Rohr, K.M.M., B. Milkereit and C.J. Yorath, Asymmetric deep crustal structure across the Juan de Fuca Ridge, *Geology*, *16*, 533-537, 1988.

Rohr, K.M.M., G.M. Purdy, B. Milkereit and N.R. Chapman, Upper oceanic crust: laterally homogeneous or heterogeneous? (abstract), *EOS Trans. AGU*, *73* (14), Spring Supp., 274, 1992.

Rosencrantz, E., The structure of sheeted dikes and associated rocks in North Arm massif, Bay of Islands ophiolite complex, and the intrusive process at oceanic spreading centers, *Can. J. Earth Sci.*, *20*, 787-801, 1983.

Schmincke, H.-U., M. Rautenschlein, P.T. Robinson and J.M. Mehegan, Troodos extrusive series of Cyprus: a comparison with oceanic crust, *Geology*, *11*, 405-409, 1983.

Spudich, P. and J. Orcutt, A new look at the seismic velocity structure of the oceanic crust, *Rev. Geophys. Space Phys.*, *18*, 627-645, 1980.

Toomey, D.R., G.M. Purdy, S.C. Solomon and W.S.D. Wilcock, The three-dimensional seismic velocity structure of the East Pacific Rise near latitude 9°30'N, *Nature, 347*, 639-645, 1990.

Vera, E.E. and J.B. Diebold, Seismic imaging of oceanic layer 2A between 9°30'N and 10°N on the East Pacific Rise from two-ship wide aperture profiles, *J. Geophys. Res.*, *in press,* 1993.

Vera, E.E., J.C. Mutter, P. Buhl, J.A. Orcutt, A.J. Harding, M.E. Kappus, R.S. Detrick and T.M. Brocher, The structure of 0- to 0.2-m.y.-old oceanic crust at 9°N on the East Pacific Rise from expanded spread profiles, *J. Geophys. Res., 95,* 15529-15556, 1990.

White, D.J. and R.M. Clowes, Shallow crustal structure beneath the Juan de Fuca Ridge from 2-D seismic refraction tomography, *Geophys. J. Int., 100,* 349-367, 1990.

Wilcock, W.S.D., S.C. Solomon, G.M. Purdy and D.R. Toomey, The seismic attenuation structure of a fast-spreading mid-ocean ridge, *Science, 258,* 1470-1474, 1992.

Table 1.1: Observed Lithology of Shallow Crust

Location	Thickness of Extrusive Sequence	Thickness of Transition Zone	Average Depth To Top Of Sheeted Dike Complex
Hess Deep*	100-200 m	50-500 m	350 m
Blanco Scarp§	475 m	785 m	1260 m
Vema Scarp†	280-420 m	60-300 m	530 m
Ophiolites‡	1000-2000 m	50-300 m	1500 m
Hole 504B¥	575 m	210 m	785 m

*Thicknesses from *Francheteau et al.* [1992].

§Thicknesses from *Naidoo et al.* [1992].

†Thicknesses from *Cannat et al.* [1991].

‡Thicknesses from [*deWit and Stern*, 1978; *Alabaster et al.*, 1982; *Schmincke et al.*, 1983]

¥Thicknesses from *Anderson et al.* [1982]

Table 1.2: Shallow Velocity Structure of Young Oceanic Crust

Spreading Rate	Seafloor velocity*	Surficial low-velocity layer thickness§	2A thickness (outside of neo-volcanic zone)†	2A thickness (within neo-volcanic zone)‡
fast	2.3 km/s	140 m	400 m	200 m
intermediate	2.6 km/s	400 m	400 m	250 m
slow	2.1 km/s	450 m	1500 m?	?

*Measurements from *Vera et al.* [1990] (fast), *Cudrak and Clowes* [1993] (intermediate), and *Purdy* [1987] (slow).

§Thicknesses from *Vera et al.* [1990] (fast), *Cudrak and Clowes* [1993] (intermediate), and *Purdy and Detrick* [1986] (slow).

†Thicknesses from *Harding et al.* [1993] (fast), *Cudrak and Clowes* [1993] (intermediate), and *Purdy and Detrick* [1986] (slow).

‡Thicknesses from *Harding et al.* [1993] (fast), and *McDonald et al.* [1993] (intermediate).
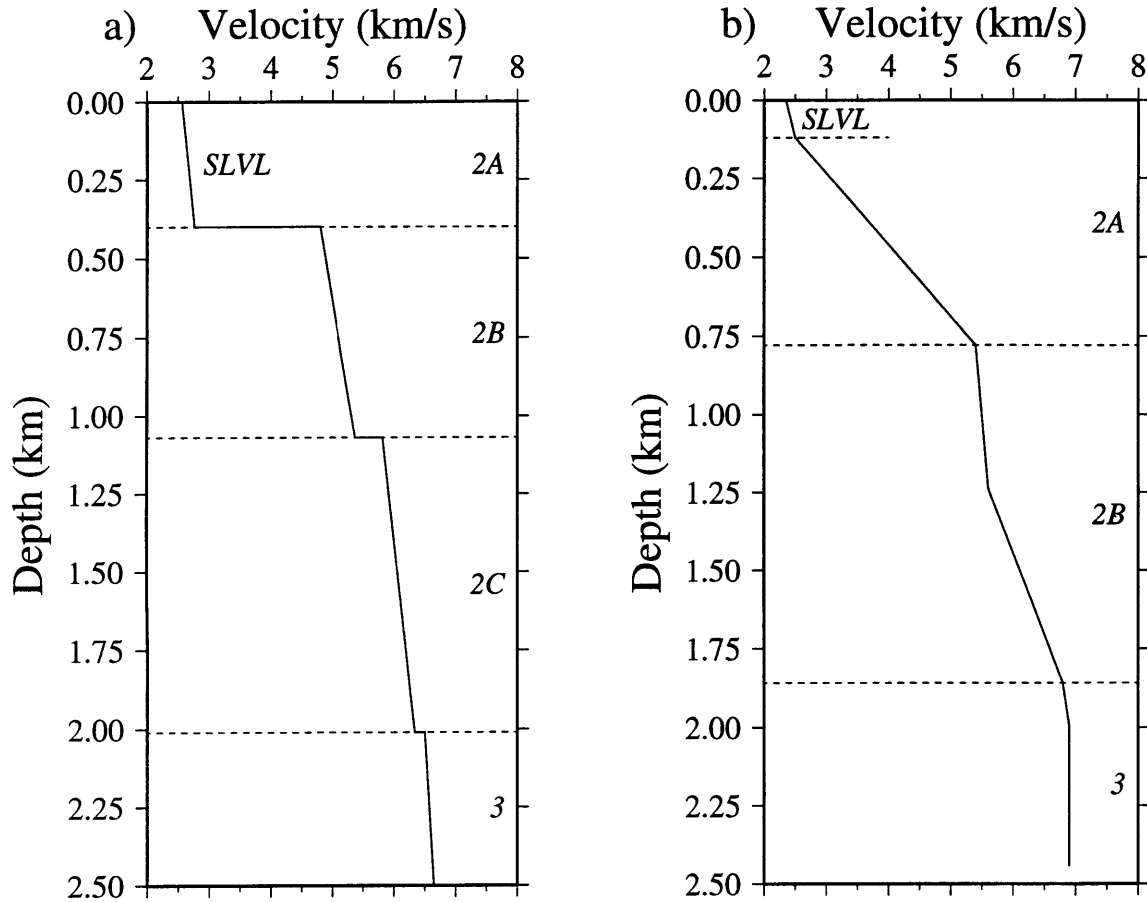
Figure 1.1. Velocity models from two recent studies, illustrating terminology commonly used in describing shallow oceanic crust. a) Average velocity model from *Cudrak and Clowes* [1993] for young crust formed at the Juan de Fuca Ridge. This model is divided into layers 2A, 2B, 2C, and 3 according to the definitions provided in the text. (Only the upper portion of layer 3 is shown.) SLVL is the abbreviation for surficial low-velocity layer. b) Velocity model from *Vera et al.* [1990] for their ESP 7, located over young crust formed at the East Pacific Rise. There is no obvious change in gradient to a region with velocities of ~6 km/s, and thus this model is only divided into layers 2A, 2B, and 3. (Only the upper portion of layer 3 is shown). The SLVL makes up only a portion of layer 2A.
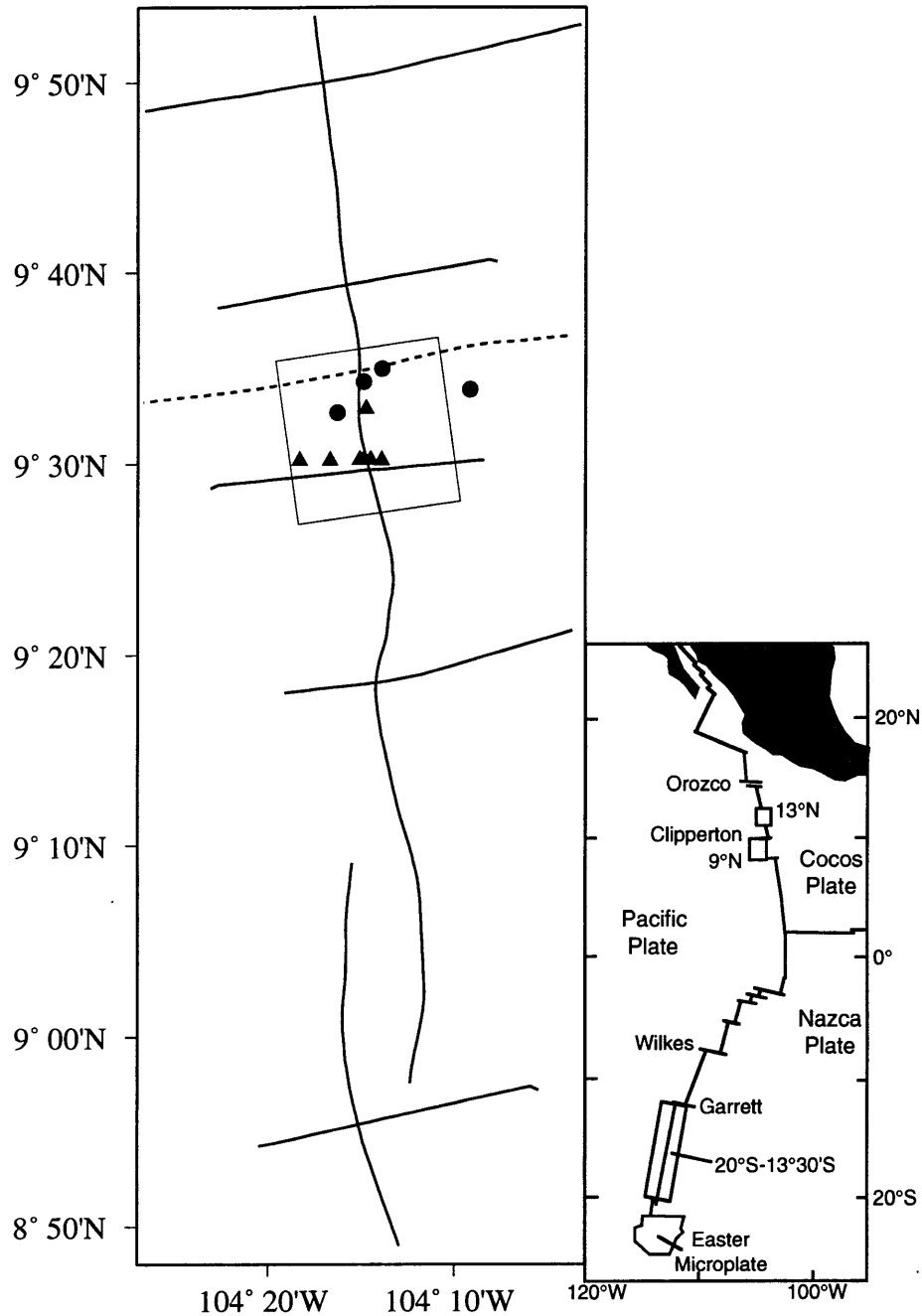
Figure 1.2. Location map for the seismic experiments carried out over crust formed at a fast-spreading center discussed in the text. Solid lines mark the shiptracks of the five cross-axis and two along-axis MCS experiments. These along-axis lines approximately delineate the rise axis of the EPR. The dashed line shows the trackline of the cross-axis WAP study. The center points of the ESPs are indicated by circles, and the locations of the on-bottom refraction experiments by triangles. The rectangular region encloses the tomography experiment of *Toomey et al.* [1990]. The inset map shows the regional setting, with boxes designating the three EPR areas discussed in the text.
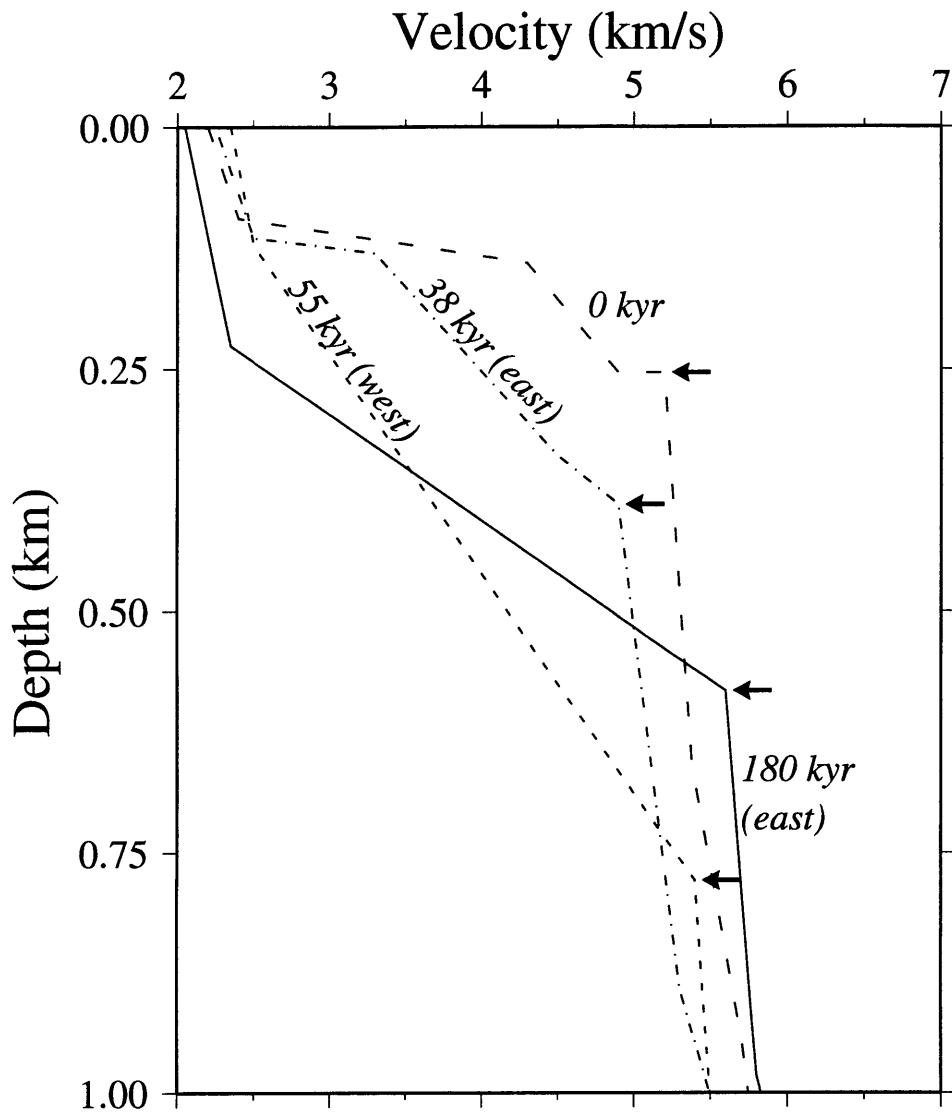
Figure 1.3. Velocity models of *Vera et al.* [1990] from expanding spread profiles located at the East Pacific Rise near 9°30'N. Annotations indicate the approximate age of each profile, and whether the profile was located to the east or west of the rise axis. Arrows indicate the base of seismic layer 2A for each model.
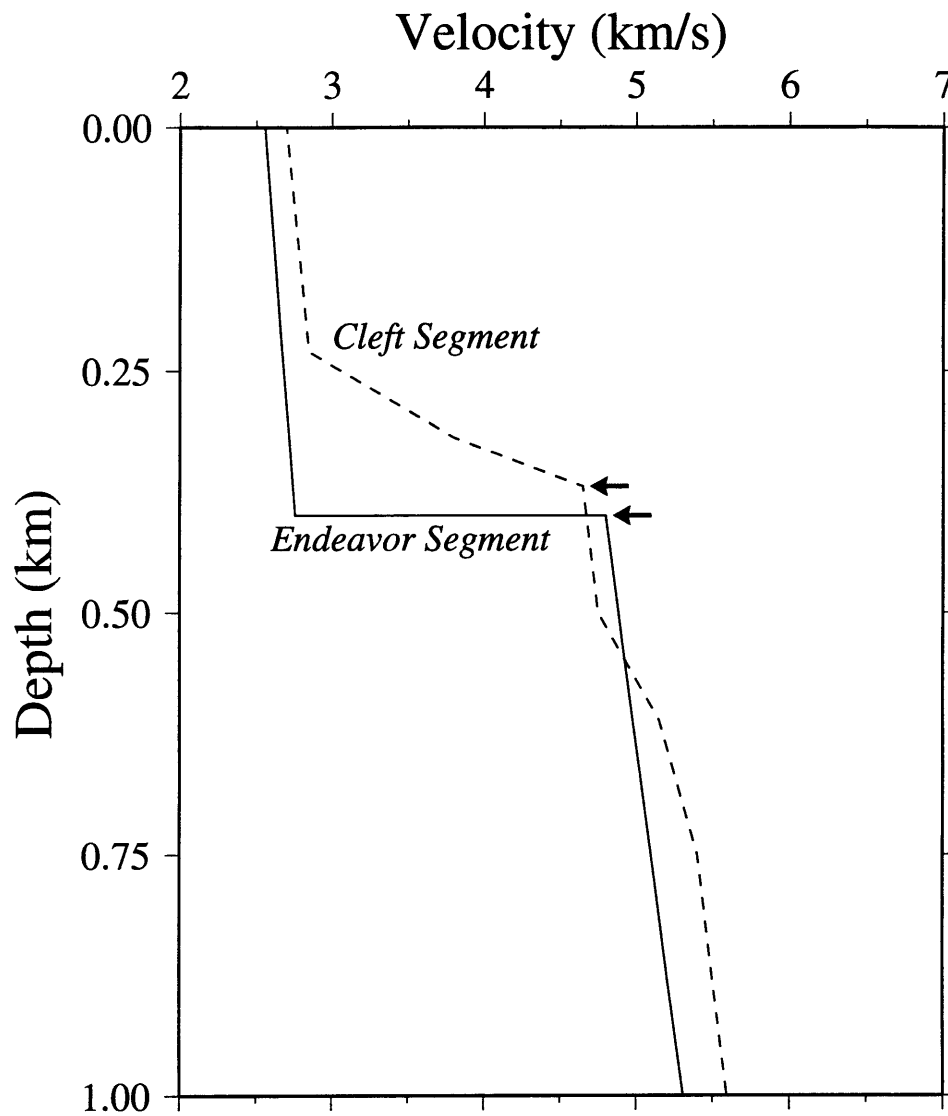
Figure 1.4. Velocity models for two segments of the Juan de Fuca Ridge [*Cudrak and Clowes*, 1993; *McDonald et al.*, 1993]. Arrows indicate the base of seismic layer 2A for each model.
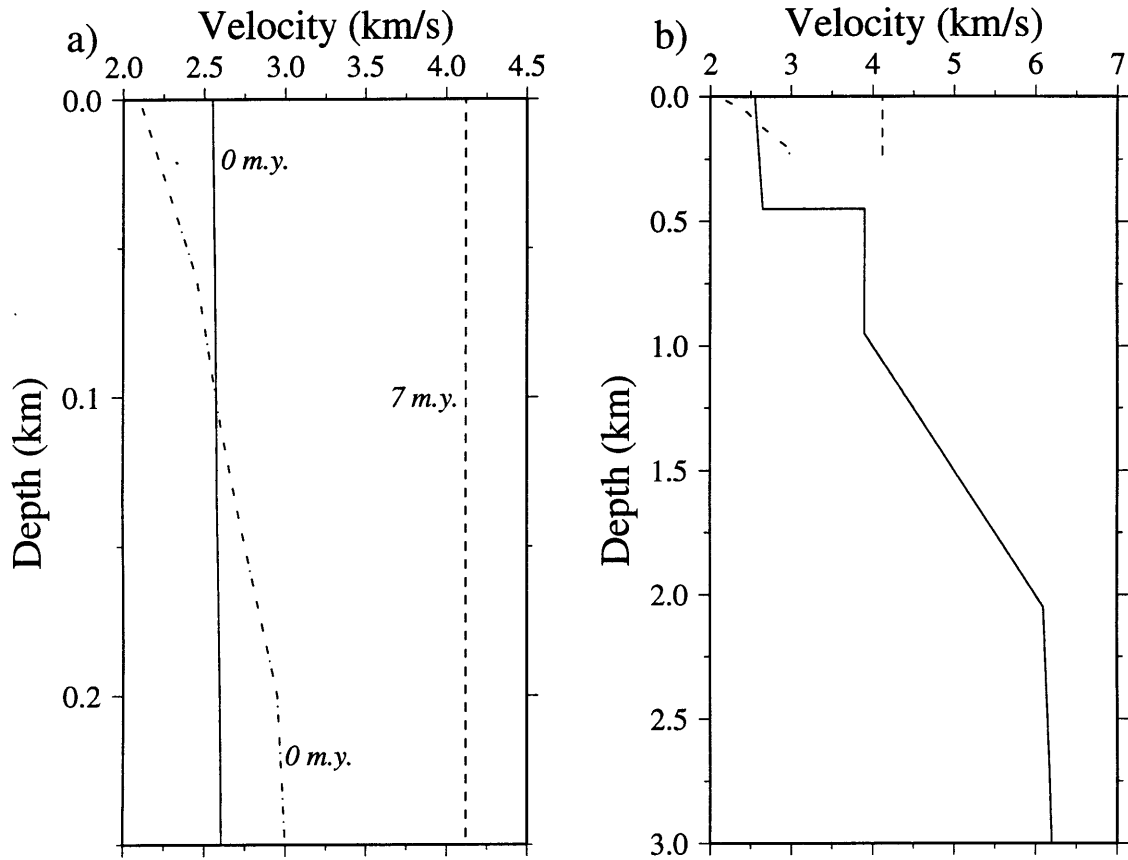
Figure 1.5. Velocity models from on-bottom refraction experiments [*Purdy*, 1987]
(dashed lines) and a conventional air gun experiment [*Purdy and Detrick*, 1986] (solid line)
of shallow crustal structure for the Mid-Atlantic Ridge near 23°N. a) Structure to a depth of
0.25 km. Approximate age of the crust at each location is indicated. b) Structure to a depth
of 3.0 km.

30

CHAPTER 2

STRUCTURE OF YOUNG UPPER CRUST AT THE EAST PACIFIC RISE NEAR 9°30'N

Abstract. Eight on-bottom seismic refraction experiments are analyzed in an effort to resolve the structure of the emplacement zone of lavas and dikes at the fast-spreading East Pacific Rise. The results suggest that the volcanic section doubles in thickness within ~1 km of the axial summit caldera (ASC) due to the emplacement of lava that either overflows the ASC or is transported through lateral tube conduits, and the depth to the top of the sheeted dike complex increases from ~160 m within the ASC to ~340 m a kilometer away on the flank.

Introduction

This chapter presents the preliminary results from eight on-bottom seismic refraction experiments, located on young crust formed at the East Pacific Rise (EPR) near 9°30'N. Traditional seismic refraction experiments with a source at the sea surface cannot resolve the velocity structure of the shallow oceanic crust, because (with a few notable exceptions, e.g. [*Harding et al.*, 1989; *Vera et al.*, 1990; *Vera and Diebold*, 1993]) the energy that turns in this region generally cannot be distinguished from the signal associated with the onset of the water wave. In contrast, on-bottom seismic refraction experiments allow direct observation of the energy turning in the uppermost several hundred meters without the interference of the water wave, providing high resolution determinations of the shallow crustal velocity structure [*Purdy*, 1987].

The East Pacific Rise near 9°30'N has been extensively studied with seismic methods, but only a few experiments have resolved the structure of the shallow crust. *Vera et al.*

[1990] identified a surficial low-velocity layer, 100-200 m thick with velocities ≤2.5 km/s, overlying a layer with a steep gradient where velocities >5 km/s are reached in a few hundred meters. The surficial low-velocity layer has been interpreted to be either a lava flow layer overlying the sheeted dike sequence [*Herron*, 1982], or a high-porosity layer overlying a layer with lower porosities [*Rohr et al.*, 1988; *Harding et al.*, 1989; *Vera et al.*, 1990]. The depth to a shallow reflector, interpreted to be formed by wide-angle reflections from the base of the surficial low-velocity layer [*Harding et al.*, 1993; *Vera and Diebold*, 1993], increases from ~100-200 m at the rise axis to ~300-600 m within 1-3 km of the rise axis, suggesting rapid variations in structure.

Knowledge of the structure of the shallow crust is needed because it is in this region that the emplacement of lavas, and possibly sheeted dikes, occurs. Observations from the ARGO imaging system indicate that the surficial expression of the emplacement zone, the ASC, varies in width from 40-150 m [*Haymon et al.*, 1991]. The on-bottom experiments discussed in this letter were placed within and close to the ASC, in an effort to resolve the structure of the emplacement zone at a fast-spreading ridge segment.

Data

On-bottom seismic refraction experiments were carried out using a unique source called NOBEL (Near Ocean Bottom Explosives Launcher). The instrument is towed within a few tens of meters of the seafloor, and upon command from the research vessel, first deploys the recording instrument, and then deploys and detonates in turn each of 47 five or ten lb (2.3 or 4.6 kg) PETN explosive charges [*Purdy*, 1987]. Figure 2.1 shows the location of the experiments conducted at 9°30'N. Three experiments were located within the ASC, two of which are labelled 0S and 0N in Figure 2.1; the third line, 0F, was located on the EPR at 12°50'N. Five lines were located outside of the ASC, labelled 10W, 20W, 20E, 70W, and 120W (their approximate age in kiloyears) in Figure 2.1. Additionally, one reversed refraction experiment was carried out (labelled 0-20R in Figure 2.1), oriented

perpendicular to the rise axis using two receivers, one located within the ASC, and the second ~1 km to the west.

Typical record sections for on-bottom seismic refraction experiments located both within the ASC (Line 0S) and on the flanks of the rise axis (Line 20W) are shown in Figures 2.2 and 2.3. Both record sections clearly show first arrivals out to ~1.6 km, but Line 20W displays first arrival travel times that are ~0.1 s greater than that for Line 0S.

Interpretation

Figure 2.4 shows a summary of the velocity-depth models for the ridge parallel experiments. The models were produced by fitting the first arrival travel times with one-dimensional ray tracing, taking into consideration the location of the triplication points observed on the record sections. The velocity structure of the three ASC lines differs systematically from that of the four flank lines, with the ASC lines reaching higher velocities at shallower depths. The model for the ASC lines consists of a surficial low-velocity layer with seafloor velocities of ~2.0-2.1 km/s and a gradient of ~6-8 s^{-1} underlain by a major boundary to a layer with velocities of ~3.6-4.7 km/s; this layer is in turn underlain by a boundary to a layer with velocities of ~5.0-5.4 km/s. The travel time curve for Line 0S is overlain on the corresponding record section in Figure 2.2. There is an excellent fit to the first arrival travel time picks and observed triplications, with the discontinuities at depths of ~0.05 km and ~0.13 km in Figure 2.4 corresponding to the triplications observed at ranges of ~0.2 km and ~0.4 km, respectively. The model for the flank lines consists of a layer with a seafloor velocity of ~2.1-2.6 km/s and several changes in gradient to a velocity of ~4.1-4.4 km/s, underlain by a major boundary to a layer with velocities of ~4.9-5.6 km/s. The travel time curve for Line 20W is overlain on the corresponding record section in Figure 2.3. The high gradient region in the upper layer of the velocity/depth model in Figure 2.4 is necessary to match the observed increase in first

arrival velocities at a range of ~0.6-0.7 km, and the discontinuity at a depth of ~0.37 km corresponds to the observed triplication at a range of ~1.3 km.

The velocity-depth models in Figure 2.4 show a dramatic change in crustal structure from the ASC to the flank lines, in a distance from the axis of < 1 km. In order to examine more closely this change, two-dimensional ray tracing [*Luetgert*, 1988] was used to fit the first arrival travel times for the one reversed on-bottom seismic experiment, Line 0-20R. The initial velocity-depth model for this line was based on the models shown in Figure 2.4 for Lines 0S, 10W, and 20W; depths to each boundary and velocities in each layer were changed until the travel time curves adequately fit the error bars associated with the first arrival travel times.

Figure 2.5 constitutes a well-constrained velocity/depth model for the region ~1 km west of the ASC to zero-age crust within the ASC. A comparison of this model with the one-dimensional model for Line 120W suggests that only minor variations occur between the shallow crust 1 km west of the rise axis and 6 km west of the rise axis.

The velocity structure discussed in this section is based entirely on ray tracing, and so ·can be improved by modelling the waveforms. However, because the total errors in the first arrival travel times and ranges were small (<±5-10 milliseconds and <5-10 m respectively), and because consideration was made of the locations of the triplication points observed in the record sections, the basic form of the velocity-depth models in Figures 2.4 and 2.5 is not expected to change with further modelling.

Discussion and Conclusions

The primary seismic results are: 1) A velocity contrast from ~4.2 km/s to ~5.0 km/s is located at a depth below the seafloor of ~0.16 km within the ASC and ~0.34 km for the crust ~1 km to the west. This corresponds to a dip on this boundary of ~10°, and is the most probable explanation for the crestal high velocity anomaly identified by *Toomey et al.* [1990]. 2) The seafloor velocity increases from ~1.95 km/s within the ASC to ~2.3 km/s

for the crust ~1 km to the west. 3) There is a major boundary at a depth of ~0.06 km within the ASC which is gradually replaced by a steep gradient, at a depth below the seafloor of ~0.11 km for 20 kiloyear crust.

One hypothesis to explain the nature of the major boundary delineating the top of the 5 km/s layer is that it is formed by a change in lithology, from lavas and sills to sheeted dikes. This has two important implications: the in situ velocity of the dikes must be substantially reduced below that measured on laboratory samples (e.g. [*Salisbury et al.*, 1985]), perhaps due to thermally induced cracking; and the thickness of the volcanic section is only ~350 m. This is far less than the ~800 m observed at DSDP Hole 504B [*Anderson et al.*, 1982], the only drill hole in normal oceanic crust that has penetrated the top of the dikes. In contrast to the EPR, however, the crust at Hole 504B was emplaced at an intermediate spreading center (half spreading rate of 36-38 mm/yr). Recent results from submersible observations at Hess Deep, a section of crust emplaced at the fast-spreading East Pacific Rise approximately 1 my ago (and thus perhaps more comparable to the seismic results of Figures 2.4 and 2.5) suggest that the average depth to the top of the dikes is only ~300-400 m [*Francheteau et al.*, 1992; *Karson et al.*, 1992]. For the contact between volcanics and sheeted dikes to be the origin of the seismic boundary, the transition zone from ~90% volcanics to ~90% dikes must have a thickness of a few tens of meters. This lithologic transition in the Samail [*Pallister*, 1981] and Bay of Islands ophiolites [*Rosencrantz*, 1983] confirm that the transition zone can be of this thickness. If this hypothesis for the origin of the seismic boundary is correct, then the dip of ~10° observed within 1 km of the rise axis for this boundary could be the expression of the subsidence of the dikes as they move away from the injection zone. This correlates relatively well with a dip of ~15°, predicted from measurements of dike attitudes, for the subsidence of the dikes in the Bay of Islands ophiolite [*Rosencrantz*, 1983].

An alternative explanation of this major boundary is that it represents a large change in porosity. The emplacement of a sill or massive flow would restrict the circulation of

seawater and allow high-temperature hydrothermal deposition, resulting in the sealing of thin cracks, a decrease in porosity, and an increase in seismic velocity [*Wilkens et al.*, 1991]. At DSDP site 504B, a sharp decrease in porosities, corresponding to a change in structure from predominantly pillow lavas and breccias to predominantly flows, was found at a depth beneath the basement of ~130 m [*Anderson et al.*, 1982; *Pezard*, 1990]. It is possible that this change in porosity correlates with the major seismic boundary at a depth below the seafloor of ~340 m for 20-120 kiloyear crust in Figures 2.4 and 2.5. However, it is difficult to imagine how this process could create such a consistent boundary as observed in Figure 2.5, as the region of high-temperature hydrothermal deposition, and thus higher seismic velocities, would reach a shallower level with each subsequent massive flow. Thus the first hypothesis is preferred.

Observations from the ARGO imaging system [*Haymon et al.*, 1991] indicate that most of the volcanic flows remain within the walls of the <200 m wide ASC, but that these flows occasionally overflow the ASC walls and travel as far as 1.8 km off axis [*Fornari et al.*, in prep.; *Edwards*, 1991]. Additionally, lava may be transported outside of the ASC through lateral tube conduits [*Fornari et al.*, in prep.]. Thus, evidence exists to suggest that the doubling of thickness of the 2.0-4.2 km/s material over a distance of ~1 km could be caused by the emplacement of lava that either overflows the ASC or is transported through lateral tube conduits. The drainback of this lava, as well as a small amount of low-temperature alteration, could substantially modify the total porosity and be responsible for the small increase of seafloor velocity shown in Figures 2.4 and 2.5.

In summary, the seismic results suggest that the thickness of the volcanic section doubles in thickness over an across-axis distance of ~1 km due to the emplacement of lava that either overflows the ASC or is transported through lateral tube conduits. The depth to the top of the sheeted dike complex increases from ~160 m within the ASC to ~340 m for the crust ~1 km to the west.

References

Anderson, R.N. et al., DSDP Hole 504B, the first reference section over 1 km through Layer 2 of the oceanic crust, *Nature, 300,* 589-594, 1982.

Edwards, M.H., The morphotectonic fabric of the East Pacific Rise: implications for fault generation and crustal accretion, Ph.D. Thesis, 160 pp., Columbia University, 1991.

Francheteau, J., R. Armijo, J.L. Cheminee, R. Hekinian, P. Lonsdale and N. Blum, Dyke complex of the East Pacific Rise exposed in the walls of Hess Deep and the structure of the upper oceanic crust, *Earth Planet. Sci. Lett., 111,* 109-121, 1992.

Harding, A.J., G.M. Kent and J.A. Orcutt, A multichannel seismic investigation of upper crustal structure at 9°N on the East Pacific Rise: Implications for crustal accretion, *J. Geophys. Res., 98,* 13925-13944, 1993.

Harding, A.J., J.A. Orcutt, M.E. Kappus, E.E. Vera, J.C. Mutter, P. Buhl, R.S. Detrick and T.M. Brocher, Structure of young oceanic crust at 13°N on the East Pacific Rise from expanding spread profiles, *J. Geophys. Res., 94,* 12163-12196, 1989.

Haymon, R.M., D.J. Fornari, M.H. Edwards, S. Carbotte, D. Wright and K. Macdonald, Hydrothermal vent distribution along the East Pacific Rise crest (9°09'-54'N) and its relationship to magmatic and tectonic processes on fast-spreading mid-ocean ridges, *Earth Planet. Sci. Lett., 104,* 513-534, 1991.

Herron, T.J., Lava flow layer - East Pacific Rise, *Geophys. Res. Lett., 9,* 17-20, 1982.

Karson, J.A., S.D. Hurst and P. Lonsdale, Tectonic rotations of dikes in fast-spread oceanic crust exposed near Hess Deep, *Geology, 20,* 685-688, 1992.

Klitgord, K.D. and J. Mammerickx, Northern East Pacific Rise: Magnetic anomaly and bathymetric framework, *J. Geophys. Res., 87,* 6725-6750, 1982.

Luetgert, J.H., Users manual for RAY84/R83PLT interactive two-dimensional ray tracing/synthetic seismogram package, U.S. Geological Survey Open File Report, *88-238,* 1988.

Pallister, J.S., Structure of the sheeted dike complex of the Samail ophiolite near Ibra, Oman, *J. Geophys. Res., 86,* 2661-2672, 1981.

Pezard, P.A., Electrical properties of mid-ocean ridge basalt and implications for the structure of the upper oceanic crust in Hole 504B, *J. Geophys. Res., 95,* 9237-9264, 1990.

Purdy, G.M., New observations of the shallow seismic structure of young oceanic crust, *J. Geophys. Res., 92,* 9351-9362, 1987.

Rohr, K.M.M., B. Milkereit and C.J. Yorath, Asymmetric deep crustal structure across the Juan de Fuca Ridge, *Geology, 16,* 533-537, 1988.

Rosencrantz, E., The structure of sheeted dikes and associated rocks in North Arm massif, Bay of Islands ophiolite complex, and the intrusive process at oceanic spreading centers, *Can. J. Earth Sci., 20,* 787-801, 1983.

Salisbury, M.H., N.I. Christensen, K. Becker and D. Moos, The velocity structure of layer 2 at Deep Sea Drilling Project site 504 from logging and laboratory experiments, *Init. Repts. DSDP, 83,* 1985.

Toomey, D.R., G.M. Purdy, S.C. Solomon and W.S.D. Wilcock, The three-dimensional seismic velocity structure of the East Pacific Rise near latitude 9°30'N, *Nature, 347,* 639-645, 1990.

Vera, E.E. and J.B. Diebold, Seismic imaging of oceanic layer 2A between 9°30'N and 10°N on the East Pacific Rise from two-ship wide aperture profiles, *J. Geophys. Res.*, *in press,* 1993.

Vera, E.E., J.C. Mutter, P. Buhl, J.A. Orcutt, A.J. Harding, M.E. Kappus, R.S. Detrick and T.M. Brocher, The structure of 0- to 0.2-m.y.-old oceanic crust at 9°N on the East Pacific Rise from expanded spread profiles, *J. Geophys. Res.*, *95,* 15529-15556, 1990.

Wilcock, W.S.D., D.R. Toomey, G.M. Purdy and S.C. Solomon, The renavigation of Sea Beam bathymetric data between 9°N and 10°N on the East Pacific Rise, *Mar. Geophys. Res.*, *15,* 1-12, 1993.

Wilkens, R.H., G.J. Fryer and J. Karsten, Evolution of porosity and seismic structure of upper oceanic crust: importance of aspect ratios, *J. Geophys. Res.*, *96,* 17981-17995, 1991.

Figure 2.1. Sea Beam bathymetry [*Wilcock et al.*, 1993] contoured at 25 meter intervals for a section of the East Pacific Rise located between the Siqueiros and Clipperton transform faults. Shiptracks for the on-bottom seismic refraction experiments are indicated with the heavy black lines; due to the undithered GPS during the cruise, the ship could be accurately navigated within tens of meters. Each shiptrack is labelled with the approximate age of the crust in kiloyears, based on a half spreading rate of 5.5 cm/yr [*Klitgord and Mammerickx*, 1982], with an 'E' or 'W' appended to indicate relationship to the rise axis, and an 'S' or 'N' appended to the southern and northern zero-age lines, respectively. The zero-age lines will also be referred to as the 'ASC' lines, and lines 10W, 20W, 20E, 70W, and 120W will also be referred to as the 'flank' lines in this chapter. An ocean bottom hydrophone (OBH) was located at the southern end of each ridge parallel line, with an OBH at both the eastern and western ends of the Line 0-20R. The inset map shows the regional setting, with triangles indicating the locations of the experiments conducted at 9°30'N and 12°50'N.
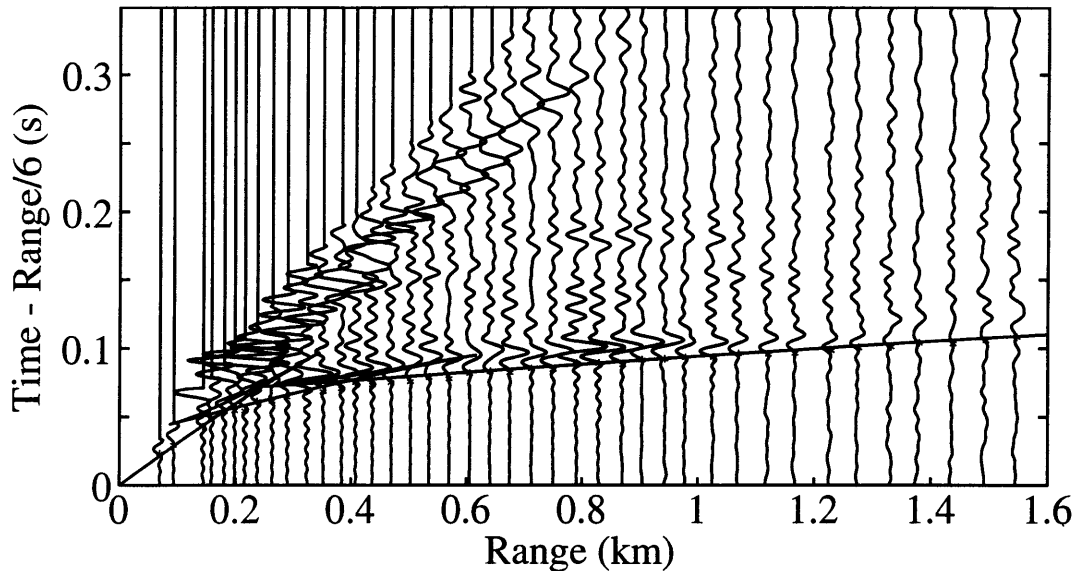
Fig. 2.2. Record section (corrected for shot height above seafloor) of the 2.3 kg (5 lb) charges detonated to the OBH for Line 0S. The recording instrument was a Woods Hole Oceanographic Institution Ocean Bottom Hydrophone with sampling at 1200 hz. For display purposes it was necessary to multiply the amplitudes of the seismograms by a factor of $R^{2.4}$, where R is the distance of the shot from the receiver. The amplitude has been set to zero at the onset of the water wave. The seismograms have been low-pass filtered with a cosine-squared filter, with an upper taper interval of 100-110 hz. The first breaks are shown with asterisks, with total errors in the first arrival travel times $<\pm5$-10 milliseconds, and range errors $<\pm5$-10 m. The seismograms are plotted with a reduction velocity of 6.0 km/s, with compressional arrivals breaking left. The solid line is the travel time curve from ray tracing of the velocity/depth model shown in Figure 2.4. The record section shows low-velocity (<2.5 km/s) arrivals emerging ahead of the water wave out to a range of ~0.2 km. Triplications at ranges of ~0.2 km and ~0.4 km are associated with the velocity discontinuities at 0.05 km and 0.13 km in Figure 2.4.
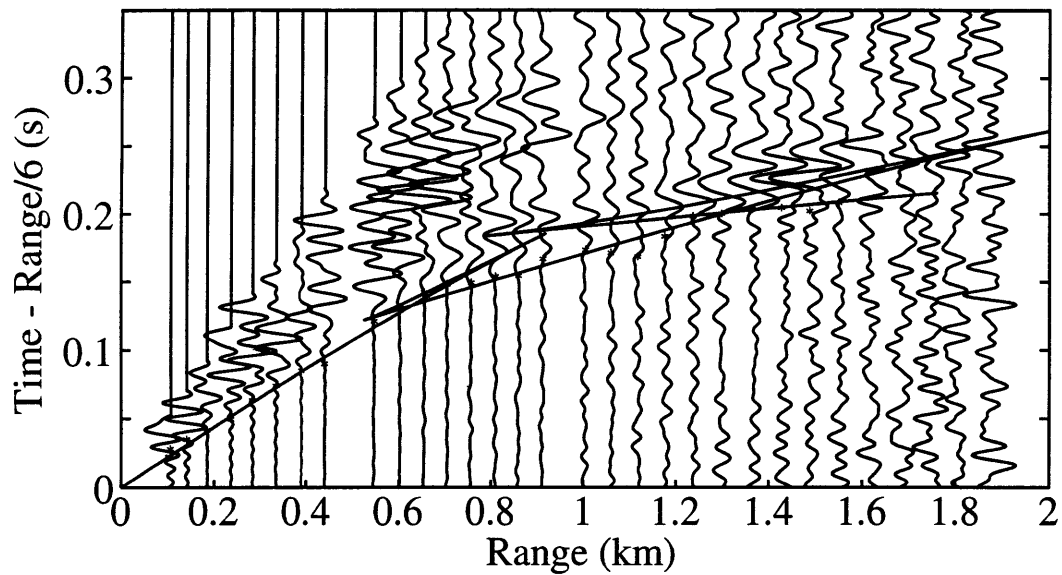
Figure 2.3. As for Figure 2.2, except that the data are shown for Line 20W, and the range scale factor is $R^{2.6}$. The record section clearly shows low-velocity (<3 km/s) arrivals emerging ahead of the water wave out to a range of ~0.7 km. A triplication is apparent at ~1.3 km associated with the ~1 km/s velocity discontinuity at 0.35 km in Figure 2.4.
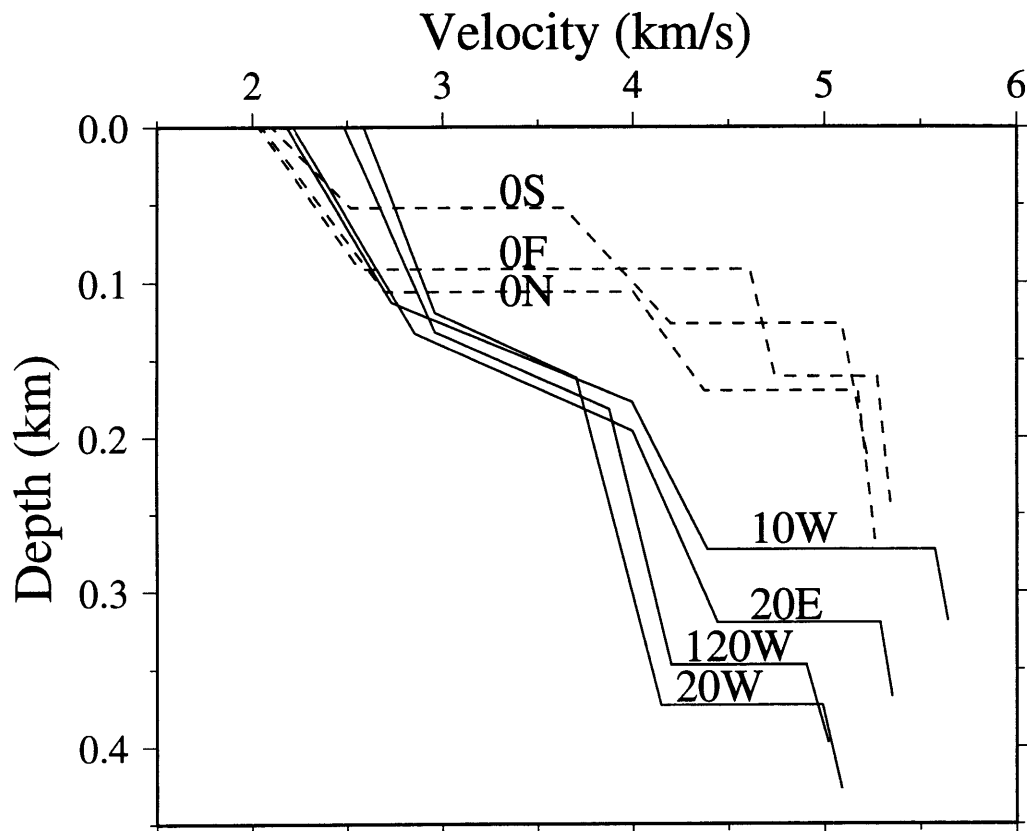
Figure 2.4. Velocity/depth models for the unreversed on-bottom seismic refraction experiments. The three lines shot within the axial summit caldera are shown as dashed lines. The model for Line 70W is not shown due to the poor signal to noise ratio associated with the first arrival travel times.
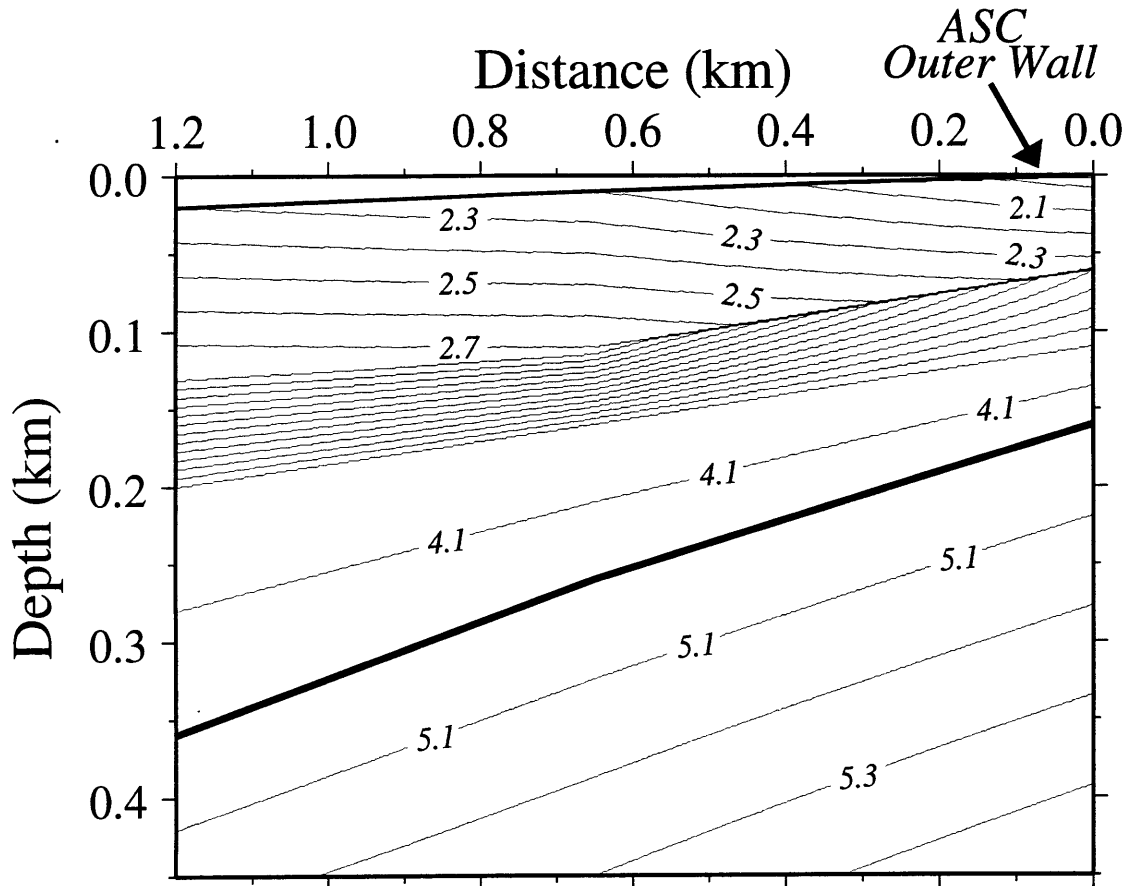
Figure 2.5. Two-dimensional velocity/depth model for Line 0-20R with a velocity contour spacing of 0.1 km/s. Distance is increasing away from the axial summit caldera, and the seafloor is dipping ~1° from east to west. The arrow points to the approximate location of the ASC outer wall. The heavy dark line indicates the boundary where the velocity increases from 4.2 km/s to 5.0 km/s; this boundary is dipping away from the ASC at ~10° from the horizontal. Note the closely spaced velocity contours in the depth range 0.05-0.2 km/s which indicate a high-gradient region in the western portion of the model and a velocity discontinuity of ~1 km/s at the far eastern portion of the model.

CHAPTER 3

SEISMIC CONSTRAINTS ON SHALLOW CRUSTAL EMPLACEMENT PROCESSES AT THE FAST-SPREADING EAST PACIFIC RISE

Abstract. We present the results of nine on-bottom seismic refraction experiments carried out over young East Pacific Rise crust. The experiments are unusual in that both the source and receiver are located within a few meters of the seafloor, allowing high-resolution determinations of shallow crustal structure. Three experiments were located within the axial summit caldera (ASC), over 'zero-age' crust. The seismic structure at these three locations is fundamentally the same, with a thin (<60 m) surficial low-velocity (<2.5 km/s) layer, an ~100-150 m thick transition zone with velocities increasing by ~2.5 km/s, and a layer with velocities of ~5 km/s at a depth beneath the seafloor of ~130-190 m. The surficial low-velocity layer and transition zone are defined as seismic layer 2A, and the ~5 km/s layer as the top of layer 2B. Both the surficial low-velocity layer and the transition zone double in thickness within ~1 km of the rise axis, with the depth to the 2A/2B boundary increasing from ~150 m to ~300-350 m over this range. The seafloor velocities increase from ~2.1-2.35 km/s for zero-age crust to ~2.4-2.85 km/s for 10,000 to 120,000 year old crust, consistent with a decrease in porosity from ~27% to ~20%. Amplitude modeling of the on-bottom seismic refraction data determines that the Poisson's ratio at the seafloor must be at least 0.43, suggesting that the shallow crustal porosity is largely due to high-aspect ratio cracks. Our preferred seismic model includes high attenuation within layer 2A (Q_p~25), and lower attenuation (Q_p~500) in layer 2B. We model layer 2A as the extrusive sequence and transition zone, and the 2A/2B boundary as the top of the sheeted dikes. The thickening of the extrusive layer is interpreted to be due to lava that either overflows the ASC walls, is emplaced through eruptions outside of the ASC, or travels

laterally from the ASC through conduits. According to this model, the shallow crustal architecture is in place within 1 km of the rise axis. A comparison with the structure observed from drilling at DSDP Hole 504B suggests that the subsidence of the sheeted dikes is more than double at intermediate-spreading centers (~800 m) than for the fast-spreading EPR (~300-350 m). Additionally, this implies that the volume of magma emplaced as extrusives at intermediate spreading centers is at least as great as that emplaced at fast-spreading centers.

Introduction

We present results from nine on-bottom seismic refraction experiments, located on young crust formed at the fast-spreading East Pacific Rise (EPR) near 9°30'N and 12°50'N (Figure 3.1). By placing both the source and receiver close to the seafloor, we can observe energy directly which has turned in the uppermost several hundred meters of the crust. This allows us to provide high resolution determinations of the shallow compressional wave velocity structure, and through amplitude modeling, to provide constraints on Poisson's ratio and attenuation.

The northern EPR has been studied extensively with seismic methods, but only a few experiments have resolved the structure of the shallow crust. High-quality expanding spread profiles [*Stoffa and Buhl*, 1979], unlike traditional seismic refraction experiments, can often identify energy that turns in the shallow crust and arrives after the onset of the water wave. Both *Vera et al.* [1990] and *Harding et al.* [1989], using expanding spread profile data, have identified a surficial low-velocity layer from experiments located near 9°30'N and 13°N respectively. This layer is 100-200 m thick, has velocities ≤2.6 km/s, has a low velocity gradient, and overlies a layer with a steep gradient where velocities >5 km/s are reached in a few hundred meters. The depth to a shallow 'reflector', interpreted to be formed by refracted energy which has turned in the steep gradient underlying the surficial low-velocity layer [*Harding et al.*, 1993; *Vera and Diebold*, 1993], increases from

~100-200 m at the rise axis to ~300-600 m within 1-3 km of the rise axis. Rapid lateral variations in shallow crustal structure are also suggested from the tomographic images of *Toomey et al.* [1990] at 9°30'N and the refraction data of *McClain et al.* [1985] at 12°50'N.

Knowledge of shallow crustal structure is useful because it is in this region that the emplacement of the volcanic section occurs. The surficial low-velocity layer is attributed to a layer of high-porosity pillows and flows [*Houtz and Ewing*, 1976; *Purdy*, 1987], with porosities possibly greater than 20% [e.g. *Hyndman and Drury*, 1976; *Wilkens et al.*, 1991; *Berge et al.*, 1992]. The higher-velocity material underlying the surficial low-velocity layer has been interpreted to be either the top of the sheeted dike sequence [*Herron*, 1982; *Christeson et al.*, 1992; *Harding et al.*, 1993] or low-porosity pillow lavas and flows [*McClain et al.*, 1985; *Rohr et al.*, 1988; *Harding et al.*, 1989; *Vera et al.*, 1990]. The deepening of this layer within a few kilometers of the rise axis is attributed to either dike subsidence [*Toomey et al.*, 1990; *Christeson et al.*, 1992; *Harding et al.*, 1993] or increased fracturing away from the emplacement zone [*McClain et al.*, 1985]. In this paper we describe a detailed modeling effort, primarily using the reflectivity method, to determine the shallow velocity structure. The velocity structure is used to constrain a geological model, which favors dike subsidence over increased fracturing as an explanation for the rapid lateral variations in shallow crustal structure.

Eight of our experiments were located over young EPR crust near 9°30'N (Figures 3.1 and 3.2), with one additional experiment located near 12°50'N (Figure 3.3). The EPR near 9°30'N is broad and rectangular in cross-section, but is asymmetric with water depth increasing more rapidly to the east than to the west [*Macdonald et al.*, 1992; *Wilcock et al.*, 1993]. The axial summit caldera (ASC), interpreted as a syn- or post-volcanic collapse feature in the 9°30'N region [*Haymon et al.*, 1991], is present along the entire rise crest in our study area [Figure 3.2]. The ASC widens to the north from an average width of ~130 m to ~275 m, and is less than 15 m deep [*Fornari, Perfit, Haymon, Edwards, and O'Brien*,

Morphology and structure of the ASC of the EPR between 9°-10°N: ARGO and Alvin observations, in prep; hereafter referred to as *Fornari et al.*, in prep]. The floor of the ASC is dominated by young volcanism and active fissuring [*Haymon et al.*, 1991]. A strong axial magma chamber (AMC) reflector, associated with the top of a low-velocity zone, is present in this region [*Detrick et al.*, 1987]. The EPR at 9°30'N is the location of ODP Site 864, the first attempt to drill zero-age crust using the diamond drilling technology demanded by bare rock [*Shipboard Eng. and Sci. Parties*, 1993]. In comparison, the EPR near 12°50'N is domed in cross-section [*Macdonald and Fox*, 1988], and the ASC is on average wider (200-400 m in width) and deeper (20-50 m deep) than observed near 9°30'N [*Gente et al.*, 1986]. An AMC reflector is imaged continuously along-axis in this region [*Detrick et al.*, 1987], but it is considerably narrower than observed near 9°30'N. The experiments discussed in this paper were placed within and close to the ASC as located by *Fornari et al.* [in prep] and *Gente et al.* [1986].

Experimental Procedure

The on-bottom seismic refraction experiments were carried out using NOBEL (Near Ocean Bottom Explosives Launcher) [*Koelsch et al.*, 1991], a unique deep-towed explosive source. NOBEL (Figure 3.4) consists of a steel frame with 47 barrels, each of which contains a five or ten lb (2.3 or 4.6 kg) PETN explosive charge. Each charge is individually released from its barrel, and is suspended beneath NOBEL by 30.5 meters of "Primacord"* (Trademark of Ensign Bickford Company). Hydrophones attached to the frame allow confirmation of a successful release, and the charge is then electrically detonated. The recording instrument is a Woods Hole Oceanographic Institution ocean bottom hydrophone (OBH) [*Peal et al.*, 1993]. The OBH has a dynamic range of 98 dB, and during these experiments sampled at a rate of 1200 samples per second. The experimental procedure for a typical experiment, with NOBEL firing shots to one OBH, is depicted in Figure 3.5. For one experiment we deployed two OBHs, one located at each

end of the shooting line, with the experimental procedure identical to that shown in Figure 3.5 with the exception that the additional OBH was deployed at the start of the operation.

Data and Interpretation

In this paper we present results from nine on-bottom refraction experiments, the location of which are shown in Figures 3.1 and 3.3. The preliminary processing for all experiments was identical. We first calculated shot-receiver ranges for each shot using the water wave, with the exception of the closest shots where the water wave arrivals exceeded the dynamic range of the instrument; for these shots we used the transponder determined ranges. We estimate that the transponder determined ranges are accurate to within 10 meters (due to the geometry), and the water wave determined ranges are accurate to within 5 meters. The travel times of first arrival refractions were picked from unfiltered seismic traces, with an estimated picking error of ± 1-4 ms at the closest ranges and $<\pm 10$ ms at the furthest ranges. The travel-time effects of shot height variations were removed from the first arrival travel times by calculating the ray entry point at the seafloor, assuming a flat seafloor and constant ray parameter. The error in this correction is estimated to be ± 2 ms due to uncertainties in shot height of ~2 m, and ± 2 ms due to a non-constant ray parameter. All shots were within 30 m of the seafloor, with the majority within 10 m. Errors due to clock drift and detonation time are ≤ 1 ms.

We fit the first arrival travel times with one-dimensional ray tracing (with the exception of Line 0-20R where we used two-dimensional ray tracing) to produce preliminary velocity-depth models for each experiment [*Christeson et al.*, 1992]. These models were then used as the starting point for reflectivity modeling [*Fuchs and Müller*, 1971], using the code described in detail in *Mallick and Frazer* [1987]. The code is based on the Kennett reflectivity algorithm [*Kennett*, 1983], uses the Filon method of quadrature of the slowness integral, and includes attenuation by using complex frequency dependent velocities. Except where stated otherwise, we used a constant Poisson's ratio of 0.3 [*Christensen*, 1972;

1978] (i.e., a V_p/V_s ratio of 1.9), set $Q_s = 0.5Q_p$, and computed densities using the relationship for basalts of *Christensen and Shaw* [1970], $\rho = 1.85 + 0.165V_p$. We used a water layer equal in thickness to the average water depth for each experiment, with the shot heights and receiver height at 10 m and 1 m, respectively, above the seafloor. The source signature for NOBEL was not known, and thus two sources for the reflectivity modeling were generated. One source was based on short range unclipped refraction arrivals, and the other on a longer range unclipped water wave arrival. The amplitudes of the resulting synthetic seismograms were nearly identical, with the source based on the water wave producing a slightly better fit to the waveforms. Therefore the water wave source was used for our final reflectivity models. In the following sections, we will present the modeling results from each line.

Line 0S

Line 0S was located within the ASC (Figure 3.2) on 'zero-age' crust; seismograms from the 42 shots are plotted in Figure 3.6a. The record section shows low-velocity (phase velocity ~2.1 km/s) arrivals emerging ahead of the water wave out to a range of ~0.2 km, first arrivals with a phase velocity of ~4.0 km/s in the 0.2-0.4 km range, and with a phase velocity of ~5.1 km/s in the 0.4-1.6 km range. Indicated on the record section are three sets of secondary arrivals with phase velocities <2.5 km/s. The frequency content of the first arrivals is much higher than observed from conventional surface shots, with first arrivals at the closest ranges having frequencies of 150-200 Hz, and first arrivals at ranges >1 km with frequencies of ~60 Hz. The corresponding seismic wavelengths are ~10-14 m for 150-200 Hz energy turning in 2.1 km/s material, and ~85 m for 60 Hz energy turning in 5.1 km/s material.

Variations in velocity gradients, Poisson's ratio, and the attenuation structure may have similar effects on amplitude patterns. Therefore our strategy in modeling was to try first to match the amplitude patterns using the reflectivity method with variations only in the

velocity gradients, with Q_p=100 and Poisson's ratio = 0.3 in each layer. The Q_p of 100 was chosen as a conservative estimate of attenuation for young upper oceanic crust [*Jacobson and Lewis*, 1990; *Wilcock et al.*, 1992b]. Then we varied Q_p and Poisson's ratio in each layer to note their effects on the amplitudes, and only altered these values if necessitated by the amplitude patterns in the data. With this method we were able to match the primary features of the data, with the exception of the high amplitude secondary arrivals immediately preceding the water wave in the 0.1-0.3 km range. The final velocity/depth model is listed in Table 1 and plotted in Figure 3.7, and the synthetic seismograms for this model are shown in Figure 3.6b.

The four primary features of the final velocity/depth model are: 1) There is a thin (<50 m thick) surficial low-velocity layer, with compressional-wave velocities <2.5 km/s and shear-wave velocities <1 km/s. 2) The Poisson's ratio of the surficial low-velocity layer is unusually high (0.48 for our best-fitting model). 3) Velocities of >5 km/s are reached within 150 m of the seafloor. 4) The 5 km/s material is associated with a much higher Q_p (~500) than the lower-velocity material above it (Q_p of ~25). We will discuss the constraints on each of these features in turn.

The compressional-wave velocity and thickness of the thin surficial low-velocity layer are constrained primarily by matching the travel times of the first arrivals, but are also influenced by the Q_p chosen for this layer, due to the effect attenuation has on apparent phase velocities (e.g. *Strick* [1970]). For a Q_p of 25, a seafloor velocity of ~2.33 ±0.15 km/s is needed to match the first arrival travel times in the 0-0.2 km range. Ray-tracing suggests that energy that multiply turns in or is reflected from the base of this layer is responsible for the low-velocity secondary arrivals indicated by the solid lines in Figures 3.6a and 3.6b. Although velocity gradients as high as 13 s^{-1} in the surficial low-velocity layer will adequately match the first arrival travel times and amplitudes, a velocity gradient of 1.6±1.6 s^{-1} is needed to correctly match the multiply turning energy, with the error bounds determined by forward modeling. With no attenuation, reflectivity modeling

predicts a large triplication for velocity gradients of <3.2 s^{-1}, which is not observed in the data. This is one of several reasons that we chose a low-Q_p for the surficial low-velocity layer.

The Poisson's ratio at the seafloor controls the fraction of energy that is transmitted, reflected, or converted from compressional to shear or vice versa. The energy that multiply turns in the surficial low-velocity layer will interact several times with the seafloor interface, and thus variations in the Poisson's ratio will have a major effect on the amplitudes of these phases. Reflectivity modeling suggests that increasing the Poisson's ratio at the seafloor results in an increase in the amplitude of this energy. For a Q_p of 100, a Poisson's ratio of at least 0.43 (i.e., V_p/V_s >3) is needed to produce three sets of multiply turning arrivals, and for a lower Q_p of 25-37, a Poisson's ratio of 0.48 (V_p/V_s = 5) is needed. These values correspond to seafloor shear wave velocities of <0.75 km/s.

Beneath the surficial low-velocity layer is a high-gradient region, where velocities increase from ~2.4 km/s to ~5.0 km/s over a depth interval of ~100 m, resulting in an average gradient of ~26 s^{-1}. This region is constrained by the first arrival travel times and amplitudes, and is needed to match the rapid increase in phase velocity of the first arrivals from ~2.1 km/s in the 0-0.2 km range to ~5.1 km/s in the 0.4-1.6 km range. The small change in gradient at a depth of ~75 m (Figure 3.7) allows energy to arrive with a phase velocity of ~4 km/s in the 0.2-0.4 km range, and also produces the small triplication observed in the data at ~0.4 km range. Underlying the high-gradient layer is a layer with velocities exceeding 5 km/s, that extends to a depth of ~200 m. The average velocity in this layer is 5.1±0.15 km/s. We have no constraints from our data beneath 200 m, as our furthest shots are at a range of 1.6 km, and the corresponding seismograms have a low signal to noise ratio. At ranges greater than 0.4 km, secondary energy associated with the region beneath the surficial low-velocity layer is visible in the synthetics (Figure 3.6b) ~50-70 ms after the first arrivals; similar energy is not clearly seen in the observed data. A model with a low Q_p for the surficial low-velocity layer and high-gradient region is

preferred, since the amplitudes of this phase are lowered, but still does not provide a good fit.

We can place constraints on the gradient and attenuation in the 5 km/s layer using the amplitudes of the first arrivals beyond 0.4 km. Figure 3.8 shows the variation of the first arrival amplitudes vs. range. This variation has a small dependency on the Poisson's ratio in each layer, but is controlled mainly by the values of the velocity gradient and attenuation. The amplitude of the first arrivals decreases rapidly with range out to ~0.6 km, with a slight flattening out at ~0.3-0.4 km range associated with a triplication. The rate of amplitude decrease with range is less in the 0.6-1.3 km range window. This amplitude pattern is consistent with either an increase in gradient or a decrease in the amount of attenuation with depth. The first arrival travel times in the 0.4-1.6 km range show no curvature as would be observed with a large velocity gradient in the lowermost layer, and thus a decrease in attenuation with depth is the preferred explanation for the change in slope beyond 0.6 km range (Figure 3.8). Plotted in Figure 3.8 are the variations in first arrival amplitude with range for three models, which differ only in the Q_p value for the 5 km/s layer. Reflectivity ·modeling indicates that a Q_p of at least 100, and perhaps higher, in this layer will better match the variation in first arrival amplitude with range in Figure 3.8. The synthetic seismograms in Figure 3.6b were generated with a Q_p value of 500 in the 5 km/s layer.

Line 0N

Line 0N was located within the ASC (Figure 3.2), with the OBH located approximately 5 km north of the OBH used in Line 0S. The record section (Figure 3.9a) is very similar to that of Line 0S (Figure 3.6a), with low-velocity (phase velocity ~2.0 km/s) arrivals emerging ahead of the water wave out to a range of ~0.3 km, first arrivals with a phase velocity of ~4.6 km/s in the 0.3-0.5 km range, and with a phase velocity of ~5.2 km/s in the 0.5-1.9 km range. Low phase-velocity (<2.5 km/s) secondary arrivals are also observed.

We used the final velocity/depth model from reflectivity modeling of Line 0S as the starting model for synthetic seismogram modeling for Line 0N, and varied the velocities and layer thicknesses to match the amplitude patterns observed in the data (Figure 3.9a). The final velocity/depth model for Line 0N is listed in Table 1 and plotted in Figure 3.7, and the synthetic seismograms for this model are shown in Figure 3.9b. The velocity/depth model is similar to that for Line 0S, with a thin (<75 m thick) surficial low-velocity (V_p <2.5 km/s, and V_s < 1.0 km/s) layer, and reaches velocities exceeding 5 km/s within 200 m of the seafloor. The surficial low-velocity layer is thicker (55 m vs. 32 m) and may have a higher compressional velocity gradient (5.3 ± 3 s^{-1} vs. 1.6 ± 1.6 s^{-1}) than in the model for Line 0S. The thicker surficial low-velocity layer is needed to match the first-arrival travel times, and the higher gradient to correctly model the secondary energy that multiply turns in or is reflected from the base of this layer. The model includes two changes in gradient in the depth interval 137-192 m, which are needed to produce the triplication observed at a range of approximately 0.5 km. The velocity in the depth interval 137-177 m is not well-constrained due to the small number of first arrival travel times in the 0.3-0.5 km range, but is at least 0.3 km/s faster than observed in the depth range 72-82 m in the model for Line 0S. The major difference between the velocity/depth models for Line 0S and Line 0N (Figure 3.7) is that material with a velocity of ~5 km/s is reached at a greater depth (192 m vs. 129 m) for Line 0N.

Line 0F

Line 0F was located near the western wall of the ASC (Figure 3.3), and was the only experiment located in the 12°50'N region. We had to make only minor changes to the final velocity-depth model from Line 0S to match the observed data, which were extremely similar in appearance to Figures 3.6a and 3.9a. The final velocity-depth model is listed in Table 1, and plotted in Figure 3.7.

Line 120W

Line 120W was located approximately 6 km west of the ASC in the 9°30'N area (Figure 3.1), over crust that is ~120,000 years old. In contrast to the record sections for Line 0S (Figure 3.6a) and Line 0N (Figure 3.9a) for which low-velocity (<3 km/s) arrivals were observed to a range of ~0.2-0.3 km, the record section for Line 120W (Figure 3.10a) shows low-velocity arrivals emerging ahead of the water wave out to a range of ~0.6-0.7 km. First arrivals with a phase velocity of ~3.8 km/s are observed in the range window 0.7-1.2 km, and first arrivals with a phase velocity of ~4.9 km/s in the 1.2-1.5 km range. At a range of 1 km, the first arrival travel times are 80-100 ms greater than observed for the lines located within the ASC. The frequency content of the first arrivals is lower than observed for the zero-age lines, with arrivals at the closest ranges having frequencies of 100-125 Hz, and arrivals at ranges >1 km with frequencies of 30-40 Hz. The corresponding seismic wavelengths are ~20-25 m for 100-125 Hz energy turning in 2.5 km/s material, and ~120-165 m for 30-40 Hz energy turning in 4.9 km/s material.

We followed the same procedure as for Line 0N for synthetic seismogram modeling of Line 120W. In contrast to the zero-age lines, there are no sets of secondary arrivals which are clearly related to energy multiply turning within or reflected off the base of the surficial low-velocity layer. Therefore we produced two models (Table 1) for Line 120W, which differ in the velocity gradient and thickness assigned to the surficial low-velocity layer. The first model has a zero gradient in the surficial layer; the synthetic seismograms for this model are shown in Figure 3.10b. Energy multiply turning within or reflected twice off the base of the surficial low-velocity layer (indicated by the dashed line in Figure 3.10b) arrives in the 0.7-1.1 km range for this model. Coherent high amplitude secondary arrivals are observed in this range window in the data (indicated by the solid line in Figure 3.10a), but this energy arrives ~30 ms earlier than the modeled energy in Figure 3.10b. The first arrivals at ranges >0.4 km are adequately modeled, with a triplication at 0.48 km producing a large amplitude arrival similar to that observed in the data at this range. First arrival

amplitudes at ranges <0.4 km could be better fit with higher attenuation in the shallow crust, but because of the sparsity of unclipped seismograms at the closest ranges we did not alter the attenuation value from that determined for Lines 0S. The second model has a velocity gradient of 5.3 s^{-1} in the surficial layer; the synthetic seismograms calculated from this model are plotted in Figure 3.10c. Energy multiply turning within or reflected twice off the base of the surficial low-velocity layer (indicated by the dashed line in Figure 3.10c) arrives in the 1.2-1.6 km range for this model, as compared to the 0.7-1.2 km range window for the zero-gradient model (Figure 3.10b). Coherent high amplitude secondary arrivals are observed in this range window in the data (indicated by the solid line in Figure 3.10a), but this energy arrives ~30 ms later than the modeled energy in Figure 3.10b. In contrast to the zero-gradient model, no triplication in the first arrival amplitudes is produced from this model at the 0.48 km range; otherwise the first arrival amplitudes are adequately modeled. The first arrival amplitudes at ranges <0.4 km are similar to those plotted in Figure 3.10b from the zero-gradient model. Both models produce secondary arriving energy that does not match the observed data. The zero-gradient model is slightly preferred ·because it produces a triplication in the first arrival amplitudes at the 0.48 km range (Figure 3.10b) similar to that observed in the data (Figure 3.10a), and this model is plotted in Figure 3.7.

The preferred model for Line 120W (Figure 3.7) includes a surficial low-velocity layer that is thicker and faster than in the zero-age models. The compressional-wave velocity and thickness of this layer are constrained by matching the travel times of the first arrivals; for a Q_p of 25, a seafloor velocity of ~2.63 ±0.15 km/s and a surficial low-velocity thickness of 107 m is needed to match the first arrival travel times in the 0-0.6 km range. The amplitudes of the first arrivals decrease rapidly with range, a pattern that is consistent with the shallow low-Q_p values obtained for the zero-age models. The surficial low-velocity layer is underlain by a high-gradient region, where velocities increase from ~2.63 km/s to ~4.18 km/s over a thickness of ~50 m. This region is in turn underlain by a region with

several changes in gradient, with velocities of ~4.9 km/s reached at a depth of ~300 m. Due to the poor signal-to-noise ratio observed in the seismograms in the 0.9-1.6 km range, the portion of the model in the depth range >200 m is not well-constrained, and the velocities have uncertainties of ±0.5 km/s.

Line 20W

Line 20W was located ~1 km west of the ASC, over ~20,000 year old crust (Figures 3.1 and 3.2). Although this experiment is located within 1 km of Line 0S, the first arrival travel times for Line 20W (Figure 3.11) are systematically greater than for Line 0S, and are similar to those of Line 120W, located 5 km to the west. The record section shows low-velocity (phase velocity <3.0 km/s) arrivals emerging ahead of the water wave out to a range of ~0.6-0.7 km, and a clear triplication at a range of ~1.4 km. Arrivals in the 0.7-1.4 km range have a phase velocity of ~4.0 km/s, and arrivals after the triplication, a phase velocity of ~5.0 km/s. There is no clear triplication in the 0.6-0.7 km range, where the phase velocities increase rapidly from ~2.6 km/s to ~4.0 km/s.

We attempted to model the amplitudes observed in Line 20W, but all models that matched the first arrival travel times produced a triplication in the 0.6-0.7 km range, a feature not observed in the data. We conclude that the structure beneath Line 20W is two-dimensional, and cannot be constrained by an unreversed refraction line. We have used ray-tracing to approximate the structure with a one-dimensional model based on Line 120W; this model is listed in Table 1, and plotted in Figure 3.7.

Line 10W, Line 20E, Line 70W

Failures of old hydrophone sensors on the OBHs used for the remaining off-axis lines (10W, 20E, and 70W) resulted in low signal-to-noise data that are poorly suited for amplitude modeling. We therefore used ray-tracing to fit the first arrival travel times, based on the final model for Line 120W. These models are listed in Table 1, and plotted in

Figure 3.7. Lines 10W, 20W, 120W, and 20E have similar shallow crustal structures, with a thin (~85-115 m) surficial low-velocity (~2.4-2.9 km/s) layer, underlain by a high gradient region where velocities increase from <3 km/s to ~4.5 km/s. The structure beneath ~200 m differs slightly for these four lines, but this portion of the models is poorly constrained due to the large uncertainties in the first arrival travel times. A coherent set of secondary arrivals are observed in the data for Line 10W, and these arrival times can only be modeled with a low-gradient surficial low-velocity layer. No coherent secondary arrivals are observed for Line 20E or Line 70W.

Line 0-20R: Cross-axis structure

Figure 3.7 shows a summary of the velocity-depth models for the ridge parallel experiments. The velocity structure of the three lines located within the ASC differs systematically from that of the other five lines, with the zero-age lines reaching higher velocities at shallower depths. Furthermore, the seafloor velocity is faster for the lines located outside of the ASC. *Christeson et al.* [1992] examined this major change in crustal structure by using two-dimensional ray tracing [*Luetgert*, 1988] to fit the first arrival travel times for Line 0-20R. Two OBHs were used for Line 0-20R, with one OBH located within the ASC, and the other located ~1.2 km to the west (Figure 3.2). Record sections from this line are plotted in Figure 3.12. Both record sections consist of low phase velocity arrivals (<3 km/s) at the closest ranges, but these extend out to ~0.6 km for the seismograms recorded by the western OBH, and only to a range of ~0.25 km for the eastern OBH located within the ASC. In addition, the phase velocity recorded by the western OBH for this set of arrivals is ~0.35 km/s faster. The phase velocities of the arrivals at the furthest ranges recorded by the eastern OBH are ~1.6 km/s slower than the phase velocities of similar arrivals recorded by the western OBH (~4.5 km/s vs. ~6.1 km/s).

The velocity/depth model shown in Figure 3.13 is based on the model of *Christeson et al.* [1992], but has been modified to be consistent with the models listed in Table 1. The principal changes made to the model presented in *Christeson et al.* [1992] are in the nature of the layer boundaries (the velocity discontinuities in *Christeson et al.* [1992] have been replaced by high-gradient regions in Figure 3.13) and in the surficial low-velocity layer velocities and velocity gradients (the surficial low-velocity layer of Figure 3.13 has lower velocity gradients and higher seafloor velocities as compared to the model of *Christeson et al.* [1992]). The four primary characteristics of the model are as follows: 1) The surficial low-velocity layer thickens away from the ASC. 2) The depth to 5.0 km/s material deepens away from the ASC. 3) The seafloor velocity increases away from the ASC. 4) The seafloor velocities are consistently lower than observed by rise-parallel refraction experiments at the same locations. We will discuss the constraints on each of these features in turn.

The thickening of the surficial low-velocity layer away from the ASC is well-constrained by the first arrival travel times. Low phase velocity (<3 km/s) arrivals are observed out to a range of ~0.25 km by the eastern receiver, and ~0.5-0.6 km by the western receiver (Figures 3.12 and 3.14). These observations are well-matched with a surficial low-velocity layer thickness that increases from ~30 m beneath the ASC to ~90 m at a range ~1.2 km off-axis. The results from modeling of Line 10W suggest that the majority of this thickening occurs within 500 m of the ASC. As previously mentioned, the phase velocities of the first arrivals at the furthest ranges are greater for the western receiver than for the eastern receiver. This is the classic indication of a dipping layer, and the first arrival travel times are well-matched (Figure 3.14) with the depth to 5 km/s material thickening from ~150 m below the seafloor within the ASC to ~310 m beneath the seafloor at a range of 1.2 km. This corresponds to a dip of ~8.5° from the horizontal, much greater than the seafloor dip of ~1°.

Plotted in Figure 3.15 are the apparent phase velocities for first arrivals interpreted to be turning within the surficial low-velocity layer for Lines 0S, 20W, and 0-20R. The apparent phase velocities of the arrivals observed by the receivers located within the ASC (Line 0S and the eastern receiver of Line 0-20R) are systematically slower than observed for the receivers located ~1 km west of the ASC (Line 20W and the western receiver of Line 0-20R), consistent with an increase in velocity of the surficial low-velocity layer by 0.4±0.3 km/s away from the ASC. The velocities of the surficial low-velocity layer indicated in Figure 3.13 are ~0.25 km/s greater than the values shown in Figure 3.15, due to the effect the high attenuation in this layer has on apparent phase velocities.

The western receiver for Line 0-20R and the receiver for Line 20W were positioned at approximately the same location (Figure 3.2), but the apparent phase velocity for the cross-axis line is slower (2.33±0.02 km/s vs. 2.59±0.05 km/s) than for the rise-parallel line (Figure 3.15). These differences in phase velocities are consistent with a velocity anisotropy in the surficial low-velocity layer of 7.5-12.5%, with the fast direction parallel to the rise axis, although shallow velocity heterogeneities provide an alternate explanation. Similarly, the eastern receiver for Line 0-20R and the receiver for Line 0S were positioned at approximately the same location (Figure 3.2), but at this location there is no evidence from the apparent phase velocities (Figure 3.15) for velocity anisotropy in the surficial low-velocity layer.

Observed in the record sections plotted in Figure 3.12 are several packets of coherent energy, similar to the multiple arrivals successfully modeled with the reflectivity method for Lines 0S and 0N (Figures 3.6 and 3.9). We have used ray-tracing to model the locations of energy multiply reflecting off the base of the surficial low-velocity layer, and indicate on Figure 3.12 (dashed lines) the secondary energy that is related to these multiples. For the eastern receiver, most of the secondary energy (with the exception of the closest ranges) can be explained by this multiple energy. For the western receiver, energy that is reflected twice off the base of the surficial low-velocity layer is predicted to arrive at ranges >0.7

km, as indicated by the dashed line in Figure 3.12b. Large amplitude secondary arrivals are also observed at ranges <0.7 km, and cannot be explained by this multiple energy. The western receiver for Line 0-20R was located at approximately the same location as the receiver used for Line 20W. The seismograms recorded for this rise-parallel experiment (Figure 3.11) also have large amplitude secondary arrivals (in the 0.4-1.0 km range) that cannot be explained by arrivals multiply turning within or reflecting off the base of the surficial low-velocity layer. The amplitudes of the first arrivals for Line 20W had previously suggested that there were lateral heterogeneities, which could perhaps result in the secondary energy observed.

Comparison of the model for Line 0-20R with the model for Line 120W suggests that only minor variations occur between the shallow crust 1 km west of the rise axis and 6 km west of the rise axis. Similarly, a comparison with Line 20E suggests that the shallow structure is approximately symmetrical about the rise axis.

Summary of modeling results

1. The velocity/depth models for all experiments include a surficial low-velocity layer. The seafloor velocity of this layer varies from ~2.1-2.35 km/s for zero-age crust to ~2.4-2.85 km/s for 10,000-120,000 year old crust.

2. Modeling of Lines 0S, 0F, 10W, and 120W constrains the velocity gradient for the surficial low-velocity layer to be <3.5 s^{-1} at these locations. For Line 0N, the velocity gradient is ~5.3±3 s^{-1}.

3. The presence of secondary arrivals associated with energy multiply turning within and reflecting off the lowermost boundary of the surficial low-velocity layer for Lines 0S, 0N, and 0F requires Poisson's ratio at the seafloor to be >0.43. The preferred value is ~0.48.

4. Reflectivity modeling suggests that the shallow crust is highly attenuative, with a Q_p value of ~25. First arrival amplitudes constrain the Q_p value of the 5 km/s material to be ~500.

5. There is a major change in structure within ~1 km of the rise axis. The surficial low-velocity layer thickens from ~30 m to ~90 m at 9°30'N, and the depth to material with a velocity of ~5 km/s deepens from ~150 m to ~310 m below the seafloor.

6. The seismic observations are consistent with an anisotropy of 0-12.5% within the surficial low-velocity layer, with the fast direction parallel to the rise axis.

DISCUSSION

Structure

In a classic paper, *Houtz and Ewing* [1976] divided the upper oceanic crust into layers 2A, 2B, and 2C according to seismic velocities. Layer 2A had an average refraction velocity of ~3.6 km/s, and was defined as "any low-velocity acoustic basement of probable igneous origin." Layers 2B and 2C had average refraction velocities of ~5.2 km/s and ~6.1 km/s, respectively. Based on the *Houtz and Ewing* [1976] definitions (which are indeed the only formal definitions), we have labeled the 2.2-5.0 km/s material as layer 2A in Figure 3.13, and the >5 km/s material as layer 2B; with this definition, significant structure exists within layer 2A. It has been argued that the layer 2A/2B boundary is either a boundary between the extrusive sequence and the sheeted dike complex [*Herron*, 1982; *Christeson et al.*, 1992; *Harding et al.*, 1993], or a porosity boundary separating high- and low-porosity extrusives [*McClain et al.*, 1985; *Rohr et al.*, 1988; *Harding et al.*, 1989; *Vera et al.*, 1990]. In the following section, we will explore the evidence in support of each of these hypotheses.

If the layer 2A/2B boundary represents the top of the sheeted dikes, then an important implication is that the final thickness of the combined extrusive sequence and transition zone is only ~300-350 m at the EPR. At present, no drill hole has penetrated more than a

few tens of meters into oceanic crust formed at a fast-spreading center, and thus we cannot directly compare the structure of the EPR at 9°30'N (half-spreading rate 5.5 cm/yr [Klitgord and Mammerickx, 1982]) with drilling results. The only drill hole in normal oceanic crust that we know to have definitely penetrated the top of the sheeted dike sequence is DSDP Hole 504B. The crust at Hole 504B was emplaced at the intermediate-spreading Costa Rica Rift (half spreading rate of ~3.6-3.8 cm/yr), and at this location the extrusive section is ~575 m thick, and is underlain by a ~210 m thick transition zone (a region that consists of pillows, flows, dikes, and possibly sills) to the top of the sheeted dike sequence at ~785 m depth (Figure 3.16) [Anderson et al., 1982]. Other locations where the depth to the top of the sheeted dike complex is known include ophiolite complexes (600-2000 m, e.g. [deWit and Stern, 1978; Alabaster et al., 1982; Schmincke et al., 1983]), the Vema fracture zone walls (~800 m [Auzende et al., 1989]), and the walls at Hess Deep (~300-400 m, [Francheteau et al., 1992]). The crust at the Vema fracture zone was emplaced at the slow-spreading Mid-Atlantic Ridge (half spreading rate of ~1.2 cm/yr), and the crust crust exposed along the walls of Hess Deep was generated ~1 Ma ago at the fast-spreading EPR (half spreading rate ~6.5-6.7 cm/yr). Ophiolites pose a problem as most are not of clear mid-ocean ridge provenance [Nicolas, 1989]. One of the few ophiolites generally thought to be of mid-ocean ridge origin and for which a spreading rate can be assigned with any confidence is the Semail ophiolite of Oman, which has an extrusive thickness of 1500-2000 m [Alabaster et al., 1982]. But Semail was formed at a half spreading rate of 3 cm/yr [Lippard et al., 1986], significantly slower than our EPR site. Because of the growing evidence that oceanic crustal structure is spreading rate dependent (e.g. [Purdy et al., 1992]), it is more appropriate to compare the results presented in the paper with the structure observed at Hess Deep than that at Hole 504B, the Vema fracture zone, or in ophiolite complexes.

Recent submersible dives at the walls of Hess Deep, a section of crust emplaced at the EPR approximately 1 my ago, provide the first direct observations of fast-spreading crustal

structure. Four dives of the submersible *Nautile* reported a sequence of extrusives overlying a mixed zone overlying a sheeted dike unit (Figure 3.16) [*Francheteau et al.*, 1992]. The extrusive sequence is only 100-200 m thick, and the top of this sequence at two of the four locations displays clear EPR abyssal hill fabric [*Searle and Francheteau*, 1986; *Lonsdale*, 1988; *Francheteau et al.*, 1992], suggesting that this is an intact unit. The mixed zone is of variable thickness (50-500 m, averaging 200 m), and consists of extrusives, dikes, and massive horizontally layered units which may represent sills [*Francheteau et al.*, 1992]. A comparison of the stratigraphy at Hess Deep with the shallow seismic structure of the EPR (Figure 3.16) suggests that layer 2A consists of both the extrusives and mixed zone, and the layer 2A/2B boundary represents the top of the sheeted dike complex.

If this interpretation is correct, then the velocities of young EPR crust are systematically lower than the velocities determined from geophysical experiments at Hole 504B. The velocities determined from an oblique seismic experiment at this location increase from ~4.8 km/s in the extrusive section (0-570 m), to ~5.5 km/s in the underlying transition zone (570-780m), to ~6.1 km/s in the upper few hundred meters of the sheeted dike complex (Figure 3.16) [*Little and Stephen*, 1985; *Collins et al.*, 1989]. Velocities determined from sonic logging are similar, with the exception that the extrusive layer consists of a thin (~100 m) layer with an average velocity of ~4.2 km/s, underlain by a 470 m thick region with velocities rapidly increasing to an average of ~5.2 km/s (Figure 3.16) [*Becker et al.*, 1988]. The most detailed and reliable determinations of the deeper velocity structure at the fast-spreading EPR at 9°30'N are from the expanding spread profiles of *Vera et al.* [1990] (Figure 3.17). The similarity of the 0 kyr ESP solution with our 10W solution is consistent with a location of the midpoint of the ESP experiment that was slightly outside of the ASC. Velocities similar to the dike velocities recorded at 504B are not reached until a depth of ~1100-1250 m both on zero-age and ~180 kyr crust, immediately above the low-velocity zone (Figure 3.16b). Based strictly on a comparison of the velocity structure of

504B and the velocity structure of this study, the entire structure shown in Figure 3.13 could represent variations in velocity and structure within the extrusive section. Logging has determined that variations in porosity are largely responsible for the velocity changes within the extrusive section at 504B [*Becker et al.*, 1982]. Thus the surficial low-velocity layer of Figure 3.13 could represent a high-porosity layer similar in thickness to the 100 m thick high-porosity layer of Hole 504B, underlain by an ~300 m thick region of rapid porosity decrease. Considering the data of *Vera et al.* [1990], this in turn could be underlain by an ~800 m thick low-porosity extrusive region and transition zone, and an ~100 m thick sheeted dike complex (based on a comparison of the Vera et al. [1990] velocities of Figure 3.17 and the velocity structure of Hole 504B). Two important implications of this interpretation are that the depth to the sheeted dike complex would be several hundred meters greater, and the thickness of the extrusive section and transition zone several hundred meters less on the EPR than observed at DSDP Hole 504B.

Hydrothermal vent fluids collected days after an eruption event on the EPR at 9°45-52'N [*Haymon et al.*, 1993] can provide further information about the structure of the fast-spreading EPR. Chemistry of vent fluids collected shortly after the eruption event and 11 months later suggest that the heat source for hydrothermal venting has deepened from ~200 m to ~1500 m over the 11 month period [*Von Damm et al.*, 1992]. *Von Damm et al.* [1992] and *Haymon et al.* [1993] propose that intrusion of dikes during the eruption to depths of ~200 m resulted in phase separation of fluids near the tops of the dikes, and that in the following 11 months these dikes were cooled so that the present day heat source is now related to the underlying magma chamber. These results are consistent with the 2A/2B boundary of Figure 3.13 representing a boundary between extrusives and the sheeted dike sequence.

In summary, there are two hypotheses to explain the nature of the 2A/2B boundary of Figure 3.13. The first hypothesis is that the boundary represents a change from high-porosity extrusives in layer 2A to low-porosity extrusives in layer 2B. This model would

be consistent with the velocities and structure observed at DSDP Hole 504B, but would infer the existence of an ~1200 m thick extrusive layer and transition zone overlying a thin (~100 m thick) sheeted dike complex (based strictly on a comparision of the 504B velocity structure with the young EPR velocity structure). The second hypothesis is that the boundary represents a change from extrusives to the sheeted dike complex. This is our preferred hypothesis, and is consistent with the structure of fast-spreading EPR crust observed at Hess Deep, and with the chemistry of hydrothermal vent fluids sampled at 9°45'-52'N. An important consequence of this interpretation is that the depth to the top of the sheeted dikes is ~300-350 m at the fast-spreading EPR and ~800 m for the intermediate-spreading crust at Hole 504B (Figure 3.16). In a later section, we will discuss this implication further.

Physical properties

The best constrained portion of our seismic model (Figure 3.13) is the compressional wave velocity structure of zero-age crust. This consists primarily of a thin surficial low-velocity (<2.5 km/s) layer, a transition zone where velocities increase by ~2.5 km/s over a thickness of ~100-150 m, and a layer with velocities of >5 km/s. A surficial low-velocity layer is not unique to young EPR crust, and has also been observed on the intermediate-spreading Juan de Fuca Ridge [*White and Clowes*, 1990; *Cudrak and Clowes*, 1993] and the slow-spreading Mid-Atlantic Ridge [*Purdy and Detrick*, 1986; *Purdy*, 1987]. Because laboratory measured velocities for fresh oceanic basalts are typically ~6 km/s, the low seismic velocities have been attributed to high porosity on scales larger than the laboratory samples [*Hyndman and Drury*, 1976; *Schreiber and Fox*, 1976; *Wilkens et al.*, 1991]. *Ludwig et al.* [*Ludwig, Fryer, Christeson, and Purdy*, Evolution of porosity of the shallow seafloor at the EPR, in prep; hereafter referred to as *Ludwig et al.*, in prep] estimate a porosity of 26-33% in the zero-age surficial low-velocity layer at 9°30'N and 12°50'N based on the velocities reported here and a Poisson's ratio of 0.48. A decrease in porosity

of ~6-8%, presumably due to a small amount of low-temperature alteration or modification during lava drainback, can explain the increased velocities in this layer off-axis [*Ludwig et al.*, in prep].

Our amplitude modeling demands a Poisson's ratio at the seafloor of >0.43, with a preferred value of ~0.48 (i.e., $V_p/V_s = 5$). Other determinations of Poisson's ratio for young oceanic crust are similar, falling in the range 0.39-0.46 [*Diachok et al.*, 1984; *Harding et al.*, 1989; *Vera et al.*, 1990]. These values are higher than the commonly assumed Poisson's ratio for oceanic crust, 0.3 ($V_p/V_s = 1.9$), which is based on laboratory measurements [*Christensen*, 1972; *Christensen*, 1978]. Theoretically, material dominated by thin cracks (i.e., aspect ratios much less than one) will have a higher Poisson's ratio than material with most of the porosity in void space much closer to unity, such as vesicles or interpillow voids [*Shearer*, 1988]. The large Poisson's ratio we find here is therefore diagnostic of a high population of thin cracks [*Ludwig et al.*, in prep]. Nothing in the seismic results gives any idea of the scale of the cracks. *Ludwig et al.* [in prep] assume random cracks, consistent with the radial and tangential cracks of pillows, but there must also be a contribution from fissures [*Vera et al.*, 1990]. Since the fissures are oriented predominantly in a rise parallel direction [*Haymon et al.*, 1991; *Wright, Haymon, and Fornari*, Crustal fissuring and its relationship to magmatic and hydrothermal processes on a 2nd-order ridge segment of the EPR (9°12'-54'N), in prep] they are also consistent with the 0-12% anisotropy observed in the surficial low-velocity layer. With time, alteration processes would tend to infill all cracks, resulting in a lower Poisson's ratio. Indeed, lower Poisson's ratios are observed for 6 Ma crust at Hole 504B (Poisson's ratios of 0.28-0.40 [*Moos et al.*, 1990]) and ~15 Ma crust (Poisson's ratios of 0.33-0.34, [*Spudich and Orcutt*, 1980]) in the Eastern Pacific.

An inversion for the attenuation structure across the EPR at 9°30'N [*Wilcock et al.*, 1992b] calculated an average Q_p value in the uppermost crust of ~35 off-axis, and ~70 on-axis; if the cross-axis variation is due to off-axis thickening of a low-Q_p layer, then the Q_p

in this layer must be ~10-20 [*Wilcock et al.*, 1992]. The results of our study also suggest that a low Q_p layer (Q_p ~25) that thickens away from the ASC provides the best fit to seismic observations. Laboratory measurements of attenuation in oceanic basalts show a positive correlation of attenuation with porosity and a negative correlation with compressional wave velocity [*Wepfer and Christensen*, 1990], and because the young basalts at the EPR are interpreted to have low velocities (<3 km/s) and high porosities (~26-33% [*Ludwig et al.*, in prep]) high attenuation would be expected.

We have interpreted the 5 km/s material as the top of the sheeted dike complex. Hole 504B is the only piece of oceanic crust where dike velocities at the scale of hundreds of meters are unequivocally known, and at this location the estimated velocity at the top of the sheeted dikes is ~5.7-5.8 km/s (Figure 3.16) [*Little and Stephen*, 1985; *Becker et al.*, 1988]. Laboratory measured velocities on eight dike samples from Hole 504B are slightly higher, 6.2-6.7 km/s [*Christensen et al.*, 1989], but are consistent with the results of full-waveform sonic logging [*Moos et al.*, 1990]. The porosity of the dike core samples from Hole 504B is very low, about 0.3% [*Christensen et al.*, 1989], but in complete agreement with electrical logs once corrections have been made to Archie's law [*Pezard*, 1990]. If we accept the Poisson's ratio of 0.3 (V_p/V_s = 1.9) inferred from the full waveform logs at Hole 504B [*Moos et al.*, 1990], the seismic measurements at Site 504 would require a large-scale porosity of about 2% [*Ludwig et al.*, in prep]. (By chance, 2% porosity is what would be inferred applying an uncorrected Archie's law to the electrical logs [*Pezard*, 1990]). If we believe the log measurements and their interpretation, we have to conclude that at Site 504 there is large-scale porosity (fracturing) which influences the seismic measurements but is not sampled at the scale of the logging. In reality, that 2% porosity figure must be regarded as a maximum; with a slightly higher Poisson's ratio the porosity could be as low as 1%, so the disagreement between seismic measurements and log results is really quite small.

Using the same Poisson's ratio (0.3) which leads to an estimate of 2% porosity at the top of the dikes at Site 504, *Ludwig et al.* [in prep] obtain a porosity of 5% for the top of the dikes at the EPR rise crest. Again, this is a maximum porosity; if shear velocities were a little lower (i.e. Poisson's ratio slightly higher) than what we assume, the porosity would also be lower. We do not feel that the 3% difference in porosity between the EPR and Site 504 is adequate to invalidate our interpretation that the 5 km/s material represents the top of the dikes, especially as that is a maximum difference. Site 504 and our EPR site are of different ages, were formed at different spreading rates, and have undergone different alteration histories. A slightly greater degree of fracturing at the EPR, or the same degree of fracturing followed by subsequent crack sealing, could explain the difference. Better constrained shear-wave velocities would go a long way to resolving these questions.

The on-bottom experiments give no constraints on Poisson's ratio or anisotropy in layer 2B, but they do suggest that the attenuation decreases from a Q_p of ~25 in layer 2A to a Q_p of ~500 in layer 2B. The increase in Q_p for the dikes is consistent with the lower porosities [*Ludwig et al.*, in prep] and higher velocities of this section.

Processes

Previously, we discussed two hypotheses which could explain the velocity model of Figure 3.13. The first hypothesis is that the 2A/2B boundary is within the extrusive section, and that layer 2A consists of high-porosity extrusives, overlying the lower-porosity extrusives of layer 2B. Our preferred hypothesis is that seismic layer 2A on the EPR represents the extrusive section and transition zone, and layer 2B represents the sheeted dike complex. In the following section we will discuss the implications of each of these hypotheses.

The primary support for the hypothesis that the shallow crust consists of a thin high-porosity extrusive layer overlying a thicker layer of lower-porosity extrusives is from geophysical logging of Hole 504B. The upper 100 m of basement at Hole 504B consists

of a fractured section of rubbly pillow basalts, breccia zones, and a few massive flows [Anderson et al., 1982], with a bulk porosity of ~12-14% [Becker et al., 1982]. This high-porosity section is bounded at its base by a 14-m-thick massive flow [Pezard, 1990], and is underlain by ~475 m of extrusives with a bulk porosity of ~7-10% [Becker et al., 1982]. The high-porosity extrusive section is correlated with low-velocities of ~4.2 km/s, with velocities rapidly increasing to a mean of ~5.2 km/s in the underlying lower-porosity extrusives (Figure 3.16) [Becker et al., 1988]. The structure at Hole 504B is the basis for several authors' interpretation that the surficial low-velocity layer at the EPR as a high-porosity layer overlying lower-porosity extrusives [McClain et al., 1985; Harding et al., 1989; Vera et al., 1990]. McClain et al. [1985] suggest that increased fracturing with distance from the rise crest could form a high-porosity layer in the shallow crust that thickens away from the rise axis. Toomey et al. [1990] disagreed with McClain et al.'s [1985] interpretation, primarily because most faulting occurs outside of the narrow zone where the thickening of the surficial low-velocity layer occurs [Macdonald, 1982; Macdonald et al., 1984; Wilcock et al., 1992a]. An alternate explanation could be that the high-porosity extrusives represent primarily pillow lavas, and the low-porosity extrusives, primarily massive flows. Submersible observations suggest that the dominant morphological flow types within and outside of the ASC are sheet flows and pillow flows, respectively [Haymon et al., 1991; Fornari et al., 1992; Perfit et al., 1992; Haymon et al., 1993]. The emplacement of a massive flow within the ASC would restrict the circulation of seawater and allow high-temperature hydrothermal deposition [Christeson et al., 1992], resulting in the sealing of thin cracks, a decrease in porosity, and an increase in seismic velocity [Wilkens et al., 1991]. As the flow is transported off-axis, eruptions outside of the ASC would emplace predominantly high-porosity pillow lavas on top of the flow, resulting in a boundary from high-porosity extrusives to low-porosity extrusives that thickens within 1-2 km of the ASC. Although we cannot disregard this hypothesis, we

prefer the alternate hypothesis, that the 2A/2B boundary at the EPR represents a change from the extrusive section to the sheeted dike complex.

The primary implication of this model is that the depth to the top of the sheeted dikes deepens from ~150 m to ~300 m within 1 km of the ASC (Figure 3.13). The rapid subsidence of the sheeted dike layer at the rise axis has been predicted from ophiolite studies [*Cann*, 1974; *Dewey and Kidd*, 1977; *Kidd*, 1977], and is the preferred explanation for the crestal high velocity anomaly identified by *Toomey et al.* [1990] in this region. *Dewey and Kidd* [1977] and *Kidd* [1977], based on ophiolite and submersible observations, predicted that dike subsidence would occur primarily within 1-2 km of the axis. This agrees remarkably well with the observations of this study.

In this interpretation, the rapid subsidence of the top of the sheeted dike complex is accompanied by a thickening of both the extrusive section and transition zone within 1 km of the rise axis. One mechanism that could contribute to the thickening of the extrusive section is the outpouring of magma that overflows the ASC walls and travels laterally [*Lonsdale*, 1977; *Macdonald and Fox*, 1988]. Along the EPR 9°09'-54'N, *Fornari et al.* [in prep], based on ARGO 100 kHz sonar backscatter data, observe several locations where this process is apparent. Lava flows that erupt outside the ASC from fissures throughout the crestal plateau could also contribute to the rapid off-axis thickening of the extrusive layer. Recent submersible dives on five transects perpendicular to the rise axis in the 9°31'N area confirm that a significant portion of the crestal plateau has been affected by recent volcanism from eruptive vents located outside of the ASC [*Fornari et al.*, 1992]. Additionally, *Fornari et al.* [in prep] and *Haymon et al.* [1993] report on observations at several sites in the 9°30-51'N area where lava was transported from the ASC through lateral tube conduits that emerge at the seafloor at distances of a few tens of meters to as great as 100-200 m outside of the ASC. There is no control on how much each of these three processes contributes to the thickening of the extrusive layer outside of the ASC.

We interpret that the transition zone, or what *Francheteau et al.* [1992] refer to as the 'mixed zone', also thickens off axis. Based on observations at 504B and Hess Deep, the transition zone is composed of pillows, flows, dikes, and sills [*Anderson et al.*, 1982; *Francheteau et al.*, 1992]. The most likely mechanism for the thickening of this layer is sill emplacement. Beneath the ASC, the dikes penetrate within 100-200 m of the surface, and thus melt transported by the dikes has a short vertical distance to travel to reach the seafloor. Outside of the ASC, the dikes rapidly subside to a depth of ~300-350 m beneath the surface. Because of the greater vertical distance to travel, a significant portion of melt might be emplaced as sills upon encountering the predominantly horizontal stratigraphy. Additionally, a portion of the lava, that is transported laterally during the drainage process creating the ASC, might also be emplaced as sills.

Another important implication of our interpretation is that half of the final thickness of the extrusive and transition zone is emplaced within the narrow ASC. Submersible and camera observations from within the ASC at both 9°30'N [*Haymon et al.*, 1991; 1993; *Fornari et al.*, in prep] and 12°50'N [*Hekinian et al.*, 1983; *Ballard et al.*, 1984; *Choukroune et al.*, 1984; *Gente et al.*, 1986] on the EPR report that the floor is covered almost universally with fresh, unsedimented lava flows. These are predominantly sheet flows, which are surmised to be more voluminous than eruptions that produce pillow flows [*Ballard et al.*, 1979], the dominant morphological flow type observed for the off-axis eruptions in this area [*Fornari et al.*, 1992; *Perfit et al.*, 1992]. The ASC walls act as a barrier to all but the most voluminous eruptions, constraining these flows to a narrow emplacement region, and resulting in the emplacement of approximately half of the extrusive layer within the ASC.

A cartoon summarizing the shallow crustal emplacement processes discussed above is shown in Figure 3.18. The shallow crust is divided into three layers, consisting of the extrusives, transition zone, and dikes. Approximately 150 m of extrusives plus transition zone are emplaced within the narrow ASC, with both the extrusive section and the

transition zone doubling in thickness within ~1 km of the ASC. The depth to the top of the dikes deepens to ~300-350 m below the seafloor within 1 km of the ASC, and then remains approximately at a constant distance below the seafloor. The thickening of the overlying extrusive layer and transition zone may be accomplished by lavas which overflow the ASC walls, lavas that are transported laterally from the ASC and either erupt at the surface or are emplaced as sills, lavas that are emplaced as off-axis flows, and additional sill emplacement from melt that does not reach the surface. The emplacement region is interpreted to be ~2 km wide, centered about the ASC. This is similar in width to the 1-2 km wide emplacement zone determined from a deep tow magnetic study of the EPR at 21°N [*Macdonald et al.*, 1980], and slightly less than the 2-4 km wide zone determined from MCS [*Harding et al.*, 1993] and tomography studies [*Toomey et al.*, 1990] along the EPR at 9°30'N.

Assuming that the sheeted dikes penetrate close to the surface to deliver melt to the seafloor at the rise axis and subsequently subside [*Cann*, 1974; *Dewey and Kidd*, 1977; *Kidd*, 1977], a fundamental implication of this model is that the subsidence of the sheeted dikes (and therefore the mechanism responsible for this subsidence) is more than double for the crust at Hole 504B formed at an intermediate-spreading center (~800 m) than for the fast-spreading EPR crust at 9°30'N (~300-350 m). The final extrusive section thickness is determined by the width of lava emplacement processes (neovolcanic zone), the volume of lava emplaced, and the amount of time a crustal section spends within the neovolcanic zone. *Sempere et al.* [1987], based on a survey of polarity transition widths determined from 3-D magnetic studies, argue that the neovolcanic zone width is narrow (1-4 km wide) for both intermediate and fast-spreading centers. At intermediate spreading ridges, if we assume a half-width of the neovolcanic zone of 1 km and a half-spreading rate of 3.7 cm/yr, then a 800 m thick extrusive section would require the emplacement of an ~3 cm thick lava layer per year. For the fast-spreading case, a half-width of the neovolcanic zone of 1 km, a half-spreading rate of 5.5 cm/yr, and a 350 m thick extrusive section would

require the emplacement of an ~2 cm thick lava layer per year. This suggests that the volume per year of melt emplaced as extrusives at intermediate-spreading centers and fast-spreading centers is comparable.

Summary of Conclusions

1. The seismic structure for zero-age crust at three locations along the fast-spreading EPR, 9°30'N, 9°34'N, and 12°50'N is fundamentally the same, with a thin (<60 m) surficial low-velocity (<2.5 km/s) layer, an ~100-150 m transition zone with velocities increasing by ~2.5 km/s, and a layer with velocities of ~5 km/s at a depth of ~130-190 m. Within 1 km of the ASC both the surficial low-velocity layer and the transition zone approximately double in thickness. The surficial low-velocity layer and transition zone correspond to seismic layer 2A, and the ~5 km/s material corresponds to the top of seismic layer 2B. With this interpretation, there is significant structure within layer 2A.

2. Our preferred explanation for the shallow crustal structure is that seismic layer 2A corresponds to the extrusive sequence and transition zone, and the 2A/2B boundary to the top of the sheeted dike complex. According to this model, the shallow crustal architecture is in place within 1 km of the rise axis. Primary implications of this model are that the extrusive sequence at the fast-spreading EPR (~5.5 cm/yr) is thinner, and the seismic velocities lower, than observed for the intermediate-spreading (~3.7 cm/yr) crust at DSDP Hole 504B.

3. The extrusive sequence doubles in thickness over an across-axis distance of ~1 km, due to lava that overflows the ASC walls, is transported laterally from the ASC through lateral tube conduits, or is emplaced by eruptions that occur outside of the ASC.

4. The transition zone doubles in thickness over an across-axis distance of ~1 km. The most probable cause of this thickening is sill emplacement outside of the ASC, either from magma that does not reach the surface in an off-axis eruption, or magma that is transported laterally during the drainage process creating the ASC.

5. A depth to the top of the sheeted dike complex of ~300-350 m for the EPR vs. a depth of ~800 m for the crust at 504B suggests that dike subsidence at intermediate spreading centers is more than double that at fast-spreading centers. Additionally, this implies that the volume per year of magma emplaced as extrusives at intermediate spreading centers is at least as great as that emplaced at fast-spreading centers.

6. The seafloor velocity for zero-age crust is ~2.1-2.35 km/s, and increases to ~2.4-2.85 km/s for 10,000-120,000 year old crust. These low seafloor velocities are compatible with a porosity of ~27% for zero-age crust, decreasing to ~20% off-axis due to crack infilling by alteration and drainback processes.

7. Amplitude modeling requires a seafloor Poisson's ratio of at least 0.43, with a preferred value of 0.48. This is consistent with a highly fractured material with a largely high-aspect ratio crack population, most likely due to massive fissuring as observed in submersible and side-scan sonar data.

8. Our preferred model includes high attenuation within the extrusives and transition zone (Q_p~25), and substantially less attenuation within the sheeted dike complex (Q_p~500). The high attenuation in the shallowmost crust is consistent with the interpreted high porosities and highly fractured nature of this material.

References

Alabaster, T., J.A. Pearce and J. Malpas, The volcanic stratigraphy and petrogenesis of the Oman ophiolite complex, *Contrib. Mineral. Petrol., 81,* 168-183, 1982.

Anderson, R.N. et al., DSDP Hole 504B, the first reference section over 1 km through Layer 2 of the oceanic crust, *Nature, 300,* 589-594, 1982.

Auzende, J.-M., D. Bideau, E. Bonatti, M. Cannat, J. Honnorez, Y. Lagabrielle, J. Malavieille, V. Mamaloukas-Frangoulis and C. Mevel, Direct observation of a section through slow-spreading oceanic crust, *Nature, 337,* 726-729, 1989.

Ballard, R.D., R. Hekinian and J. Francheteau, Geological setting of hydrothermal activity at 12°50'N on the East Pacific Rise: a submersible study, *Earth Planet. Sci. Lett., 69,* 176-186, 1984.

Ballard, R.D., R.T. Holcomb and T.H. van Andel, The Galapagos rift at 86°W: 3. Sheet flows, collapse pits, and lava lakes of the rift valley, *J. Geophys. Res., 84,* 5407-5422, 1979.

Becker, K., H. Sakai and et al., *Proc. ODP, Init. Repts., 111,* Ocean Drilling Program, College Station, TX, 1988.

Becker, K. et al., *In situ* electrical resistivity and bulk porosity of the oceanic crust Costa Rica Rift, *Nature, 300,* 594-598, 1982.

Berge, P.A., G.J. Fryer and R.H. Wilkens, Velocity-porosity relationships in the upper oceanic crust: theoretical considerations, *J. Geophys. Res., 97,* 15239-15254, 1992.

Cann, J.R., A model for oceanic crustal structure developed, *Geophys. J. R. Astron. Soc., 39,* 169-187, 1974.

Choukroune, P., J. Francheteau and R. Hekinian, Tectonics of the East Pacific Rise near 12°50'N: a submersible study, *Earth Planet. Sci. Lett., 68,* 115-127, 1984.

Christensen, N.I., Compressional and shear wave velocities at pressures to 10 kilobars for basalts from the East Pacific Rise, *Geophys. J. R. Astron. Soc., 28,* 425-429, 1972.

Christensen, N.I., Ophiolites, seismic velocities and oceanic crustal structure, *Tectonophysics*, *47*, 131-157, 1978.

Christensen, N.I. and G.H. Shaw, Elasticity of mafic rocks from the Mid-Atlantic Ridge, *Geophys. J. R. Astron. Soc.*, *20*, 271-284, 1970.

Christensen, N.I., W.W. Wepfer and R.D. Baud, Seismic properties of sheeted dikes from Hole 504B, ODP Leg 111, *Proc. ODP, Sci. Results*, *111*, 171-176, 1989.

Christeson, G.L., G.M. Purdy and G.J. Fryer, Structure of young upper crust at the East Pacific Rise near 9°30'N, *Geophys. Res. Lett.*, *19*, 1045-1048, 1992.

Collins, J.A., G.M. Purdy and T.M. Brocher, Seismic velocity structure at Deep Sea Drilling Project site 504B, Panama Basin: evidence for thin oceanic crust, *J. Geophys. Res.*, *94*, 9283-9302, 1989.

Cudrak, C.F. and R.M. Clowes, Crustal structure of Endeavour ridge segment, Juan de Fuca ridge, from a detailed seismic refraction survey, *J. Geophys. Res.*, *98*, 6329-6349, 1993.

Detrick, R.S., P. Buhl, E. Vera, J. Mutter, J. Orcutt, J. Madsen and T. Brocher, Multichannel seismic imaging of an axial magma chamber along the East Pacific Rise between 9°N and 13°N, *Nature*, *326*, 35-41, 1987.

Dewey, J.F. and R.G.W. Kidd, Geometry of plate accretion, *Geol. Soc. Am. Bull.*, *79*, 411-423, 1977.

deWit, M.J. and C. Stern, Pillow talk, *J. Volcanol. Geotherm. Res.*, *4*, 55-80, 1978.

Diachok, O.I., R.L. Dicus and S.C. Wales, Elements of a geoacoustic model of the upper crust, *J. Acoust. Soc. Am.*, *75*, 324-334, 1984.

Fornari, D.J., M.R. Perfit, R. Batiza and M.H. Edwards, Submersible transects across the East Pacific Rise crest and upper-flanks at 9°31'-32'N: 1. Observations of seafloor morphology and evidence for young volcanism off-axis (abstract), *EOS Trans. AGU*, *73* (43), Fall Supp., 525, 1992.

Francheteau, J., R. Armijo, J.L. Cheminee, R. Hekinian, P. Lonsdale and N. Blum, Dyke complex of the East Pacific Rise exposed in the walls of Hess Deep and the structure of the upper oceanic crust, *Earth Planet. Sci. Lett.*, *111*, 109-121, 1992.

Fuchs, K. and G. Müller, Computation of synthetic seismograms with the reflectivity method and comparison with observations, *Geophys. J. R. Astron. Soc.*, *23*, 417-433, 1971.

Gente, P., J.M. Auzende, V. Renard, Y. Fouquet and D. Bideau, Detailed geological mapping by submersible of the East Pacific Rise axial graben near 13°N, *Earth Planet. Sci. Lett.*, *78*, 224-236, 1986.

Harding, A.J., G.M. Kent and J.A. Orcutt, A multichannel seismic investigation of upper crustal structure at 9°N on the East Pacific Rise: Implications for crustal accretion, *J. Geophys. Res.*, *98*, 13925-13944, 1993.

Harding, A.J., J.A. Orcutt, M.E. Kappus, E.E. Vera, J.C. Mutter, P. Buhl, R.S. Detrick and T.M. Brocher, Structure of young oceanic crust at 13°N on the East Pacific Rise from expanding spread profiles, *J. Geophys. Res.*, *94*, 12163-12196, 1989.

Haymon, R.M., D.J. Fornari, M.H. Edwards, S. Carbotte, D. Wright and K. Macdonald, Hydrothermal vent distribution along the East Pacific Rise crest (9°09'-54'N) and its relationship to magmatic and tectonic processes on fast-spreading mid-ocean ridges, *Earth Planet. Sci. Lett.*, *104*, 513-534, 1991.

Haymon, R.M. et al., Volcanic eruption of the mid-ocean ridge along the East Pacific Rise crest at 9°45-52'N: I. Direct submersible observations of seafloor phenomena associated with an eruption event in April, 1991, *Earth Planet. Sci. Lett.*, *in press*, 1993.

Hekinian, R. et al., East Pacific Rise near 13°N: geology of new hydrothermal fields, *Science*, *219*, 1321-1324, 1983.

Herron, T.J., Lava flow layer - East Pacific Rise, *Geophys. Res. Lett.*, *9*, 17-20, 1982.

Houtz, R. and J.I. Ewing, Upper crustal structure as a function of plate age, *J. Geophys. Res.*, *81*, 2490-2498, 1976.

Hyndman, R.D. and M.J. Drury, The physical properties of oceanic basement rocks from deep drilling on the Mid-Atlantic Ridge, *J. Geophys. Res.*, *81*, 4042-4052, 1976.

Jacobson, R.S. and B.T.R. Lewis, The first direct measurements of upper oceanic crustal compressional wave attenuation, *J. Geophys. Res.*, *95*, 17417-17429, 1990.

Kennett, B.L.N., *Seismic Wave Propagation in Stratified Media*, 342 pp., Cambridge University Press, Cambridge, UK, 1983.

Kidd, R.G.W., A model for the process of formation of the upper oceanic crust, *Geophys. J. R. Astron. Soc.*, *50*, 149-183, 1977.

Klitgord, K.D. and J. Mammerickx, Northern East Pacific Rise: Magnetic anomaly and bathymetric framework, *J. Geophys. Res.*, *87*, 6725-6750, 1982.

Koelsch, D.E., G.M. Purdy and J.E. Broda, A multiple charge deep deployed explosive source for high resolution seismic refraction experiments in the deep ocean, Fall MTS Conference, New Orleans, 1991.

Lippard, S.J., A.W. Shelton and I.G. Gass, *The Ophiolite of Northern Oman*, 178 pp., Blackwell Scientific Publications, London, England, 1986.

Little, S.A. and R.A. Stephen, Costa Rica Rift borehole seismic experiment, Deep Sea Drilling Project Hole 504B, Leg 92, *Init. Repts. DSDP*, *83*, 517-528, 1985.

Lonsdale, P., Structural geomorphology of a fast-spreading rise crest: the East Pacific Rise near 3°25'S, *Mar. Geophys. Res.*, *3*, 251-293, 1977.

Lonsdale, P., Structural pattern of the Galapagos microplate and evolution of the Galapagos triple junctions, *J. Geophys. Res.*, *93*, 13551-13574, 1988.

Luetgert, J.H., Users manual for RAY84/R83PLT interactive two-dimensional ray tracing/synthetic seismogram package, U.S. Geological Survey Open File Report, *88-238*, 1988.

Macdonald, K., J.-C. Sempere and P.J. Fox, East Pacific Rise from Siqueiros to Orozco fracture zones: along-strike continuity of axial neovolcanic zone and structure and evolution of overlapping spreading centers, *J. Geophys. Res.*, *89*, 6049-6069, 1984.

Macdonald, K.C., Mid-ocean ridges: fine scale tectonic, volcanic and hydrothermal processes within the plate boundary zone, *Ann. Rev. Earth Planet. Sci.*, *10*, 155-190, 1982.

Macdonald, K.C. and P.J. Fox, The axial summit graben and cross-sectional shape of the East Pacific Rise as indicators of axial magma chambers and recent volcanic eruptions, *Earth Planet. Sci. Lett.*, *88*, 119-131, 1988.

Macdonald, K.C. et al., The East Pacific Rise and its flanks 8-18°N: history of segmentation, propagation and spreading direction based on SeaMARC II and Sea Beam studies, *Mar. Geophys. Res.*, *14*, 299-344, 1992.

Macdonald, K.C., S.P. Miller, S.P. Huestis and F.N. Spiess, Three-dimensional modeling of a magnetic reversal boundary from inversion of deep-tow measurements, *J. Geophys. Res.*, *85*, 3670-3680, 1980.

Mallick, S. and L.N. Frazer, Practical aspects of reflectivity modeling, *Geophysics*, *52*, 1355-1364, 1987.

McClain, J.S., J.A. Orcutt and M. Burnett, The East Pacific Rise in cross section: a seismic model, *J. Geophys. Res.*, *90*, 8627-8639, 1985.

Moos, D., P. Pezard and M. Lovell, Elastic wave velocities within oceanic layer 2 from sonic full waveform logs in Deep Sea Drilling Project Holes 395A, 418A, and 504B, *J. Geophys. Res.*, *95*, 9189-9207, 1990.

Nicolas, A., *Structure of Ophiolites and Dynamics of Oceanic Lithosphere*, 367 pp., Kluwer Academic Publishers, Dordrecht, the Netherlands, 1989.

Peal, K.R., G.M. Purdy, D.E. Koelsch and F.B. Wooding, A simple ocean bottom hydrophone with 200 megabyte data capacity, Woods Hole Oceanogr. Inst., *Tech. Rep. in press*, 1993.

Perfit, M.R., M.C. Smith, D.J. Fornari, R. Batiza and M.H. Edwards, Submersible transects across the East Pacific Rise crest and upper-flanks at 9°31'-32'N: 2. Small-

scale spatial variations in lava geochemistry and implications for temporal variability (abstract), *EOS trans. AGU, 73* (43), Fall Supp., 525, 1992.

Pezard, P.A., Electrical properties of mid-ocean ridge basalt and implications for the structure of the upper oceanic crust in Hole 504B, *J. Geophys. Res., 95,* 9237-9264, 1990.

Purdy, G.M., New observations of the shallow seismic structure of young oceanic crust, *J. Geophys. Res., 92,* 9351-9362, 1987.

Purdy, G.M. and R.S. Detrick, The crustal structure of the mid-Atlantic Ridge at 23°N from seismic refraction studies, *J. Geophys. Res., 91,* 3739-3762, 1986.

Purdy, G.M., L.S.L. Kong, G.L. Christeson and S.C. Solomon, Relationship between spreading rate and the seismic structure of mid-ocean ridges, *Nature, 355,* 815-817, 1992.

Rohr, K.M.M., B. Milkereit and C.J. Yorath, Asymmetric deep crustal structure across the Juan de Fuca Ridge, *Geology, 16,* 533-537, 1988.

Schmincke, H.-U., M. Rautenschlein, P.T. Robinson and J.M. Mehegan, Troodos extrusive series of Cyprus: a comparison with oceanic crust, *Geology, 11,* 405-409, 1983.

Schreiber, E. and P.J. Fox, Compressional wave velocities and mineralogy of fresh basalts from the Famous area and the Oceanographer fracture zone and the texture of layer 2A of the oceanic crust, *J. Geophys. Res., 81,* 4071-4076, 1976.

Searle, R. and J. Francheteau, Morphology and tectonics of the Galapagos triple junction, *Mar. Geophys. Res., 8,* 95-129, 1986.

Sempere, J.-C., K. Macdonald, S. Miller and L. Shure, Detailed study of the Brunhes/Matayama reversal boundary on the East Pacific Rise at 19°30'S: implications for crustal emplacement processes at an ultra fast spreading center, *Mar. Geophys. Res., 9,* 1-23, 1987.

Shearer, P.M., Cracked media, Poisson's ratio and the structure of the upper oceanic crust, *Geophys. J. R. Astron. Soc.*, *92*, 357-362, 1988.

Shipboard Eng. and Sci. Parties, Introduction, background, and scientific objectives: Engineering Leg 142 at the East Pacific Rise, *Proc. ODP, Init. Repts.*, *142*, 31-40, 1993.

Spudich, P. and J. Orcutt, Petrology and porosity of an oceanic crustal site: results from wave form modeling of seismic refraction data, *J. Geophys. Res.*, *85*, 1409-1433, 1980.

Stoffa, P.L. and P. Buhl, Two ship multichannel seismic experiments for deep crustal studies: Expanded spread and constant offset profiles, *J. Geophys. Res.*, *84*, 7645-7660, 1979.

Strick, E., A predicted pedestal effect for pulse propagation in constant-Q solids, *Geophysics*, *35*, 387-403, 1970.

Toomey, D.R., G.M. Purdy, S.C. Solomon and W.S.D. Wilcock, The three-dimensional seismic velocity structure of the East Pacific Rise near latitude 9°30'N, *Nature*, *347*, 639-645, 1990.

Vera, E.E. and J.B. Diebold, Seismic imaging of oceanic layer 2A between 9°30'N and 10°N on the East Pacific Rise from two-ship wide aperture profiles, *J. Geophys. Res.*, *in press*, 1993.

Vera, E.E., J.C. Mutter, P. Buhl, J.A. Orcutt, A.J. Harding, M.E. Kappus, R.S. Detrick and T.M. Brocher, The structure of 0- to 0.2-m.y.-old oceanic crust at 9°N on the East Pacific Rise from expanded spread profiles, *J. Geophys. Res.*, *95*, 15529-15556, 1990.

Von Damm, K.L., D.C. Colodner and H.N. Edmonds, Hydrothermal fluid chemistry at 9-10°N EPR '92: big changes and still changing (abstract), *EOS Trans. AGU*, *73* (43), Fall Supp., 524, 1992.

Wepfer, W.W. and N.I. Christensen, Compressional wave attenuation in oceanic basalts, *J. Geophys. Res.*, *95*, 17431-17439, 1990.

White, D.J. and R.M. Clowes, Shallow crustal structure beneath the Juan de Fuca Ridge from 2-D seismic refraction tomography, *Geophys. J. Int.*, *100*, 349-367, 1990.

Wilcock, W.S.D., G.M. Purdy, S.C. Solomon, D.L. DuBois and D.R. Toomey, Microearthquakes on and near the East Pacific Rise, 9°-10°N, *Geophys. Res. Lett.*, *19*, 2131-2134, 1992a.

Wilcock, W.S.D., S.C. Solomon, G.M. Purdy and D.R. Toomey, The seismic attenuation structure of a fast-spreading mid-ocean ridge, *Science*, *258*, 1470-1474, 1992b.

Wilcock, W.S.D., D.R. Toomey, G.M. Purdy and S.C. Solomon, The renavigation of Sea Beam bathymetric data between 9°N and 10°N on the East Pacific Rise, *Mar. Geophys. Res.*, *15*, 1-12, 1993.

Wilkens, R.H., G.J. Fryer and J. Karsten, Evolution of porosity and seismic structure of upper oceanic crust: importance of aspect ratios, *J. Geophys. Res.*, *96*, 17981-17995, 1991.

Table 3.1: Final Velocity-Depth Models

Depth (m)	V_p (km/s)	V_s (km/s)	Q_p	g_p (s^{-1})
Line 0S				
0-32	2.33-2.38	0.47-0.48	25	1.6
32-72	2.38-4.18	0.48-2.21	25	45
72-82	4.18-4.19	2.21-2.26	25	1.0
82-129	4.19-5.00	2.26-2.67	25	20
129-209	5.00-5.21	2.67-2.78	500	2.6
Line 0N				
0-55	2.11-2.40	0.42-0.48	25	5.3
55-137	2.40-4.90	0.48-2.65	25	30
137-177	4.90-4.97	2.65-2.68	25	1.8
177-192	4.97-5.17	2.68-2.79	25	10
192-322	5.17-5.21	2.79-2.81	500	0.3
Line 0F				
0-42	2.25-2.28	0.45-0.46	25	0.7
42-122	2.28-5.14	0.46-2.78	25	36
122-132	5.14-5.16	2.78-2.79	25	2
132-162	5.16-5.29	2.79-2.86	25	4.3
162-222	5.29-5.37	2.86-2.90	500	1.3
Line 120W (a)				
0-107	2.63-2.63	0.53-0.53	25	0
107-157	2.63-4.18	0.53-2.26	25	31
157-287	4.18-4.50	2.26-2.43	25	2.5
287-307	4.50-4.90	2.43-2.65	25	20
307-357	4.90-5.02	2.65-2.71	500	2.4
Line 120W (b)				
0-137	2.63-3.35	0.53-0.70	25	5.3
137-187	3.35-4.18	0.70-2.26	25	17
187-317	4.18-4.50	2.26-2.43	25	2.5
317-337	4.50-4.90	2.43-2.65	25	20
337-387	4.90-5.02	2.65-2.71	500	2.4

Table 3.1: Final Velocity-Depth Models (cont.)

Depth (m)	V_p (km/s)	V_s (km/s)	Q_p	g_p (s^{-1})
Line 20W				
0-112	2.85-2.85	0.57-0.57	25	0
112-162	2.85-4.30	0.57-2.32	25	29
162-367	4.30-4.60	2.32-2.48	25	1.5
367-387	4.60-5.00	2.48-2.70	25	20
387-437	5.00-5.10	2.70-2.75	500	2
Line 10W				
0-87	2.43-2.43	0.49-0.49	25	0
87-137	2.43-4.25	0.49-2.30	25	36
137-217	4.25-4.45	2.30-2.40	25	2.5
217-257	4.45-5.30	2.40-2.86	25	21
257-307	5.30-5.40	2.86-2.90	500	2
Line 20E				
0-102	2.46-2.46	0.49-0.49	25	0
102-152	2.46-4.30	0.49-2.32	25	37
152-282	4.30-4.60	2.32-2.48	25	2.3
282-302	4.60-5.20	2.48-2.81	25	30
302-352	5.20-5.30	2.81-2.86	500	2
Line 70W				
0-65	2.68-2.68	0.54-0.54	25	0
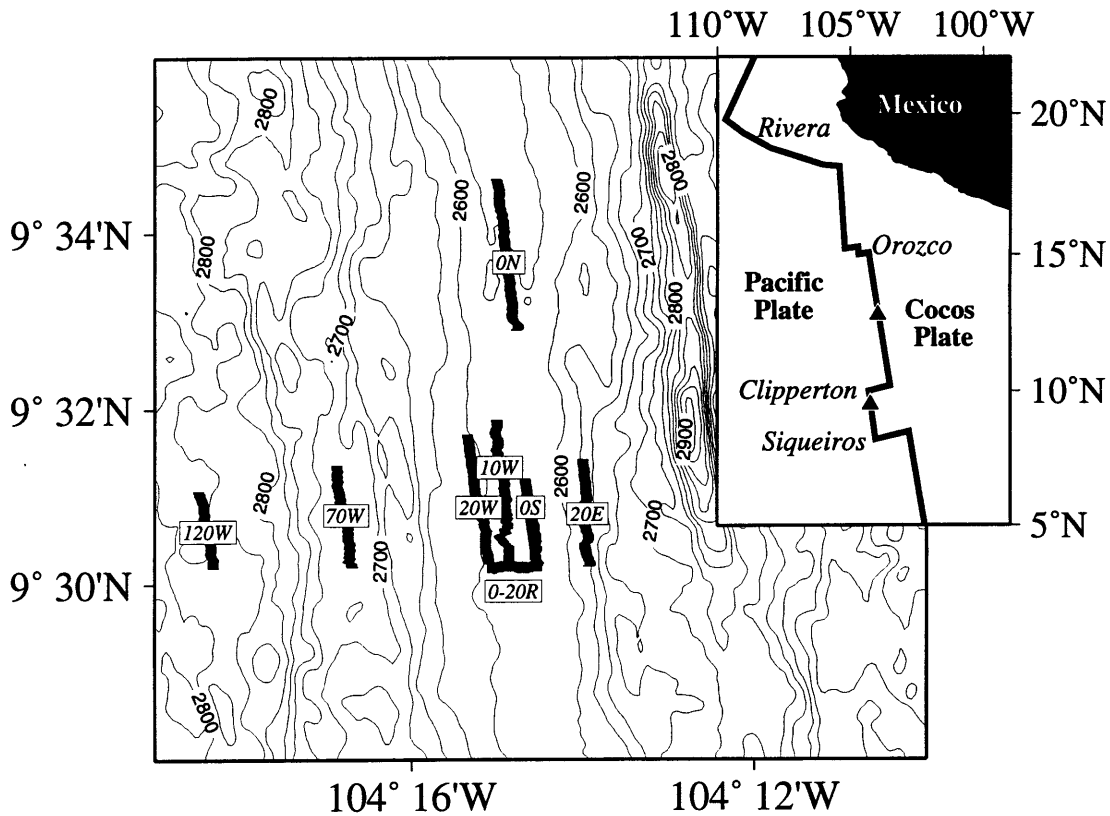
Figure 3.1. Sea Beam bathymetry [*Wilcock et al.*, 1993] contoured at 25 meter intervals for a section of the EPR located between the Siqueiros and Clipperton transform faults. Shiptracks for the on-bottom seismic refraction experiments are indicated with the heavy black lines; due to the undithered GPS during the cruise, the ship could be accurately navigated within tens of meters. Each shiptrack is labeled with the approximate age of the crust in kiloyears, based on a half spreading rate of 5.5 cm/yr [*Klitgord and Mammerickx*, 1982], with an 'E' or 'W' appended to indicate relationship to the rise axis, and an 'S' or 'N' appended to the southern and northern zero-age lines, respectively. An ocean bottom hydrophone (OBH) was located at the southern end of each ridge parallel line, with an OBH at both the eastern and western ends of the Line 0-20R. The inset map shows the regional setting, with triangles indicating the locations of the experiments conducted at 9°30'N and 12°50'N.
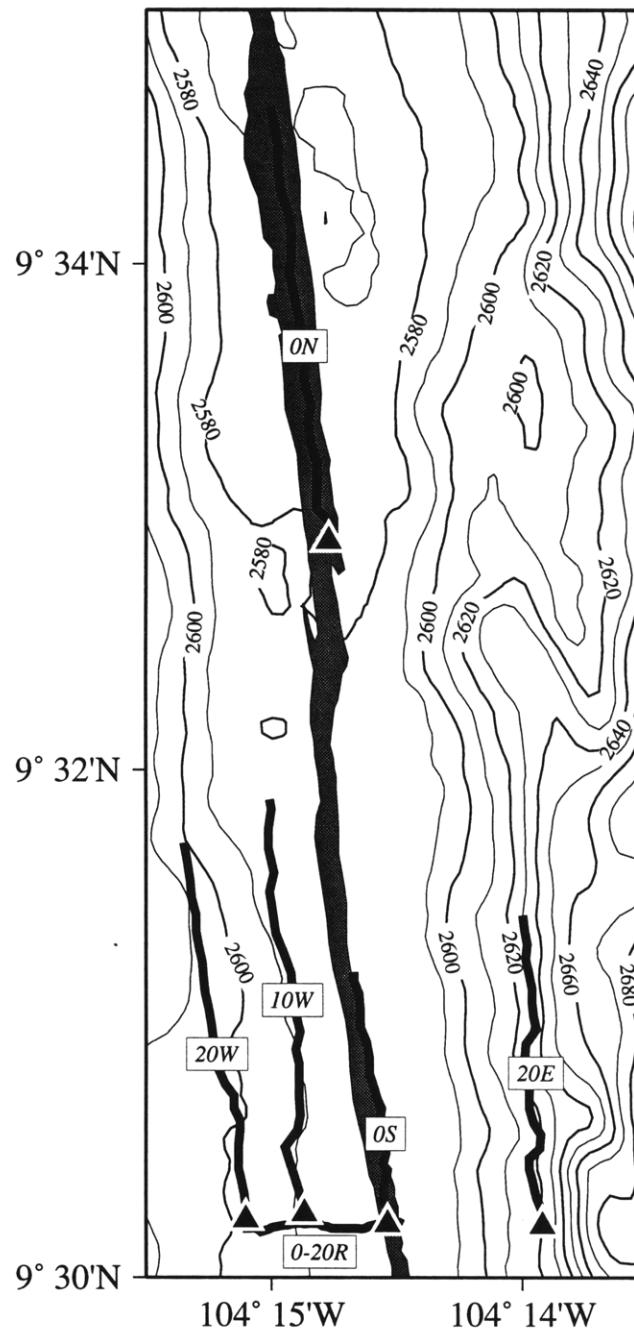
Figure 3.2. Expanded location map showing the shiptracks for the experiments located within and close to the ASC. The contour interval is 10 m. The ASC, as mapped by *Fornari et al.* [in prep], is shown in gray. The triangles indicate the positions of the OBHs used in each experiment. The average width of the ASC is 130 m where Line 0S was located, and 275 m where Line 0N was located.
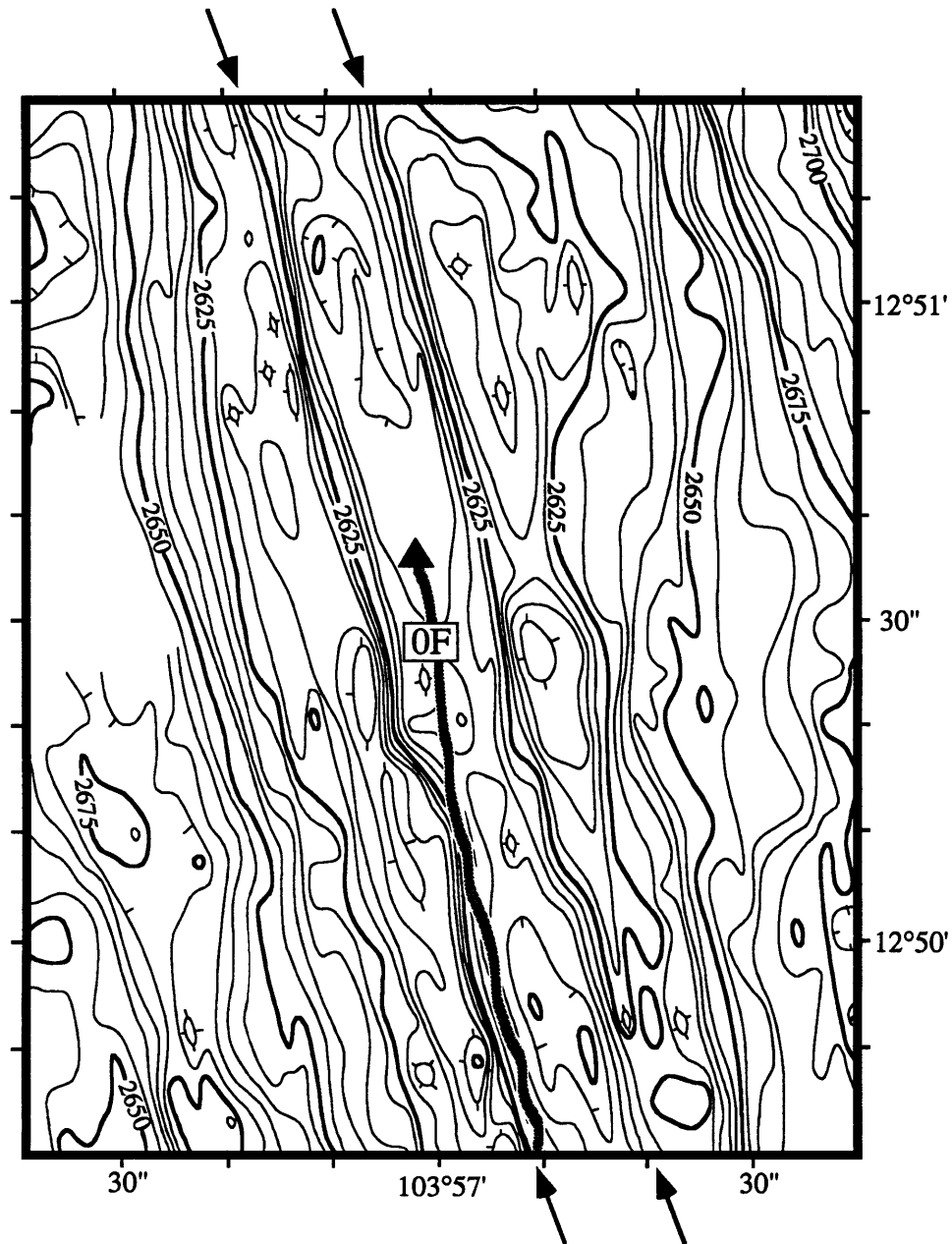
Figure 3.3. Detailed bathymetric map (modified from *Gente et al.*, 1986) showing the location of Line OF. The triangle indicates the position of the OBH used in the experiment, and the gray line marks the location of the shiptrack. The contour interval is 5 m. Arrows indicate the approximate location of the ASC walls, which are ~250 m wide. We shifted the bathymetric map of *Gente et al.* [1986] 80 m to the east based on a GPS navigated Sea Beam swath collected in this region during our cruise.
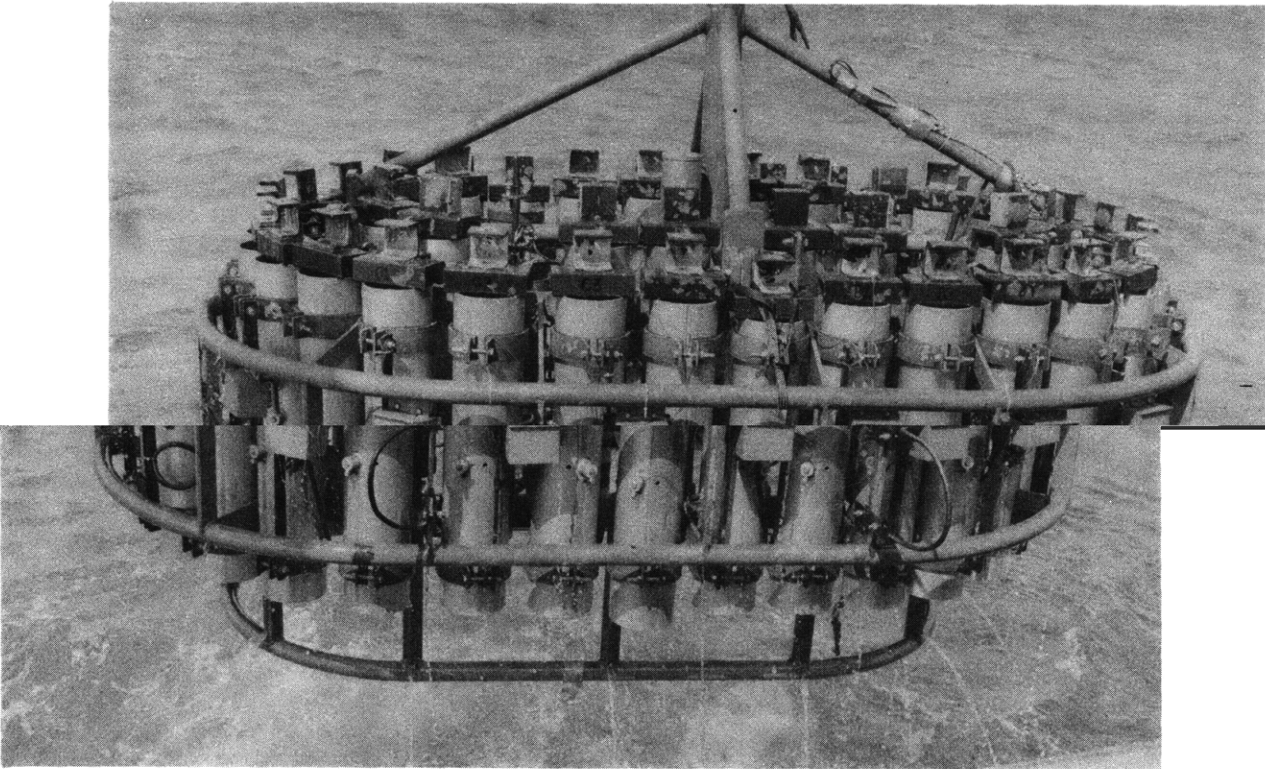
Figure 3.4. Photograph of NOBEL upon recovery. Each of the 47 firing barrels was loaded with either 2.3 or 4.6 kg of PETN, and is attached to two detonators. The first detonator is used to release the charge from the barrel, and the second to fire the charge upon confirmation of release.
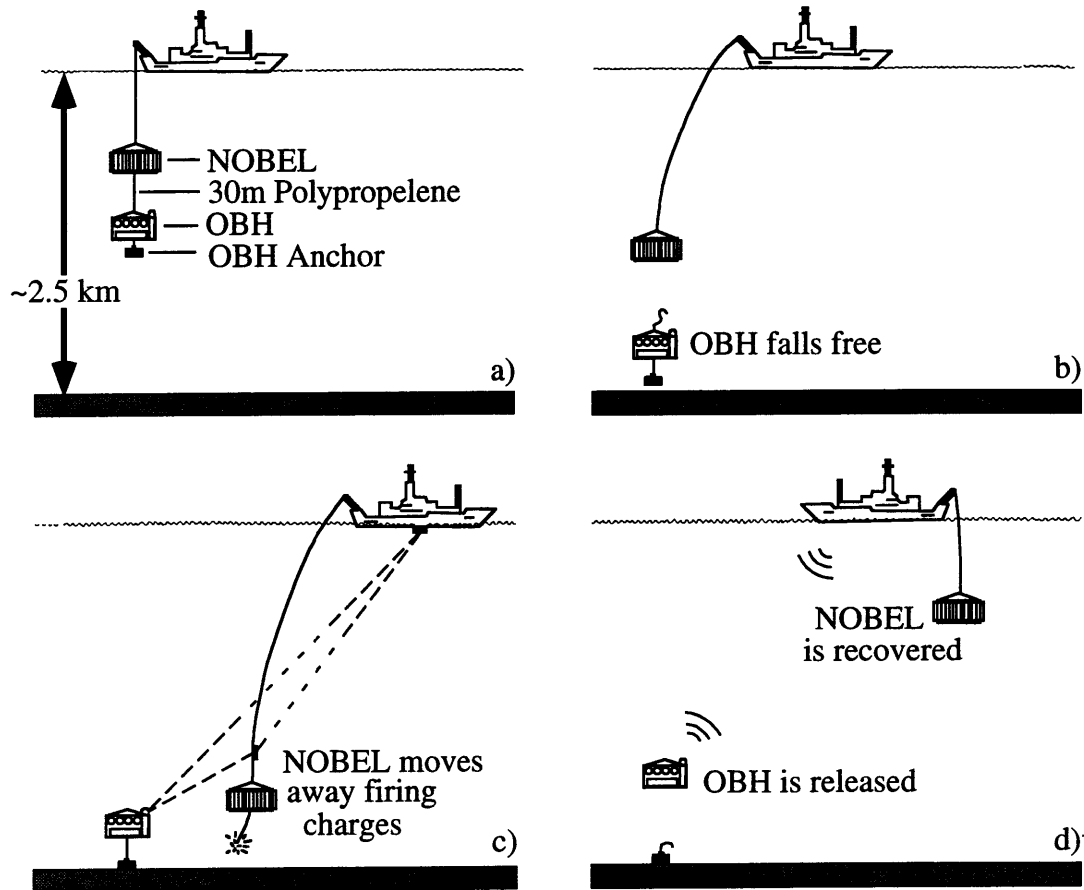
Figure 3.5. Cartoon of a typical on-bottom refraction experiment. (a) NOBEL is lowered to the seafloor. Attached to NOBEL by 30 m of polypropelene is the OBH. (b) When NOBEL is approximately 130 m above the seafloor (as determined from the 12 kHz pinger record from a pinger attached to the NOBEL frame), the OBH is released. (c) The ship starts to move along the shooting track at ~0.5 knots. An acoustic system (represented by the dashed lines) is used to determine the range between NOBEL and the OBH; when NOBEL is at a safe distance from the OBH (at least 100 m) charges are released and fired at a steady interval. (d) When all charges are fired, NOBEL and the OBH are recovered to the ship.
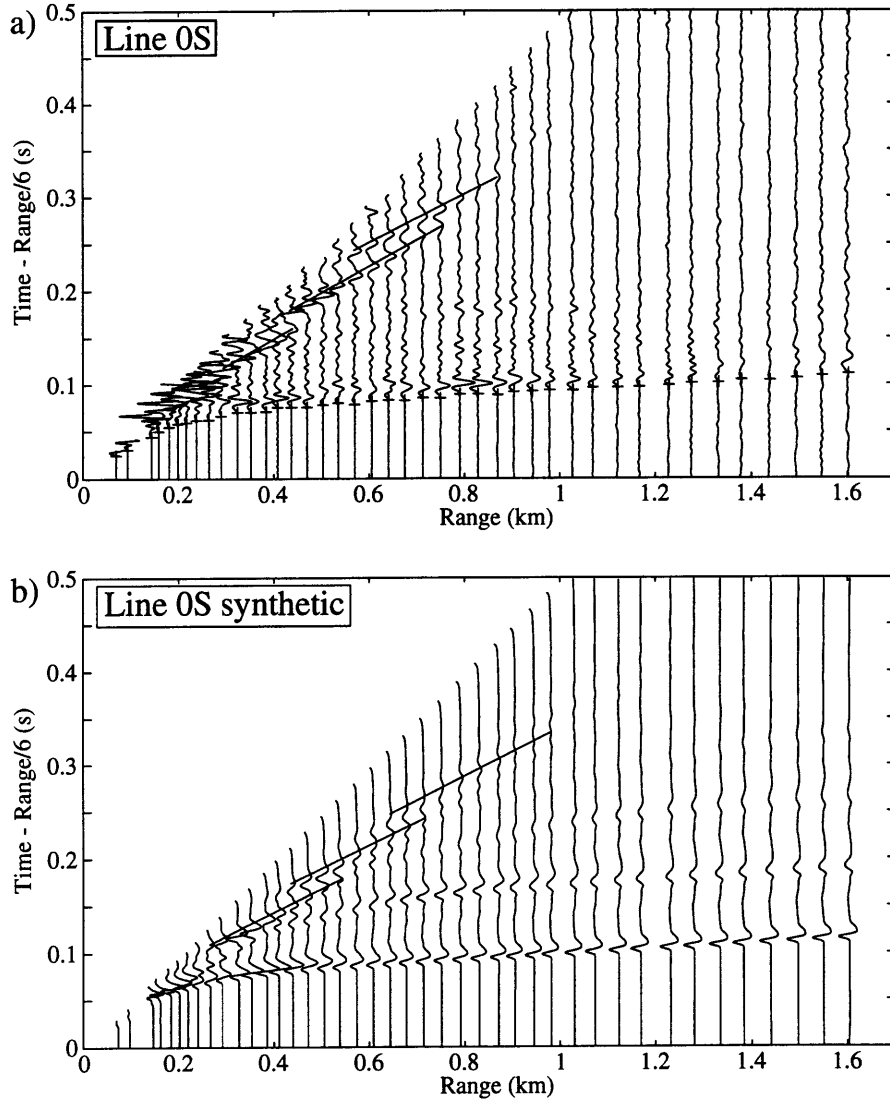
Figure 3.6. (a) Record section (corrected for shot height above seafloor) of the 2.3 kg (5 lb) charges detonated to the OBH for Line 0S. The maximum shot height was ~11 m above the seafloor. For display purposes it was necessary to multiply the amplitudes of the seismograms by a factor of $R^{2.4}$, where R is the distance of the shot from the receiver. The seismograms have been truncated at the onset of the direct water wave, and seismograms at a range greater than 500 m have been low-pass filtered with a cosine-squared filter, with an upper taper interval of 130-150 Hz. The seismograms are plotted with a reduction velocity of 6.0 km/s, with compressional arrivals breaking left. The first breaks are shown with a plus (+) sign, and the solid lines indicate the location of multiples discussed in the text. (b) Record section of the synthetic seismograms for Line 0S. The amplitudes have been range scaled as for Figure 3.6a, and the reduction velocity is 6.0 km/s.
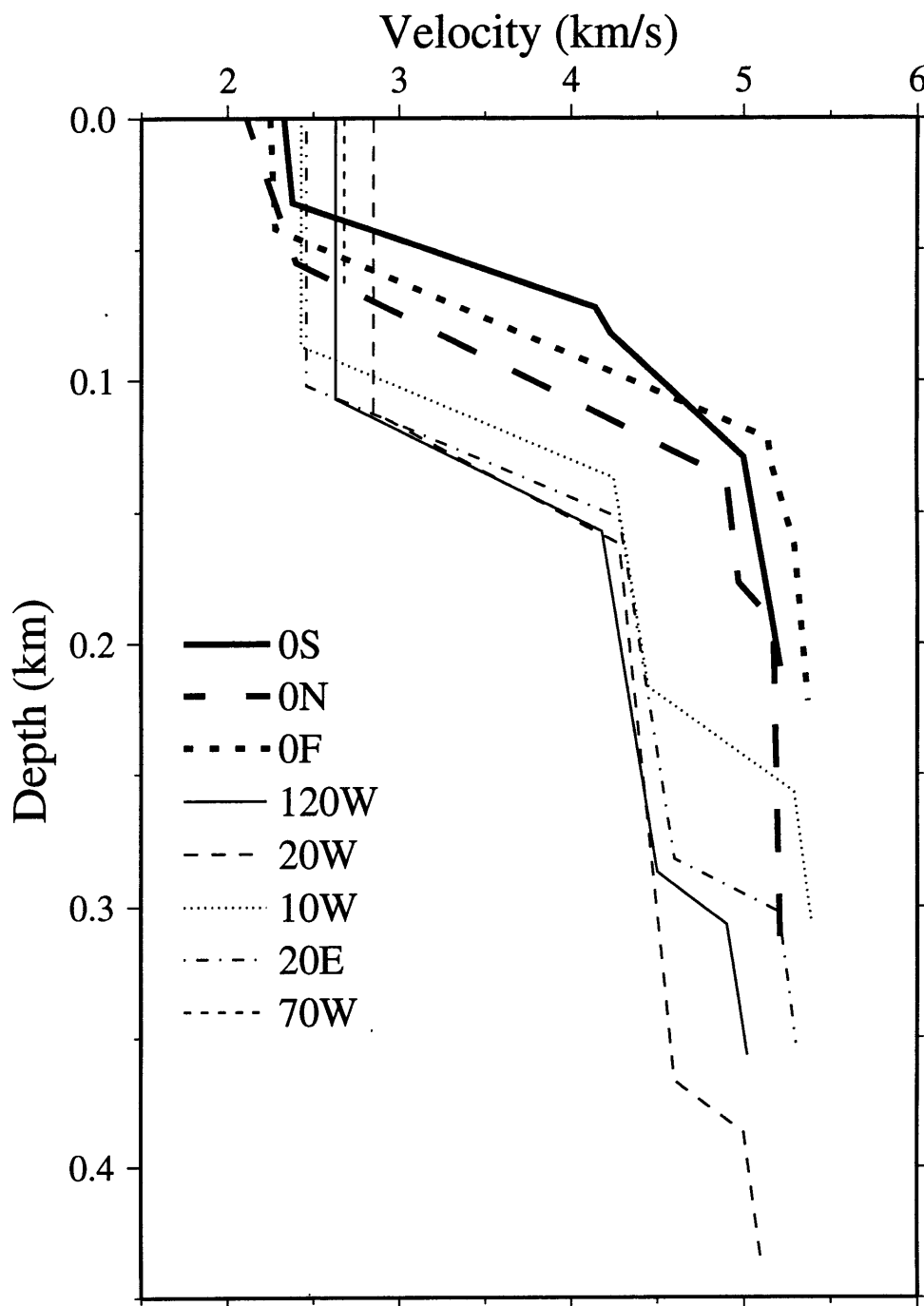
Figure 3.7. Compressional velocity/depth models for the rise-parallel on-bottom seismic refraction experiments. For Line 70W, only the seafloor velocity could be constrained due to the poor signal-to-noise ratio associated with the first arrival travel times.
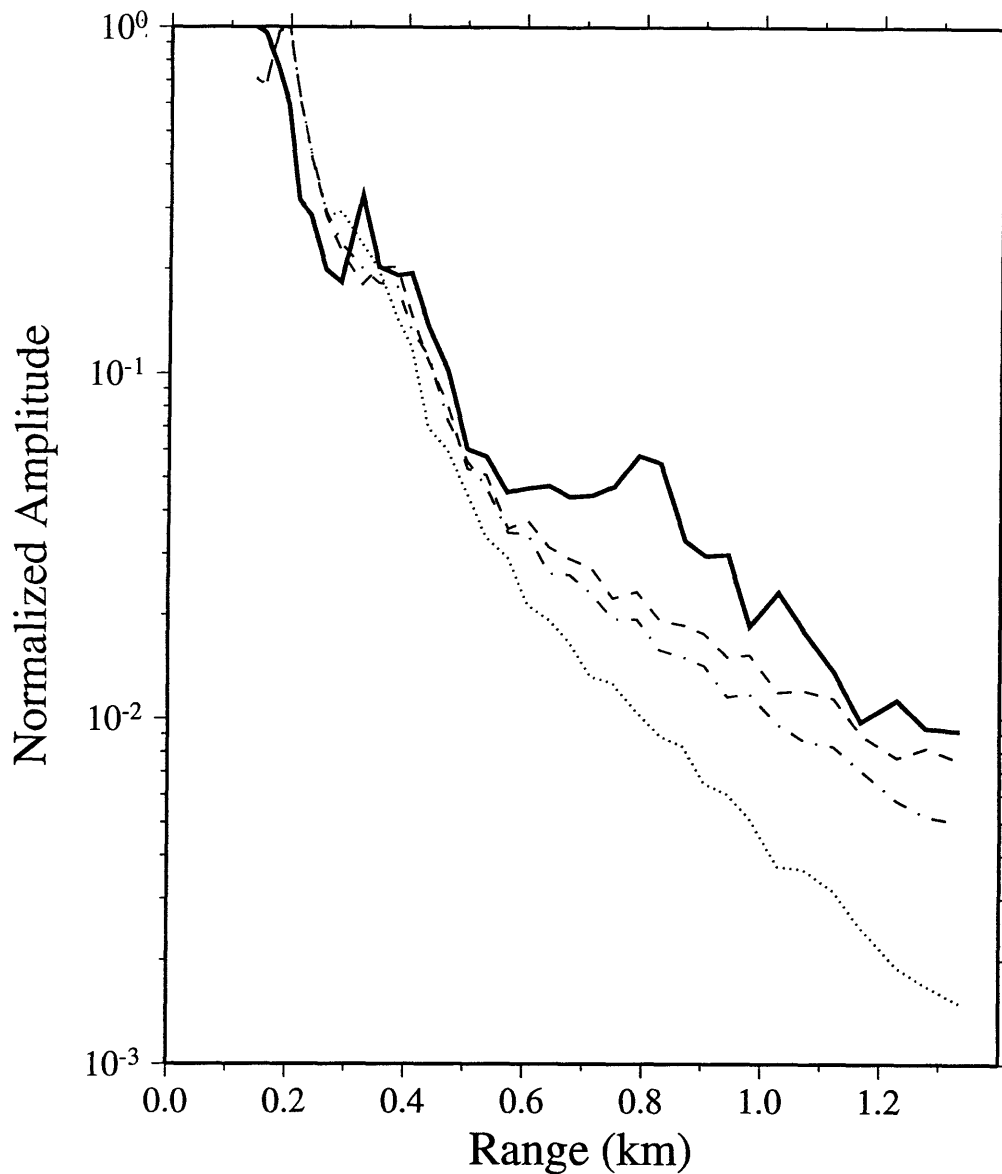
Figure 3.8. First arrival amplitudes vs. range for Line 0S. The observed data are indicated by the solid line. The vertical scale is logarithmic. Amplitudes were measured as the absolute value of the first peak of the arrival, and were normalized by the maximum value. Amplitudes at ranges >1.3 km are not shown due to the low signal to noise ratio. Notice the decrease in slope at ~0.5-0.6 km range. Also plotted are amplitudes from synthetic seismogram data for three different models, with Q_p=25 above a depth of 130 m, and Q_p=500 (dashed line), 100 (dash-dot line), and 25 (dotted line) below a depth of 130 m.
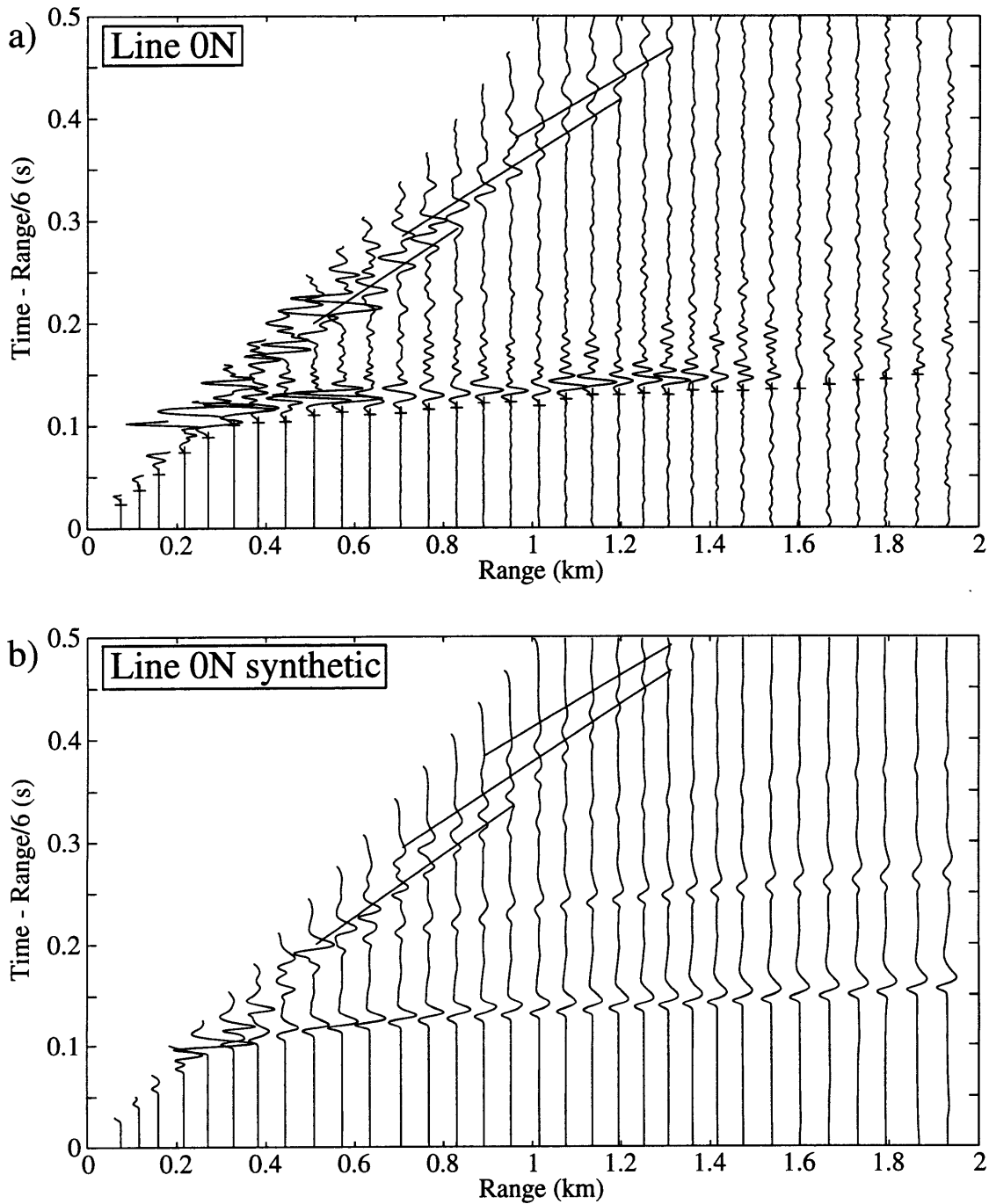
Figure 3.9. (a) As for Figure 3.6a, for 2.3 kg (5 lb) charges detonated to the OBH for Line 0N. The maximum shot height was ~13 m above the seafloor. (b) As for Figure 3.6b, for the synthetic seismograms of Line 0N.
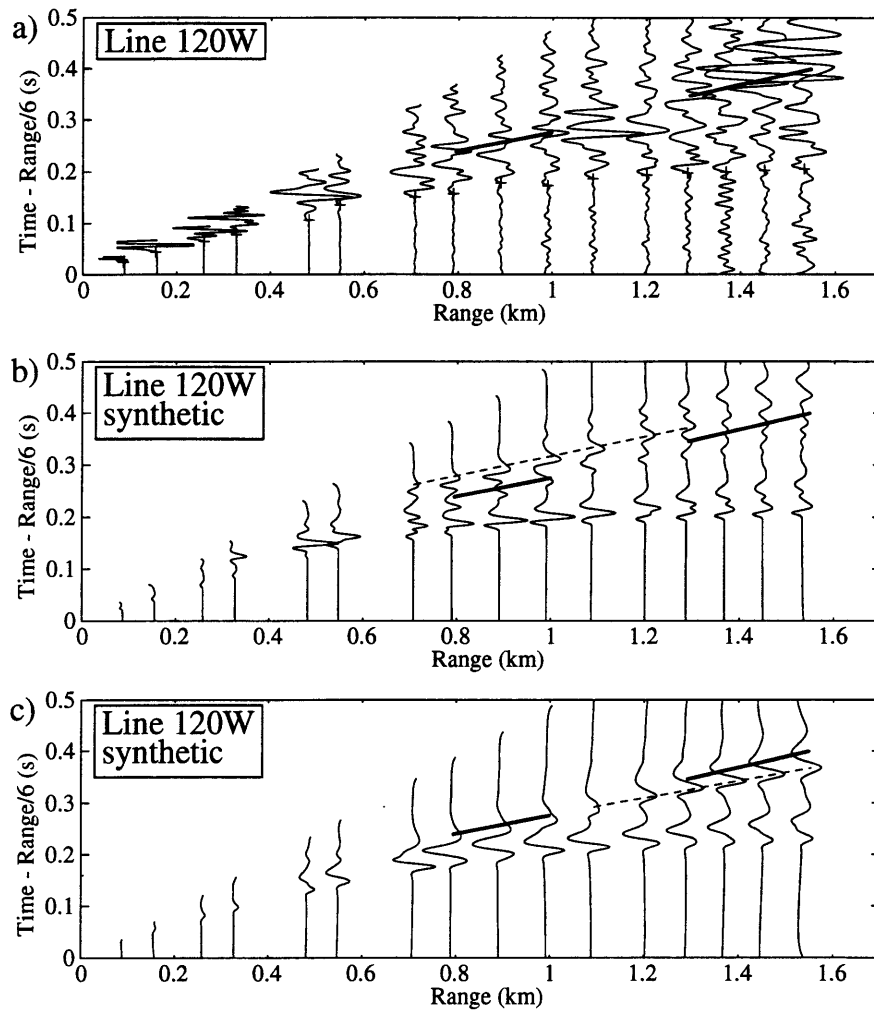
Figure 3.10. (a) As for Figure 3.6a, for 2.3 kg (5 lb) charges detonated to the OBH for Line 120W. For display purposes, it was necessary to multiply the amplitudes of the seismograms by a factor of $R^{2.6}$, where R is the distance of the shot from the receiver. The amplitudes of the first two seismograms exceed the dynamic range of the instrument, and have been clipped for plotting purposes. Seismograms at a range greater than 400 m have been low-pass filtered with a cosine-squared filter, with an upper taper interval of 80-100 Hz. The solid lines indicate secondary energy discussed in the text. The maximum shot height was ~30 m above the seafloor. (b) As for Figure 3.6b, for the synthetic seismograms for Line 120W. The velocity/depth model includes a zero gradient in the surficial low-velocity zone. The solid lines indicate the secondary energy noted in Figure 3.10a, and the dashed line indicates secondary energy discussed in the text. (c) As for Figure 3.6c, for a velocity/depth model that includes a gradient of 5.3 s^{-1} in the surficial low-velocity zone.
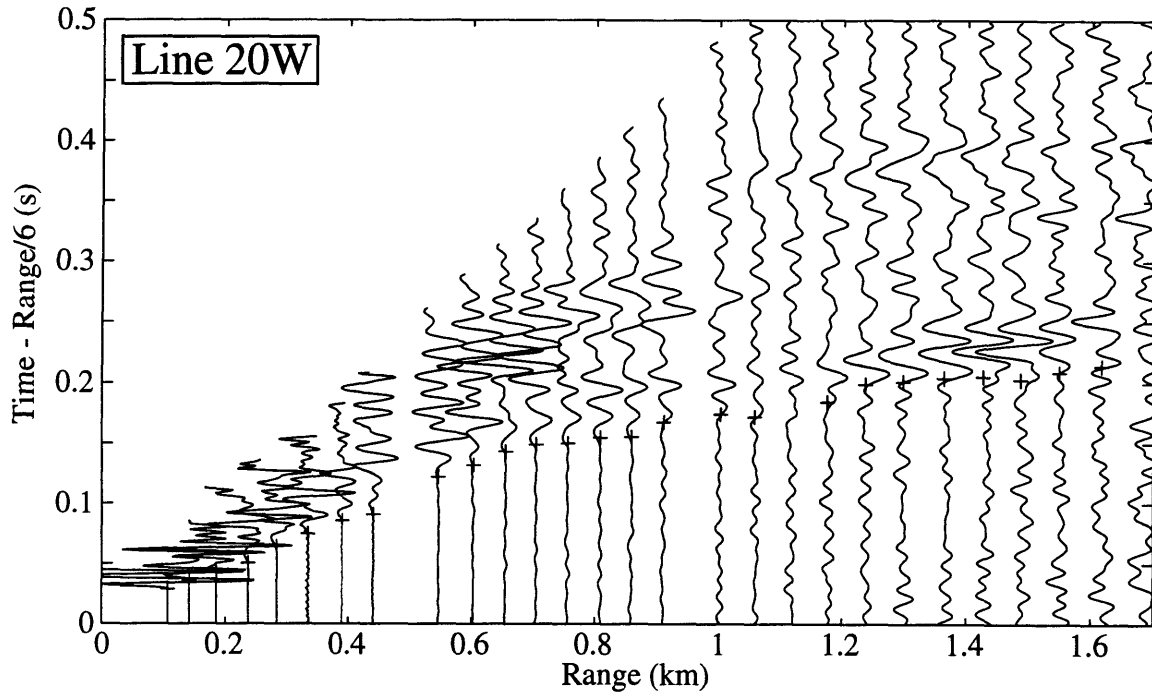
Figure 3.11. As for Figure 3.6a, for 2.3 kg (5 lb) charges detonated to the OBH for Line 20W. For display purposes, it was necessary to multiply the amplitudes of the seismograms by a factor of $R^{2.6}$, where R is the distance of the shot from the receiver. Seismograms at a range greater than 500 m have been low-pass filtered with a cosine-squared filter, with an upper taper interval of 80-100 Hz. The maximum shot height was ~14 m above the seafloor.
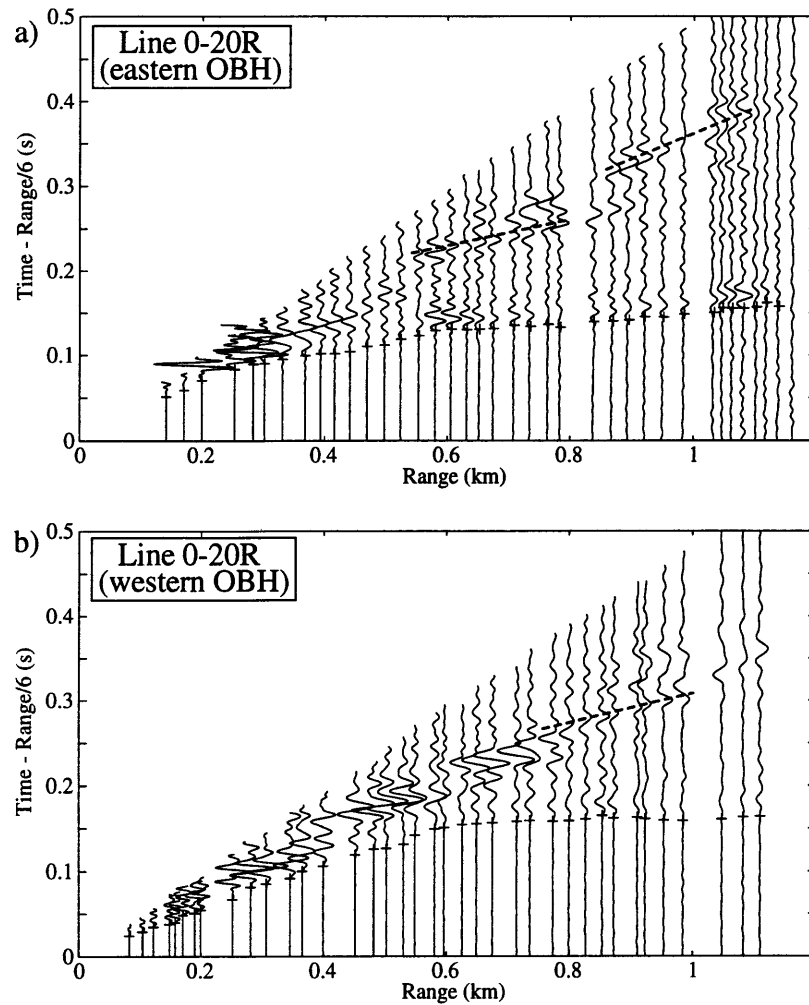
Figure 3.12. As for Figure 3.6a, for charges detonated to the OBHs for Line 0-20R. For display purposes, it was necessary to multiply the amplitudes of the seismograms by a factor of $R^{3.0}$, where R is the distance of the shot from the receiver. (a) Seismograms recorded by the eastern OBH, located within the ASC (Figure 3.2). The two seismograms at a range <0.2 km, and the four seismograms at a range >1.1 km are from 2.3 kg (5 lb.) charges, and the remaining seismograms are from 4.6 kg (10 lb.) charges. Seismograms at a range >0.31 km have been low-pass filtered with a cosine-squared filter, with an upper taper interval of 80-100 Hz. The dashed lines indicate secondary arrivals discussed in the text. b) Seismograms recorded by the western OBH, located ~1.2 km west of the ASC (Figure 3.2). The four seismograms at a range <0.15 km, and the two seismograms at a range >1.05 km are from 2.3 kg (5 lb.) charges, and the remaining seismograms are from 4.6 kg (10 lb.) charges. Seismograms at a range >0.4 km have been low-pass filtered with a cosine-squared filter, with an upper taper interval of 80-100 Hz. The dashed line indicates secondary arrivals discussed in the text.
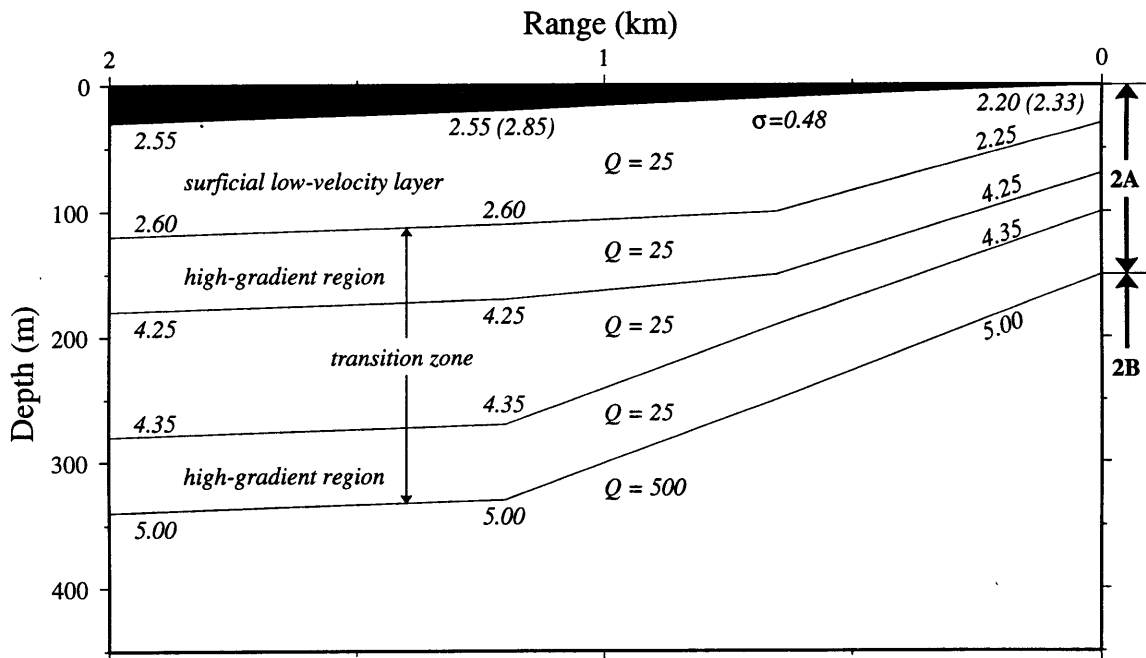
Figure 3.13. Two-dimensional velocity/depth model for the EPR at 9°30'N. Distance is increasing away from the ASC, and the seafloor is dipping ~1° from east to west. The model in the 0-1.2 km range is based on Line 0-20R. Indicated on the model are the velocities at the top and bottom of each layer, in units of km/s. The seafloor velocities in parantheses are the values obtained for Line 0S (at 0 km) and Line 20W (at 1.2 km). The vertical exaggeration is 4:1. The data from Line 120W suggests that there is no resolvable change in structure from 1.2-6 km, and the data from Line 20E suggests that this model is symmetrical about the rise axis. The Q values and Poisson's ratio at the seafloor are from reflectivity modeling of Line 0S.
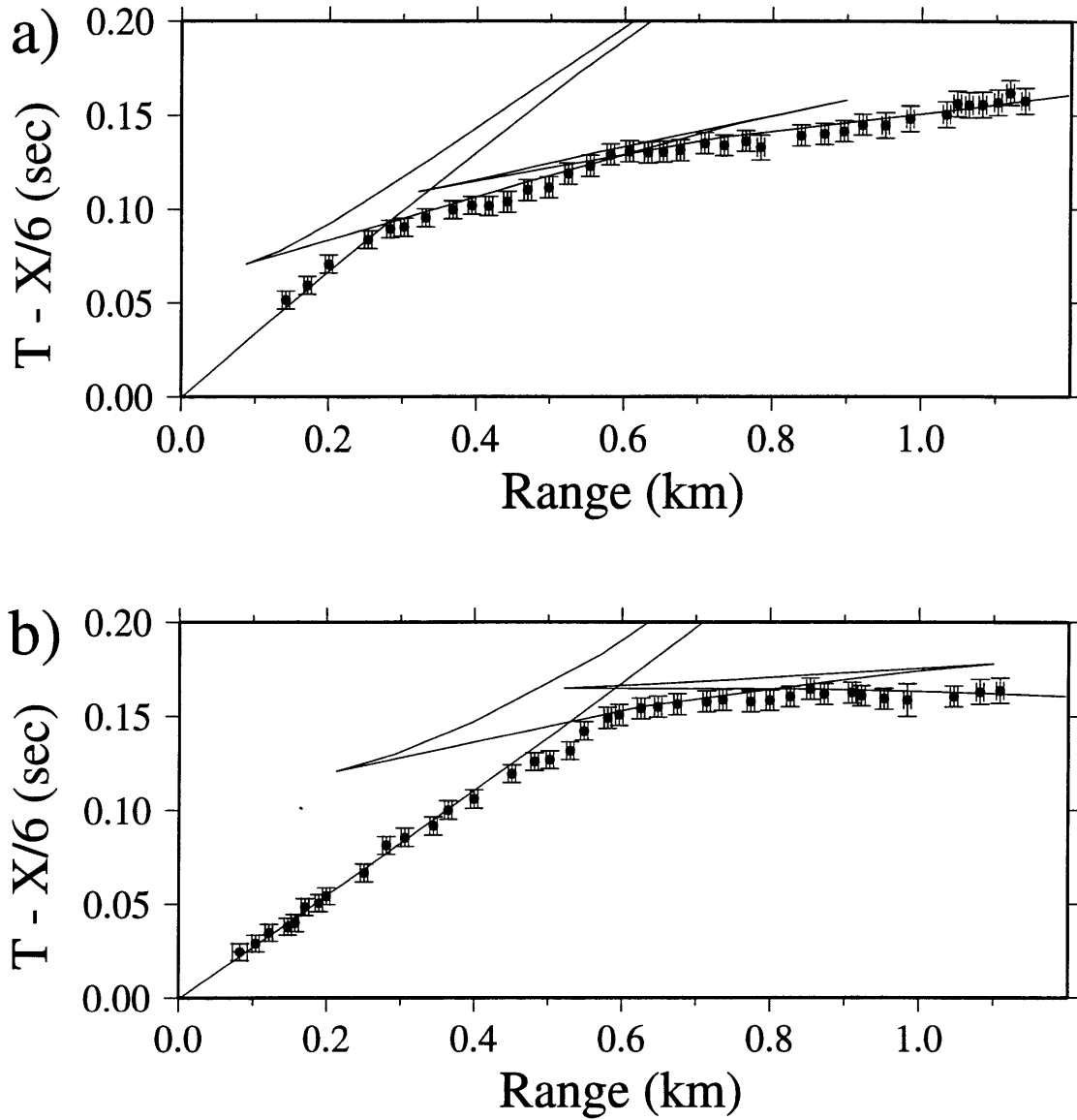
Figure 3.14. (a) First arrival travel times (solid circles) with error bars for the eastern receiver on Line 0-20R. Solid lines show the calculated travel time curves from two-dimensional ray-tracing for the velocity/depth model of Figure 3.13. (b) As for Figure 3.14a, but for the western receiver on Line 0-20R.
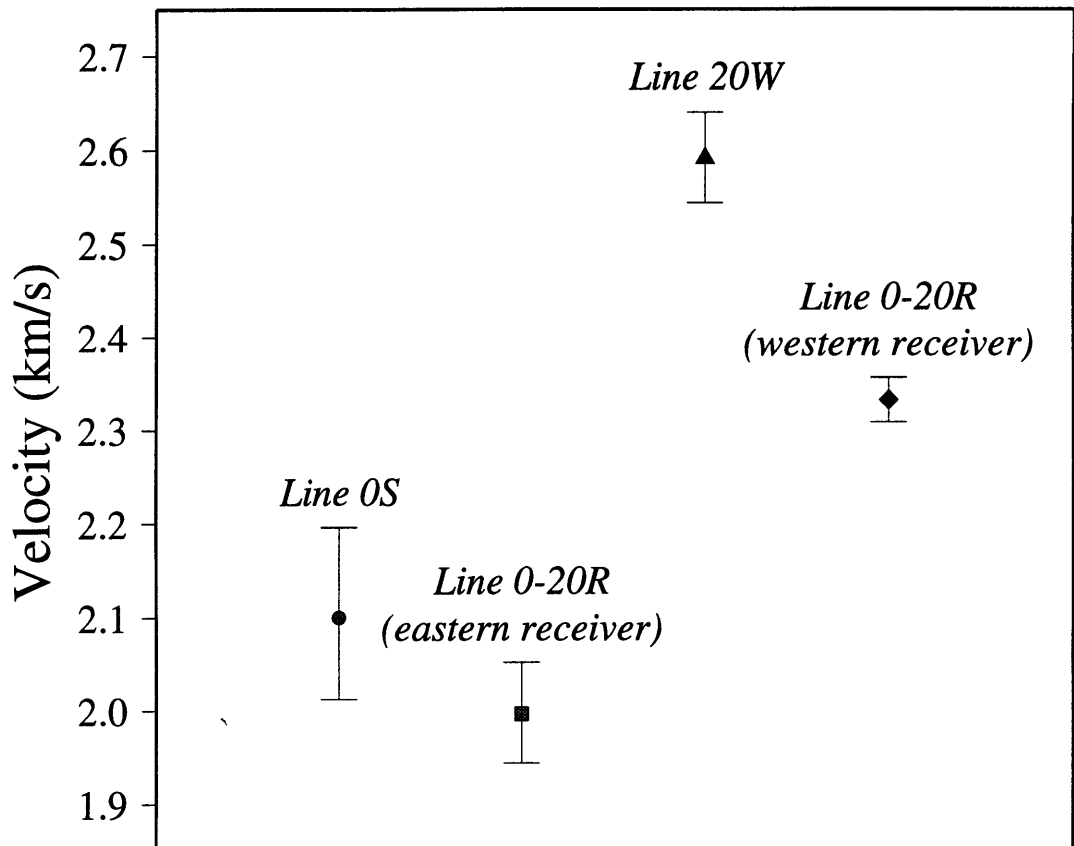
Figure 3.15. Apparent phase velocities for arrivals turning in the surficial low-velocity layer for Lines 0S, 20W, and 0-20R. Phase velocities were computed by a least squares linear fit through the first arrival travel times (corrected for topography), with the linear fit constrained to pass through the origin (0 km, 0 km/s). The error bars represent two standard deviations. The phase velocities for the arrivals observed for the cross-axis line (Line 0-20R) are consistently slower than observed by receivers located in approximately the same locations for rise parallel lines (Line 0S and Line 20W).
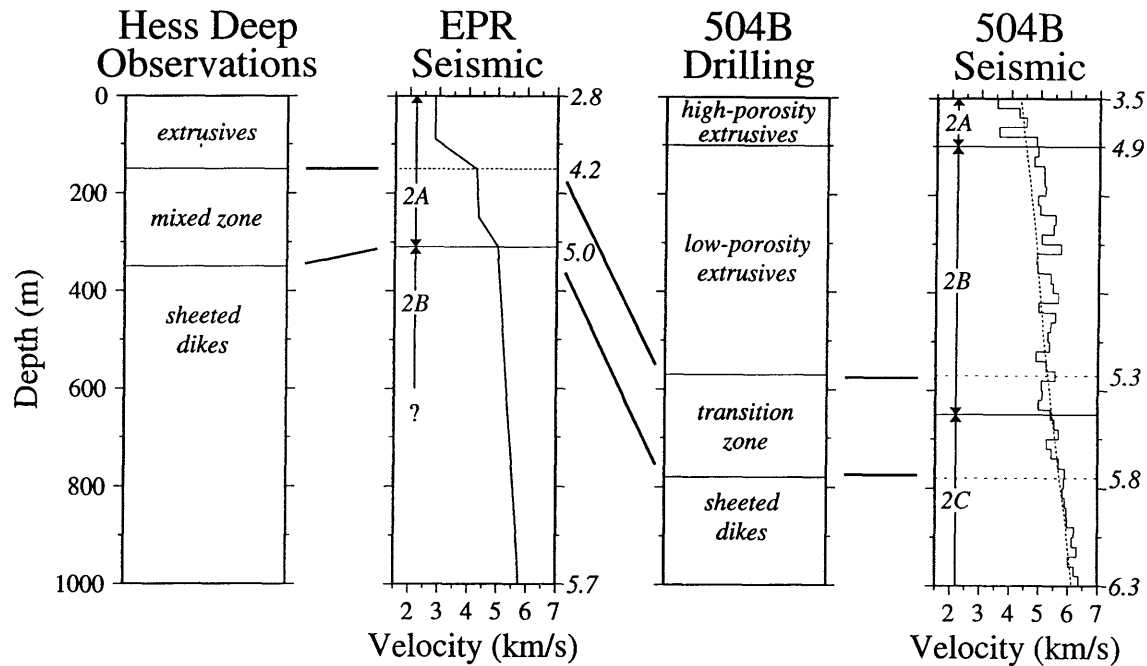
Figure 3.16. Column 1) Stratigraphy observed at Hess Deep as reported by *Francheteau et al.* [1992]. Column 2) Seismic structure of the EPR at 9°30'N. Structure in the 0-310 m depth interval is from the western portion of Line 0-20R, and in the 310-1000 m depth interval from ESP 5 of *Vera et al.* [1990]. The dashed and solid lines are the interpreted boundaries from extrusives to transition zone, and transition zone to sheeted dikes, respectively. Velocities at 0, 150, 310, and 1000 m are indicated to the right of the column. The Layer 2A/2B boundary is from the definition of *Houtz and Ewing* [1976] as discussed in the text; there is no obvious 2B/2C boundary. Column 3) Stratigraphy observed from drilling at DSDP Hole 504B, as reported by *Anderson et al.* [1982]. Column 4) Seismic structure at DSDP Hole 504B from the sonic log of Leg 111 (solid line) [*Becker et al.*, 1988] and an oblique seismic experiment (dashed line) [*Little and Stephen*, 1985]. The sonic log has been averaged over 20 m windows before plotting. Velocities from the sonic log at 100, 570, 780, and 1000 m are indicated to the right of the column. The 2A/2B and 2B/2C boundaries (solid lines) are defined primarily from resistivity logging [e.g. Figure 5 of *Becker et al.*, 1982]. The dash-dot lines indicate the upper and lower boundaries of the transition zone as shown in Column 3. The heavy solid lines between columns indicate the favored interpretation of this paper. Note that with the favored interpretation the sheeted dike complex is more than twice as deep for Columns 3 and 4 vs. Columns 1 and 2.
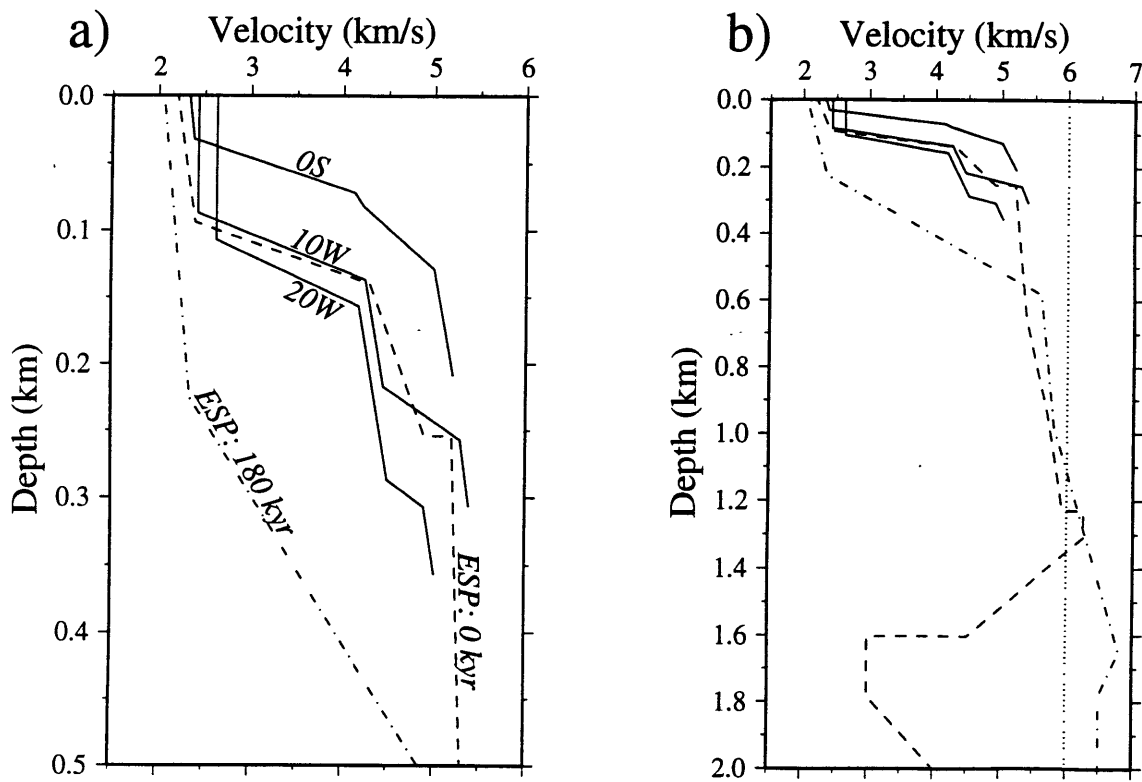
Figure 3.17. Velocity/depth profiles of Lines 0S and 20W from this study, and from the expanding spread profiles solutions of *Vera et al.* [1990] located at ~zero-age (their ESP5) and ~180 kyr (their ESP1). Depth ranges shown are a) 0-500 m and b) 0-2000 m. The dotted line in Figure 3.16b marks an isovelocity of 6 km/s.

extrusives

transition
zone
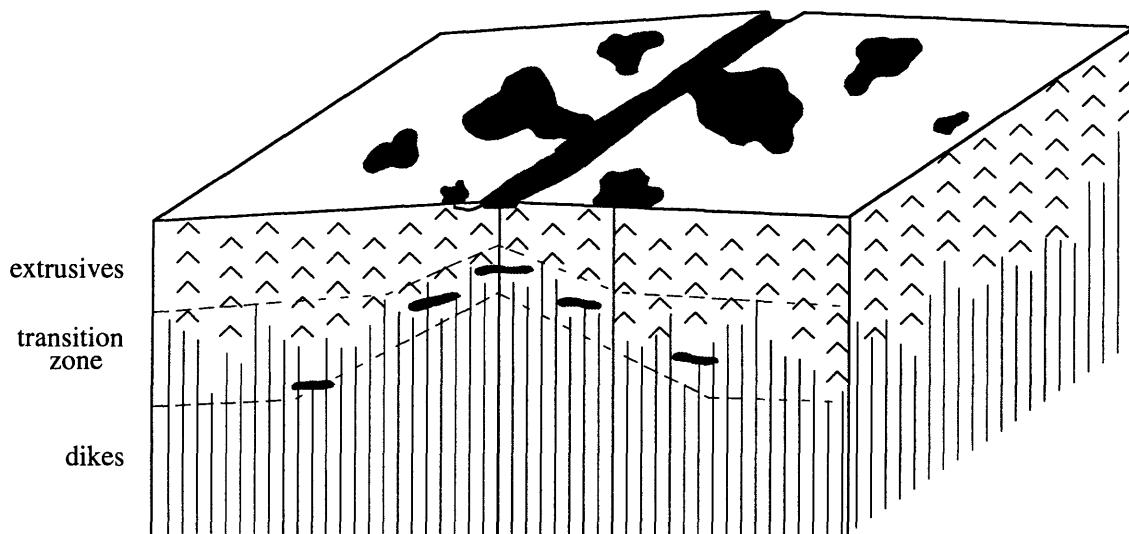
dikes

Figure 3.18. Cartoon depicting the emplacement process for lavas and dikes at the fast-spreading EPR. The cartoon shows a snapshot in time, with the shaded areas showing the most recent lava flows and sills. The extrusive layer doubles in thickness within 1 km of the ASC due to lava that overflows the walls of the ASC, lava flows which are emplaced outside of the ASC, and lava that travels laterally from the ASC through conduits. The transition zone also doubles in thickness within 1 km of the rise axis, due to off-axis sill emplacement. The shallow structure is approximately symmetrical about the rise axis, and exhibits only minor thickness variations at distances greater than 1 km from the ASC. The dashed lines show the 4.2 and 5.0 km/s isovelocity contours from Figure 3.13, which are interpreted to be the upper and lower boundaries of the transition zone (equivalent to the mixed zone described by *Francheteau et al.* [1992] at Hess Deep).

CHAPTER 4

THE SHALLOW ATTENUATION STRUCTURE OF THE FAST-SPREADING EAST PACIFIC RISE NEAR 9°30'N

Abstract. Seven on-bottom seismic refraction experiments are analyzed in an effort to resolve the shallow compressional wave attenuation structure of young crust at the fast-spreading East Pacific Rise. All models depict a low-Q layer 2A (apparent Q=11-22), and several models resolve a layer 2B with a much higher Q (apparent $Q > 70$). This structure is consistent with a layer 2A composed of extrusives overlying a layer 2B composed of sheeted dikes.

Introduction

The fast-spreading East Pacific Rise (EPR) at latitude 9°30'N has been the site of several seismic experiments which have resolved substantial velocity variations in the upper crust, most notably the lateral thickening of seismic layer 2A within 1-2 km of the rise axis [*Toomey et al.*, 1990; *Christeson et al.*, 1992; *Harding et al.*, 1993; *Vera and Diebold*, 1993]. In addition, *Wilcock et al.* [1992] estimate high attenuation (average Q=35-70) in the upper 1 km; however, the vertical resolution of these conventional measurements is poor in the shallow crust due to the lack of energy turning in this region. *Jacobson and Lewis* [1990] have measured Q values for layer 2A directly. Their values of 20-50 for 0.4 my old oceanic crust formed at the intermediate-spreading Juan de Fuca Ridge are similar to the average values for the upper 1 km measured by *Wilcock et al.* [1992].

This letter presents new attenuation measurements from data collected during seven seismic refraction experiments over young crust at the EPR (Figure 4.1) carried out with both the source and the receiver on the ocean floor. The purpose of this study is to

ascertain if the 2A/2B boundary is an attenuation boundary as well as a velocity boundary as suggested by previous studies [*Wilcock et al.*, 1992; *Christeson, Purdy, and Fryer*, 'Seismic constraints on shallow crustal emplacement processes at the fast-spreading East Pacific Rise', submitted to JGR, 1993; hereafter referred to as *Christeson et al.*, submitted].

Method

The quality factor Q is related to P_E, the power spectrum resulting from propagation through the earth by

$$\int_s \frac{1}{VQ} ds = t^* = -\frac{1}{2\pi} \frac{d\ln[P_E(f)]}{df} \tag{1}$$

where V is the seismic velocity, f is the frequency, and s is the wavepath. P_E is related to P, the power spectrum of the recorded waveform by

$$P_E(f) = \frac{P(f)}{P_S(f) \, P_I(f)} \tag{2}$$

where P_S and P_I are the power spectra of the source and the instrument response, respectively.

For the seven on-bottom refraction lines, P was calculated for each shot from a 0.06 s time window using the multiple-window spectral analysis technique [*Thomson*, 1982; *Park et al.*, 1987] with 2-π prolate tapers. The length of the time window was chosen to be long enough to include the waveform of the first arrival, while short enough to preclude secondary energy generated by multiples (as identified by *Christeson et al.*, submitted). The source signature of NOBEL (the source for the on-bottom seismic refraction experiments), and thus the source-receiver correction, is poorly known. However, the attenuation in the water column is extremely low (Q>100,000 for 100 Hz energy [*Urick*, 1967]), and the power spectrum of the water wave arrival can be used as a substitute for the source-receiver correction if the assumption is made that this arrival has not interacted with the earth. We calculated the spectrum from a 0.06 s time window for all water wave

arrivals that did not exceed the dynamic range of the recording instrument, normalized each spectrum by the maximum power, and determined the average water wave spectrum. This spectrum was then used to correct for the source and receiver characteristics according to Eq. (2), and a t* value was determined for each shot using a least-squares fit to Eq. (1). Figure 4.2 shows a sample t* estimation. The lower frequency limit for all shots was 32 Hz., and the upper limit was determined by the signal to noise ratio for each shot, but was a minimum of 130 Hz. There was no evidence for frequency dependent attenuation, although the measurements are not particularly sensitive given the spectral resolution of approximately ±33 Hz. The addition of the source-receiver correction changed the mean correlation coefficient for the natural log of the power spectrum from -0.87 to -0.97, which suggests the use of the water wave as a source-receiver correction is a satisfactory approximation.

For the three zero-age lines (Lines 0F, 0N, and 0S), the t* values were inverted for a layered attenuation structure with a $\ln(Q^{-1})$ parameterization of Eq. (1) using an inversion technique described in detail by *Wilcock* [1992] and *Wilcock et al.* [1992]. One-dimensional ray-tracing using the velocity models of *Christeson et al.* [submitted] was used to calculate the wave paths for the first arrivals. Inversions for each line were computed for a 1-layer constant-Q model and a 2-layer Q model, with the boundary for the 2-layer model placed at the 2A/2B boundary of *Christeson et al.* [submitted]. For Lines 20W, 120W, and 20E only 1-layer constant-Q models were solved for, as no t* values were obtained for wave paths that turned within layer 2B due to poor spectral signal to noise ratios. For the rise-perpendicular on-bottom refraction line (Line 0-20R) the t* data were inverted for a two-dimensional attenuation structure.

Results

Estimates of t* are plotted in Figure 4.3a against shot range for one of the three zero-age lines (Line 0N). The five t* estimates at the shortest ranges are for raypaths which turn

within seismic layer 2A, with the remaining t* estimates for raypaths that turn within seismic layer 2B (Figure 4.3b). A 1-layer constant-Q model predicts an increase in t* values with range (dash-dot line in Figure 4.3a) that is not observed. A 2-layer attenuation model, with Q increasing from ~13-15 in layer 2A to >120 in layer 2B (Figure 4.3b; Table 4.1) matches the data well (Figure 4.3a), with the low attenuation in layer 2B resulting in t* values that are approximately independent of range for raypaths which turn in this layer. An F-test shows that the decrease in variance between the 2-layer attenuation model and the constant attenuation model is significant at the 99% confidence level. Similar models are found for the two other on-axis lines (Table 4.1). Typical t* estimates for an off-axis line (Line 20W) are plotted against range in Figure 4.4a. In contrast to the on-axis lines, raypaths for the off-axis t* estimates turn entirely within layer 2A (Figure 4.4b). Constant-Q models, with Q=12-22, provided good fits to the t* estimates (Figure 4.4a; Table 4.1).

The t* estimates for the rise-perpendicular line (Line 0-20R) are shown in Figures 4.5a and 4.5b. Unlike the rise-parallel lines, the velocity structure for this reversed cross-axis line is clearly two-dimensional [*Christeson et al.*, submitted], with layer 2A thickening from ~150 m within the axial summit caldera (approximately zero-age crust) to ~330 m 1.2 km to the west. An inversion for a 2-layer Q model, with the upper layer thickening away from the rise axis, indicates that Q increases from 14-16 in layer 2A to >50 in layer 2B, similar to the results of the rise-parallel lines (model 1 in Table 4.1). Because this line had two receivers and close shot spacing, we performed two additional inversions with different parametrizations. A model (Figure 4.5c and model 2 in Table 4.1) that allowed Q^{-1} to vary linearly in layer 2A between the two receivers (at x=0 km and x=1.2 km) provided a better fit to the data at the 99% confidence level than the model without lateral variation, with Q in layer 2A decreasing from 18-23 at x=0 km (zero-age crust) to 10-12 at x=1.2 km (~20,000 year old crust). A third model that allowed further lateral variation in Q with the addition of a node at x=0.6 km provided a better fit to the data at the 99%

confidence level, with Q in layer 2A varying from ~7-47 over the 1.2 km line (model 3 in Table 4.1).

Table 4.1: Model Values

Line	Layer 2A thickness	Q in Layer 2A [†]	Q in Layer 2B [‡]
Line 0F	160 m	14-16 (15)	>115
Line 0N	190 m	13-15 (14)	>120
Line 0S	130 m	16-19 (17)	>70
Line 20W	390 m	12-16 (14)	
Line 120W	310 m	11-16 (13)	
Line 20E	300 m	18-22 (20)	
Line 0-20R (1)	150 m [0] [§] 330 m [1.2]	14-16 (15)	>50
Line 0-20R (2)	150 m [0] [§] 330 m [1.2]	18-23 (20) [0] [§] 10-12 (11) [1.2]	>70
Line 0-20R (3)	150 m [0] [§] 250 m [0.6] 330 m [1.2]	10-14 (12) [0] [§] >24 (47) [0.6] 6-8 (7) [1.2]	>25

[†]Range of Q values to 95% certainty. Number in parantheses is the best-fitting Q value.

[‡]Minimum Q value to 95% certainty (maximum value not resolved by inversion).

[§]Indicated in brackets is the node location (in km) for this thickness or Q value. Range is measured from the eastern receiver, which is located on the rise axis. Q^{-1} values are linearly interpolated between the nodes.

Discussion and Conclusions

The final attenuation models for all lines (Table 4.1) include a highly-attenuating layer 2A (Q=11-22 for the 1-D models). *Wilcock et al.* [1992] measured an average Q value in the uppermost crust of ~35 off-axis, and ~70 on-axis; if the cross-axis variation is due to off-axis thickening of a highly-attenuating layer 2A, then the Q in this layer must be ~10-20. Our layer 2A Q values are consistent with the estimates of *Wilcock et al.* [1992], and

are slightly lower than the measurements of *Jacobson and Lewis* [1990] (Q=20-50). Inversions for our lines which included raypaths turning within layer 2B suggest that the 2A/2B transition is an attenuation boundary as well as a velocity boundary, with Q values for layer 2B (Q>70 for the 1-D models) significantly higher than those measured for layer 2A.

Toksöz et al. [1987] suggest that Coulomb friction, fluid flow, and scattering are the primary sources of seismic attenuation in continental rocks. Coulomb friction is caused by the sliding of crack surfaces and grain boundaries during passage of a seismic wave [*Walsh*, 1966]. *Toksöz et al.* [1987] argue that fluid flow is a principal source of attenuation only at frequencies near 1 Hz, below the frequency range of this study. Attenuation due to scattering is important for *ka* values between 1-2 [*Frankel and Clayton*, 1986], where *k* is the seismic wave number, and *a* is the heterogeneity length scale; for the frequency range and velocities of this study, *ka* will fall between 1-2 for velocity heterogeneities on the length scale of ~5-100 m.

From submersible observations and camera tows, we know that the shallow EPR crust is composed primarily of sheet flows, pillow lavas, and rubble layers [*Choukroune et al.*, 1984; *Gente et al.*, 1986; *Haymon et al.*, 1991]. Scattering will be an important source of attenuation in the upper crust, as variability in lithology may form velocity heterogeneities on a length scale of 5-100 m [*Wilkens et al.*, 1991]. Cooling and contraction forms cracks in both sheet flows and pillow lavas, and thus Coulomb friction could also be a principal cause of seismic dissipation. Therefore the low Q values for layer 2A are not unexpected.

One hypothesis for the nature of the 2A/2B boundary is that it is a lithologic boundary between the extrusive sequence and the sheeted dikes [*Herron*, 1982; *Christeson et al.*, 1992; *Harding et al.*, 1993]. Based on ophiolite observations (e.g. [*Pallister*, 1981; *Nehlig and Juteau*, 1988]), the sheeted dike complex is structurally homogeneous as compared to the overlying extrusive sequence, and therefore we predict a decrease in attenuation due to scattering across this boundary. In addition, crack density (and therefore attenuation due to

Coulomb friction) decreases from the extrusive sequence to the dike unit [*Nehlig and Juteau*, 1988]. Thus, a model of extrusives overlying sheeted dikes predicts an increase in Q across the 2A/2B boundary, consistent with the results in Table 4.1. *Rohr et al.* [1988] argue that the 2A/2B boundary is a metamorphic front within the extrusive section generated by secondary mineralization. Laboratory measurements of basaltic rocks indicate that attenuation increases with the volume of secondary minerals present [*Wepfer and Christensen*, 1990]. Although it is not certain if the laboratory results are applicable on the larger scale of seismic wavelengths, they do suggest that a 2A/2B boundary formed by a metamorphic front should be associated with an increase in attenuation for layer 2B, inconsistent with the results in Table 4.1. Within the resolution of our inversions, there is no evidence for a systematic change in attenuation for layer 2A with distance from the rise axis, although rapid lateral variability in attenuation is indicated by the models for Line 0-20R (Table 4.1).

In summary, the attenuation structure for young oceanic crust consists of a highly attenuating layer 2A (Q=11-22) overlying a layer 2B with a much higher Q (Q>70). This structure is consistent with a layer 2A composed of extrusives and a layer 2B consisting of sheeted dikes.

References

Choukroune, P., J. Francheteau and R. Hekinian, Tectonics of the East Pacific Rise near 12°50'N: a submersible study, *Earth Planet. Sci. Lett.*, *68*, 115-127, 1984.

Christeson, G.L., G.M. Purdy and G.J. Fryer, Structure of young upper crust at the East Pacific Rise near 9°30'N, *Geophys. Res. Lett.*, *19*, 1045-1048, 1992.

Frankel, A. and R.W. Clayton, Finite difference simulations of seismic scattering: implications for the propagation of short-period seismic waves in the crust and models of crustal heterogeneity, *J. Geophys. Res.*, *91*, 6465-6489, 1986.

Gente, P., J.M. Auzende, V. Renard, Y. Fouquet and D. Bideau, Detailed geological mapping by submersible of the East Pacific Rise axial graben near 13°N, *Earth Planet. Sci. Lett.*, *78*, 224-236, 1986.

Harding, A.J., G.M. Kent and J.A. Orcutt, A multichannel seismic investigation of upper crustal structure at 9°N on the East Pacific Rise: Implications for crustal accretion, *J. Geophys. Res.*, *98*, 13925-13944, 1993.

Haymon, R.M., D.J. Fornari, M.H. Edwards, S. Carbotte, D. Wright and K. Macdonald, Hydrothermal vent distribution along the East Pacific Rise crest (9°09'-54'N) and its relationship to magmatic and tectonic processes on fast-spreading mid-ocean ridges, *Earth Planet. Sci. Lett.*, *104*, 513-534, 1991.

Herron, T.J., Lava flow layer - East Pacific Rise, *Geophys. Res. Lett.*, *9*, 17-20, 1982.

Jacobson, R.S. and B.T.R. Lewis, The first direct measurements of upper oceanic crustal compressional wave attenuation, *J. Geophys. Res.*, *95*, 17417-17429, 1990.

Klitgord, K.D. and J. Mammerickx, Northern East Pacific Rise: Magnetic anomaly and bathymetric framework, *J. Geophys. Res.*, *87*, 6725-6750, 1982.

Nehlig, P. and T. Juteau, Flow porosities, permeabilities and preliminary data on fluid inclusions and fossil thermal gradients in the crustal sequence of the Sumail ophiolite (Oman), *Tectonophysics*, *151*, 199-221, 1988.

Pallister, J.S., Structure of the sheeted dike complex of the Samail ophiolite near Ibra, Oman, *J. Geophys. Res.*, *86*, 2661-2672, 1981.

Park, J., C.R. Lindberg and F.L. Vernon III, Multitaper spectral analysis of high-frequency seismograms, *J. Geophys. Res.*, *92*, 12675-12684, 1987.

Rohr, K.M.M., B. Milkereit and C.J. Yorath, Asymmetric deep crustal structure across the Juan de Fuca Ridge, *Geology*, *16*, 533-537, 1988.

Thomson, D.J., Spectrum estimation and harmonic analysis, *Proc. I.E.E.E.*, *70*, 1055-1096, 1982.

Toksöz, M.N., R.S. Wu and D.P. Schmitt, Physical mechanisms contributing to seismic attenuation in the crust, in *Strong Ground Motion Seismology*, edited by M. O. Erdik and M. N. Toksöz, 225-247, D. Reidel Publishing Company, Dordrecht, Holland, 1987.

Toomey, D.R., G.M. Purdy, S.C. Solomon and W.S.D. Wilcock, The three-dimensional seismic velocity structure of the East Pacific Rise near latitude 9°30'N, *Nature*, *347*, 639-645, 1990.

Urick, R.J., *Principles of Underwater Sound for Engineers*, 342 pp., McGraw-Hill, U.S.A., 1967.

Vera, E.E. and J.B. Diebold, Seismic imaging of oceanic layer 2A between 9°30'N and 10°N on the East Pacific Rise from two-ship wide aperture profiles, *J. Geophys. Res.*, *in press*, 1993.

Walsh, J.B., Seismic wave attenuation in rock due to friction, *J. Geophys. Res.*, *71*, 2591-2599, 1966.

Wepfer, W.W. and N.I. Christensen, Compressional wave attenuation in oceanic basalts, *J. Geophys. Res.*, *95*, 17431-17439, 1990.

Wilcock, W.S.D., The seismic attenuation structure of the East Pacific Rise, Ph.D. Thesis, 337 pp., WHOI/MIT Joint Program in Oceanography, 1992.

Wilcock, W.S.D., S.C. Solomon, G.M. Purdy and D.R. Toomey, The seismic attenuation structure of a fast-spreading mid-ocean ridge, *Science*, *258*, 1470-1474, 1992.

Wilcock, W.S.D., D.R. Toomey, G.M. Purdy and S.C. Solomon, The renavigation of Sea Beam bathymetric data between 9°N and 10°N on the East Pacific Rise, *Mar. Geophys. Res.*, *15*, 1-12, 1993.

Wilkens, R.H., G.J. Fryer and J. Karsten, Evolution of porosity and seismic structure of upper oceanic crust: importance of aspect ratios, *J. Geophys. Res.*, *96*, 17981-17995, 1991.
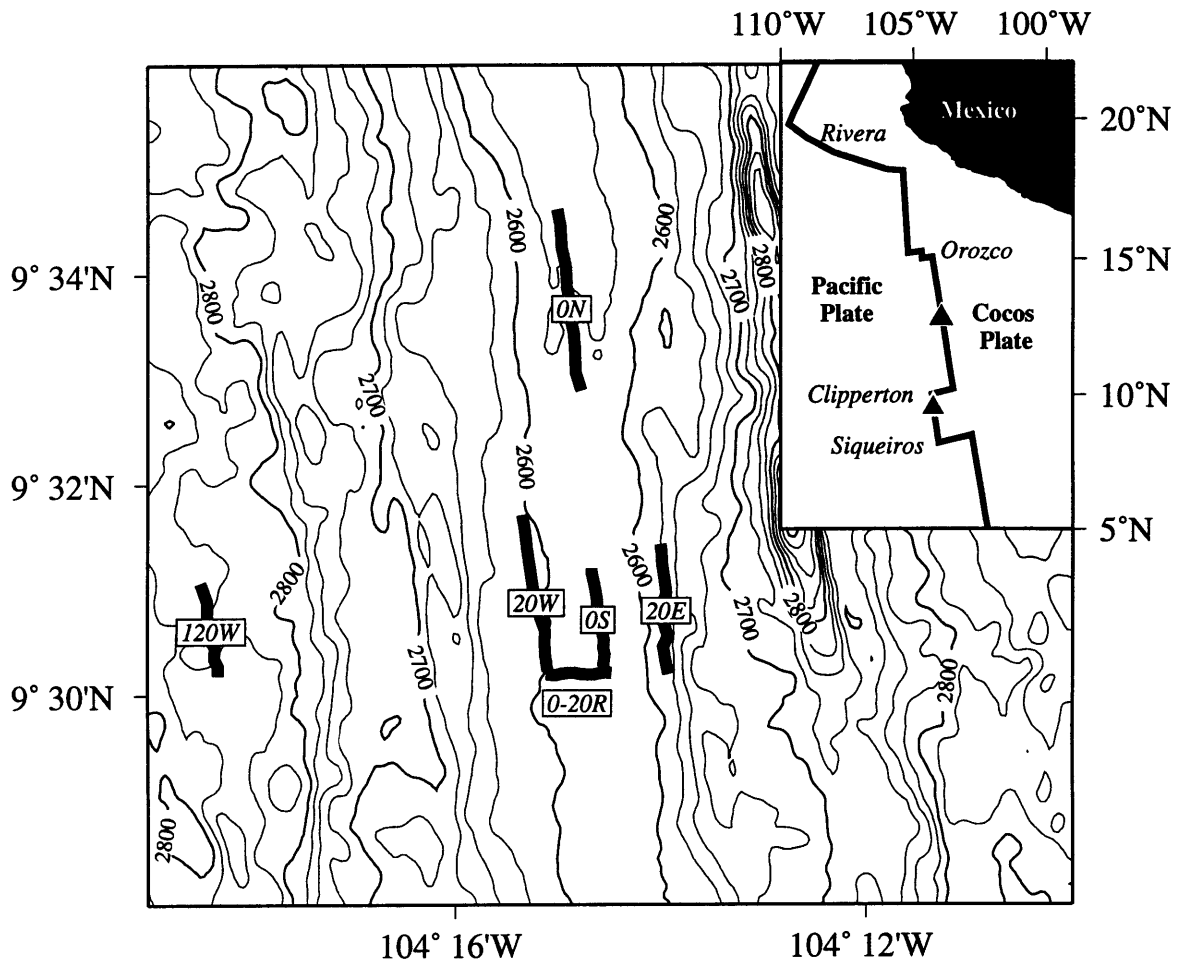
Figure 4.1. Sea Beam bathymetry [*Wilcock et al.*, 1993] contoured at 25 meter intervals for a section of the East Pacific Rise located between the Siqueiros and Clipperton transform faults. Shiptracks for the on-bottom seismic refraction experiments are indicated with the heavy black lines. Each shiptrack is labelled with the approximate age of the crust in kiloyears, based on a half spreading rate of 5.5 cm/yr [*Klitgord and Mammerickx*, 1982]. An ocean bottom hydrophone (OBH) was located at the southern end of each ridge parallel line, with an OBH at both the eastern and western ends of the Line 0-20R. An additional refraction line (Line OF) was located over zero-age crust at 12°50'N. The inset map shows the regional setting, with triangles indicating the locations of the experiments conducted at 9°30'N and 12°50'N.
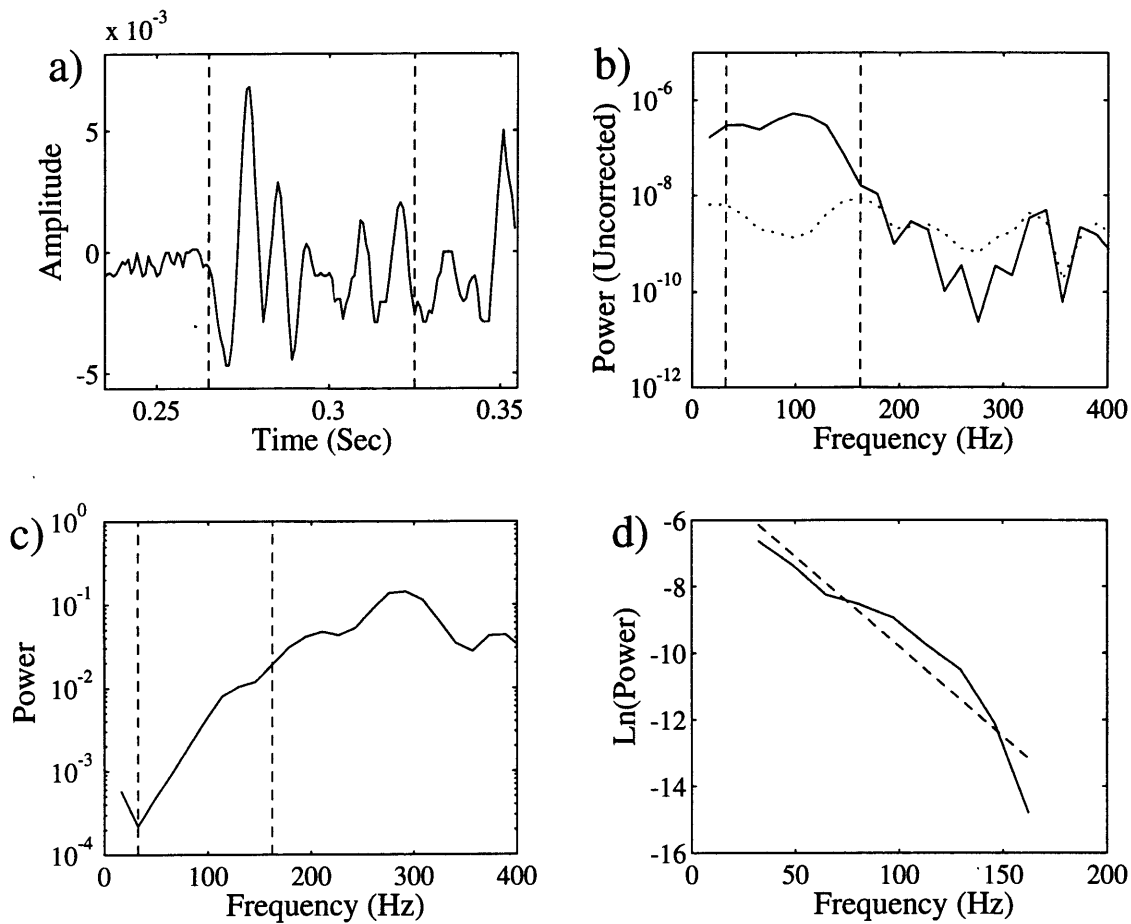
Figure 4.2. Sample t* estimation. a) Time series used for calculation. The dashed lines indicate the 0.06 sec time window used for the power calculation, with the first dashed line at the onset of the refracted arrival. b) The power spectrum obtained for the waveform (solid) and noise (dotted). The noise spectrum was calculated for a 0.06 sec time window located entirely before the onset of the refracted arrival. The dashed lines indicate the frequency interval used for this t* estimation. c) Source-receiver correction obtained from the average water-wave spectrum. The dashed lines indicate the frequency interval used for the t* estimation. d) Natural log of the waveform power (corrected for the source-receiver correction) vs. frequency (solid line). The dashed line shows the least squares straight line fit used to obtain the t* estimate.
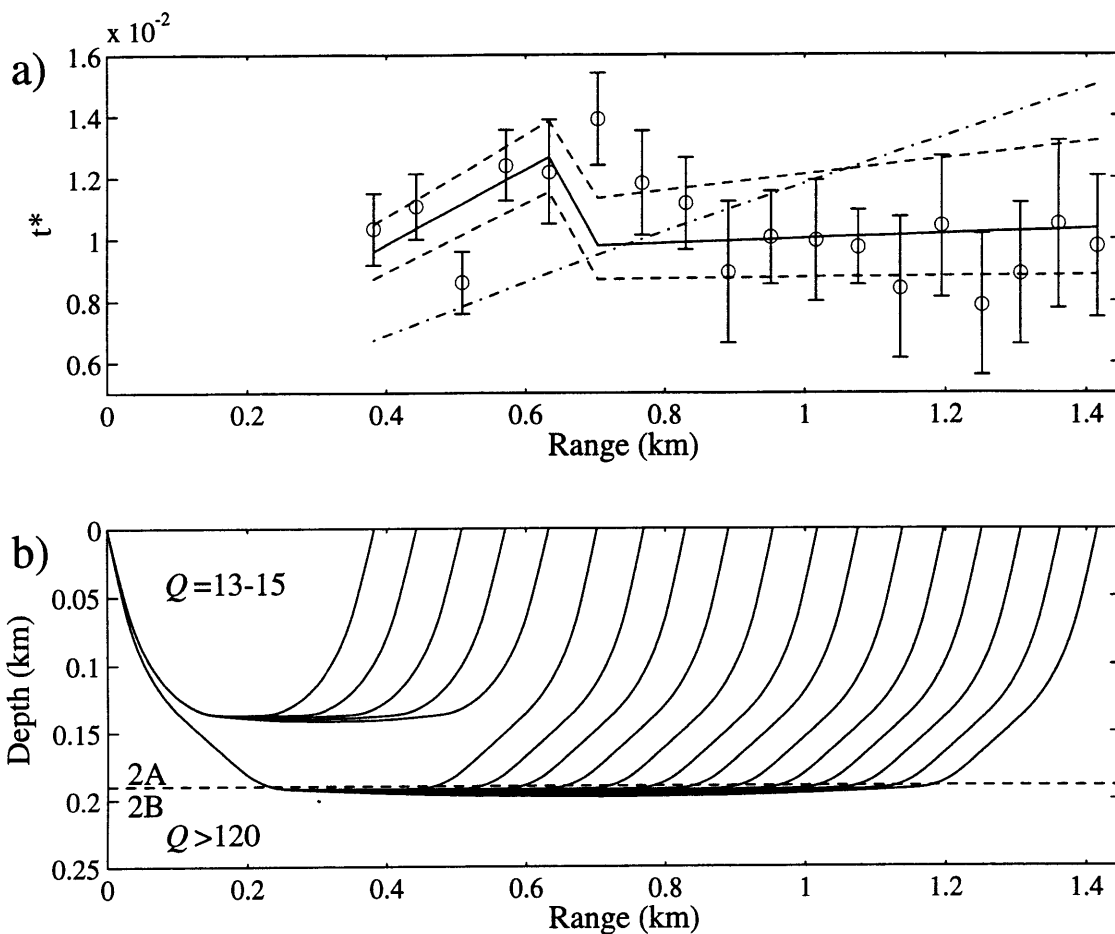
Figure 4.3. Line ON. (a) t* vs. shot range for the data (circles with 1σ error bars) and calculated for the preferred two-layer attenuation model (solid line). The calculated t* values for the best-fitting constant-Q model is shown by the dash-dot line. The dashed lines indicate the t* values calculated for the error bounds on the preferred attenuation model. Note that the t* values are to first-order constant vs. range. (b) Raypaths calculated from the velocity model of *Christeson et al.* [submitted] for the t* values in Figure 4.3a. Also indicated are the modeled Q values for layers 2A and 2B.
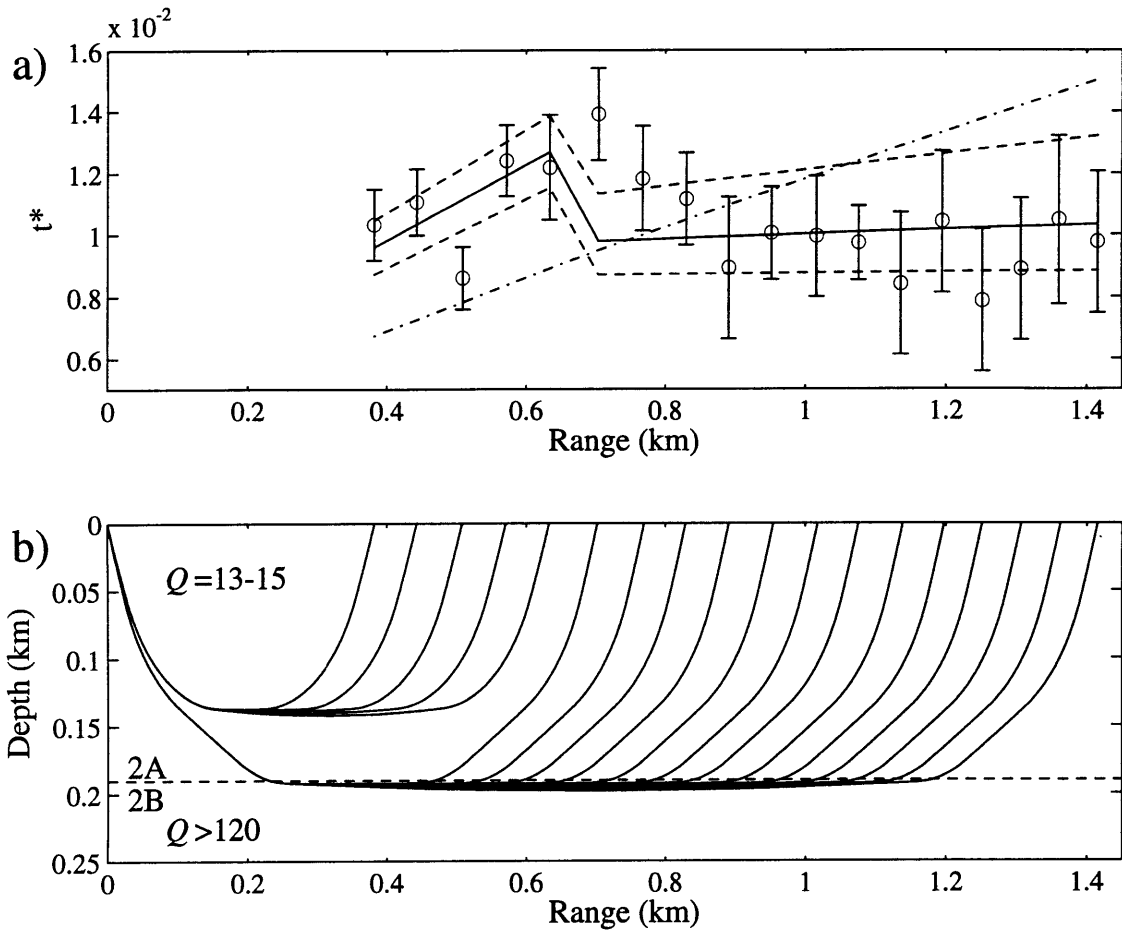
Figure 4.4. Line 20W. (a) t* vs. shot range for the data (circles with 1σ error bars) and calculated for the best-fitting constant-Q model (solid line). The dashed lines indicate the t* values calculated for the error bounds on the attenuation model. (b) Raypaths calculated from the velocity model of *Christeson et al.* [submitted] for the t* values in Figure 4.3a. Also indicated are the 2A/2B boundary and the modeled Q value for layer 2A.

119
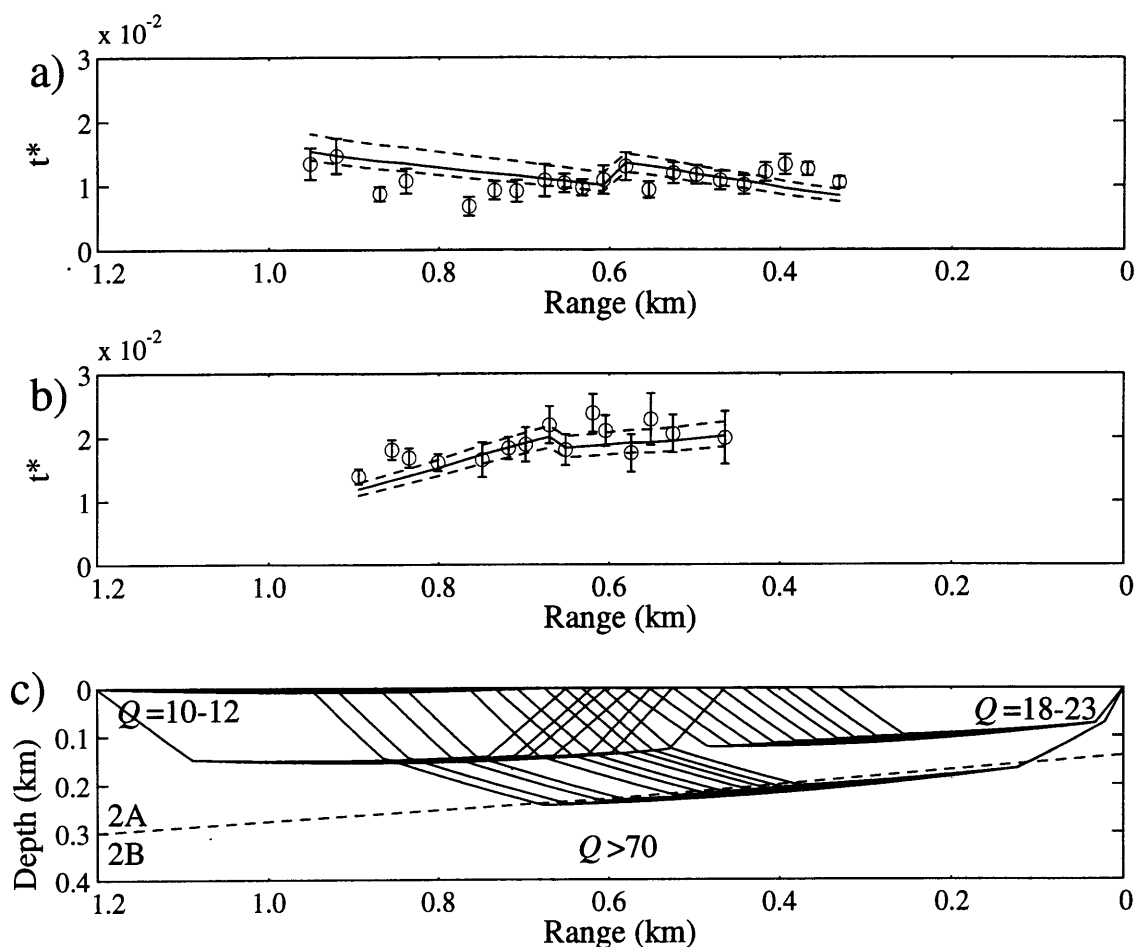
Figure 4.5. Line 0-20R. (a) t* vs. shot range for the data (circles with 1σ error bars) recorded by the eastern receiver and for the preferred attenuation model (solid line). Range is measured from the eastern receiver, which is located on the rise axis. Dashed lines indicate the t* values calculated for the error bounds on the preferred attenuation model. (b) As for Figure 4.5a, except for the western receiver which is located ~1.2 km off-axis. (c) One possible attenuation model for Line 0-20R. The model consists of two layers, with the boundary at the seismic 2A/2B boundary. The zero range is located at the eastern receiver on the rise axis. Q^{-1} in layer 2A was allowed to vary linearly between x=0 and x=1.2. Q in layer 2A decreases from ~18-23 for the zero-age crust at x=0 to ~10-12 for the ~20,000 year old crust located ~1.2 km to the west. Layer 2B was constrained to have a constant attenuation; the best-fitting value was a Q >70. Also plotted are the raypaths from the velocity model of *Christeson et al.* [submitted].

CHAPTER 5

SEISMIC TECHNIQUES AND RESOLUTION IN THE SHALLOW CRUST

Introduction

On-bottom seismic refraction measurements provide high-resolution determinations of shallow crustal velocities, but over only a limited area. In contrast, multi-channel seismic (MCS) profiles are ideal for mapping regional variability in structure, but require knowledge of crustal velocities to be properly interpreted. *Harding et al.* [1993] reprocessed five cross-axis MCS lines in the 9°30'N region of the EPR (Figure 1.2), in order to image lateral changes in depth to a shallow event, termed the layer 2A reflection. The authors argue that if layer 2A consists of a surficial low-velocity layer overlying a high-gradient region, then the shallow event is formed by refracted energy that has turned in the steep gradient at the base of layer 2A, and corresponds in depth to the layer 2A/2B boundary. On four of the cross-axis MCS lines, the depth to the reflector is a minimum at the axial summit caldera, and deepens substantially within 1-2 km of the axis. No further systematic increase in depth is observed. These results are similar to those obtained from modeling the on-bottom refraction data, except that the average depth to the reflector outside of the neovolcanic zone is 440-560 m [*Harding et al.*, 1993], significantly greater than the 300-390 m layer 2A thickness determined from the NOBEL experiments (Table 3.1). The depth to a shallow event imaged in the one cross-axis wide-angle profile (WAP) shot in the region is 200-300 m [*Vera and Diebold*, 1993], which is substantially less than the 440-560 m depth from MCS data, and is slightly less than the 300-390 m depth from the NOBEL experiments. Either the shallow event in the MCS profiles is imaged 100-200 m deeper than the layer 2A/2B boundary, perhaps because layer 2A structure is more complex than the simple structure assumed by the authors, or layer 2A is anomalously thin

at the locations of the WAP and on-bottom seismic refraction experiments. The distinction between these two hypotheses is important, because the layer 2A/2B boundary has been interpreted to mark the top of the sheeted dike complex, and changes in layer 2A thickness provide valuable information about temporal and spatial variability of volcanic emplacement processes.

In this paper, we predict quantitatively MCS and wide-angle experiments over two plausible velocity models. Layer 2A in the first model (which we will refer to as the 'gradient' model) consists of a surficial low-velocity layer overlying a steep gradient, similar to the velocity structure assumed by *Harding et al.* [1993] in their interpretation of reprocessed MCS data. The structure of layer 2A in the second model (which we will refer to as the 'step' model) is more complex, and is based on the high-resolution velocity models constructed from the on-bottom refraction experiments. We conclude that the accuracy of correlating the shallow event observed in MCS and WAP data with the layer 2A/2B boundary is strongly dependent on the structure within layer 2A, and does not depend significantly on the different source-receiver geometries of the MCS and WAP techniques. In order to obtain independent estimates of layer 2A thickness, we also analyze conventional airgun refraction data from the 9°30'N region. These results suggest that the differences in depth to the shallow reflector imaged in the MCS and WAP data are not due to structure within layer 2A, but represent true variability in layer 2A thickness of several hundred meters over distances of less than 10 km.

Reflectivity Modeling

Plotted in Figure 5.1 are velocity profiles of the gradient and step models chosen as contrasting representations of typical off-axis crust. The step model, with a layer 2A thickness of 310 m, is taken from Figure 3.13 at a range of 2 km. To create the gradient model, we kept the thickness of the surficial low-velocity layer identical to that of the step model, and simplified the underlying structure to produce velocity gradients similar to

those assumed by *Harding et al.* [1993]. Synthetic seismograms were calculated from the two models with the reflectivity technique [*Fuchs and Müller*, 1971], using the code described in detail in *Mallick and Frazer* [1987]. We used a Poisson's ratio of 0.48 and a Q_p of 25 in layer 2A, and a Poisson's ratio of 0.3 and a Q_p of 500 in layer 2B. Q_s was set to $0.5Q_p$, and densities were computed from the relationship for basalts of *Christensen and Shaw* [1970], $\rho = 1.85 + 0.165V_p$. The source-time function was derived from a near-offset stack of the along-axis MCS data described in *Kent et al.* [1990]. A water depth of 2800 m was used, with shots and receivers located at the sea surface.

The synthetic seismograms for the gradient model are plotted in Figure 5.2a. Travel time curves calculated from ray-tracing predict a triplication approximately 0.1 sec behind the water wave at a range of ~2.5 km (Figure 5.2b), formed by the sharp change in velocity gradient at the base of layer 2A (Figure 5.1). This caustic is clearly observed in the synthetic data, with large amplitudes in the range window 2.5-4.0 km associated with energy turning within the steep gradient at the base of layer 2A. The low amplitude event emerging from the water wave arrival at ~3.5 km is energy refracted through layer 2B. A second triplication is apparent in the synthetic data at a range of 3.5-5.0 km. Ray-tracing suggests that this event is a multiple of the first triplication, with energy traveling twice through layer 2A.

In comparison, the synthetic seismograms for the step model are plotted in Figure 5.3. The events are not as clearly delineated as in Figure 5.2, due to the more complicated shallow velocity structure. Ray-tracing indicates that the caustic is formed by a combination of energy turning at the base of each of the two high-gradient regions within layer 2A. The onset of the triplication in the synthetic data is not as sharp as for the gradient model, and there appears to be pre-critical energy in the 0-2.5 km range window. Similar to Figure 5.2, a multiple associated with the caustic and a low-amplitude layer 2B refraction event are also observed.

Harding et al. [1993] used constant velocity panels to select stacking velocities that best imaged the layer 2A reflection. The identical process was performed on the synthetic data, and is illustrated in Figures 5.4 and 5.5. For the gradient model, the caustic is nearly flat when a normal moveout (NMO) velocity of 1600 m/s is applied, and thus this stacking velocity produces a large amplitude layer 2A reflection (Figure 5.4c). The caustic is not flattened for lower or higher NMO velocities, and consequently the event is not enhanced at these velocities. The calculated rms velocity to the base of layer 2A is 1605 m/s, virtually identical to the chosen stacking velocity. *Harding et al.* [1993] argue that although the shallow event is not a true reflection, it will be located at a travel time equivalent to the vertical incidence two-way travel time (TWTT) to the base of layer 2A. This is true for the gradient model, as the TWTT of the shallow event, for a stacking velocity of 1600 m/s, is nearly identical to the TWTT to the layer 2A/2B boundary (Figure 5.4c). For the step model, the amplitude of the layer 2A reflector is greatest for a stacking velocity of 1550 m/s, and does not correspond with the base of layer 2A (Figure 5.5b). Instead, the TWTT to the shallow event is 3.86 sec, and correlates with the TWTT to the base of the upper high-gradient layer. A stacking velocity of 1650 m/s does place the event at the layer 2A/2B horizon (Figure 5.5d), but produces an amplitude which is significantly less than for a 1550 m/s stacking velocity. The waveforms in the final stacked sections for the two models are similar, with the layer 2A reflector phase shifted with respect to the water wave (Figure 5.6). If the shallow event is interpreted to correspond with depth to the layer 2A/2B boundary, then the calculated layer 2A thickness is correct for the gradient model, but too thin for the step model.

The velocity models for the on-bottom refraction experiments located within the axial summit caldera also indicate layer 2A structure more complex than a surficial low-velocity layer overlying a steep gradient region. Therefore, we carried out an identical analysis of on-axis gradient and step models. The step model is from Figure 3.13, at a range of 0 km. The gradient model is identical to the step model, except that the transition from the

surficial low-velocity layer to the top of layer 2B takes the form of a single steep velocity gradient (Figure 5.7). Layer 2A thickness for both models is 150 m.

Plotted in Figure 5.8 are synthetic seismograms calculated by the reflectivity method for the on-axis gradient model with a water depth of 2625 m. The record section is similar to that for the off-axis gradient model (Figure 5.2), and includes a triplication associated with energy turning at the base of layer 2A. A comparison with Figure 5.2 indicates that the onset of the caustic is located closer to the water wave and at a shorter range for the on-axis gradient model than for the off-axis gradient model. In addition, more than one multiple of this event is clearly observed in the synthetic data (Figure 5.8a). The synthetic seismograms for the on-axis step model are plotted in Figure 5.9. As for the off-axis sections, the caustic is a more complicated feature for the step model than for the gradient model. The onset of the triplication is ~0.5 km closer than predicted by ray-tracing (Figure 5.9b), and is apparently associated with pre-critical energy.

A series of constant velocity panels were compared for each model, and stacking velocities chosen that produced the maximum amplitude for the shallow event. Plotted in Figure 5.10 are the final stacked sections for the two on-axis models. For both models, the layer 2A reflector is phase shifted with respect to the water wave, as previously observed for the off-axis models. For the step model, the TWTT to the reflector is located approximately halfway between the TWTTs to the base of the upper high-gradient region and the base of layer 2A. In contrast, the TWTT to the shallow event for the gradient model is almost identical to the TWTT to the layer 2A/2B boundary.

Harding et al. [1993] argue that the stacking velocity which produces the best image of the layer 2A reflection is sensitive to the range window over which the data is stacked, in part because the event is not a true reflection. In order to properly compare data sets collected with different streamer lengths or processed with different mutes, it is necessary to determine the effects the range windows used to stack the shallow event have on the resulting TWTTs. Constant velocity panels were calculated from the off-axis gradient and

step models for four different offset geometries, and stacking velocities chosen that produced the maximum amplitude for the layer 2A reflector. The final stacks are summarized in Figure 5.11. For the step model, varying the range window used to stack the reflector has little effect, and the TWTTs to the shallow event are nearly identical (Figure 5.11a-d). This is demonstrated in Figure 5.5b, where a NMO velocity of 1550 m/s flattens the caustic for offsets from 2-5 km. In contrast, varying the range window has a significant effect on the time of the layer 2A reflector for the gradient model. For offsets from 0-3.0 km, a NMO velocity of 1650 m/s flattens the caustic (Figure 5.4d) and produces the best image of the reflector. The TWTT to the shallow event using this stacking velocity is 20-30 ms greater than the TWTT to the layer 2A/2B boundary (Figure 5.11e-f), corresponding to a depth discrepancy of ~30-50 m. If greater offsets are included, a lower NMO velocity of 1600 m/s constructs the largest amplitude event (Figure 5.4c), which aligns almost exactly with the TWTT to the base of layer 2A (Figure 5.11g-h). For both the step and gradient models, including greater offsets increases the amplitude of the shallow reflector (Figure 5.11).

In summary, one-dimensional synthetic modeling indicates that the accuracy of correlating the shallow event observed in MCS and WAP data with the layer 2A/2B boundary is strongly dependent on the structure within layer 2A. If layer 2A consists of a surficial low-velocity layer overlying a steep velocity gradient (our gradient model), then there is an excellent correspondence between the TWTT to the shallow reflector and the TWTT to the base of layer 2A. However, if there is considerable structure within layer 2A (our step model), such as suggested from on-bottom refraction experiments, then the shallow event may correlate with the base of a steep gradient within layer 2A, and not with the layer 2A/2B boundary. In addition, our modeling indicates that the source-receiver geometry may effect the TWTT to the layer 2A reflector, in agreement with the results of *Harding et al.* [1993]. However, this effect is not large enough to explain the 100-200 m

discrepancy in depth to the layer 2A reflector between the WAP of *Vera and Diebold* [1993] and MCS profiles of *Harding et al.* [1993] near 9°30'N on the EPR.

Finite Difference Modeling

The two-dimensional nature of rise axis topography and layer 2A structure precludes the direct comparison of our reflectivity synthetics with field data; therefore, we have used a finite difference technique to address these effects over two-dimensional extensions of the gradient and step models (Figure 5.12). The code utilized is the ProMAX® "acoustic_fd" algorithm, a fourth order acoustic finite difference program, commercially available through Advance Geophysical Corporation. We used the reflectivity technique to estimate the validity of the finite difference results, since a primary limitation to the algorithm is the inability to model elastic and attenuation effects. Synthetic seismograms were calculated, with the reflectivity code in an acoustic mode, for the off-axis gradient and step model; the results are referred to as the acoustic gradient and acoustic step models. The principal difference between the acoustic gradient model (Figure 5.13a) and the off-axis gradient model (Figure 5.2a) is in the amplitudes of the caustic and multiples. In Figure 5.13a, the onset of the caustic and multiple are earlier, and the amplitudes greater, than in Figure 5.2a. In addition, a second multiple is clearly observed with the acoustic gradient model. The record section for the acoustic step model contains numerous high-amplitude events behind the water wave (Figure 5.13b). The caustic and multiple identified for the off-axis step model (Figure 5.3a) match two of these events in travel time, with the other arrivals apparently formed by pegleg multiples both within the surficial low-velocity layer and the entire layer 2A region. Although the synthetic seismograms for the acoustic models (Figure 5.13) are different in amplitude character from those for the off-axis models (Figure 5.2 and Figure 5.3), the location and shape of the caustic are similar. For each model, we produced constant velocity panels, and chose a stacking velocity that maximized

128

the amplitude of the layer 2A reflector. These velocities were identical to those chosen for the off-axis gradient and step models.

The finite difference method requires the source pressure and displacement field at a time shortly after explosion, and for this reason the source is often chosen to be an analytic function. In our calculations, we used a zero phase Ricker wavelet with a center frequency of 20 Hz to approximate the source-time function of a typical MCS airgun array. Figure 5.14 shows a comparison of stacked sections for the acoustic step model calculated with the Ricker wavelet source (Figure 5.14a) and for the off-axis step model (Figure 5.14b). Although the waveforms differ for the two sources, the time of the shallow event is nearly identical. A comparison of stacked sections for the acoustic (Figure 5.14c) and off-axis gradient (Figure 5.14d) models yields similar results. These comparisons indicate that use of an acoustic approximation and Ricker wavelet source will have only a minor effect on the travel time to the stacked layer 2A reflector.

The two-dimensional gradient and step models are shown in Figure 5.12. The seafloor topography is taken from a Sea Beam profile across the EPR near 9°30'N. Layer 2A thickens from 150 m to 300 m within 1 km of the rise axis, based on the results of the cross-axis NOBEL profile (Figure 3.13). We allowed minor variations in the depth to the layer 2A/2B boundary outside of the neovolcanic zone, with layer 2A thickening to 400 m at CDP 1800 (3 km west of the rise axis), and thinning to 200 m at CDP 1720 (4 km west of the rise axis). Observations at Hess Deep [*Francheteau et al.*, 1992] suggest that the greatest variability in shallow structure occurs within the transition zone, which we interpret to be the steep gradient layer in the gradient model, and the basal gradient in the step model. Therefore, the layer 2A thickness variations were at the expense or gain of these regions in our models. The velocity structure extends to the east and west of the models in Figure 5.12, with the base of layer 2A at a constant 300 m below the seafloor.

For each model, 361 shot gathers were calculated at 25 m spacing, from CDP 1360 (8 km west of the rise axis) to CDP 2080 (1 km east of the rise axis). The model grid spacing

was 7.5 m, and the gridtime step was 0.79 ms. To save computational time, the synthetic experiment was conducted 500 m above the rise axis. Shot and receiver gathers were subsequently forward extrapolated to the sea surface (2100 m) using a phase shift operator in FK space [*Gazdag*, 1978]. The forward extrapolation process was carried out in two-steps: (1) the receiver wavefield was upward continued to the sea surface through migration of individual shot gathers, (2) the source wavefield was then upward continued to the sea surface through migration of individual common receiver gathers (Figure 5.15). Finally, the data were gathered into common-mid-point (CMP) bins 12.5 m apart which produced a nominal CMP fold of 80.

Constant velocity panels were created for the gradient and step models, stacking velocities chosen every 200 m, and stacked sections produced (Figure 5.16a and Figure 5.17a). These sections were FK migrated [*Stolt*, 1978], with a constant velocity of 1500 m/s (Figure 5.16b and Figure 5.17b). The more cpu intensive finite difference migration, with correct layer 2A rms velocities, produced nearly identical results. For the gradient model, the reflector closely follows the base of layer 2A, as predicted by the one-dimensional reflectivity modeling (Figure 5.16a). Over most of the stacked section, the shallow event is within 5-10 ms of the actual travel time to the layer 2A/2B boundary, with a maximum deviation of 25 ms. Stacking velocities for the reflector varied from 1575-1675 m/s outside of the neovolcanic zone, and were within 25 m/s of the rms velocities to the base of layer 2A. The stacking velocity at the rise axis was 1550 m/s, almost identical to the calculated rms velocity of 1545 m/s. The event approximately 100 ms after the layer 2A reflector is a multiple, and is larger in amplitude than predicted from reflectivity modeling (Figure 5.14) because the finite difference calculations do not account for attenuation effects. The stacked and migrated sections for the step model are plotted in Figure 5.17. As demonstrated previously by reflectivity modeling, the shallow reflector images structure within layer 2A rather than the layer 2A/2B boundary. There is no expression in the migrated section of the lateral thickness variations in the basal gradient

region. The stacking velocity varied from 1550-1575 m/s, similar to the rms velocity to the base of the upper high-gradient region, which averaged 1545 m/s.

In addition to processing the data with a 4.0 km aperture receiver array, we did identical analyses for a 2.675 km aperture streamer length, similar to the experimental geometry used to collect the MCS data of *Harding et al.* [1993]. The best image for the gradient model was created with stacking velocities that were ~25 m/s greater than for the larger offset data, resulting in an increased TWTT to the layer 2A reflector. This difference converts to an approximate 30-50 m increase in calculated layer 2A thickness. For the step model, a shorter streamer length had a negligible effect.

In summary, the results from two-dimensional finite-difference calculations agree with previous conclusions based on reflectivity modeling. Synthetic modeling indicates that the accuracy of correlating the shallow event observed in MCS and WAP data with the layer 2A/2B boundary is strongly dependent on the structure within layer 2A, and does not depend significantly on the different source-receiver geometries of the MCS and WAP techniques. Therefore, the difference in layer 2A reflector depth between the WAP and MCS data may represent either true layer 2A thickness changes in the 9°30'N region, or variability in gradient structure within the shallow crust. In the following section, we examine conventional airgun refraction profiles which can provide the independent estimates of layer 2A thickness necessary to distinguish between these two possibilities.

Conventional Airgun Data

During the tomography experiment on the EPR near 9°30'N [*Toomey et al.*, 1990], several airgun lines were shot over young crust close to the locations of our on-bottom seismic refraction experiments (Figure 5.19). The purpose of these profiles was to provide the close shot spacing needed for determination of shallow crustal structure. The source consisted of four guns (2 x 550 cu. in. and 2 x 300 cu. in.) totaling 1700 cu. in. in volume. The receivers were seven Woods Hole Oceanographic Institution analog ocean

bottom hydrophones (OBHs), and were located by *Toomey* [1990] using an inversion of direct water-wave arrival time and navigational data [*Creager and Dorman*, 1982].

The data recorded by the OBHs was converted from analog to digital format, and shot-receiver ranges were computed from the direct water wave arrival. Examples of the data quality are shown in Figure 5.20; there is good signal-to-noise ratios out to ranges of ~6-8 km. Travel time picks were made for all first arrivals, with picking errors approximately ±20 ms. Finally, corrections for topography were made using the water path correction method [*Purdy*, 1982], which uses a cubic spline fit to the bathymetry profile beneath the shooting line to compute ray entry points. The uncertainty in these corrections is estimated to be approximately ±10 ms.

Plotted in Figure 5.21 are the first arrival travel times, corrected for topography, for an on-axis (Figure 5.21a) and off-axis profile (Figure 5.21b and 5.21c). On the basis of the on-bottom experiment results, the thickness of layer 2A should be greater, and the first arrival travel times systematically later, along airgun lines A and C as compared to line B. This is indeed observed in the data, with the travel time picks for the off-axis profiles ~50-150 ms later than for the on-axis profile (Figure 5.21). Also plotted in Figure 5.21 are the first arrival travel times for typical on-bottom refraction experiments. The major difference between the two data sets is the range at which arrivals are observed emerging ahead of the water wave; for the airgun shots this range is 1-2 km, and thus none of the first arrival travel time picks are associated with energy turning within layer 2A. Additionally, the scatter in the travel times for the airgun picks is greater than for the NOBEL picks.

The primary purpose for analyzing the conventional airgun data is to estimate regional variations in shallow structure. The uppermost velocity structure will be poorly constrained, because energy turning within layer 2A arrives after the water wave onset. However, several of the receivers, both on-axis and off-axis, recorded airgun data that is in excellent agreement with the NOBEL data (Figures 5.21a and 5.21b), suggesting that the structure at these sites is consistent with that modeled from the on-bottom refraction

experiments. For each OBH, we used ray-tracing to fit the first arrival travel times from the airgun profiles, using a starting model based on the NOBEL results (Table 3.1). We then varied the thickness of layer 2A to match the travel time picks. Several velocity models could successfully fit the first arrival travel times, each with slightly different structure within layer 2A. Therefore our strategy, when allowed by the data, was to alter equally the thickness of both the surficial low-velocity layer and the ~4 km/s low-gradient region (Figures 3.7 and 3.13). No attempt was made to match the amplitude patterns found in the data.

For on-axis profile B (Figure 5.19), Line ON was used as the starting model. There is excellent agreement between the first arrival times of Line ON and the airgun shots to OBH 5 (Figure 5.21a) and OBH 3; thus, only minor thickness adjustments were needed to match the observed data. We estimate layer 2A thicknesses of 180 m and 150 m near OBH 5 and OBH 3, respectively, similar to the measurements in the region from on-bottom experiments (Figure 5.22a). For off-axis profile A, there is good correspondence between the travel time picks for OBH 1 and Line 20W (Figure 5.21b), suggesting a 340 m thick layer 2A. However, the shots recorded by OBH 2 have first arrival times that are ~50-80 ms later than for OBH 1 (Figure 5.21c), indicating two-dimensional structure along the profile. For each receiver, a one-dimensional velocity model was obtained using Line 20W as a starting model. Layer 2A thicknesses of 340 m and 490 m matched the first arrival travel times corresponding to the shots recorded by OBH 1 and OBH 2, respectively. From these models a two-dimensional model for the profile was produced, and subsequently modified using ray-tracing [Luetgert, 1988]. A thickening of layer 2A from 310 m at OBH 1 to 490 m at OBH 2 provides the best fit to the data (Figure 5.23).

Only one OBH recorded the shots from profile C (Figure 5.19), so a two-dimensional model along the profile is not feasible. However, the analysis of profile A suggests that one-dimensional modeling adequately represents the shallow structure near each receiver, as raypaths primarily sample upper crust within 1-2 km of each receiver (Figure 5.23).

Since shots both north and south of OBH 7 were recorded (Figure 5.19), a one-dimensional model was fit to each data set. The average layer 2A thickness of the two models is 350 m. Three OBHs recorded the shots from cross-axis profile D (Figure 5.19), and thus a two-dimensional model along the line is possible. However, the spacing of the receivers is insufficient to constrain the rapid thickening of layer 2A known to occur near the axial summit caldera (ASC). Therefore, one-dimensional models were fit to the first arrival travel times corresponding to the shots east and west of OBH 4 and OBH 6, and layer 2A thicknesses were estimated for each receiver (Figure 5.22a).

In most respects, the results obtained from analysis of the airgun data are consistent with the NOBEL experiments (Figure 5.22a). Near OBHs 3 and 5, layer 2A thicknesses of 150-180 m are estimated, compatible with the models for Lines 0N and 0S (130-180 m). Likewise, the depth to the base of layer 2A for OBHs 1 and 7 (310-350 m) and the off-axis NOBEL lines (300-390 m) is similar. In contrast, a thicker layer 2A (490-580 m) is estimated for OBHs 2, 4, and 6.

Discussion

The region of the fast-spreading EPR near 9°30'N provides an excellent opportunity to compare the shallow structure determined from high-resolution on-bottom experiments with the layer 2A reflector imaged along MCS profiles. In addition, the dense seismic coverage in the area (Figure 6.24) allows the estimation of lateral changes in layer 2A thickness, which can be interpreted in terms of temporal and spatial variability in the volcanic emplacement process. According to the NOBEL profiles, the thickness of layer 2A increases from ~130 m over zero-age crust to ~300-390 m within 1 km of the rise axis (Figure 5.24 and Table 3.1). The shallow event imaged on nearby MCS line 31 exhibits similar behavior (Figure 5.25), with the depth to the layer 2A reflection increasing from ~175 m at the ASC to ~275-325 m at a range of 1 km from the ASC [*Harding et al.*, 1993]. The close correlation between the depth to the base of layer 2A from the on-bottom profiles

and the depth to the shallow event observed on the MCS line indicates that the reflector is probably following the layer 2A/2B boundary, and not structure internal to layer 2A. At no location is the reflector as shallow as 150 m, the average depth predicted from the step-like features modeled within layer 2A from the NOBEL lines. However, the layer 2A event on MCS profile 31 is unusual in that it has two distinct minima in depth at the rise axis, and remains shallow over a total width of 3 km [*Harding et al.*, 1993] (Figure 5.25). It is possible that one of the depth minima does not represent a true thinning of layer 2A, but instead a lateral change in gradient structure. The model for the on-bottom refraction experiment shot 6 km west of the rise axis includes a 310 m thick layer 2A and a step-like velocity structure, whereas a reflector is imaged at ~400 m depth at this same range from the rise axis on MCS line 31. This indicates that there is both a change in gradient structure and a 100 m change in layer 2A thickness over a distance of 1-2 km. Thickness variations of this amplitude and wavelength are compatible with observed changes in depth to the shallow reflector along the MCS profile.

The comparison of results from on-bottom refraction experiments and an adjacent MCS line in this area suggests that a correlation can be made between the depth to a prominent shallow reflector and the base of layer 2A. Summarized in Figure 5.24a are the average layer 2A reflection depths in the 9°30'N region of the EPR from four cross-axis MCS profiles and one cross-axis WAP. A thinning of layer 2A at the rise axis is observed on all lines, as predicted from the on-bottom refraction profiles, conventional airgun data, ESPs [*Vera et al*, 1990], and tomographic imaging [*Toomey et al.*, 1990] (Figure 5.24b). Off-axis, a striking feature of the data is a 150-200 m decrease in depth to the layer 2A reflector at the WAP location. The longer offsets used in stacking the WAP data can account for the minor difference in layer 2A thickness estimates at the rise axis, but for only a small portion (~30-50 m) of the 150-200 m thickness decrease observed outside of the neovolcanic zone. If the layer 2A reflector is imaging the layer 2A/2B boundary throughout the entire region, then the decrease in depth at the WAP represents a 150-200 m

thinning of layer 2A. Alternatively, the decrease in reflector depth might result from a change to a gradient structure similar to the step model, with no decrease in layer 2A thickness. Fortunately, both conventional airgun profiles and tomographic imaging have been carried out in this area (Figure 5.24b), and can provide independent estimates of layer 2A thickness.

An increase in depth to the layer 2A/2B boundary from the north to south is required by conventional airgun data in the region (Figures 5.22 and 5.23). The estimated depth to the base of layer 2A is ~300-350 m near the WAP, increasing to ~500-600 m close to the MCS line at 9°30'N (Figure 5.24). These values are slightly greater than the average reflector depths on the MCS line and WAP, but within the observed variability. In fact, the layer 2A reflection in the MCS data deepens to ~600 m in the range 7-11 km west of the rise axis [*Harding et al.*, 1993], consistent with the 580 m estimate at OBH 4 (Figure 5.25). A lateral variation in layer 2A thickness is also suggested by tomography data [*Toomey, Solomon, and Purdy*, Tomographic imaging of the shallow crustal structure of the East Pacific Rise at 9°30'N, in prep]. The image at depths from 0-600 m indicates a decrease in average velocity of 0.2 km/s from north to south on the flanks of the rise axis. Because layer 2A has a lower velocity than layer 2B, a decrease in average velocity corresponds to an increase in layer 2A thickness. The tomography data also suggest a decrease in average velocity from the east to west, which is consistent with the asymmetry in layer 2A reflection depth across the rise axis observed on both the WAP and MCS line 31 (Figure 5.24).

A 100-200 m decrease in layer 2A thickness outside of the neovolcanic zone at 9°35'N is consistent with MCS, WAP, conventional airgun refraction, and tomography data (Figure 5.24). On the cross-axis WAP near 9°35'N, the depth to the layer 2A reflector outside of the neovolcanic zone is 200-325 m [*Vera and Diebold*, 1993], in contrast to a depth of 350-700 m on four nearby MCS lines [*Harding et al.*, 1993]. In previous chapters, we have interpreted the layer 2A/2B boundary as the top of the sheeted dike

complex. Therefore, the seismic data suggest that there is approximately a 50% decrease in thickness of the extrusive layer and transition zone near 9°35'N, as compared to cross-axis profiles near 9°20'N, 9°30'N, 9°40'N, and 9°50'N (Figure 5.24). The MCS and wide-angle profiles extend to a distance of 10-15 km from the rise axis, and indicate that consistently (at least for the past 175,000-275,000 years) fewer extrusives have been emplaced in the 9°35'N area.

The rise axis at 9°35'N correlates with a deviation from axial linearity (deval) [*Toomey et al.*, 1990; *Wilcock et al.*, 1993], a decrease in anomaly amplitude of the crustal low-velocity volume [*Toomey et al.*, 1990], a narrow AMC reflector [*Kent et al.*, 1993], and an absence of hydrothermal activity [*Haymon et al.*, 1991]. These observations, and the local thinning of extrusives, are consistent with a low axial magma supply. In contrast, there is no expression in the cross-sectional area of the rise crest, an indicator of melt volume within the crust and mantle [*Macdonald and Fox*, 1988; *Scheirer and Macdonald*, 1993], of a decrease in magma chamber size near 9°35'N (Figure 5.19, 5.22). Devals are thought to form by the misalignment of magma pulses travelling laterally along the rise axis [*Macdonald et al.*, 1984; *Langmuir et al.*, 1986; *Toomey et al.*, 1990], and are expected to have a lifetime of $\leq 10^4$-10^5 yr [*Langmuir et al.*, 1986]. The 50% decrease in layer 2A thickness along the entire wide-angle profile, as compared to nearby MCS lines, would suggest that the 9°35'N deval has persisted for 175,000-275,000 yrs. The longevity of the deval is perhaps related to asymmetry in the underlying magma chamber, which is offset to the west of the rise axis south of 9°35'N [*Toomey et al.*, 1990; *Kent et al.*, 1993]. We attribute the 50% decrease in layer 2A thickness near 9°35'N with a local minimum in axial magma supply. It is interesting that there is no expression in the bathymetric data of the substantial variability in layer 2A in this region (Figures 5.19 and 5.22). We will speculate on this observation in detail in Chapter 6.

The reflectivity and finite difference analysis of shallow velocity models indicates that a correlation between the depth to the layer 2A/2B boundary and to the reflection observed in

MCS data is plausible for structure similar to the gradient model, but not the step model. Therefore, the overall agreement between layer 2A thicknesses from on-bottom and conventional airgun experiments with those determined from MCS and WAP images suggests that velocity gradients similar in character to the step model are generally not a component of the shallow crust in the 9°30'N region of the EPR. Several studies of young EPR crust have been interpreted to require a structure similar to the step model. A consistent feature in the two on-bottom seismic refraction lines located over zero-age crust within the ASC near 9°30'N (Lines 0N and 0S) is the presence of a pair of triplications at ranges of 200-300 m and 400-500 m (Figures 3.6 and 3.9); this amplitude pattern demands a step-like shallow velocity structure. There is also evidence in the zero-age ESP data located near 13°N, 9°30'N, and 17°09'S for this type of model, where the presence of precritical energy (the layer 2A reflection of *Harding et al.* [1989] and RA arrival of *Vera et al.* [1990]) is used to define a high-gradient region within layer 2A [*Harding et al.*, 1989; *Vera et al.*, 1990; *Detrick et al.*, 1993]. At locations outside of the neovolcanic zone, the amplitude of the precritical energy decreases, and the structure becomes closer in appearance to the gradient model [*Harding et al.*, 1989; *Vera et al.*, 1990; *Harding et al.*, 1993]. A reexamination of the amplitudes on the off-axis NOBEL lines reveals no clear triplication related to a sharp boundary within layer 2A on Lines 20E and 20W, although a change in gradient is needed to match the travel times. On a rise-parallel WAP located over 40,000 yr crust near 13°N, the structure varies along the profile from a gradient model to a step model [*Kappus*, 1991]. It is probable that the gradient and step models represent end-members of the velocity structures present at the EPR, with the gradients at zero-age crust similar to the step model, and the gradients outside of the neovolcanic zone closer in shape to the gradient model. The rapid thickening of layer 2A with distance from the rise axis is believed to occur, in part, through off-axis sill and extrusive emplacement [*Lonsdale*, 1977; *Macdonald and Fox*, 1988; *Fornari et al.*, 1992]. This process could also be

responsible for the destruction, within a lateral distance of 1-2 km, of the step-like structure as the crust is transported away from the ASC.

Summary of Conclusions

1. Synthetic modeling indicates that MCS studies can image the layer 2A/2B boundary, if layer 2A consists of a surficial low-velocity layer overlying a simple high-gradient region (our gradient model). However, the shallow reflector may follow structure within layer 2A, if the upper crust contains more than one high-gradient region (our step model). This implies that independent estimates of layer 2A structure are needed to properly interpret MCS images.

2. The depths to the shallow reflector imaged in MCS and WAP data in the 9-10°N region of the EPR generally correlate with estimated layer 2A thicknesses from on-bottom refraction profiles and conventional airgun refraction lines.

3. A shallow structure similar to the step model is consistent with on-bottom refraction profiles and ESPs located over zero-age EPR crust near 13°N, 9°30'N, and 17°09'S. With distance from the rise axis, this step-like structure is apparently destroyed, perhaps through the processes of off-axis sill and extrusive emplacement.

4. A 100-200 m decrease in layer 2A thickness outside of the neovolcanic zone at 9°35'N is consistent with MCS, WAP, conventional airgun refraction, and tomography data, and correlates with the location of a deval at the rise axis. A low axial magma supply at the deval location is compatible with tomography and MCS seismic data. The decrease in layer 2A thickness, interpreted to consist of the extrusive section and transition zone, suggests that the 9°35'N deval has persisted for 175,000-275,000 yrs.

References

Christensen, N.I. and G.H. Shaw, Elasticity of mafic rocks from the Mid-Atlantic Ridge, *Geophys. J. R. Astron. Soc., 20,* 271-284, 1970.

Creager, K.C. and L.M. Dorman, Location of instruments on the seafloor by joint adjustment of instrument and ship positions, *J. Geophys. Res.*, *87*, 8379-8388, 1982.

Detrick, R.S., A.J. Harding, G.M. Kent, J.A. Orcutt, J.C. Mutter and P. Buhl, Seismic structure of the southern East Pacific Rise, *Science*, *259*, 499-503, 1993.

Fornari, D.J., M.R. Perfit, R. Batiza and M.H. Edwards, Submersible transects across the East Pacific Rise crest and upper-flanks at 9°31'-32'N: 1. Observations of seafloor morphology and evidence for young volcanism off-axis (abstract), *EOS Trans. AGU*, *73* (43), Fall Supp., 525, 1992.

Francheteau, J., R. Armijo, J.L. Cheminee, R. Hekinian, P. Lonsdale and N. Blum, Dyke complex of the East Pacific Rise exposed in the walls of Hess Deep and the structure of the upper oceanic crust, *Earth Planet. Sci. Lett.*, *111*, 109-121, 1992.

Fuchs, K. and G. Müller, Computation of synthetic seismograms with the reflectivity method and comparison with observations, *Geophys. J. R. Astron. Soc.*, *23*, 417-433, 1971.

Gazdag, J., Wave-equation migration by phase shift, *Geophysics*, *49*, 1342-1351, 1978.

Harding, A.J., G.M. Kent and J.A. Orcutt, A multichannel seismic investigation of upper crustal structure at 9°N on the East Pacific Rise: Implications for crustal accretion, *J. Geophys. Res.*, *98*, 13925-13944, 1993.

Harding, A.J., J.A. Orcutt, M.E. Kappus, E.E. Vera, J.C. Mutter, P. Buhl, R.S. Detrick and T.M. Brocher, Structure of young oceanic crust at 13°N on the East Pacific Rise from expanding spread profiles, *J. Geophys. Res.*, *94*, 12163-12196, 1989.

Haymon, R.M., D.J. Fornari, M.H. Edwards, S. Carbotte, D. Wright and K. Macdonald, Hydrothermal vent distribution along the East Pacific Rise crest (9°09'-54'N) and its relationship to magmatic and tectonic processes on fast-spreading mid-ocean ridges, *Earth Planet. Sci. Lett.*, *104*, 513-534, 1991.

Kappus, M.E., A baseline for upper crustal velocity variations along the East Pacific Rise, Ph.D. Thesis, 158 pp., University of California, San Diego, 1991.

Kent, G.M., A.J. Harding and J.A. Orcutt, Evidence for a smaller magma chamber beneath the East Pacific Rise at 9°30'N, *Nature*, *344*, 650-653, 1990.

Kent, G.M., A.J. Harding and J.A. Orcutt, Distribution of magma beneath the East Pacific Rise between the Clipperton Transform and the 9°17'N deval from forward modeling of common depth point data, *J. Geophys. Res.*, *98*, 13945-13969, 1993.

Langmuir, C.H., J.F. Bender and R. Batiza, Petrological and tectonic segmentation of the East Pacific Rise, 5°30'-14°30'N, *Nature*, *322*, 422-429, 1986.

Lonsdale, P., Structural geomorphology of a fast-spreading rise crest: the East Pacific Rise near 3°25'S, *Mar. Geophys. Res.*, *3*, 251-293, 1977.

Luetgert, J.H., Users manual for RAY84/R83PLT interactive two-dimensional ray tracing/synthetic seismogram package, U.S. Geological Survey Open File Report, *88-238*, 1988.

Macdonald, K., J.-C. Sempere and P.J. Fox, East Pacific Rise from Siqueiros to Orozco fracture zones: along-strike continuity of axial neovolcanic zone and structure and evolution of overlapping spreading centers, *J. Geophys. Res.*, *89*, 6049-6069, 1984.

Macdonald, K.C. and P.J. Fox, The axial summit graben and cross-sectional shape of the East Pacific Rise as indicators of axial magma chambers and recent volcanic eruptions, *Earth Planet. Sci. Lett.*, *88*, 119-131, 1988.

Mallick, S. and L.N. Frazer, Practical aspects of reflectivity modeling, *Geophysics*, *52*, 1355-1364, 1987.

Purdy, G.M., The correction for the travel time effects of seafloor topography in the interpretation of marine seismic data, *J. Geophys. Res.*, *87*, 8389-8396, 1982.

Scheirer, D.S. and K.C. Macdonald, Variation in cross-sectional area of the axial ridge along the East Pacific Rise: evidence for the magmatic budget of a fast spreading center, *J. Geophys. Res.*, *98*, 7871-7885, 1993.

Stolt, R.H., Migration by Fourier transform, *Geophysics*, *43*, 23-48, 1978.

Toomey, D.R., G.M. Purdy, S.C. Solomon and W.S.D. Wilcock, The three-dimensional seismic velocity structure of the East Pacific Rise near latitude 9°30'N, *Nature*, *347*, 639-645, 1990.

Vera, E.E. and J.B. Diebold, Seismic imaging of oceanic layer 2A between 9°30'N and 10°N on the East Pacific Rise from two-ship wide aperture profiles, *J. Geophys. Res.*, *in press*, 1993.

Vera, E.E., J.C. Mutter, P. Buhl, J.A. Orcutt, A.J. Harding, M.E. Kappus, R.S. Detrick and T.M. Brocher, The structure of 0- to 0.2-m.y.-old oceanic crust at 9°N on the East Pacific Rise from expanded spread profiles, *J. Geophys. Res.*, *95*, 15529-15556, 1990.

Wilcock, W.S.D., D.R. Toomey, G.M. Purdy and S.C. Solomon, The renavigation of Sea Beam bathymetric data between 9°N and 10°N on the East Pacific Rise, *Mar. Geophys. Res.*, *15*, 1-12, 1993.

Figure 5.1. Compressional velocity/depth profiles for the off-axis gradient (dashed line) and step (solid line) models.

143
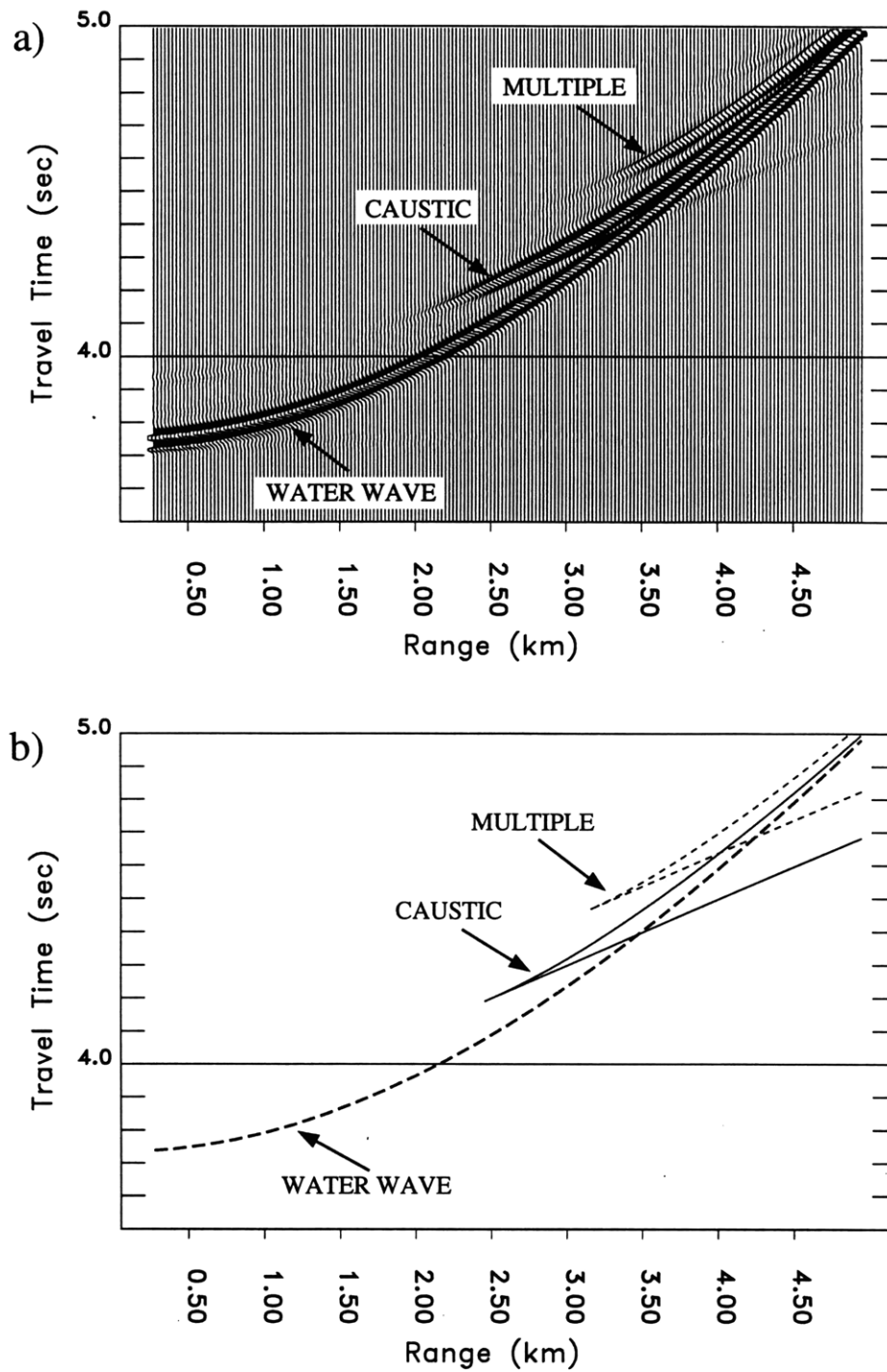
Figure 5.2. (a) Synthetic seismograms for the off-axis gradient model, for a water depth of 2800 m. For clarity, the source-time function is truncated at the onset of the bubble pulse. (b) Theoretical travel time curves, calculated from ray-tracing, for the off-axis gradient model.
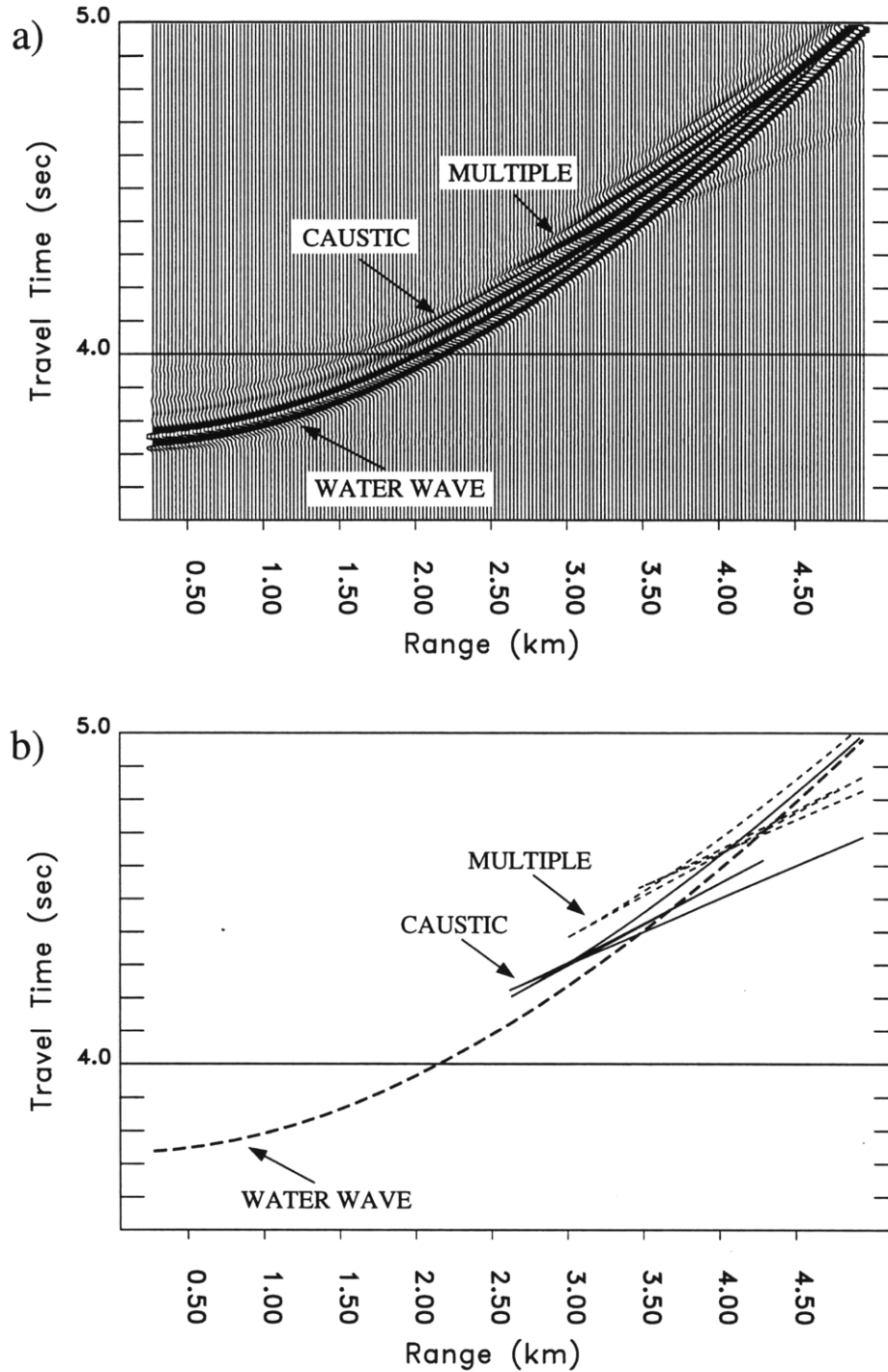
Figure 5.3. (a) Synthetic seismograms for the off-axis step model, for a water depth of 2800 m. For clarity, the source-time function is truncated at the onset of the bubble pulse. (b) Theoretical travel time curves, calculated from ray-tracing, for the off-axis step model.
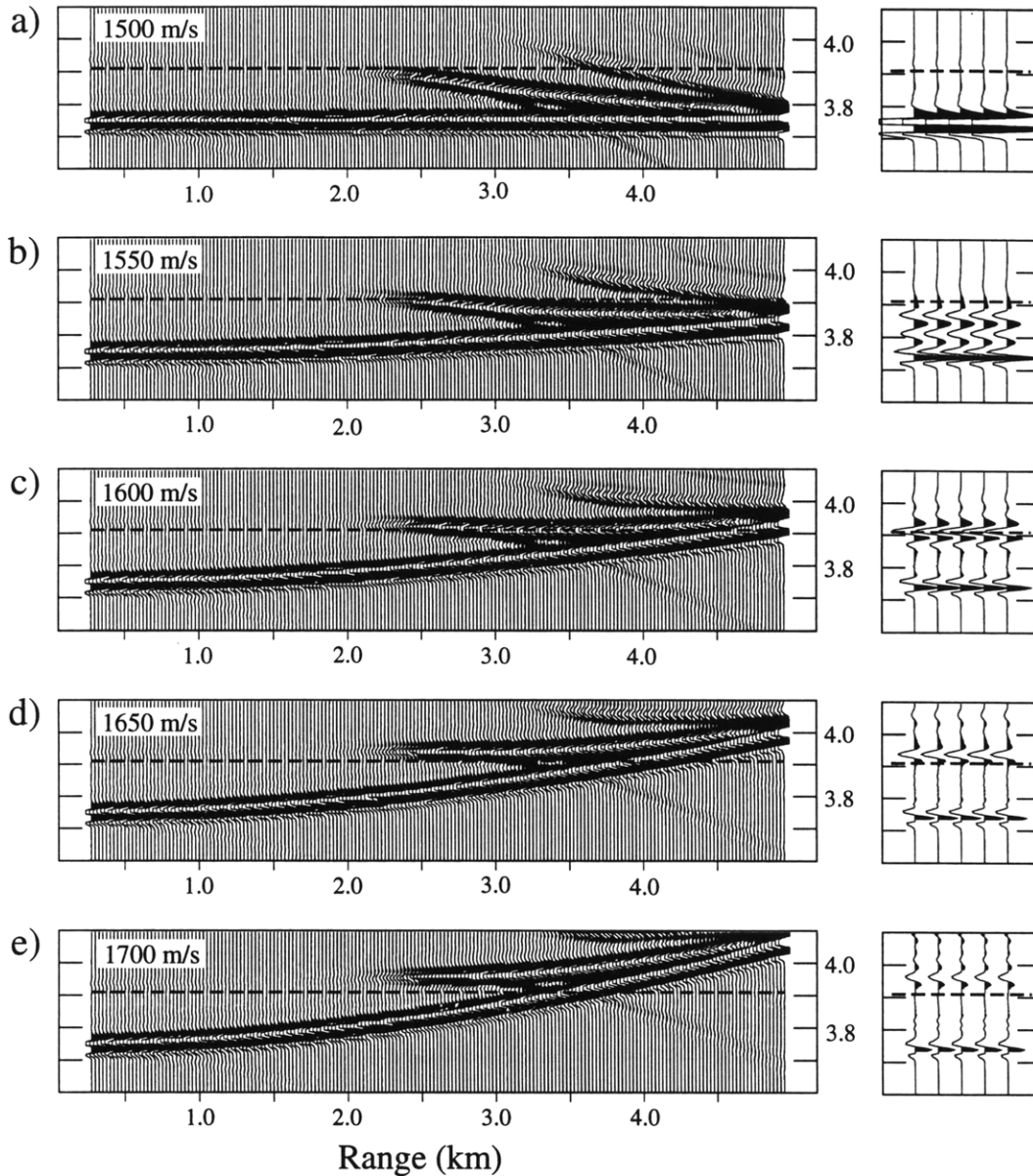
Figure 5.4. (a) Normal moveout (NMO) correction, for a single moveout velocity of 1500 m/s, applied to the synthetic data for the off-axis gradient model. The two way travel time, at vertical incidence, to the layer 2A/2B boundary is indicated by the dashed line at 3.91 sec. The plot on the right is a stack of the NMO corrected data, for ranges from 0.275-4.250 km. For clarity, the stacked trace is plotted five times. (b-e) As for Figure 5.4a, for moveout velocities of 1550 m/s, 1600 m/s, 1650 m/s, and 1700 m/s. The calculated rms velocity to the layer 2A/2B boundary is 1605 m/s. Note that the caustic stacks best at 1600 m/s, and that the negative peak of the waveform aligns almost exactly at 3.91 sec.
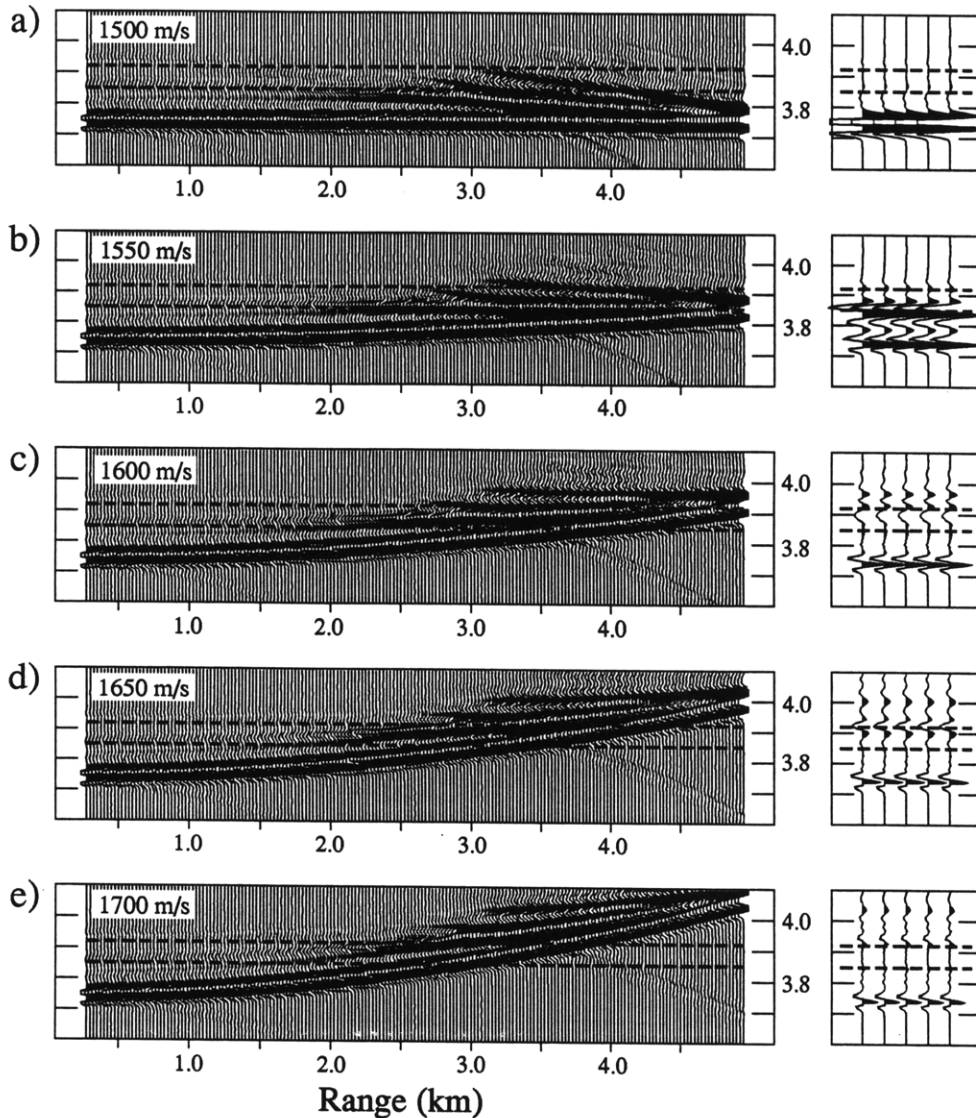
Figure 5.5. (a) Normal moveout (NMO) correction, for a single moveout velocity of 1500 m/s, applied to the synthetic data for the off-axis step model. The two way travel time, at vertical incidence, to the base of the two high-gradient regions at 150 m and 300 m (depth below seafloor) are indicated by the dashed lines at 3.85 and 3.92 sec. The plot on the right is a stack of the NMO corrected data, for ranges from 0.275-4.250 km. For clarity, the stacked trace is plotted five times. (b-e) As for Figure 5.5a, for moveout velocities of 1550 m/s, 1600 m/s, 1650 m/s, and 1700 m/s. The calculated rms velocities to the base of the two high-gradient regions are 1545 m/s and 1639 m/s. Note that the caustic stacks best at 1550 m/s, and that the negative peak of the waveform aligns at ~3.85 sec. At a moveout velocity of 1650 m/s, the waveform aligns at ~3.92 sec, but the amplitude is significantly less than for a moveout velocity of 1550 m/s.

147
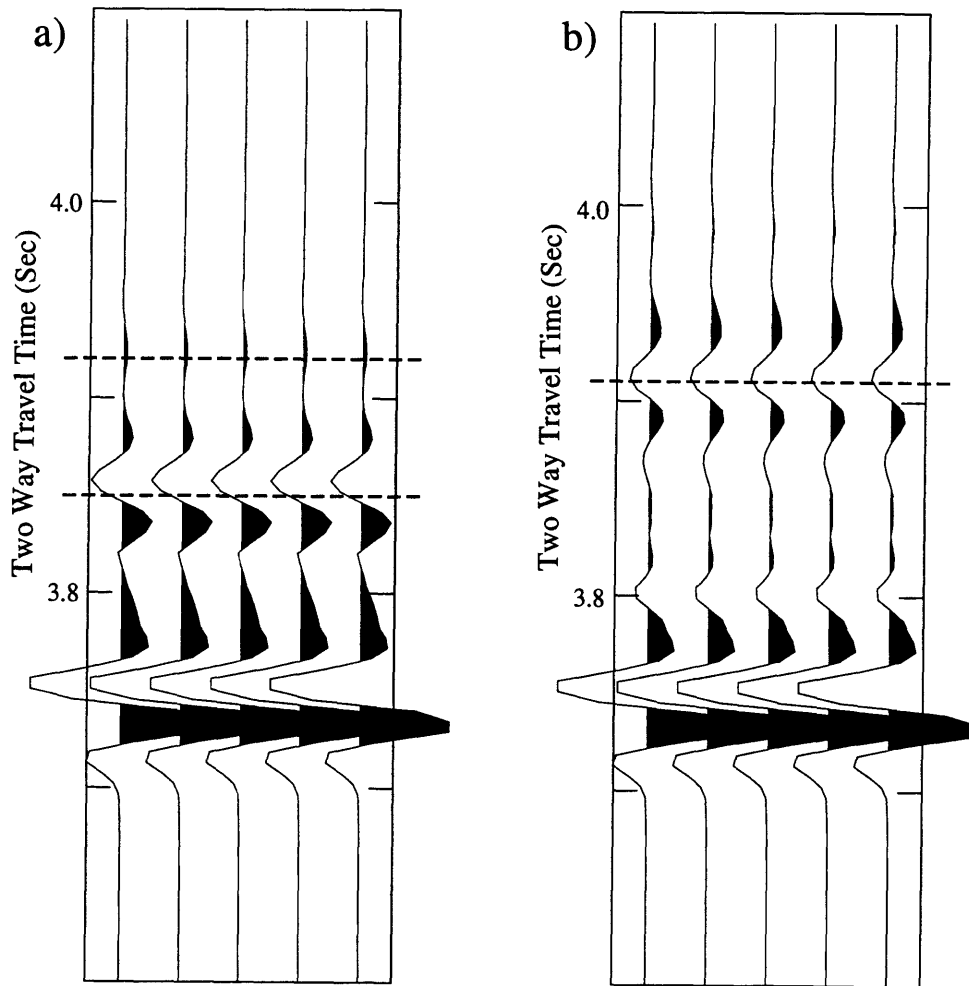
Figure 5.6. (a) Final stack of the synthetic data for the off-axis step model, for ranges from 0.275-4.250 km. A stacking velocity of 1500 m/s was used from 0-3.78 sec, and 1550 m/s from 3.82-5.0 sec. From 3.78-3.82 sec, the stacking velocity linearly increased from 1500 m/s to 1550 m/s. The dashed lines are as for Figure 5.5. Stacked sections calculated with the entire source-time function (including the bubble pulse) are nearly identical. (b) Final stack of the synthetic data for the off-axis gradient model, for ranges from 0.275-4.250 km. A stacking velocity of 1500 m/s was used from 0-3.78 sec, and 1600 m/s from 3.83-5.0 sec. From 3.78-3.83 sec, the stacking velocity linearly increased from 1500 m/s to 1600 m/s. The dashed line is as for Figure 5.4. Stacked sections calculated with the entire source-time function (including the bubble pulse) are nearly identical.
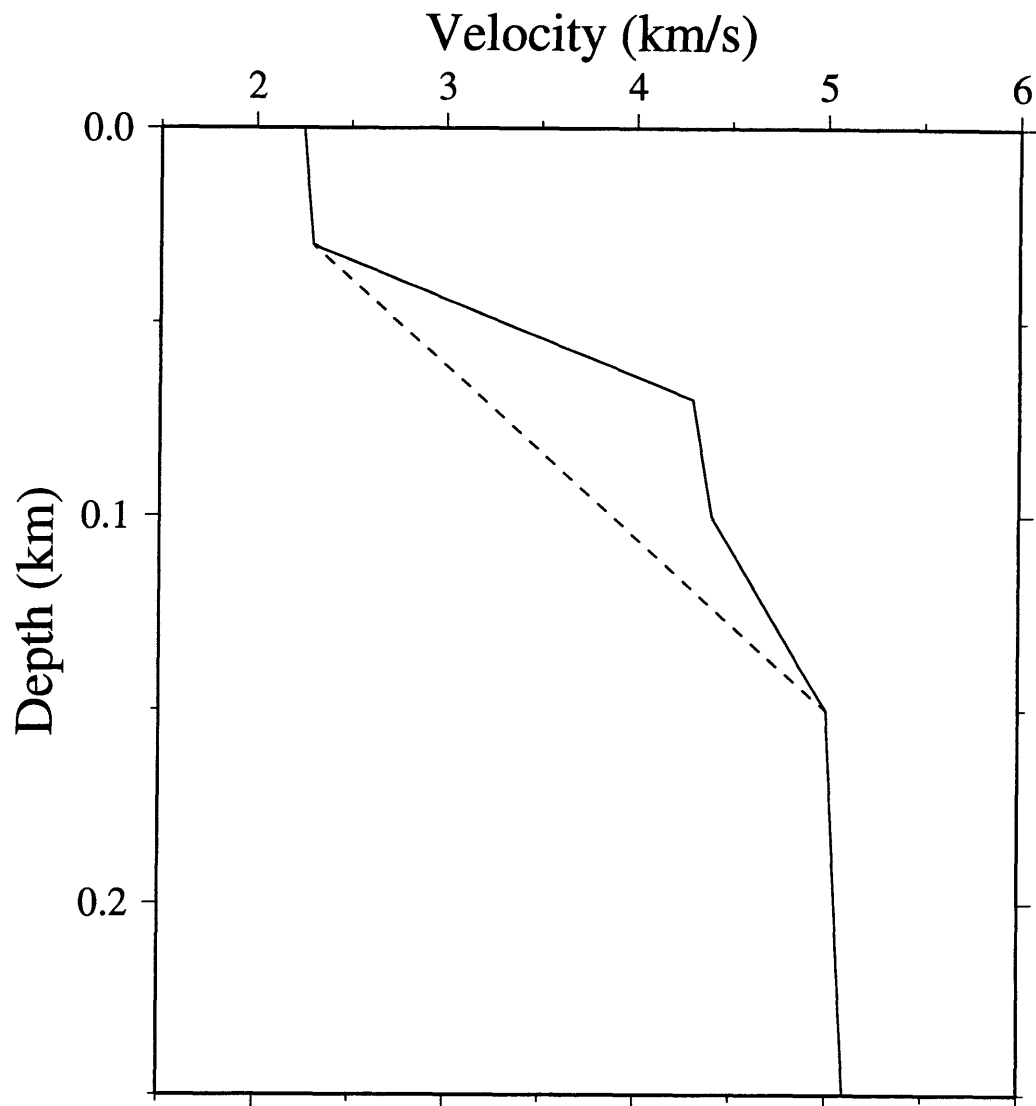
Figure 5.7. Compressional velocity/depth profiles for the on-axis gradient (dashed line) and step (solid line) models.
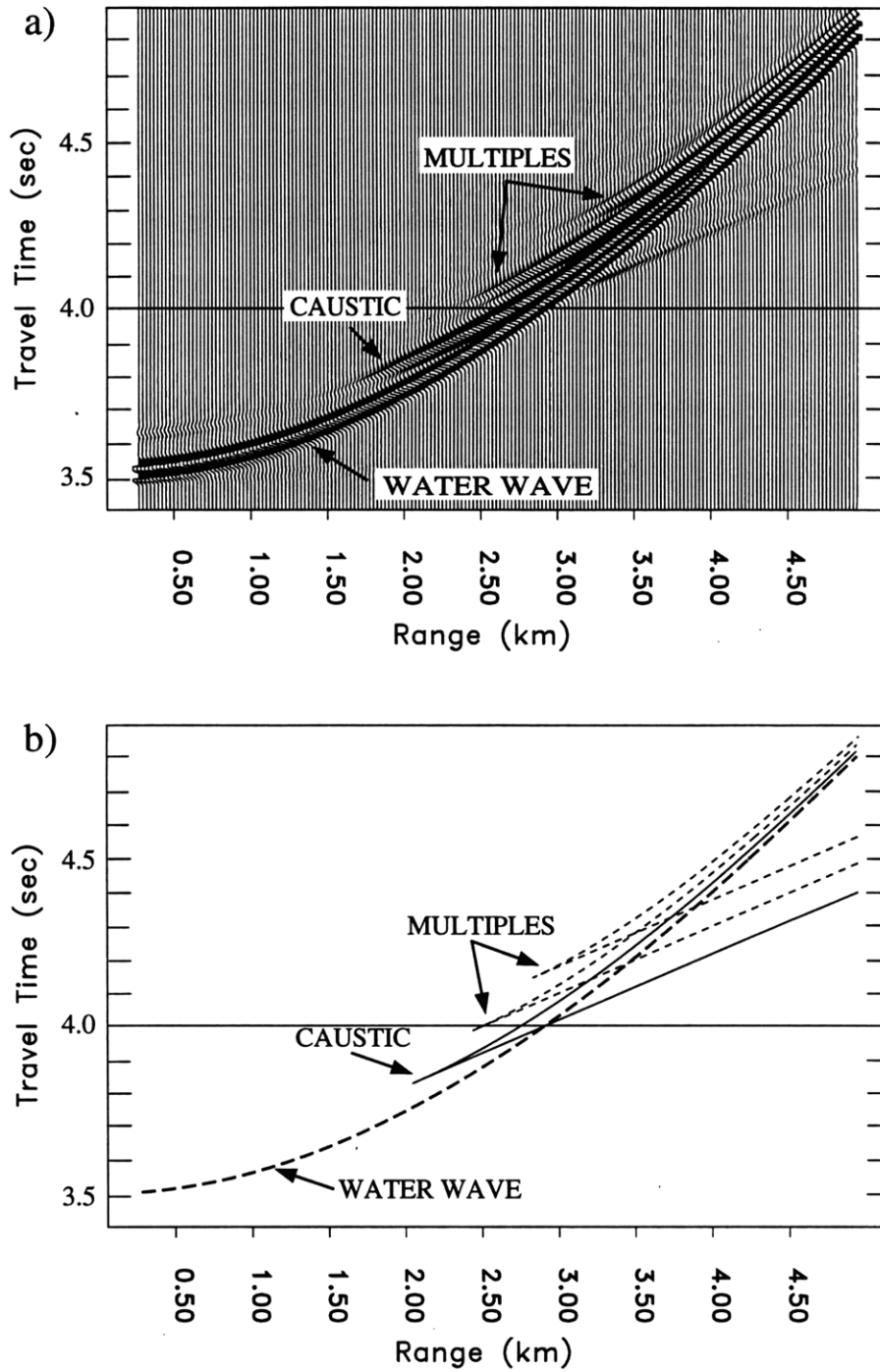
Figure 5.8. (a) Synthetic seismograms for the on-axis gradient model, for a water depth of 2625 m. For clarity, the source-time function is truncated at the onset of the bubble pulse. (b) Theoretical travel time curves, calculated from ray-tracing, for the on-axis gradient model.
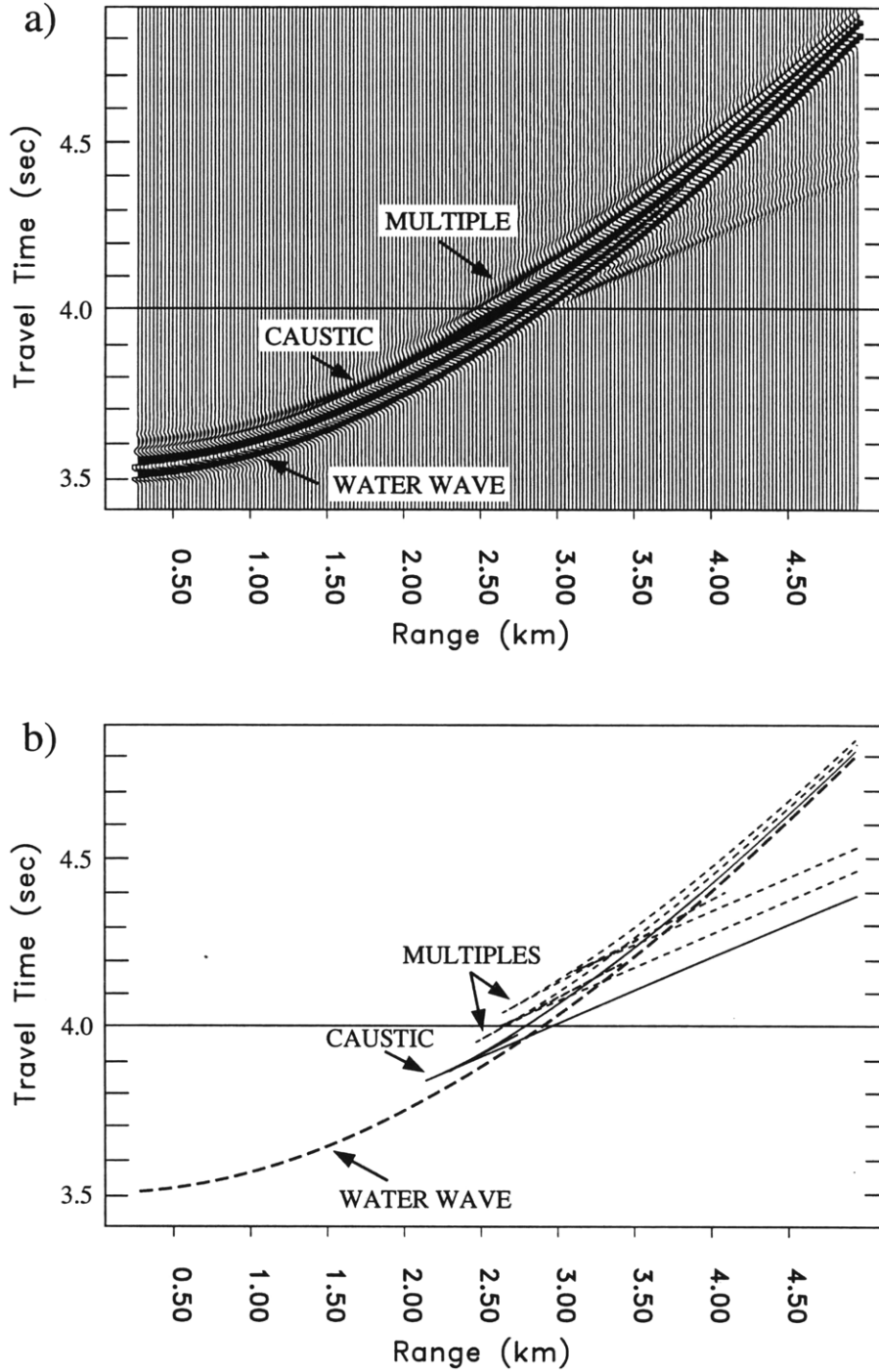
Figure 5.9. (a) Synthetic seismograms for the on-axis step model, for a water depth of 2625 m. For clarity, the source-time function is truncated at the onset of the bubble pulse. (b) Theoretical travel time curves, calculated from ray-tracing, for the on-axis step model.
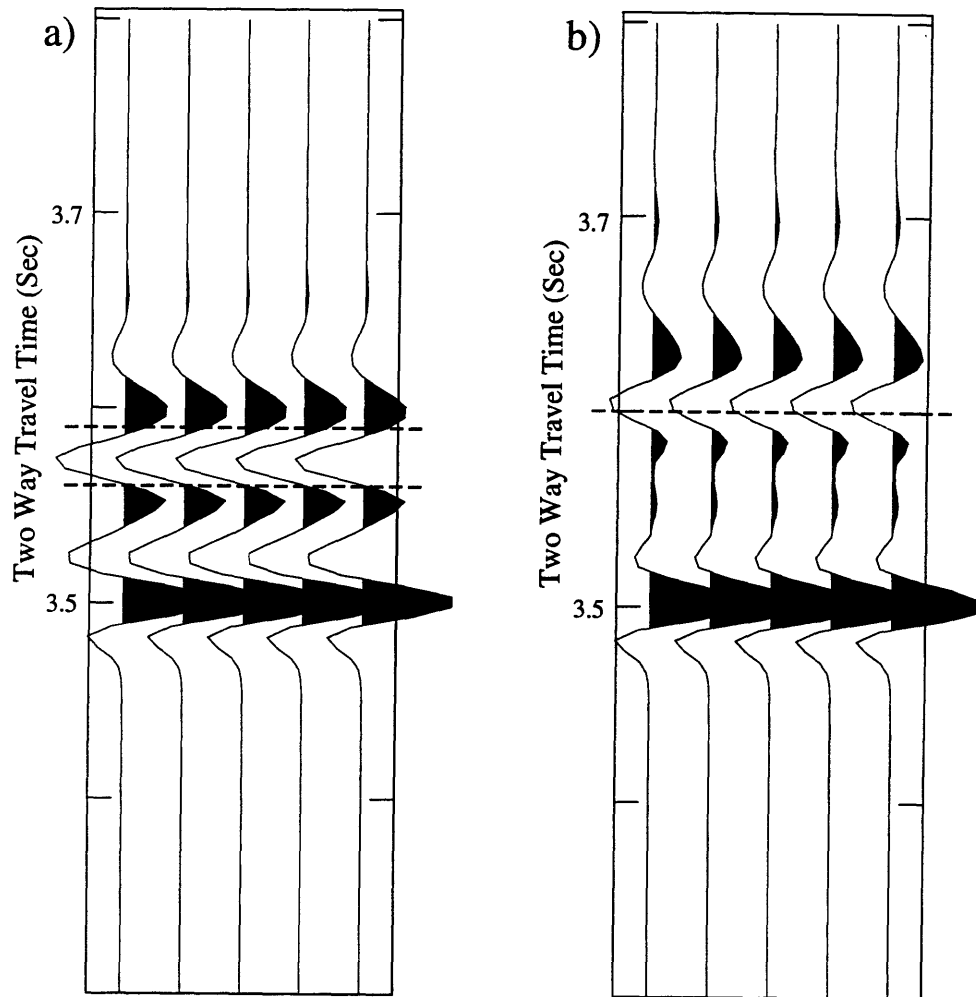
Figure 5.10. (a) Final stack of the synthetic data for the on-axis step model, for ranges from 0.275-4.250 km. A stacking velocity of 1500 m/s was used from 0-3.50 sec, and 1525 m/s from 3.54-5.0 sec. From 3.50-3.54 sec, the stacking velocity linearly increased from 1500 m/s to 1525 m/s. The two way travel time, at vertical incidence, to the base of the two high-gradient regions at 70 m and 150 m (depth below seafloor) are indicated by the dashed lines at 3.56 and 3.59 sec. Stacked sections calculated with the entire source-time function (including the bubble pulse) are nearly identical. (b) Final stack of the synthetic data for the on-axis gradient model, for ranges from 0.275-4.250 km. A stacking velocity of 1500 m/s was used from 0-3.5 sec, and 1550 m/s from 3.54-5.0 sec. From 3.50-3.54 sec, the stacking velocity linearly increased from 1500 m/s to 1600 m/s. The two way travel time, at vertical incidence, to the base of layer 2A is indicated by the dashed line at 3.60 sec. Stacked sections calculated with the entire source-time function (including the bubble pulse) are nearly identical.
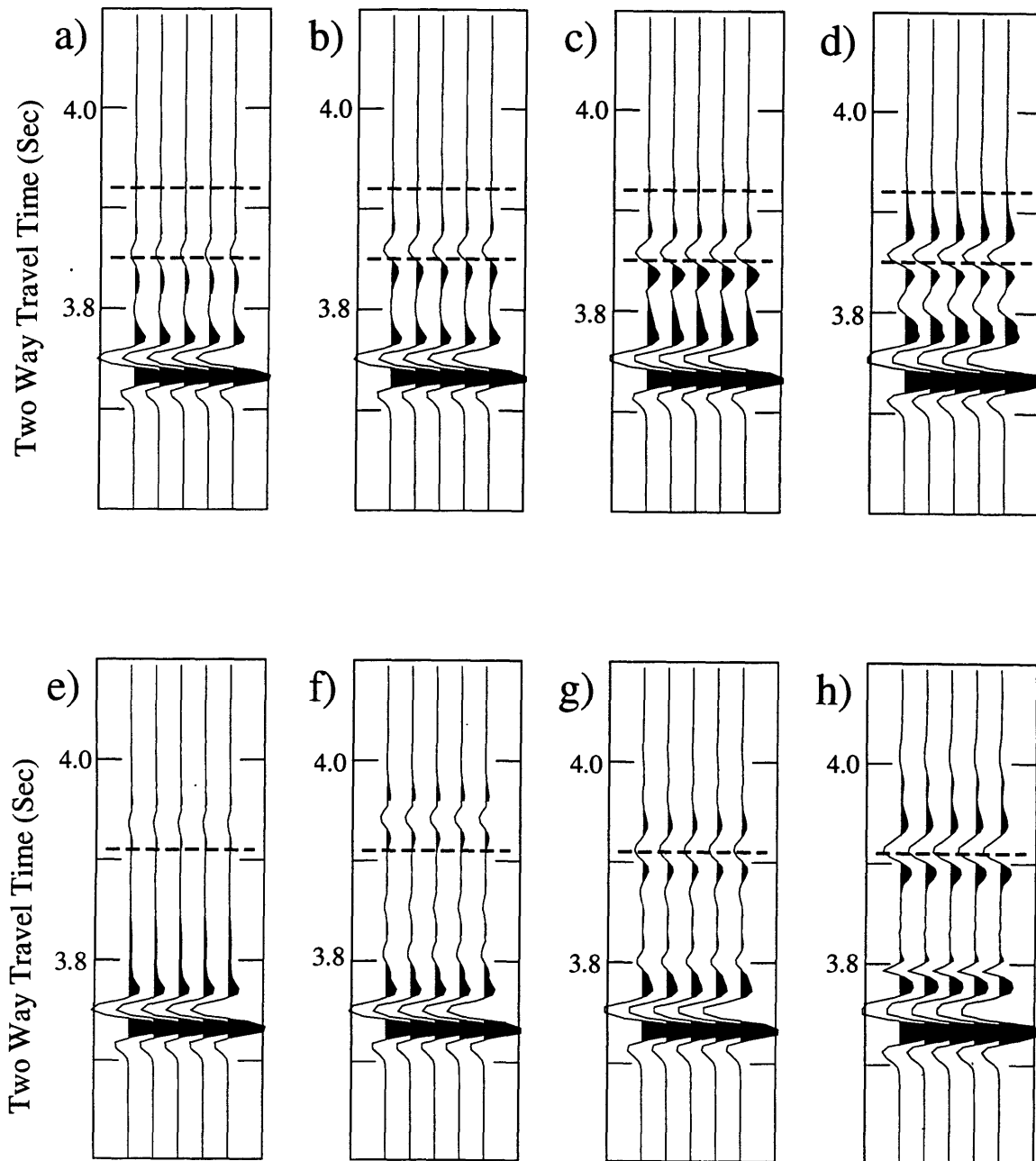
Figure 5.11. Final stacks of the synthetic data for the off-axis step model, for different range windows. (a) Range window 0.275-2.675 km. (b) Range window 0.275-3.200 km. (c) Range window 0.275-4.250 km. (d) Range window 2.600-4.950 km. Final stack of the synthetic data for the off-axis gradient model, for different range windows. (e) Range window 0.275-2.675 km. (f) Range window 0.275-3.200 km. (g) Range window 0.275-4.250 km. (h) Range window 2.600-4.950 km.
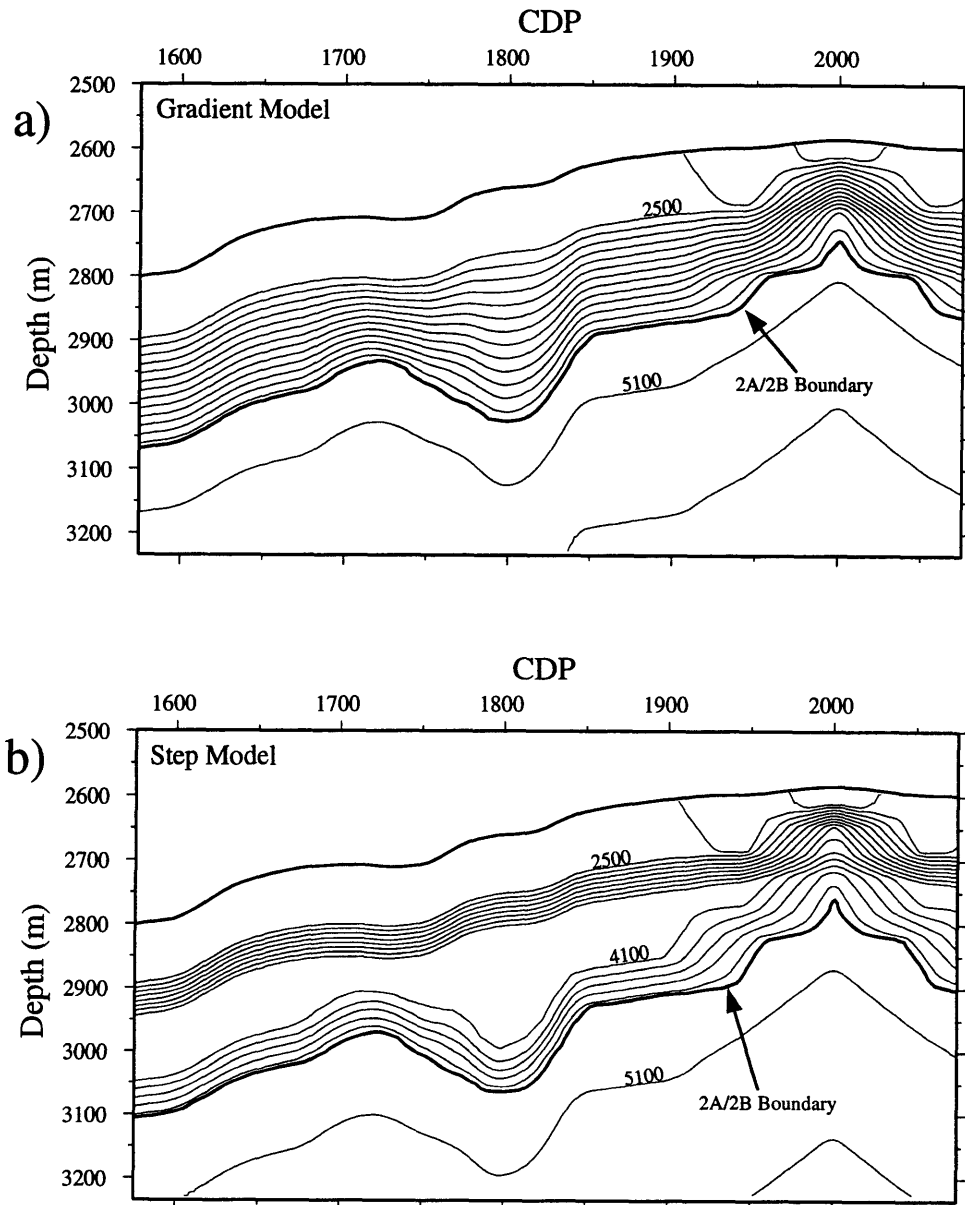
Figure 5.12. Two-dimensional velocity models used for the finite difference calculations. Velocity contours are plotted every 200 m/s, and vary from 2100 m/s to 5300 m/s. The thick black line marks the layer 2A/2B boundary. 80 CDPs are equivalent to 1 km. (a) Gradient model. (b) Step model.
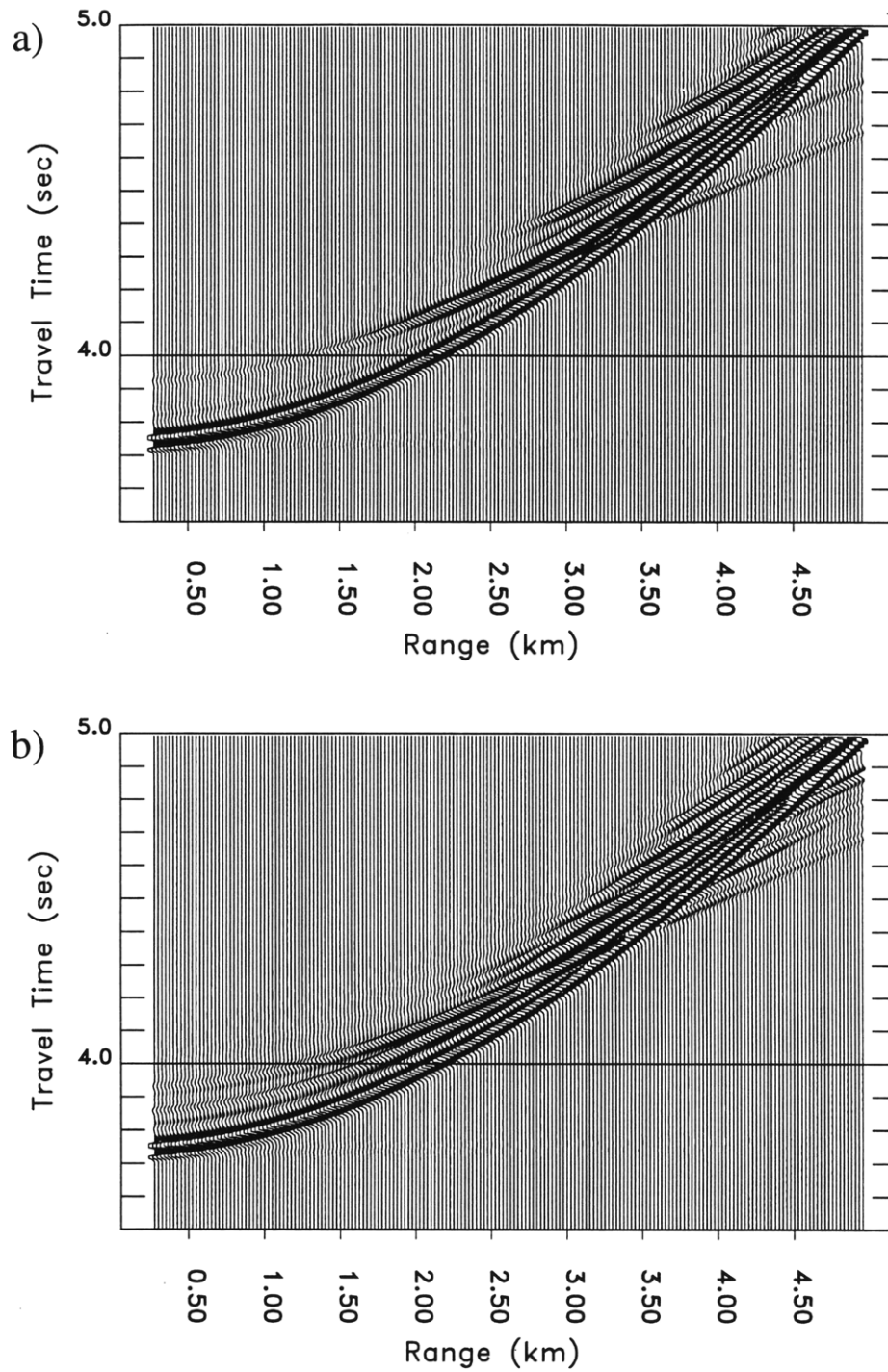
Figure 5.13. (a) Gradient model: As for Figure 5.2a, except the synthetic seismograms were calculated using a reflectivity code in an acoustic mode. (b) Step model: As for Figure 5.3a, except the synthetic seismograms were calculated using a reflectivity code in an acoustic mode.

155
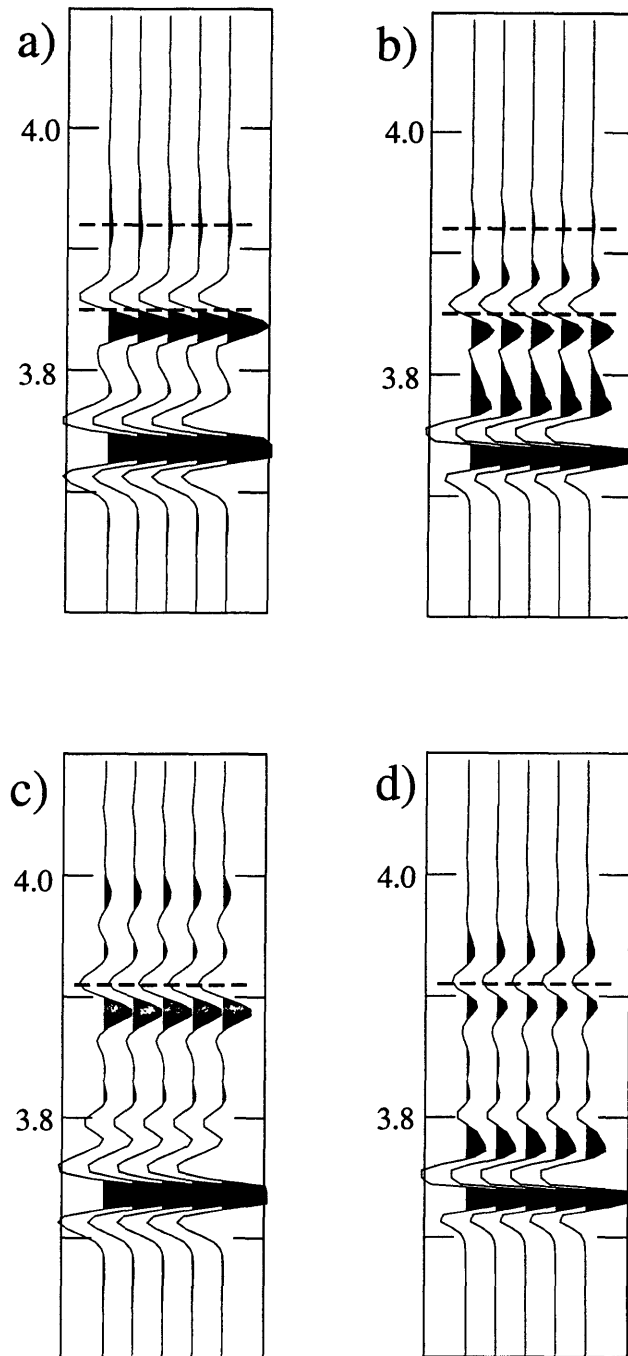
Figure 5.14. (a) As for Figure 5.6a, except the source is a Ricker wavelet with a center frequency of 20 Hz, and the synthetics were calculated using an acoustic reflectivity code with no attenuation. (b) As for Figure 5.6a. (c) As for Figure 5.10a, except the source is a Ricker wavelet with a center frequency of 20 Hz, and the synthetics were calculated using an acoustic reflectivity code with no attenuation. (d) As for Figure 5.10a.
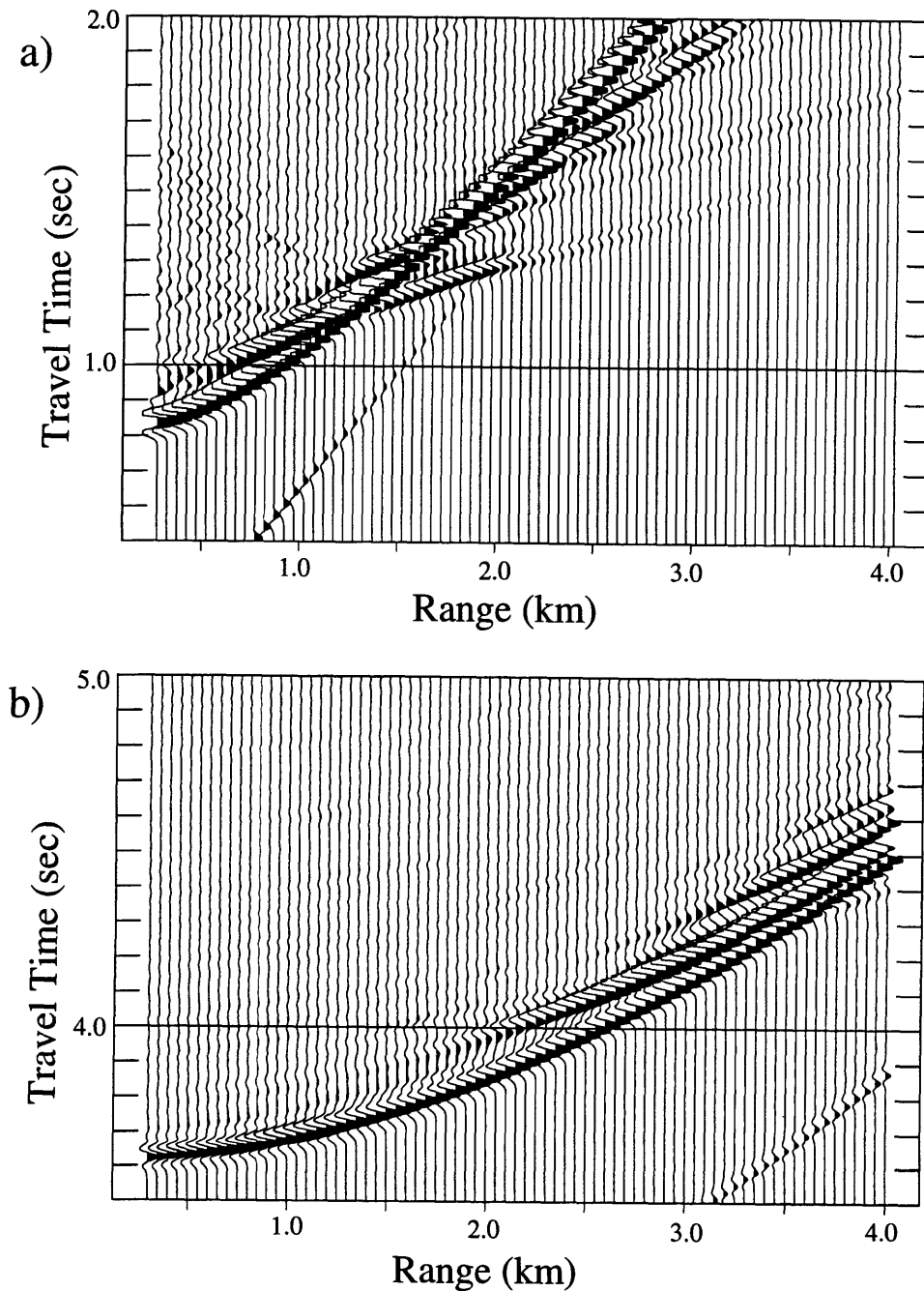
Figure 5.15. (a) Shot gather, with source and receivers 500 m above the rise axis, calculated with the finite difference technique for the gradient model (Figure 5.12a). The source is at CDP 1680, and the receivers extend out to CDP 2040. (b) CDP gather at CDP 1680 after the data has been extrapolated to the sea surface. Synthetic modeling indicates that all energy is correctly upward continued, with the exception of the direct water wave (the event in the lower right hand corner).
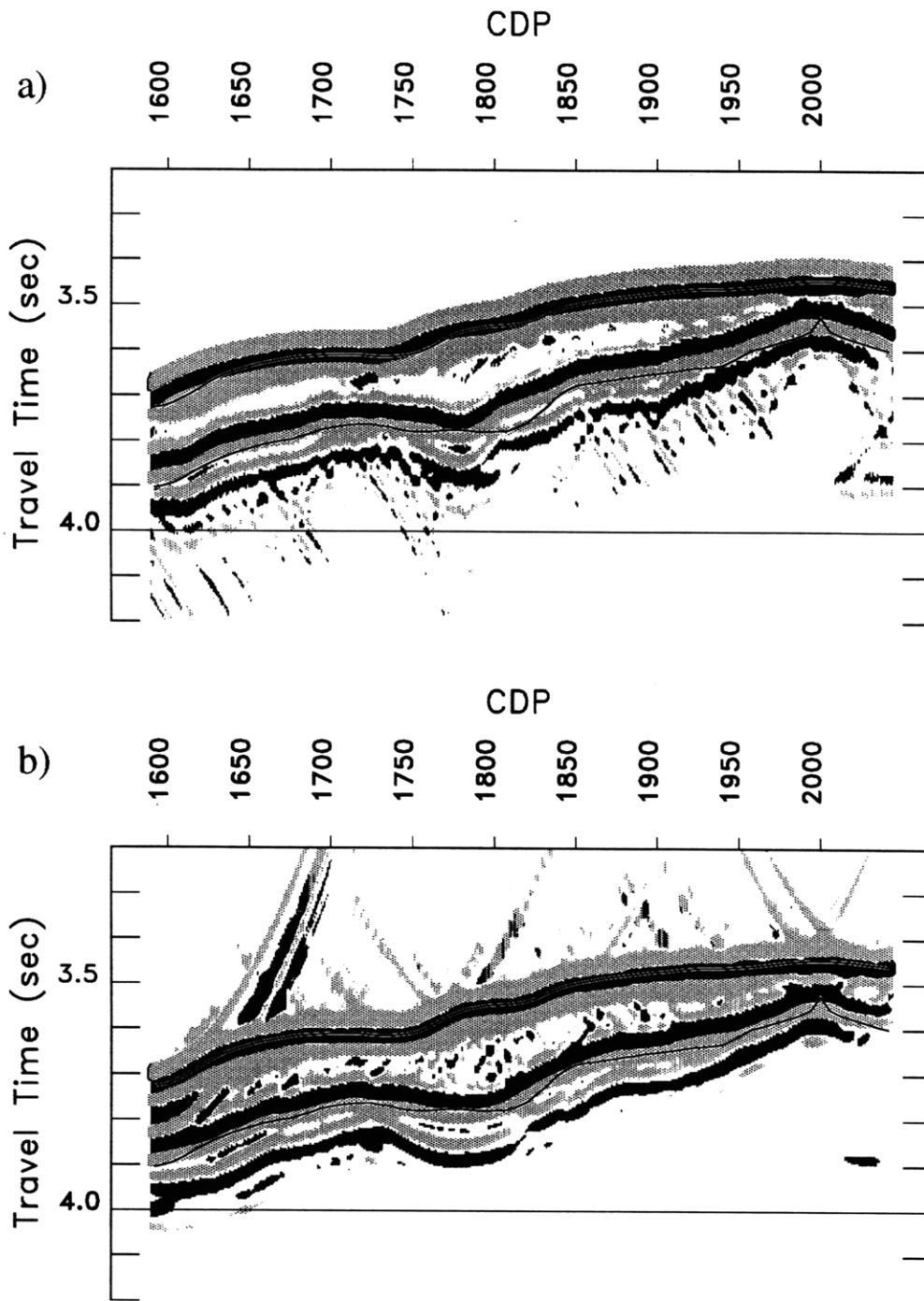
Figure 5.16. (a) Stacked section for the gradient model, for an aperture out to 4.0 km. Positive and negative amplitude are shaded black and gray, respectively. The thin solid lines mark the theoretical depth to the seafloor and layer 2A/2B boundary. (b) Migrated section of above.
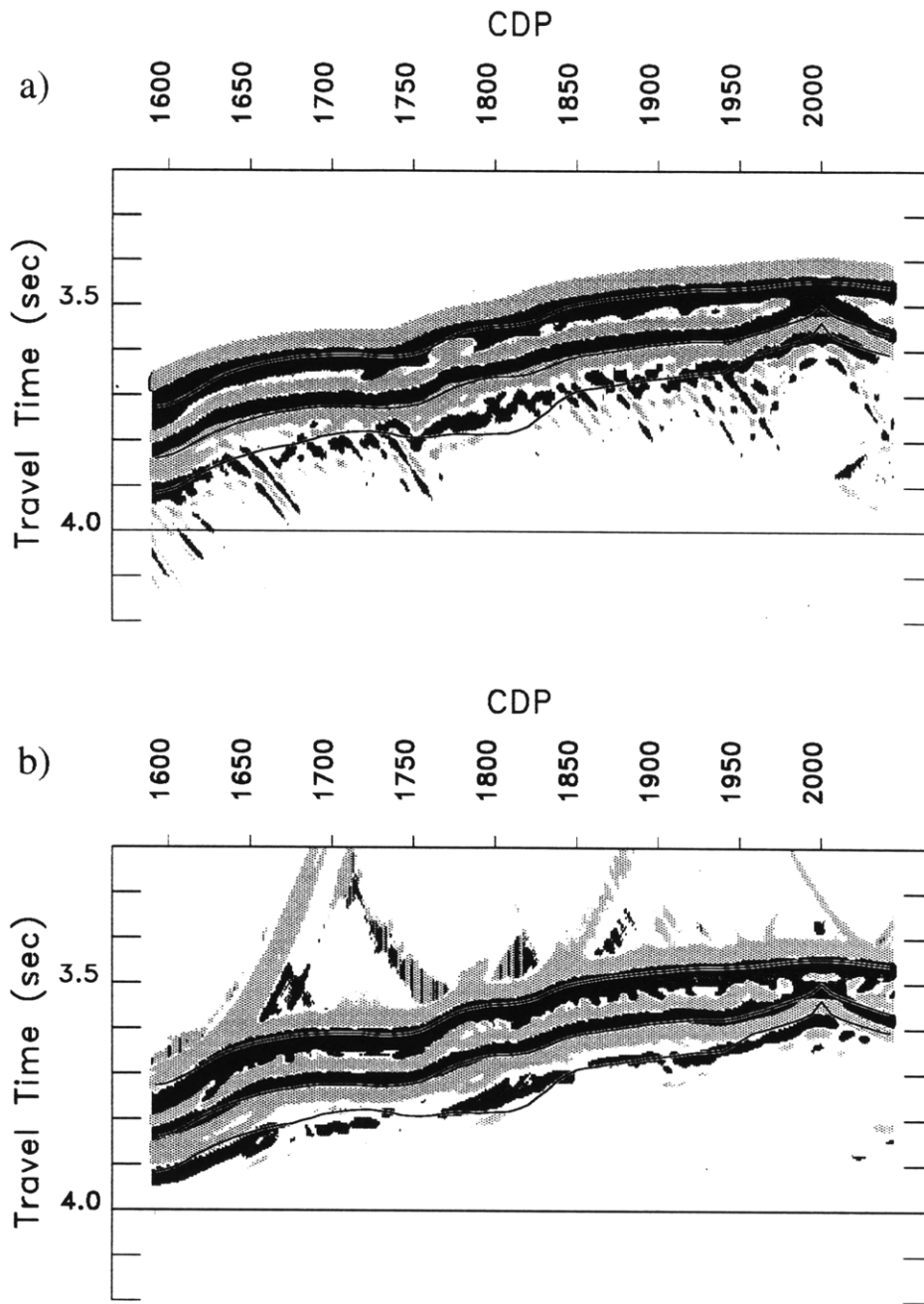
Figure 5.17. As for Figure 5.16, except for the step model. The thin solid lines mark the theoretical depth to the seafloor and base of each of the high-gradient regions.
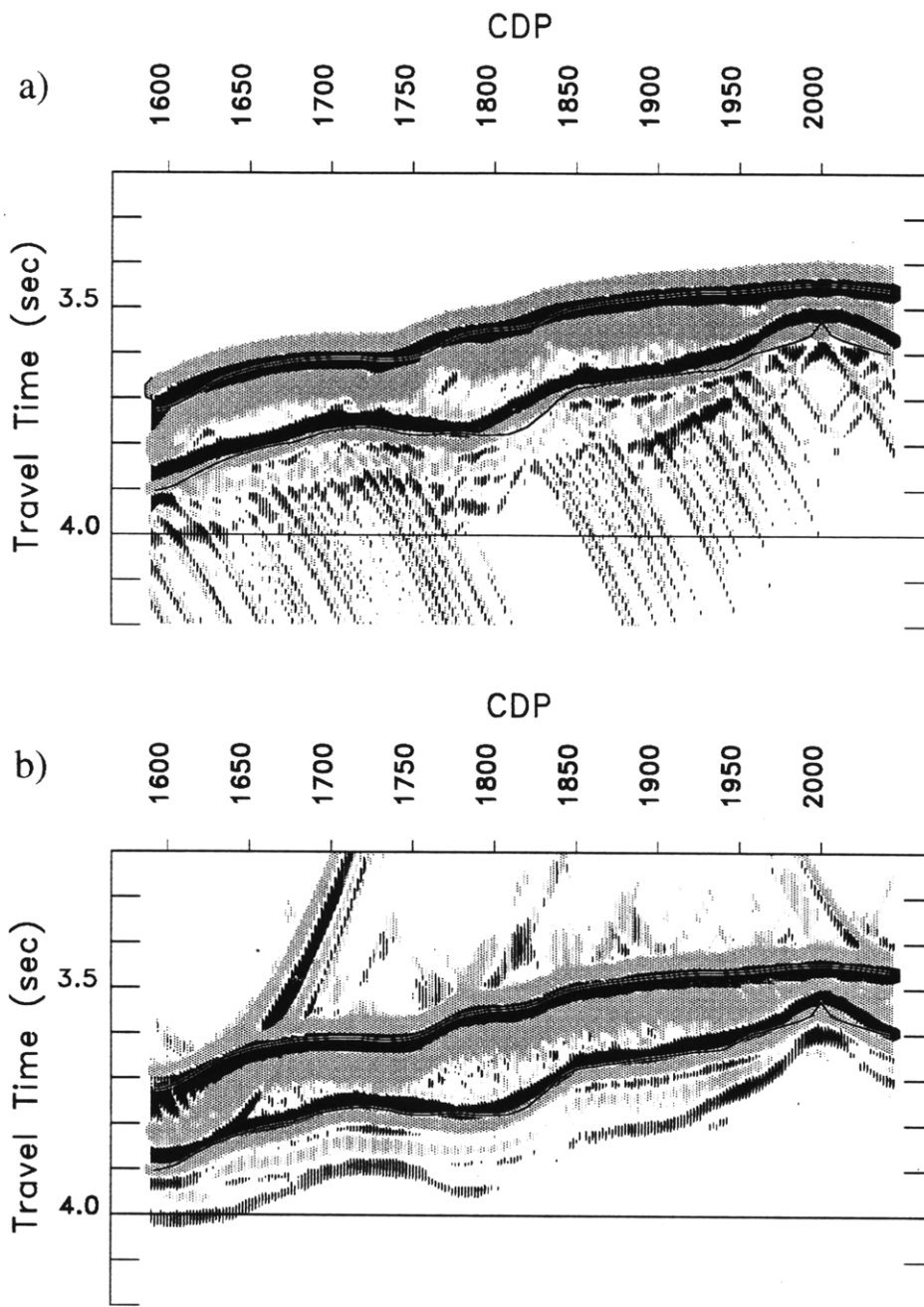
Figure 5.18. As for Figure 5.16, except that the data were stacked with an aperture out to 2.675 m.

a)

9° 40'N

9° 30'N

104° 30'W   104° 20'W   104° 10'W

b)

9° 40'N

9° 30'N

104° 30'W   104° 20'W   104° 10'W
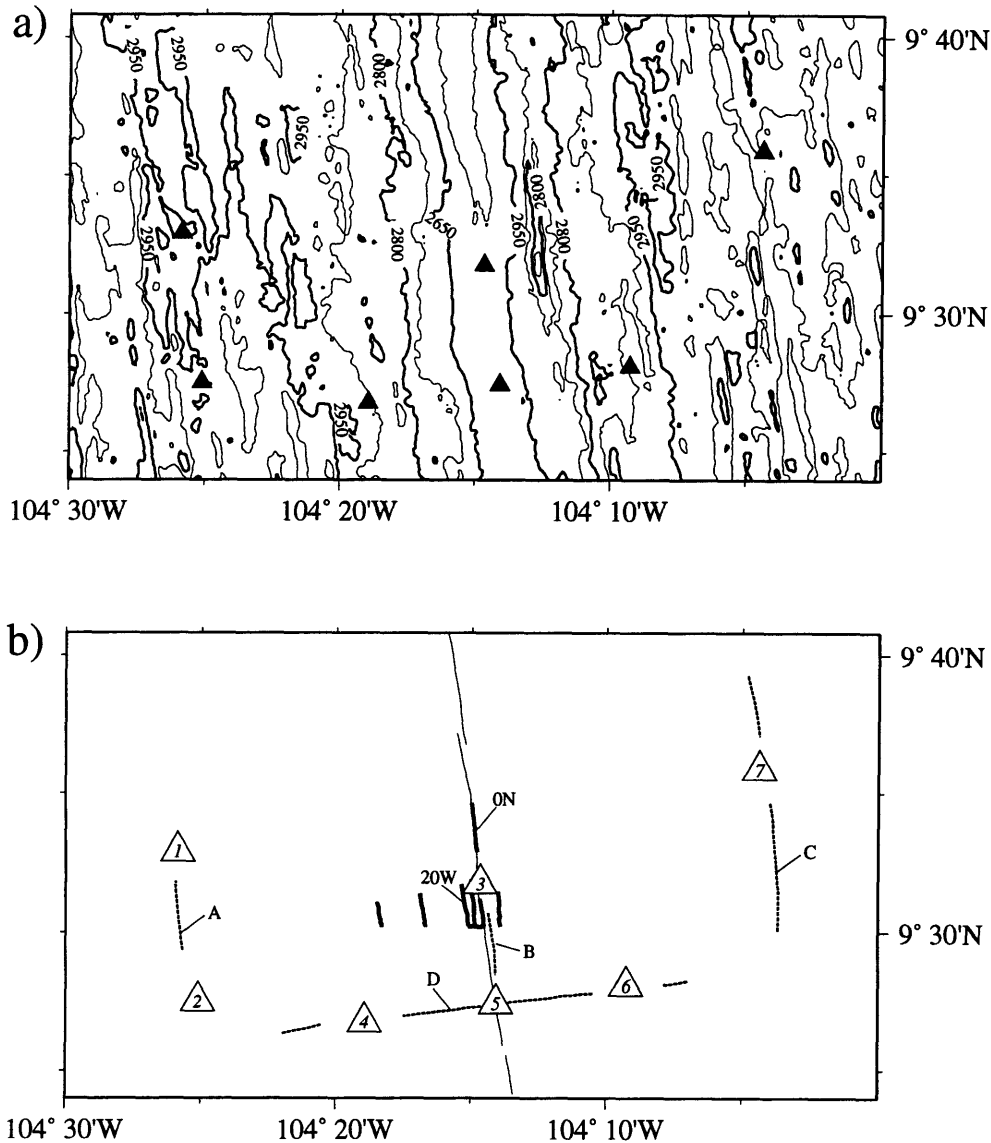
Figure 5.19. (a) Sea Beam bathymetry [*Wilcock et al.*, 1993] contoured at 75 meter intervals for a section of the East Pacific Rise located between the Siqueiros and Clipperton transform faults. Triangles mark OBH locations. (b) Experiment location map for the region shown in Figure 5.19a. Dashed lines show the positions of the airgun shots, and triangles mark the OBH locations. Shiptracks for the on-bottom seismic refraction experiments are indicated with the thick solid lines, and Lines 0N and 20W are labeled. The thin solid line marks the location of the axial summit caldera (ASC) as mapped by *Fornari et al.* [*Fornari, Perfit, Haymon, Edwards, and O'Brien*, Morphology and structure of the ASC of the EPR between 9°-10°N: ARGO and Alvin observations, in prep]. The along-axis airgun profiles are labeled A, B, and C, and the cross-axis profile is labeled D. The OBHs are numbered from 1-7.
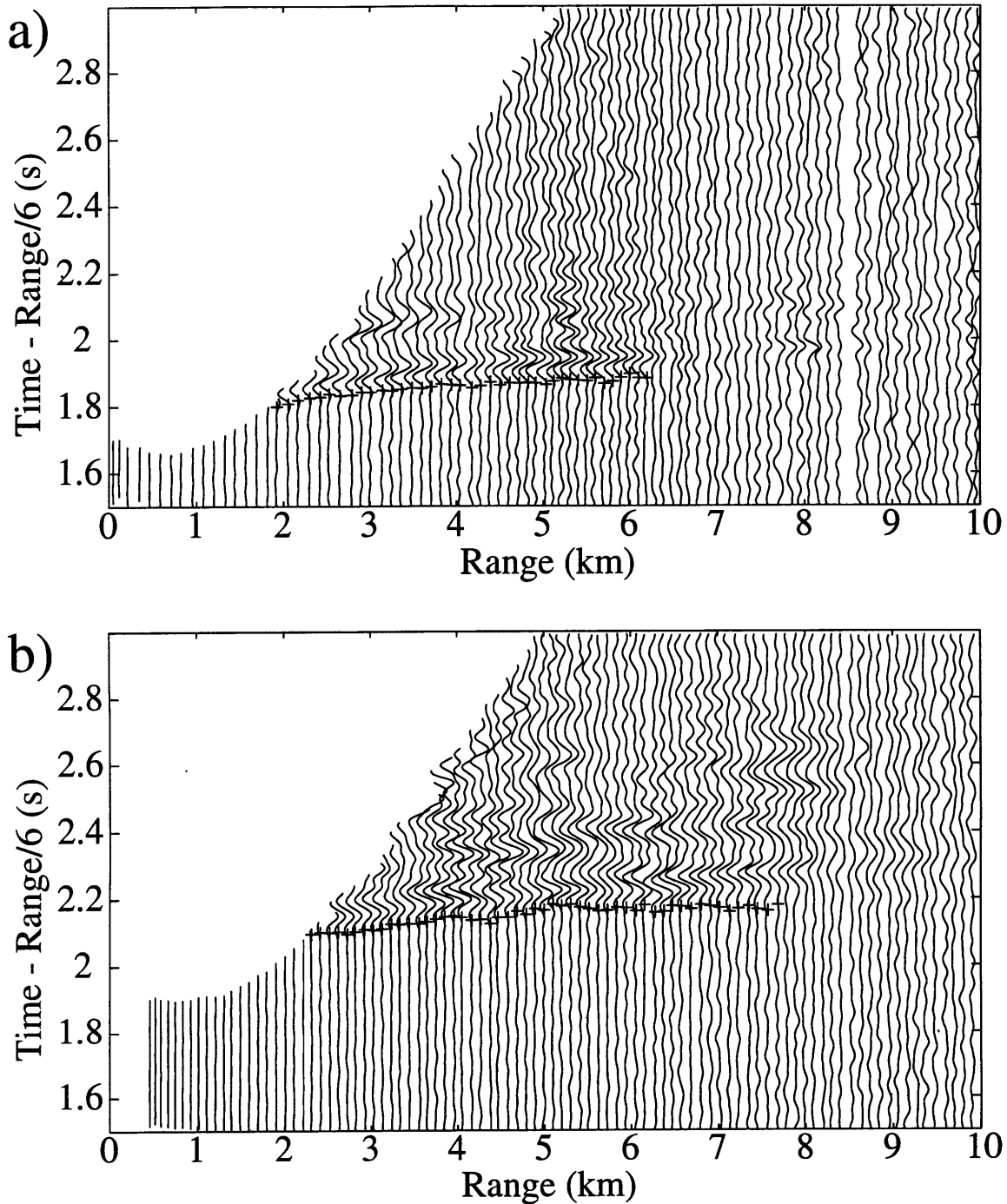
Figure 5.20. (a) Record section for the airgun shots north of OBH 5. The data have been filtered with a Butterworth filter. A high cut of 15 Hz, and a rolloff of 48 db/octave were used. The amplitude scale has been increased linearly with range, and no topographic correction has been applied. The seismograms are truncated at the water wave, and are plotted with a reduction velocity of 6.0 km/s. First arrival travel time picks are indicated by plus signs. (b) As for Figure 5.20a, for the airgun shots south of OBH 1.

162
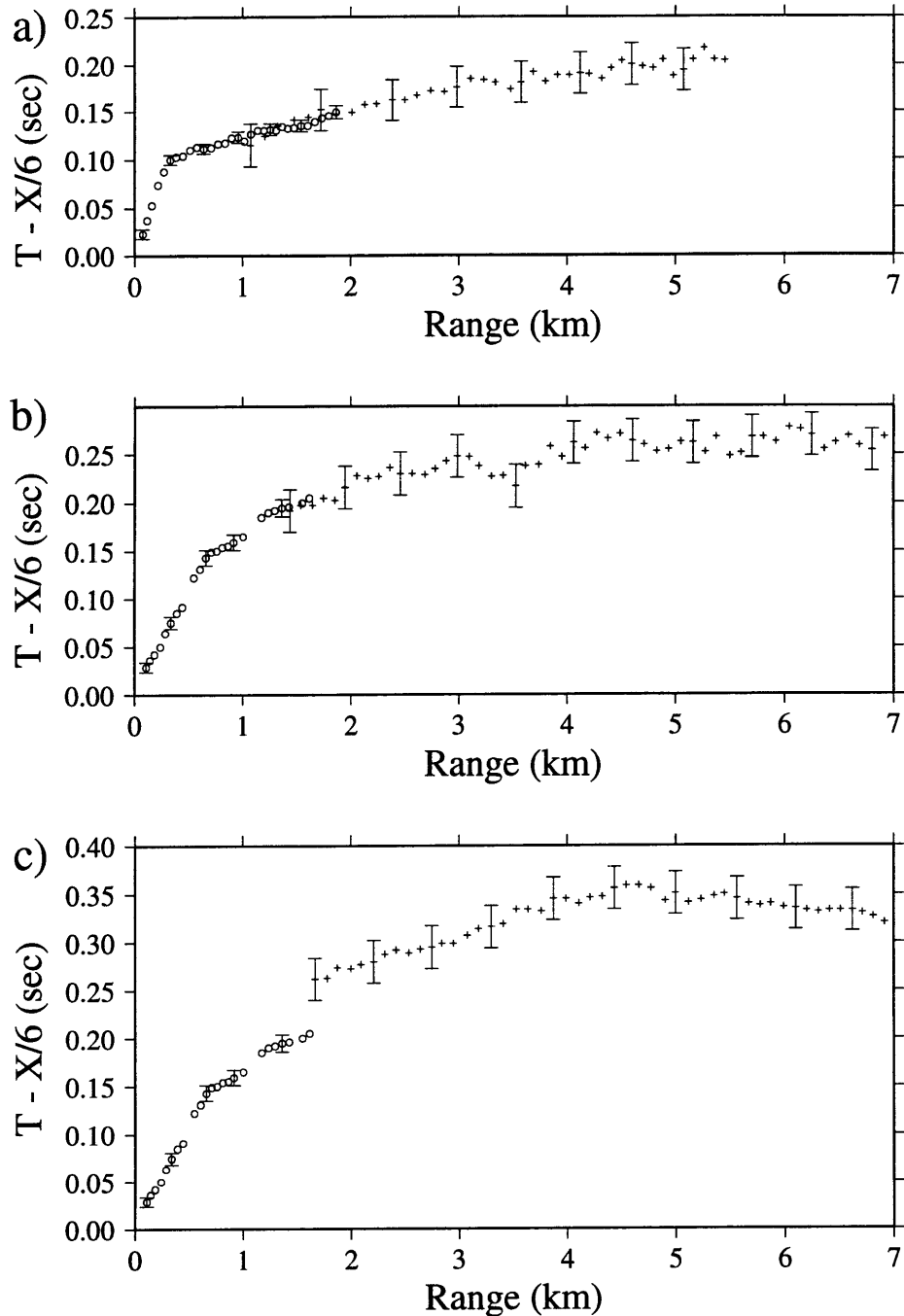
Figure 5.21. (a) First arrival travel time picks for the airgun shots north of OBH 5 (plus signs) and for on-bottom refraction experiment Line ON (circles). Representative error bars are shown for every fifth travel time pick, and are <10 ms for the on-bottom picks, and >20 ms for the airgun picks. (b) As for Figure 5.21a, for the data south of OBH 1 (plus signs) and for Line 20W (circles). (c) As for Figure 5.21a, for the data north of OBH 2 (plus signs) and for Line 20W (circles).
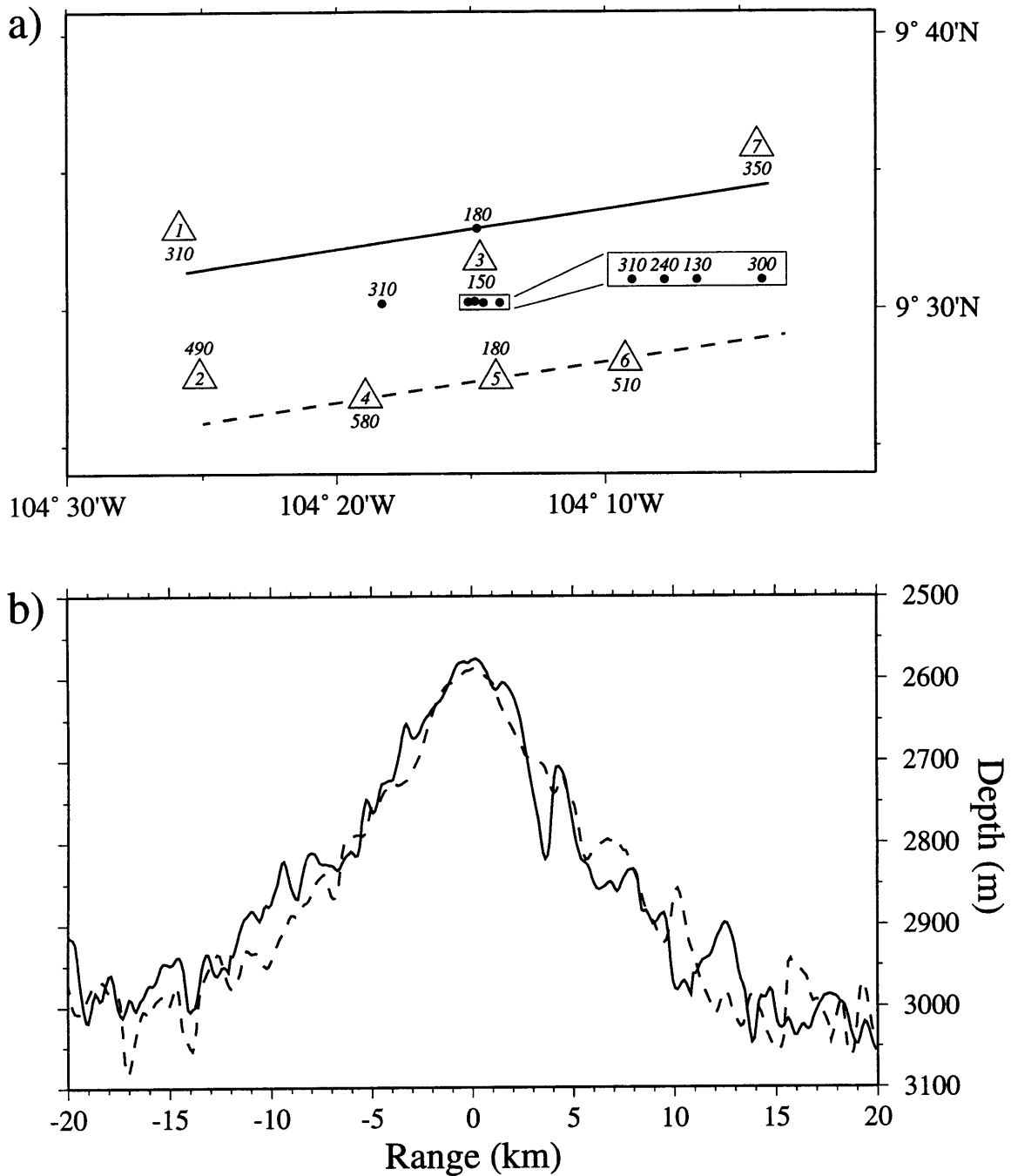
Figure 5.22. (a) Estimated layer 2A thicknesses in the vicinity of the seven OBHs (triangles) and for the NOBEL lines (circles). The solid and dashed lines mark the locations of the bathymetry profiles shown in Figure 5.22b. (b) Northern (solid) and southern (dashed) cross-axis bathymetry profiles across the study region. The thickening of layer 2A to the south is not reflected in the topography.
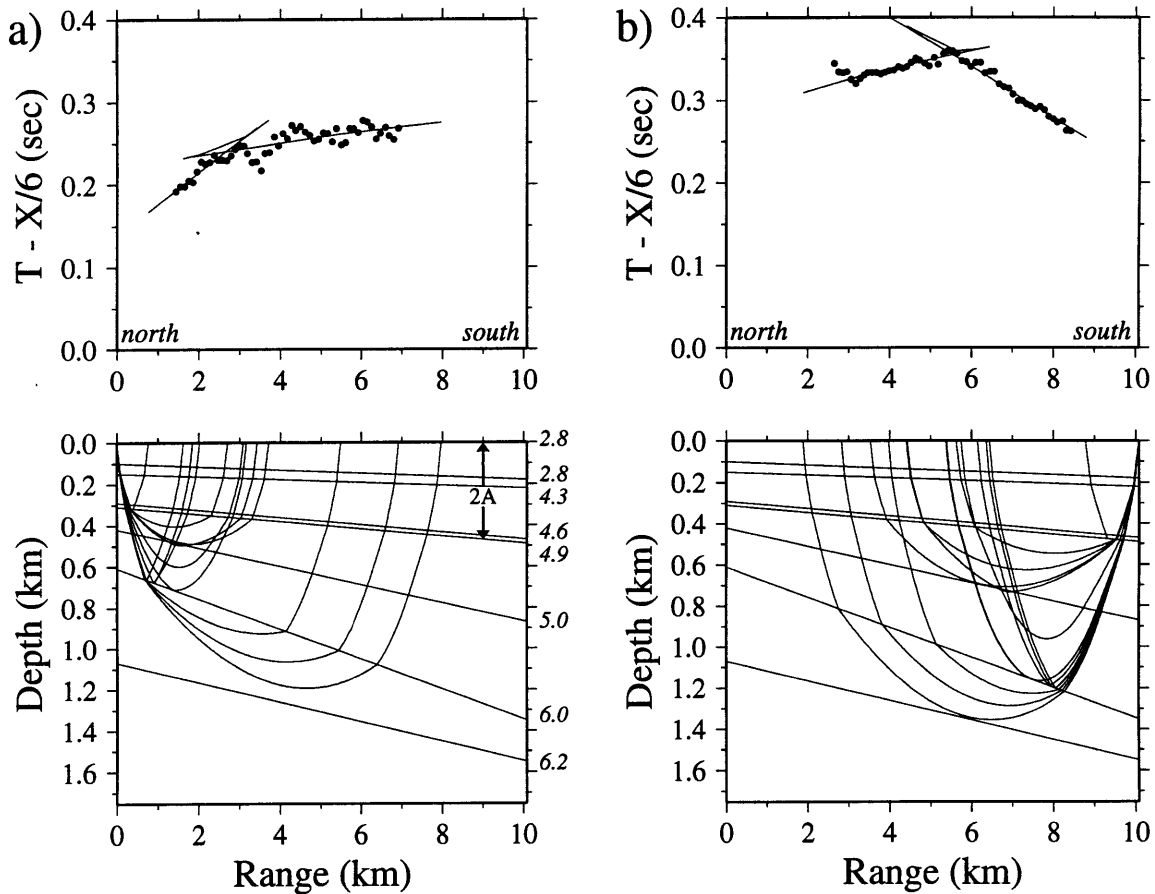
Figure 5.23. (a) Upper panel: Travel time picks for OBH 1 (circles) for shots south of the receiver. Solid lines show the calculated travel time curves for the rays plotted in the velocity model in the lower panel. Lower panel: Velocity model and rays traced south of OBH 1. Indicated to the right of the model are the velocities at each interface. Raypaths were calculated using the two-dimensional ray-tracing program of *Luetgert* [1988]. Note the thickening of layer 2A from 310 m at the northern end of the profile to 490 m at the southern end. (b) As for Figure 5.23a, except travel time picks and rays traced north of OBH 2.

a)

460 250 460
9° 50'N

440 450
225
280 135 250
9° 40'N

490 175 400
9° 30'N

580 200 450
9° 20'N

104° 20'W 104° 00'W

b)
9° 40'N

225 450
440

WAP

250
350

135
255 390
580
280
780 180
310 150
310 240 130 300
310
175 400
9° 30'N

490 490 175
180
580 510

MCS Line 31

104° 30'W 104° 20'W 104° 10'W
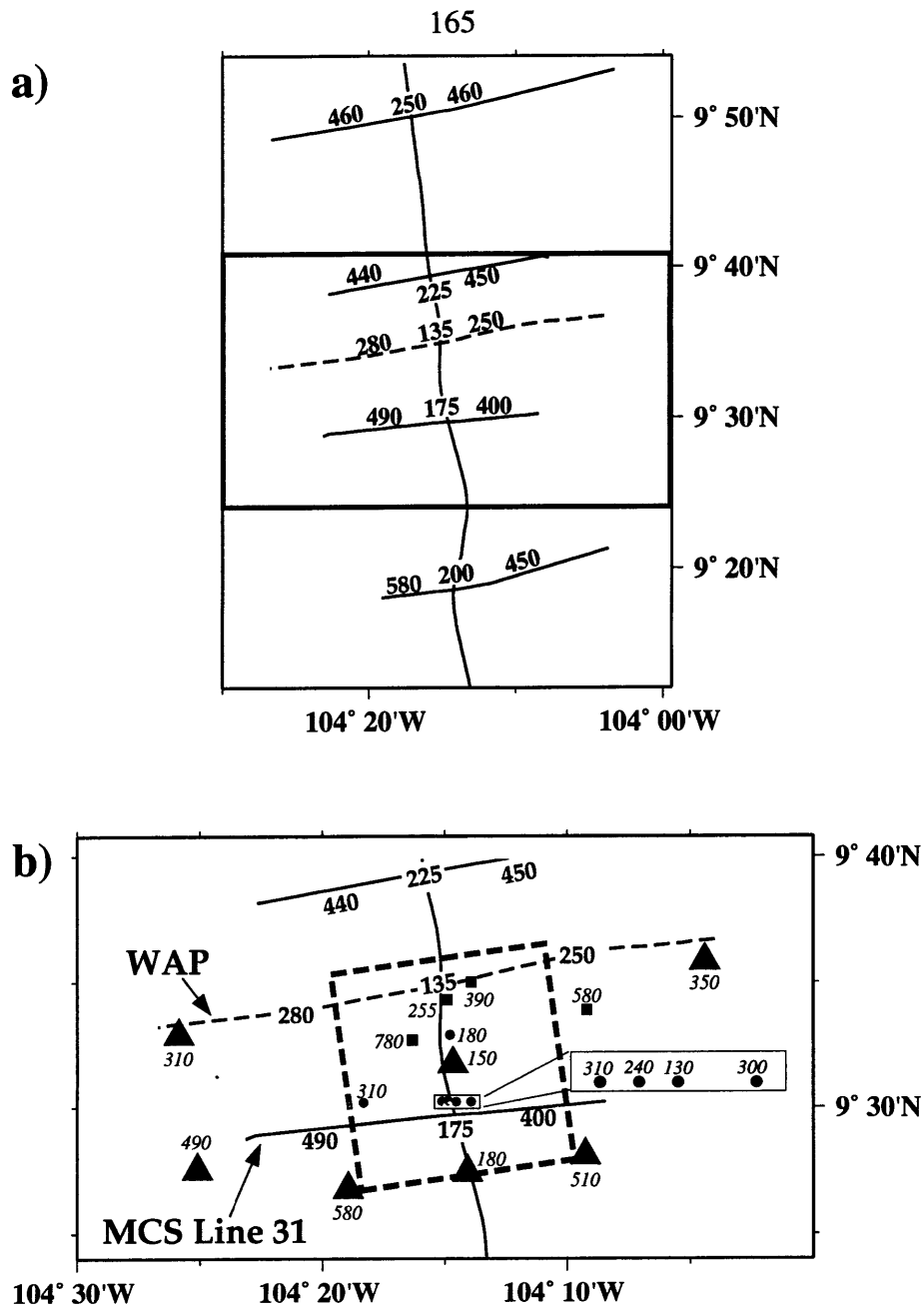
Figure 5.24. (a) Average depth to the layer 2A reflector from *Harding et al.* [1993] for four cross-axis MCS profiles (solid line), and from *Vera and Diebold* [1993] for one cross-axis WAP (dashed line). The inset rectangle identifies the region shown in closer detail in Figure 5.24b. (b) Summary figure of calculated layer 2A thicknesses in the 9°30'N EPR region from on-bottom refraction experiments (circles), ESPs (squares, [*Vera et al.*, 1990]), conventional airgun data (triangles), MCS profiles (solid lines [*Harding et al.*, 1993]), and a WAP (dashed line [*Vera and Diebold*, 1993]). The rectangular region encloses the tomography experiment of *Toomey et al.* [1990; in prep].
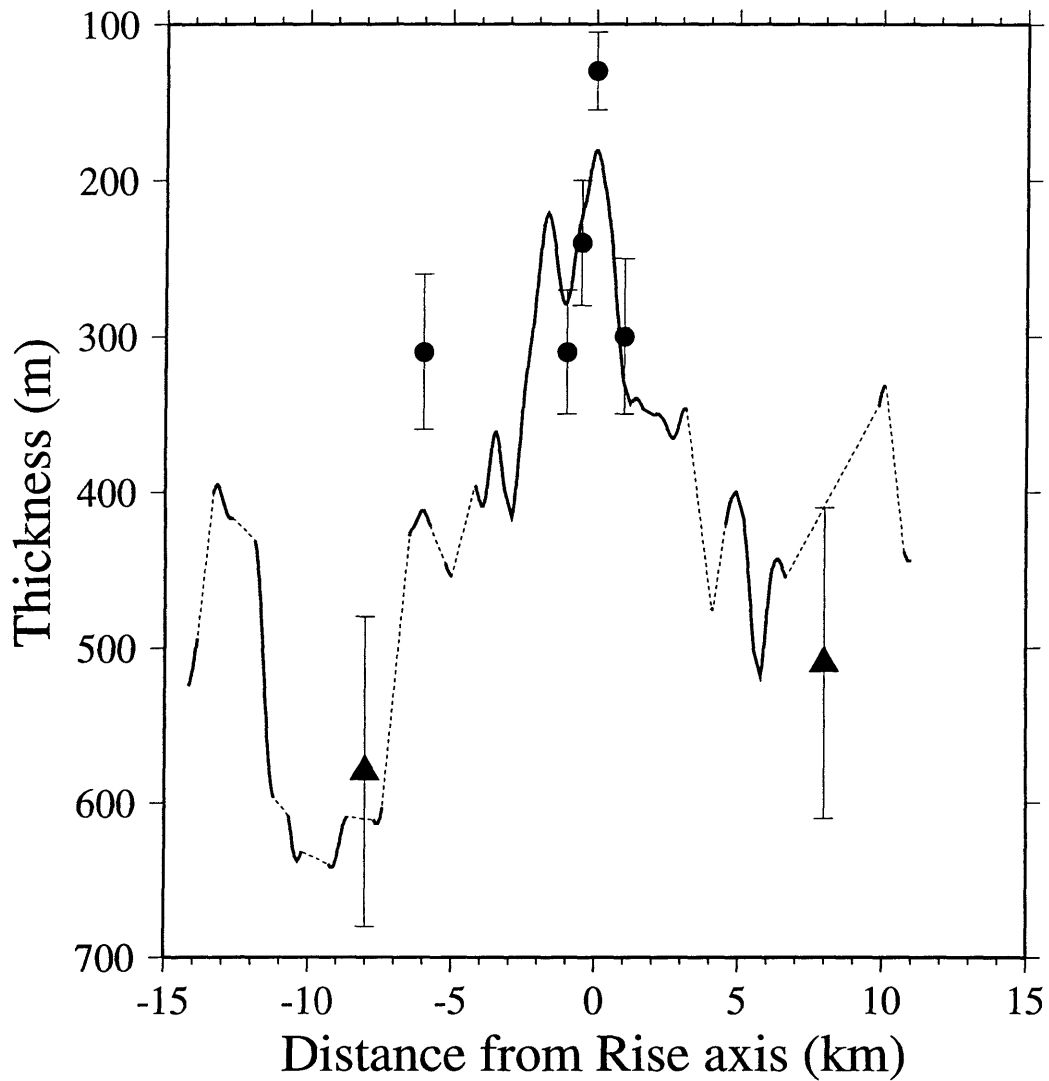
Figure 5.25. Layer 2A thickness as a function of distance from the rise axis from seismic data near 9°30'N. Solid and dashed line - thickness estimates from CDP 31 of *Harding et al.* [1993]. Only the solid portion is constrained by the data. Errors for the thickness estimates are difficult to assess, but are approximately ±50 m (G. Kent, personal communication, 1993]. Circles - estimates from on-bottom seismic refraction profiles. Triangles - estimates from conventional airgun refraction lines.

CHAPTER 6

CONCLUSIONS

Review of Primary Results

On-bottom seismic refaction experiments located over young crust on the fast-spreading

East Pacific Rise (EPR) illustrate that there is a dramatic change in shallow structure within

1 km of the axial summit caldera (ASC). Within the ASC, the upper crust consists of a

thin (<60 m) surficial low-velocity (<2.5 km/s) layer, a 100-150 m thick transition zone

with velocities increasing by 2.5 km/s, and a layer with velocities of ~5 km/s at a depth

beneath the seafloor of ~130-190 m (Figure 3.7). The surficial low-velocity layer and

transition zone are defined as seismic layer 2A, and the ~5 km/s layer as layer 2B. Both

the surficial low-velocity layer and the transition zone double in thickness within 1 km of

the rise axis, with the depth to the 2A/2B boundary increasing from ~150 m to ~300-350 m

over this range. The doubling of layer 2A thickness within 1-2 km of the rise axis is

confirmed by multi-channel seismic (MCS) and wide-angle profile (WAP) data, which also

indicate that there is no further systematic change in thickness with greater range from the

rise axis. However, there does appear to be along-axis variability in layer 2A thickness

outside of the ASC, with the depth to the base of layer 2A consistently thinner (250 m vs.

450 m) near 9°35'N than for adjacent profiles at 9°20'N, 9°30'N, 9°40'N, and 9°50'N.

Inversions for attenuation structure demonstrate that the layer 2A/2B interface is not only a

velocity boundary, but also an attenuation boundary, with Q increasing from 10-20 within

layer 2A to >70 in layer 2B. Layer 2A is interpreted to be composed of the extrusive

section and transition zone, with layer 2B consisting of the sheeted dike complex. This

implies that the top of the dikes subsides from 150-200 m to 250-450 m within 1-2 km of

the rise axis, and then remains at a relatively constant depth beneath the seafloor. The

thickening of the extrusive layer is interpreted to be due to lava that either overflows the ASC walls, is emplaced through eruptions outside of the ASC, or travels laterally from the ASC through subseafloor conduits. According to this model, the shallow crustal architecture is in place within 1-2 km of the rise axis.

Dike Subsidence

The cross-axis distance over which dike subsidence occurs is similar to the lateral extent (~1 km half-width) of the primary low-velocity volume imaged by the tomographic inversions of *Toomey et al.* [1990], and slightly greater than the width of the axial magma chamber (AMC) reflector (~250 m half-width) observed in MCS data [*Kent et al.*, 1993a; *Kent et al.*, 1993b; *Kent et al.*, 1993c]. We suggest that the process of dike subsidence is controlled by the axial magma chamber. A possible explanation is that buoyancy forces associated with the AMC are supporting the extrusive layer and sheeted dikes at the neovolcanic zone. With distance from the rise axis, the AMC solidifies, the crust cools, the buoyancy forces are reduced, and the sheeted dike complex subsides. Concurrently, the extrusive layer thickens resulting in significantly less subsidence of the seafloor.

To test the validity of this model, we can determine if vertical columns through the crust within and outside of the neovolcanic zone are in local isostatic equilibrium. This can show whether thickening of the extrusive layer can balance the reduced buoyancy forces associated with solidification of the magma chamber. Isostasy is a good approximation at the EPR crest, based on the small elastic plate thicknesses (~0.1-0.5 km) needed to match gravity and bathymetry profiles [*Madsen et al.*, 1984; *Kuo et al.*, 1986; *Wang and Cochran*, 1993]. In order to carry out our calculations, assumptions had to be made concerning the density contrasts introduced by the magma chamber and thickened extrusive layer (Table 6.1). The magma chamber is based on the model of *Sinton and Detrick* [1992], and consists of a thin layer of 100% melt, underlain by a larger crystal mush zone, which is in turn underlain by a zone with a small amount of partial melt (Figure 6.1).

Seismic studies at the EPR indicate that the thickness of the melt lens is ~50 m [Kent et al., 1993a], and the thickness of the mush zone does not exceed 1 km [Wilcock et al., 1992]. The amount of partial melt within the mush zone is not well constrained, but is probably between 20-75% [Sinton and Detrick, 1992]. For our calculations, we assumed thicknesses for the melt lens and mush zone of 50m and 1000m, respectively, and that the mush zone contains 40% partial melt. In the upper crust, a 1350 m thick sheeted dike complex, and an extrusive layer that thickened from 150 m at the rise crest to 300-450 m outside the neovolcanic zone were assumed. In our model we used a layer 3 thickness of 5150-5300 m outside of the neovolcanic zone, in order to achieve a crustal thickness of 6950 m as measured by ESP data at the EPR [Vera et al., 1990]. We made the assumption that layer 3 is formed at the rise axis, which requires a 150-300 m decrease in zero-age crustal thickness to compensate for the thinner extrusive section within the neovolcanic zone. Average seismic velocities for the extrusive section, dike complex, and layer 3 were converted to densities using the relationship of Christensen and Shaw [1970], $\rho = 1850 + 0.165V_p$ (for velocity in m/s and density in kg/m^3). For an average layer 2A velocity of 3500 m/s and layer 2B/2C velocity of 5500 m/s, the resulting densities are 2420 kg/m^3 and 2760 kg/m^3, respectively (Table 6.1). Near-bottom gravity measurements determined a density of 2520 kg/m^3 for the upper 200 m of young crust on the Juan de Fuca Ridge, which is slightly greater than our estimated extrusive density [Holmes and Johnson, 1993]. For layer 3 we assumed an average velocity of 6750 m/s [Vera et al., 1990], which results in a density of 2950 kg/m^3. We used a density of 2700 kg/m^3 for the melt lens [Stolper and Walker, 1980; Hooft and Detrick, 1993], and 2850 kg/m^3 for the mush zone (calculated assuming 40% partial melt and a matrix density of 2950 kg/m^3). We assumed a density of 3270 kg/m^3 for the mantle [Wang and Cochran, 1993]. There are few constraints on densities beneath the mush zone. Delay time and attenuation tomographic inversions suggest that the maximum melt fraction in this region is <3-5%, but a narrow zone of higher melt fraction would not be resolved by these techniques [Toomey et al.,

1990; *Caress et al.*, 1992; *Wilcock*, 1992]. We assumed a density contrast of 3-35 kg/m^3 between the AMC root and the surrounding layer 3 crust; this represents a 1-14% partial melt fraction beneath the mush zone if the melt density is 2700 kg/m^3 and the matrix density is 2950 kg/m^3. With the assumptions described above and summarized in Table 6.1 and Figure 6.1, we determined that the crust is in local isostatic equilibrium, with a depth of compensation at the base of the crust.

Table 6.1: Values Used in Isostatic Calculation

layer	'0 km' column: thickness (m)	'1 km' column: thickness (m)	density (kg/m^3)
extrusives	150	300-450	2420
dikes	1350	1350	2760
'normal' layer 3	0	5150-5300	2950
melt lens	50	0	2700
mush zone	1000	0	2850
AMC root	4100-4250	0	2915-2947
mantle	150-300	0	3270
total	6950	6950	

The isostatic calculations suggest that a model with the magma chamber controlling the amount of dike subsidence is not unreasonable, where we define the magma chamber as the melt lens and underlying mush zone. The primary implication of this model is that dikes will subside to a greater depth for a robust magma chamber than for a weaker magma chamber. In addition, isostasy requires that the buoyancy forces associated with the magma chamber must be balanced by either the addition of low-density material (i.e. extrusives) to the crust, or seafloor subsidence, as the crust is translated laterally. Since bathymetry profiles indicate that seafloor subsidence is only ~20 m within 1 km of the ASC, this suggests that extrusive thickening is associated with the dike subsidence. This

in turn implies that a robust magma chamber will produce a thicker extrusive layer (and transition zone) and greater dike subsidence than a weaker magma chamber.

With this model for dike subsidence, we can gain additional insight into the emplacement processes at the EPR. A prominent feature of the shallow crust in the 9°20'N-9°50'N region is that layer 2A is ~50% thinner (250 m vs. 450 m) on a cross-axis WAP line near 9°35'N than on four adjacent MCS lines. This implies that there has consistently been 50% less subsidence of the sheeted dikes in the 9°35'N region over at least the past 175,000-275,000 yrs (based on the length of the MCS and wide-angle profiles). The disparity in the amount of dike subsidence would therefore suggest that the magma chamber near 9°35'N has been considerably weaker, for an extended period of time, than for the rest of the rise axis in the 9°20'N-9°50'N area. This is consistent with available MCS data, which indicates that the present-day width of the AMC reflector is only 250 m near 9°35'N, as compared to 500-4150 m along the rest of the rise crest from 8°50'N-9°50'N [*Kent et al.*, 1993a; *Kent et al.*, 1993b]. *Scheirer and McDonald* [1993] argue that variation in cross-sectional area of the axial ridge correlates with differences in the volume of melt within the crust and mantle within about 10 km of the rise axis. Therefore, a decrease in cross-sectional area might be expected near 9°35'N; however, no significant variability is observed (Figure 5.22). This suggests that the volume of low-density mantle material is essentially constant along the ridge segment, but that efficient delivery of melt to a crustal magma chamber has been impeded near the 9°35'N deval for the past 350,000 years. Along-axis MCS [*Harding et al.*, 1993], WAP [*Vera and Diebold*, 1993], and conventional airgun refraction data show no significant variation in zero-age layer 2A thickness near 9°35'N, in contrast to the 50% thickness decrease observed outside of the neovolcanic zone from 9°30'N to 9°35'N. This implies that the extrusive volume emplaced at zero-age crust along this ridge segment is relatively constant despite variability in magma chamber dimensions. One possibility is that the plumbing system for a narrow

melt lens directs dikes primarily into the ASC, while for a wider melt lens eruptions occur both within and outside of the ASC (Figure 6.2).

The magma chamber along the EPR near 13°N is generally believed to be smaller in comparison to 9°N, based on the decrease in cross-sectional area [*Macdonald and Fox*, 1988] and gravity anomaly [*Madsen et al.*, 1993] at the northern site. Thus we would expect to observe a decrease in extrusive thickness and in the amount of dike subsidence from the 9°N region to the 13°N region. This hypothesis is not inconsistent with seismic data, which indicates that the depth to the layer 2A/2B boundary is ~300-400 m below the seafloor near 13°N [*Harding et al.*, 1989; *Kappus*, 1991], in contrast to a depth of ~400-500 m [*Harding et al.*, 1993] near 9°N. Along-axis MCS and WAP data demonstrates that the thickness of layer 2A for zero-age crust is ~200 m in both regions [*Kappus*, 1991; *Harding et al.*, 1993], again suggesting that the volume of extrusives emplaced *within the ASC* is largely independent of magma chamber dimension. Estimates of layer 2A thicknesses have also been obtained on the EPR near 14°15'S (~7.5 cm/yr half spreading rate). Similar to the EPR at 9°N, the depth to the base of layer 2A at this location increases from ~200-250 m to ~500-600 m within 1-2 km of the rise axis [*Kent et al.*, 1993c], implying that magma chamber dimensions are comparable for the two regions, even though the spreading rates differ by 35%. Indeed, no systematic change in melt lens width is observed between the two areas in MCS data [*Kent et al.*, 1993c]. At the southern EPR, there is little variability outside the neovolcanic zone in layer 2A thickness on cross-axis MCS profiles, which would indicate that the magma chamber size has been relatively constant for the past 130,000 years. In contrast, the depth to the base of layer 2A outside of the neovolcanic zone varies by several hundreds of meters on cross-axis MCS profiles at the northern EPR, suggesting that changes in magma chamber size occur more frequently as spreading rate decreases.

Intermediate-Spreading Ridges

The layer 2A/2B boundary at intermediate-spreading ridges has generally been interpreted as a porosity boundary within the extrusive section, primarily because of the discrepancy between the average thickness of layer 2A (~400-600 m) and the depth to the top of the sheeted dike complex at Hole 504B (~800 m) [*Rohr et al.*, 1988; *White and Clowes*, 1990; *Cudrak and Clowes*, 1993]. Deeptow magnetic data indicate that seismically defined layer 2A thicknesses correlate quite well with magnetic source layer thicknesses at the Endeavour, Cleft, and Vance segments of the Juan de Fuca Ridge [*Tivey*, 1993; *Tivey and Johnson*, 1993]. In addition, a study of the Blanco scarp (also located on the Juan de Fuca Ridge) found excellent agreement between a decrease in magnetization and the top of the sheeted dikes, suggesting that the extrusive section and transition zone form the magnetic source layer [*Naidoo et al.*, 1992; *Tivey*, 1992]. Thus the magnetic data indicates a correlation between the magnetic source layer, seismic layer 2A, and the extrusive section and transition zone at the Juan de Fuca Ridge. If the layer 2A/2B boundary does represent the top of the sheeted dike complex at intermediate-spreading ridges, then seismic refraction data argues that the average depth to the sheeted dikes is 400±200 m [*White and Clowes*, 1990; *Cudrak and Clowes*, 1993; *McDonald et al.*, 1993]. The similarity in layer 2A thicknesses between the intermediate spreading Juan de Fuca Ridge and the fast-spreading East Pacific Rise suggests that magma chamber dimensions are similar at these two ridges. However, this is speculative, as there are few constraints on the emplacement process at the rise axis. The layer 2A reflector in MCS data is absent at the rise crest [*Rohr et al.*, 1988], and the geometry of the seismic refraction experiments shot to date have not been designed to resolve rapid variability in shallow structure. Inversions of deep-tow magnetic data from two of three segments surveyed at the Juan de Fuca Ridge indicate a thinning of the magnetic source layer, interpreted to be the extrusive section [*Tivey*, 1993; *Tivey and Johnson*, 1993]. This is consistent with dike subsidence at the rise axis. *Kappel and Ryan* [1986] have suggested that volcanic

processes at intermediate spreading centers are episodic in nature, with a period of accretion alternating with a period of extension. We speculate that during the accretion cycle, a large volume of extrusives are emplaced from a robust magma chamber (Figure 6.3). This is followed by a cycle in which a large magma chamber is not present, and few extrusives are emplaced.

Future Work

Recent seismic studies have greatly increased our understanding of the process of volcanic emplacement at the fast-spreading East Pacific Rise. However, with the exception of Hole 504B, there has been no correlation of seismic structure with lithology. The primary disadvantage with using a drill hole to ground truth seismic velocities is that the seismic wavelength is on the order of several hundred meters, but the lithology is only observed in a small diameter core sample. Submersible observations at both the Blanco scarp [*Naidoo et al.*, 1992] and Hess Deep [*Francheteau et al.*, 1992; *Karson et al.*, 1992] have mapped the top of the sheeted dike sequence, and thus seismic experiments at either location could directly link velocity structure to lithology and determine the nature of the layer 2A/2B boundary. These locations have the advantage that two-dimensional variability can be followed for several kilometers. The thickness of the extrusive layer and transition zone at Hess Deep and the Blanco scarp differ by more than a factor of three (350 m vs. 1250 m) [*Francheteau et al.*, 1992; *Naidoo et al.*, 1992], and a comparison of velocity structure at the two locations could ascertain if layer 2B velocity is dependent on the thickness of layer 2A.

The shallow structure of intermediate-spreading ridges is not as well resolved as at the fast-spreading EPR. Seismic refraction and reflection data constrain the average extrusive thickness at the intermediate-spreading Juan de Fuca Ridge to be ~400 m, and suggest that thickness variability is greater than observed on the EPR. However, no study has mapped the base of layer 2A across the rise axis, which would provide better understanding of

emplacement processes within the neovolcanic zone. *Rohr et al.* [1988] have imaged the layer 2A reflector in a cross-axis MCS line, but it is intermittent in nature at the rise crest. The twin factors of streamer length and scattering from rough topography are probably contributing to their inability to continuously image the base of layer 2A. Additional MCS data, using the 4 km streamer presently available on the *R/V Maurice Ewing*, could probably produce a better image of layer 2A, and constrain the geometry of dike subsidence. Alternatively, a series of on-bottom refraction lines or a conventional airgun survey to a dense grid of receivers could be used to map variability in the depth to the layer 2A/2B boundary.

In contrast to fast-spreading and intermediate-spreading ridges, there are virtually no good constraints on the thickness of layer 2A at slow-spreading centers. At one location *Purdy and Detrick* [1986] do measure a 450 m thick surficial low-velocity layer, but it is underlain by no obvious layer 2A/2B boundary. *Smith and Cann* [1992] speculate that the sheeted dike complex at slow-spreading centers could be almost non-existent if the extrusive layer is built from a succession of small magma bodies, which might account for the lack of a prominent layer 2A/2B boundary. However, it is not at all certain that the shallow structure is fundamentally different from faster spreading-rate ridges. A series of on-bottom refraction experiments, complemented with conventional airgun refraction data, could test the *Smith and Cann* [1992] model by determining if a systematic stratigraphy is present similar to that observed on intermediate- and fast-spreading ridges.

In summary, knowledge of shallow crustal structure is the key to understanding emplacement processes at mid-ocean ridges. Seismic studies at the fast-spreading East Pacific Rise indicate that each technique has advantages and disadvantages. On-bottom seismic refraction experiments can provide high-resolution determinations of upper crustal velocities, but only for limited areas. Conventional airgun refraction studies can extend the velocity structure to a larger region, at the expense of resolution. Multi-channel seismic and wide-angle profile data can map horizons in the shallow crust over large areas, but

require good velocity information to be properly interpreted. Future work can ground truth seismic observations with observed lithology, and expand our knowledge of emplacement processes to intermediate-spreading and slow-spreading ridges.

References

Caress, D.W., M.S. Burnett and J.A. Orcutt, Tomographic image of the axial low-velocity zone at 12°50'N on the East Pacific Rise, *J. Geophys. Res.*, *97*, 9243-9263, 1992.

Christensen, N.I. and G.H. Shaw, Elasticity of mafic rocks from the Mid-Atlantic Ridge, *Geophys. J. R. Astron. Soc.*, *20*, 271-284, 1970.

Cudrak, C.F. and R.M. Clowes, Crustal structure of Endeavour ridge segment, Juan de Fuca ridge, from a detailed seismic refraction survey, *J. Geophys. Res.*, *98*, 6329-6349, 1993.

Francheteau, J., R. Armijo, J.L. Cheminee, R. Hekinian, P. Lonsdale and N. Blum, Dyke complex of the East Pacific Rise exposed in the walls of Hess Deep and the structure of the upper oceanic crust, *Earth Planet. Sci. Lett.*, *111*, 109-121, 1992.

Harding, A.J., G.M. Kent and J.A. Orcutt, A multichannel seismic investigation of upper crustal structure at 9°N on the East Pacific Rise: Implications for crustal accretion, *J. Geophys. Res.*, *98*, 13925-13944, 1993.

Harding, A.J., J.A. Orcutt, M.E. Kappus, E.E. Vera, J.C. Mutter, P. Buhl, R.S. Detrick and T.M. Brocher, Structure of young oceanic crust at 13°N on the East Pacific Rise from expanding spread profiles, *J. Geophys. Res.*, *94*, 12163-12196, 1989.

Holmes, M.L. and H.P. Johnson, Upper crustal densities derived from sea floor gravity measurements: northern Juan de Fuca Ridge, *Geophys. Res. Lett.*, *20*, 1871-1874, 1993.

Hooft, E.E. and R.S. Detrick, The role of density in the accumulation of basaltic melts at mid-ocean ridges, *Geophys. Res. Lett.*, *20*, 423-426, 1993.

Kappel, E.S. and W.B.F. Ryan, Volcanic episodicity and a non-steady state rift valley along the northeast Pacific spreading centres: evidence from SeaMARC I, *J. Geophys. Res.*, *91*, 13925-13940, 1986.

Kappus, M.E., A baseline for upper crustal velocity variations along the East Pacific Rise, Ph.D. Thesis, 158 pp., University of California, San Diego, 1991.

Karson, J.A., S.D. Hurst and P. Lonsdale, Tectonic rotations of dikes in fast-spread oceanic crust exposed near Hess Deep, *Geology*, *20*, 685-688, 1992.

Kent, G.M., A.J. Harding and J.A. Orcutt, Distribution of magma beneath the East Pacific Rise between the Clipperton Transform and the 9°17'N deval from forward modeling of common depth point data, *J. Geophys. Res.*, *98*, 13945-13969, 1993a.

Kent, G.M., A.J. Harding and J.A. Orcutt, Distribution of magma beneath the East Pacific Rise near the 9°03'N overlapping spreading center from forward modeling of common depth point data, *J. Geophys. Res.*, *98*, 13971-13995, 1993b.

Kent, G.M., A.J. Harding, J.A. Orcutt, R.S. Detrick, J.C. Mutter and P. Buhl, The uniform accretion of oceanic crust south of the Garrett Transform at 14°15'S on the East Pacific Rise, *J. Geophys. Res.*, *in press*, 1993c.

Kuo, B.Y., D.W. Forsyth and E.M. Parmentier, Flexure and thickening of the lithosphere at the East Pacific Rise, *Geophys. Res. Lett.*, *13*, 681-684, 1986.

Macdonald, K.C. and P.J. Fox, The axial summit graben and cross-sectional shape of the East Pacific Rise as indicators of axial magma chambers and recent volcanic eruptions, *Earth Planet. Sci. Lett.*, *88*, 119-131, 1988.

Madsen, J., D.W. Forsyth and R.S. Detrick, A new isostatic model for the East Pacific Rise crest, *J. Geophys. Res.*, *89*, 9997-10016, 1984.

Madsen, J.A., R.S. Detrick, J.C. Mutter, P. Buhl and J.A. Orcutt, A two- and three-diimensional analysis of gravity anomalies associated with the East Pacific Rise at 9°N and 13°N, *J. Geophys. Res.*, *95*, 4967-4987, 1993.

McDonald, M.A., J.A. Hildebrand, S.C. Webb and C.G. Fox, Seismic structure and anisotropy of the Juan de Fuca Ridge at 45°N, *J. Geophys. Res.*, *in press*, 1993.

Naidoo, D.D., J.R. Delaney and T. Juteau, A scarp-map profile of upper oceanic crust at the West Blanco Transform (WBT): insights into magmatic accretion (abstract), *EOS Trans. AGU*, *73* (43), Fall Supp., 502, 1992.

Purdy, G.M. and R.S. Detrick, The crustal structure of the mid-Atlantic Ridge at 23°N from seismic refraction studies, *J. Geophys. Res.*, *91*, 3739-3762, 1986.

Rohr, K.M.M., B. Milkereit and C.J. Yorath, Asymmetric deep crustal structure across the Juan de Fuca Ridge, *Geology*, *16*, 533-537, 1988.

Scheirer, D.S. and K.C. Macdonald, Variation in cross-sectional area of the axial ridge along the East Pacific Rise: evidence for the magmatic budget of a fast spreading center, *J. Geophys. Res.*, *98*, 7871-7885, 1993.

Sempere, J.-C., K. Macdonald, S. Miller and L. Shure, Detailed study of the Brunhes/Matayama reversal boundary on the East Pacific Rise at 19°30'S: implications for crustal emplacement processes at an ultra fast spreading center, *Mar. Geophys. Res.*, *9*, 1-23, 1987.

Sinton, J.M. and R.S. Detrick, Mid-ocean ridge magma chambers, *J. Geophys. Res.*, *97*, 197-216, 1992.

Smith, D.K. and J.R. Cann, The role of seamount volcanism in crustal construction at the Mid-Atlantic Ridge (24°-30°N), *J. Geophys. Res.*, *97*, 1645-1658, 1992.

Stolper, E. and D. Walker, Melt density and the average composition of basalt, *Contrib. Mineral. Petrol.*, *74*, 7-12, 1980.

Tivey, M.A., A measurement of the vertical magnetic structure of ocean crust using near-bottom sensors (abstract), *EOS Trans. AGU*, *73* (14), Spring Supp., 90, 1992.

Tivey, M.A., The fine-scale magnetic anomaly field over the Southern Juan de Fuca Ridge: the axial magnetization low and implications for crustal structure, *J. Geophys. Res.*, *in press*, 1993.

Tivey, M.A. and H.P. Johnson, Variations in oceanic crustal structure and implications for the fine-scale magnetic anomaly signal, *Geophys. Res. Lett.*, *20*, 1879-1882, 1993.

Toomey, D.R., G.M. Purdy, S.C. Solomon and W.S.D. Wilcock, The three-dimensional seismic velocity structure of the East Pacific Rise near latitude 9°30'N, *Nature*, *347*, 639-645, 1990.

Vera, E.E. and J.B. Diebold, Seismic imaging of oceanic layer 2A between 9°30'N and 10°N on the East Pacific Rise from two-ship wide aperture profiles, *J. Geophys. Res.*, *in press*, 1993.

Vera, E.E., J.C. Mutter, P. Buhl, J.A. Orcutt, A.J. Harding, M.E. Kappus, R.S. Detrick and T.M. Brocher, The structure of 0- to 0.2-m.y.-old oceanic crust at 9°N on the East Pacific Rise from expanded spread profiles, *J. Geophys. Res.*, *95*, 15529-15556, 1990.

Wang, X. and J.R. Cochran, Gravity anomalies, isostasy, and mantle flow at the East Pacific Rise crest, *J. Geophys. Res.*, *98*, 19505-19531, 1993.

White, D.J. and R.M. Clowes, Shallow crustal structure beneath the Juan de Fuca Ridge from 2-D seismic refraction tomography, *Geophys. J. Int.*, *100*, 349-367, 1990.

Wilcock, W.S.D., The seismic attenuation structure of the East Pacific Rise, Ph.D. Thesis, 337 pp., WHOI/MIT Joint Program in Oceanography, 1992.

Wilcock, W.S.D., S.C. Solomon, G.M. Purdy and D.R. Toomey, The seismic attenuation structure of a fast-spreading mid-ocean ridge, *Science*, *258*, 1470-1474, 1992.
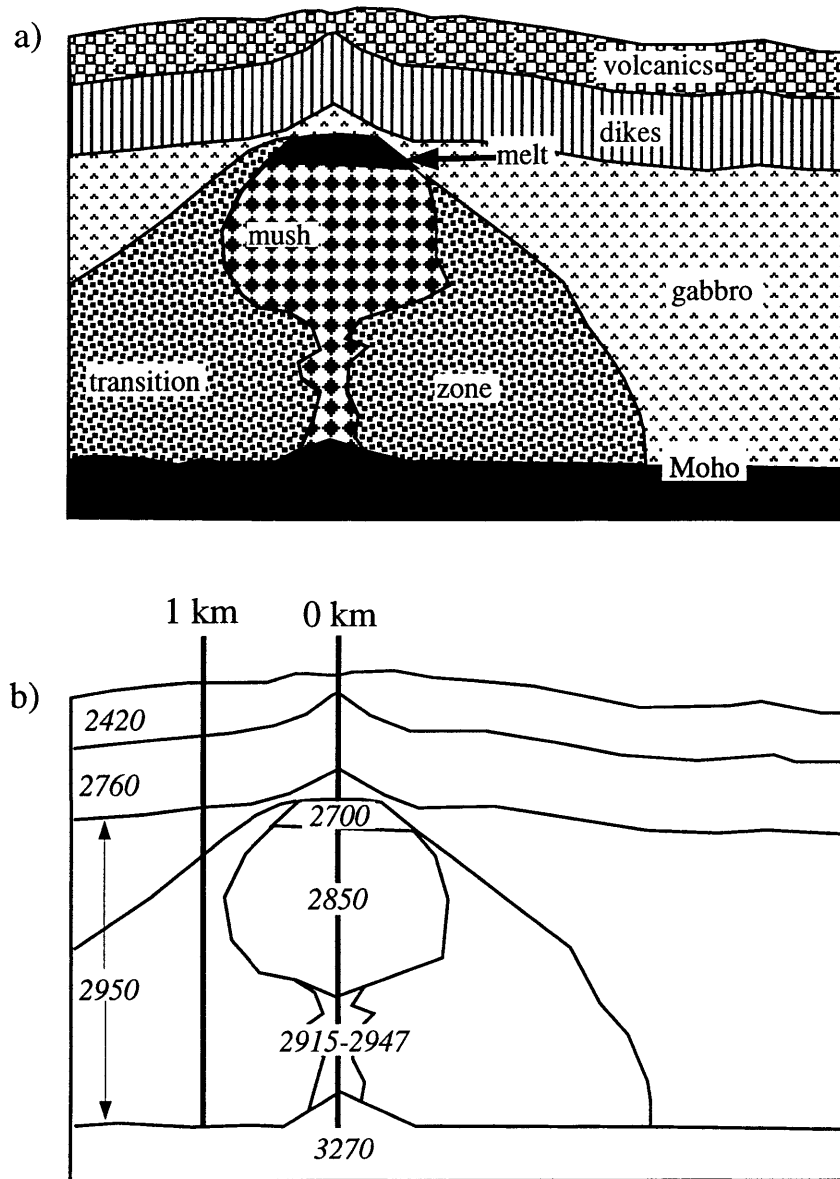
Figure 6.1. (a) Composite magma chamber model of *Sinton and Detrick* [1992], modified to include rapid thickening of the volcanic layer. (b) Density values (in kg/m^3) associated with the model pictured in Figure 6.1a. The location of the isostasy calculations are indicated by the heavy vertical lines.

ASC

a)

ASC

b)
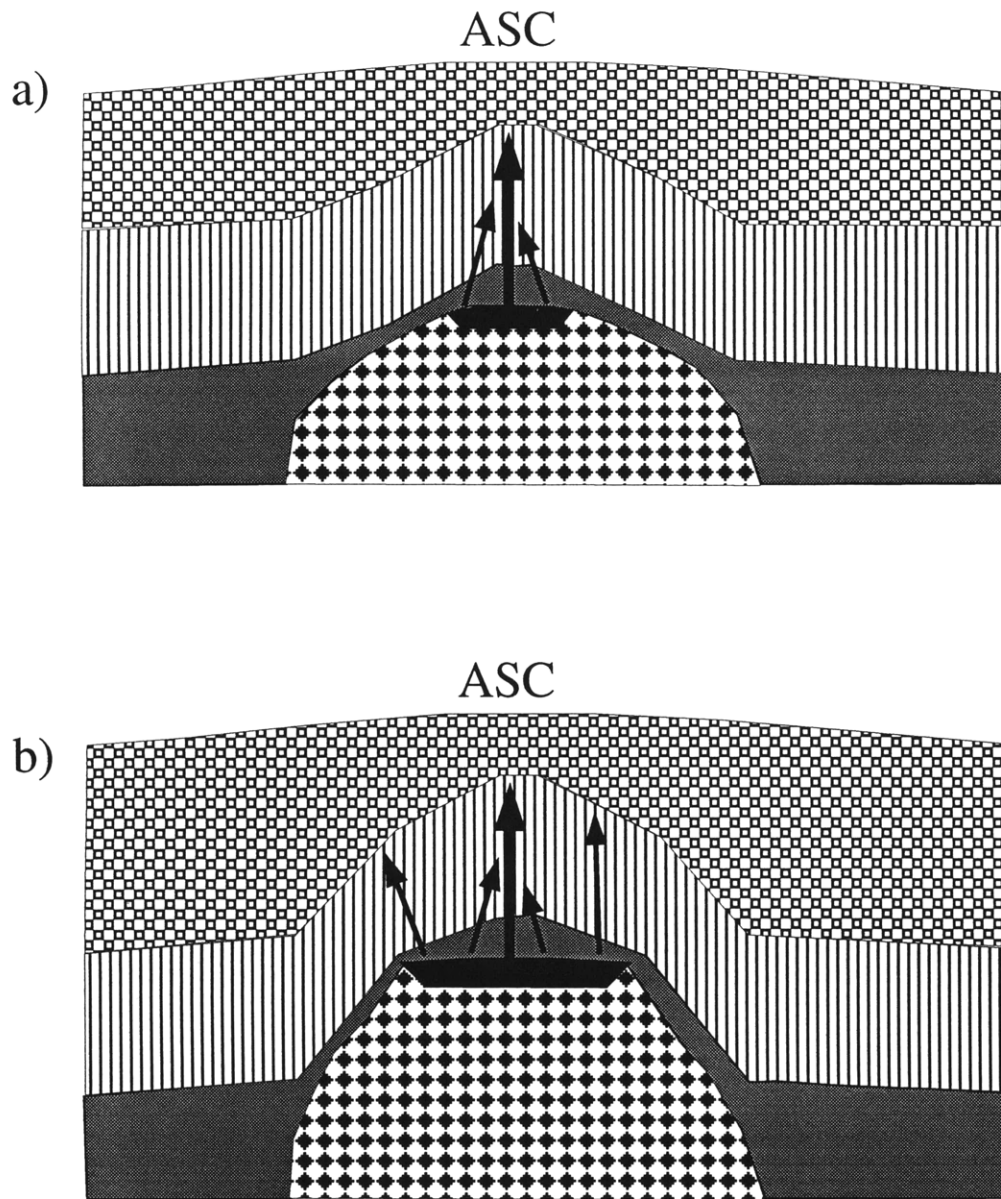
Figure 6.2. Schematic illustrating emplacement processes associated with a robust and a weak magma chamber. (a) Weak magma chamber. Dike injection primarily occurs in a narrow zone centered over the melt lens. (b) Robust magma chamber. Dike subsidence is greater than for (a). Compared to the weak magma chamber, dike injection occurs over a wider region, emplacing a greater proportion of extrusives outside the axial summit caldera.
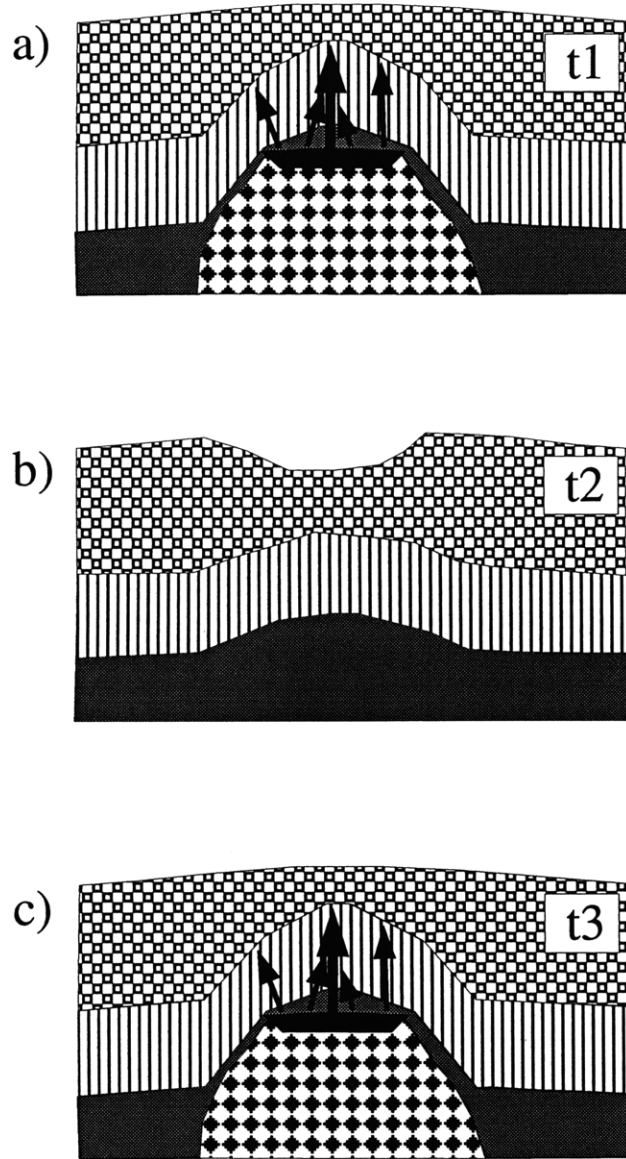
Figure 6.3. Schematic illustrating episodic nature of emplacement processes at an intermediate-spreading center, based on the model of *Kappel and Ryan* [1986]. (a) Robust magma chamber, similar in dimension to that believed to exist at a fast-spreading center. There is a considerable amount of dike subsidence. (b) Phase of volcanic inactivity. No larger magma chamber is present. (c) Renewed cycle of accretion.